

# **Myoglobin and Nitrite: An Electron Paramagnetic Resonance Led Investigation**

**Matthew John Bawn**

**School of Chemistry**

**University of East Anglia**

**A thesis submitted to the University of East Anglia in part-fulfillment of the  
degree of Doctor of Philosophy**

This copy of the thesis has been supplied on condition that anyone who consults it is understood to recognise that its copyright rests with the author and that use of any information derived there from must be in accordance with current UK Copyright Law. In addition, any quotation or extract must include full attribution.

**© January 2012**

---

**DECLARATION**

I declare that the work contained in this thesis, submitted by me for the degree of Ph.D., is my own work, except where due reference is made to other authors, and has not been previously submitted by me for a degree at any other university.

Matthew John Bawn,

January 2012.

---

## Abstract

The primary function of myoglobin (Mb) has long been considered to be the cellular storage and supply of oxygen. Recently, however, a role has been suggested for Mb as a nitrite reductase under hypoxic conditions. In this circumstance Mb is theorized to reduce myocardial oxygen consumption and thereby to reduce the risk of ischemic-reperfusion injury, a major source of tissue damage after periods of vasoconstriction as may be experienced after a stroke or heart attack. To understand the mechanism of nitrite reduction by Mb it is necessary to examine the binding of the anion to the protein substrate, which is the iron centre of a heme moiety. Crystal structures of horse-heart Mb and human hemoglobin (Hb) (hypothesized to be functionally related to Mb), suggested that the anion adopts the uncommon *O*-nitrito binding mode, in which the heme iron is directly coordinated to an oxygen of nitrite. In order to determine whether this binding mode occurs in protein unconstrained by crystallization, EPR spectroscopy was employed. To better understand the behavior of Mb under varying physiological conditions the protein was examined over a range of pH values [pH 5.0-10.8]. The EPR results suggested that the nitrite was able to bind to the heme in both conformations depending on the pH of the protein environment. The mechanistic implications of this were investigated using Density Functional Theory (DFT). The combined findings suggest that the two binding modes tune nitrite reductase activity of Mb to different degrees of hypoxia. Under severe hypoxic conditions there is indeed a nitrite reductase activity, but under mild hypoxia the protein behaves more as a nitrite sequestering protein preventing the production of nitric oxide from nitrite via the more conventional nitrite reductases. The implications of this for a proposed mechanism are discussed.

---

---

## Contents

<b>1</b>	<b>An Introduction to EPR.....</b>	<b>1</b>
1.1	Introduction.....	1
1.2	The Static Spin Hamiltonian .....	2
1.2.1	The Electronic Zeeman Effect.....	3
1.2.2	Zero-Field splitting .....	5
1.2.3	The Hyperfine Interaction .....	6
1.2.4	Nuclear Quadrupole Interaction .....	8
1.2.5	From the Hamiltonian to something Useful .....	9
1.3	Relaxation.....	9
1.3.1	General Introduction .....	10
1.3.2	The Rotating Frame .....	10
1.3.3	Polarization and Coherence .....	13
1.3.4	Longitudinal Relaxation .....	14
1.3.5	Transverse Relaxation.....	15
1.3.6	Phase-Memory Time.....	16
1.4	Orientation Selectivity .....	16
<b>2</b>	<b>An Introduction to Heme Proteins.....</b>	<b>19</b>
2.1	Introduction.....	19
2.2	Structure.....	19
2.2.1	Iron.....	20
2.2.2	Porphyrin.....	22

---

---

2.2.3	Protein.....	26
2.3	Globins .....	29
<b>3</b>	<b>HYSCORE EPR of Heme Proteins.....</b>	<b>35</b>
3.1	Introduction.....	35
3.2	Overview of the HYSCORE experiment.....	35
3.3	Low-Spin Systems .....	40
3.3.1	Cobalt Model Complexes .....	40
3.3.2	Iron Model Complexes.....	41
3.3.3	Van Doorslaer Low-Spin Ferric Complexes Methodology .....	42
3.3.4	Nitrosyl-Hemoglobin.....	43
3.3.5	Cytochrome b <sub>559</sub> .....	46
3.3.6	Nitrosyl cd <sub>1</sub> Nitrite Reductase .....	47
3.3.7	Cytochrome P450 .....	49
3.4	Nitrosyl Myoglobin .....	49
3.5	High-spin hemes .....	51
3.5.1	Problems associated with high-spin hemes for hyperfine EPR.....	51
3.5.2	Neuroglobin.....	52
3.5.3	Aquometmyoglobin .....	53
<b>4</b>	<b>Myoglobin and Nitrite.....</b>	<b>67</b>
4.1	Research Motivation.....	67
4.2	Biological background.....	68
4.2.1	Introduction.....	68
4.2.2	Role of Myoglobin in Nitrite Reduction .....	68
4.2.3	Nitrite Anion Binding to Globins <i>N-nitro</i> versus <i>O-nitrito</i> .....	69
4.2.4	Richter-Addo H-bonding residue mutant investigation .....	72

---

---

4.3	Experimental Characterization of Myoglobin and Nitrite-Myoglobin.....	74
4.3.1	Reagents and Chemicals .....	74
4.3.2	Buffers.....	75
4.3.3	Optical spectroscopy of ferric myoglobin.....	76
4.3.4	Optical characterization of myoglobin at differing pH .....	77
4.3.5	pH Titration of Myoglobin-Nitrite .....	81
4.3.6	Spectral changes with the addition of nitrite .....	83
4.3.7	Evaluation of reported extinction coefficients .....	85
4.3.8	CW-EPR Investigation of Myoglobin.....	88
4.3.9	Investigation of Nitrite Ligated Myoglobin .....	91
<b>5</b>	<b>EPR Investigation of Nitrite Binding Mode.....</b>	<b>97</b>
5.1	Introduction.....	97
5.2	Nitrite Binding to Myoglobin over Time Using CW-EPR .....	97
5.3	Pulsed-EPR Investigation of nitrite binding Mode .....	104
5.3.1	Introduction to Field-Swept Echo (FSE) .....	104
5.3.2	Orientation of g-value Axes within Molecular Frame .....	105
5.3.3	Introduction to Electron Spin Echo Envelope Modulation (ESEEM) .....	106
5.3.4	Initial characterization of low-spin myoglobin.....	110
5.3.5	Pulsed-EPR Investigation of Low-Spin Myoglobin Nitrite.....	113
5.3.6	Three-Pulse ESEEM of Myoglobin Nitrite .....	114
5.3.7	Isotope labeled nitrite.....	117
5.3.8	Simulation of Nitrite Nuclear Couplings .....	119
5.3.9	HYSCORE .....	122
5.3.10	HYSCORE of LS Mb .....	125
5.3.11	HYSCORE of Mb-NO <sub>2</sub> <sup>-</sup> .....	129

---

---

<b>6</b>	<b>Further Elucidations for Myoglobin.....</b>	<b>135</b>
6.1	Introduction.....	135
6.2	Myoglobin at a low pH.....	135
6.3	Multi-frequency continuous-Wave EPR.....	137
6.4	Matched-Pulse HYSCORE of Low-Spin Myoglobin-Nitrite .....	139
6.4.1	Matched HYSCORE.....	139
6.4.2	DONUT-HYSCORE.....	142
6.5	Two-Dimensional Three-Pulse ESEEM.....	144
6.6	High-Spin Myoglobin.....	145
6.6.1	Proton HYSCORE.....	148
6.7	ENDOR.....	149
6.7.1	ENDOR of Low-Spin Species .....	150
<b>7</b>	<b>Computational Investigation.....</b>	<b>154</b>
7.1	Computational Chemistry .....	154
7.2	Hartree-Fock.....	155
7.3	Electron Correlation.....	155
7.4	Density Functional Theory .....	155
7.4.1	Quantum Chemistry Basis Sets.....	156
7.5	Functionals .....	157
7.6	Orca.....	157
7.7	Choice of Functional .....	157
7.8	DFT calculations of nitrite binding modes .....	158
7.8.1	Constructing Model Geometries .....	159
7.9	Relaxed surface-scans.....	164
7.10	Indication of High-Spin State of N-bound Form.....	165

---

---

7.11	Conclusion .....	167
<b>8</b>	<b>Conclusions and Outlook.....</b>	<b>170</b>
8.1	Conclusions.....	170
8.1.1	EPR Insights to Nitrite Binding in Myoglobin .....	170
8.1.2	General insights for EPR.....	172
8.1.3	Density Functional Theory .....	173
8.2	Role of Mb as a Nitrite Reductase .....	173
8.3	Outlook.....	175
<b>1</b>	<b>Appendix: S-band CW-EPR: Complex I.....</b>	<b>178</b>
1.1	Introduction.....	178
1.2	Structure.....	178
1.3	The Present Conflict within Complex I.....	181
1.4	Experimental Procedure .....	183
1.5	Conclusion .....	189
<b>2</b>	<b>Appendix: PELDOR: Ferric Binding Protein.....</b>	<b>193</b>
2.1	Introduction.....	193
2.2	Ferric Binding Protein .....	194
2.3	PELDOR.....	195
2.4	Experimental Procedure .....	196
2.5	Results .....	200
2.6	Data Analysis .....	201
2.7	Discussion.....	202
2.8	Outlook.....	203
<b>3</b>	<b>Appendix: REFINE: Cytochrome <i>bc</i><sub>1</sub>.....</b>	<b>207</b>
3.1	Introduction.....	207

---

3.2	Background.....	208
3.3	Experimental Procedure .....	211
3.4	Conclusions.....	215

Complete references for each chapter are located at the end of the relevant chapter.

---

---

## List of Figures

### Chapter 1

<b>Figure 1.2.1-1</b> , Divergence of energy level of discrete spin states with application of magnetic field .....	3
<b>Figure 1.2.1-2</b> , Effect of g anisotropy on the EPR spectrum of a sample. ....	5
<b>Figure 1.2.3-1</b> , Energy level diagram for an electron spin $S=1/2$ coupled to a nuclear spin $I=1/2$ . ....	7
<b>Figure 1.3.2-1</b> , Definition of the lab-axes system .....	10
<b>Figure 1.3.2-2</b> , Precession of vectors representing the magnetic moments ( $\mu$ ) of electrons .....	11
<b>Figure 1.3.2-3</b> , The representation of linearly polarized microwaves .....	12
<b>Figure 1.3.3-1</b> , Precession of an ensemble of vectors with a random phase in the xy-plane .....	14
<b>Figure 1.3.6-1</b> , Calculated absorption spectra and orientation selectivity .....	17

### Chapter 2

<b>Figure 2.2.1</b> , $d(z^2, x^2-y^2)$ (top left and right respectively) electron orbitals. Schematic of heme centre .....	21
<b>Figure 2.2.2</b> , A Porphyrin macro-cycle (with positions labelled in conventional Fischer notation).....	22
<b>Figure 2.2.3</b> , Commonly encountered heme types. Heme <i>a</i> from 1QLE [11] .....	24
<b>Figure 2.2.4</b> , Chemical (left) and crystal (right) structure of heme <i>b</i> .....	25
<b>Figure 2.2.5</b> , the structure of tetraphenylporphyrin (TPP).....	26
<b>Figure 2.2.6</b> , CATH [21] assignment of hemoprotein secondary structure .....	27
<b>Figure 2.2.7</b> , Representation of frequency of amino acid residues commonly Found In heme .....	28
<b>Figure 2.2.8</b> , crystal structure of myoglobin nitrite complex showing secondary structure .....	29
<b>Figure 2.3-1</b> , crystal structure of mouse neuroglobin 2VRY .....	30

---

---

<b>Figure 2.3.2</b> , Examples of penta and hexa coordination .....	31
---	----

### Chapter 3

<b>Figure 3.2-1</b> , The standard HYSCORE pulse sequence.....	36
<b>Figure 3.2-2</b> , Simulated HYSCORE plot indicating weak and strong coupling .....	37
<b>Figure 3.2-3</b> , energy level diagrams for $S = 1/2$ $I = 1/2$ (top), and $S = 1/2$ $I = 1$ under cancellation .....	38
<b>Figure 3.3-1</b> , Structure of cobaltous Tetraphenylporphyrin (pyridine).....	40
<b>Figure 3.3-2</b> , Model of $^{15}\text{N}$ -porphyrin-Fe(II)-NO TPP complex .....	41
<b>Figure 3.3-3</b> , Conformational state of nitrosyl (nitric oxide) ligated heme-complexes ...	44
<b>Figure 3.3-4</b> , Simulation of HYSCORE spectrum of Cyt $b_{559}$ .....	47
<b>Figure 3.3-5</b> , Hyperfine couplings determined for coordinating nitrogens in nitrosyl $\text{cd}_1$ nitrite.....	48
<b>Figure 3.4-1</b> , H-bonding in nitrosyl myoglobin (red lines). .....	50
<b>Figure 3.5-1</b> , Summary of experiments used to determine hyperfine couplings in aquomet-Mb at X-band.....	53

### Chapter 4

<b>Figure 4.2.3-1</b> , N-nitro versus O-nitrito binding modes of the nitrite anion to a heme centre.....	69
<b>Figure 4.2.3-2</b> , N-nitro nitrate binding to heme centre in A) Cytochrome c nitrite reductase .....	70
<b>Figure 4.2.4-1</b> , Heme centre from crystal structures of Mb with ligated nitrite anion.	73
<b>Figure 4.3.3-1</b> , optical spectrum of high-spin and low-spin met-myoglobin .....	76
<b>Figure 4.3.4-1</b> , results from pH titration of Mb .....	78
<b>Figure 4.3.4-2</b> , wavelength of Soret Band maximum versus pH for myoglobin. ....	79
<b>Figure 4.3.4-3</b> , Intensity profile of LS bands of Mb as a function of pH. ....	80
<b>Figure 4.3.5-1</b> , results from pH titration of Mb in the presence of 240-fold excess nitrite.....	81

---

---

<b>Figure 4.3.5-2</b> , wavelength of Soret Band maximum versus pH for myoglobin with nitrite.....	82
<b>Figure 4.3.6-1</b> , Spectral changes during the reaction of metmyoglobin with nitrite ....	84
<b>Figure 4.3.7-1</b> , Mb titration difference spectrum .....	86
<b>Figure 4.3.8-1</b> , CW-EPR spectrum of 100 $\mu$ M horse heart myoglobin .....	88
<b>Figure 4.3.8-2</b> , CW-EPR spectrum of 100 $\mu$ M horse heart myoglobin pH range .....	89
<b>Figure 4.3.9-1</b> , Top: CW-EPR spectrum of 100 $\mu$ M horse heart myoglobin nitrite.....	91

## Chapter 5

<b>Figure 5.3.1-1</b> , X-band CW-EPR spectra at 10 K of 2 mM Mb pH 10.8 .....	98
<b>Figure 5.3.1-2</b> , Simulation of data in Figure 5.3.1-1 pH 10.8.....	99
<b>Figure 5.3.1-3</b> , CW-EPR showing spectra of Mb before and after the addition of nitrite (top) .....	102
<b>Figure 5.3.1-1</b> , Simulated spectrum of LS-Mb (top) shown in absorbance (dashed) and derivative (solid) .....	104
<b>Figure 5.3.2-1</b> , g-value definition of FSE (top) and relation to geometry of heme in Mb (bottom) .....	105
<b>Figure 5.3.3-1</b> , Pulse sequence for three-pulse ESEEM (bottom).....	107
<b>Figure 5.3.3-2</b> , Energy level diagram for $S=1/2$ , $I=1$ under cancellation condition. ....	108
<b>Figure 5.3.4-1</b> , FSE spectra of LS-Mb measured with $\tau$ -values of 120 and 240 ns .....	110
<b>Figure 5.3.4-2</b> , Frequency domain three-Pulse ESEEM of 1mM Myoglobin .....	111
<b>Figure 5.3.4-3</b> , Simulated three-pulse ESEEM spectra of myoglobin.....	112
<b>Figure 5.3.5-1</b> , FSE spectra measured at 10 K of Mb-NO <sub>2</sub> <sup>-</sup> .....	113
<b>Figure 5.3.6-1</b> , Three-Pulse ESEEM frequency domain spectra of Mb pH 10.8 and Mb-NO <sub>2</sub> <sup>-</sup> .....	114
<b>Figure 5.3.6-2</b> , Three-Pulse ESEEM time domain and frequency domain spectra of Mb .....	116
<b>Figure 5.3.7-1</b> , FSE of Mb- <sup>14</sup> NO <sub>2</sub> and Mb- <sup>15</sup> NO <sub>2</sub> (red) measured at 10 K with a $\tau$ -value of 120 ns .....	117
<b>Figure 5.3.7-2</b> , Three-Pulse ESEEM spectra of Mb-nitrite .....	118

---

---

<b>Figure 5.3.8-1</b> , Simulation of Mb-NO <sub>2</sub> <sup>-</sup> three-pulse ESEEM spectrum .....	119
<b>Figure 5.3.9-1</b> , the standard HYSCORE pulse sequence .....	122
<b>Figure 5.3.9-2</b> , HYSCORE Simulation of two <sup>1</sup> H and one <sup>13</sup> C nuclei.....	123
<b>Figure 5.3.10-1</b> , HYSCORE of LS-Mb measured at 10 K near canonical positions .....	126
<b>Figure 5.3.10-2</b> , Easyspin simulation of HYSCORE spectrum of LS-Mb .....	127
<b>Figure 5.3.10-3</b> , HYSCORE spectra of LS-Mb near canonical positions .....	128
<b>Figure 5.3.11-1</b> , HYSCORE spectra of Mb-NO <sub>2</sub> <sup>-</sup> at pH 7.5 at 10 K. ....	129
<b>Figure 5.3.11-2</b> , HYSCORE spectra of LS-Mb and Mb-NO <sub>2</sub> <sup>-</sup> .....	130

## Chapter 6

<b>Figure 6.2-1</b> , Spectral changes observed for Mb-NO in five and six coordinate environments.....	136
<b>Figure 6.3-1</b> , EPR spectra of Mb and Mb-NO <sub>2</sub> <sup>-</sup> complexes .....	138
<b>Figure 6.4.1-1</b> , Pulse Sequence used for matched-HYSCORE experiments.....	139
<b>Figure 6.4.1-2</b> , Matched-HYSCORE frequency-domain spectra of Mb- <sup>15</sup> NO <sub>2</sub> <sup>-</sup> .....	140
<b>Figure 6.4.1-3</b> , Matched-pulse HYSCORE of the g <sub>z</sub> -position of Mb-NO <sub>2</sub> <sup>-</sup> .....	141
<b>Figure 6.4.2-1</b> , DONUT-HYSCORE pulse sequence .....	142
<b>Figure 6.4.2-2</b> , Comparison of HYSCORE and DONUT-HYSCORE of Mb <sup>15</sup> NO <sub>2</sub> <sup>-</sup> .....	143
<b>Figure 6.5-1</b> , Two-dimensional three-pulse ESEEM spectra of Mb-NO <sub>2</sub> <sup>-</sup> .....	144
<b>Figure 6.6-1</b> , Field-swept echo spectrum of high-spin Mb .....	145
<b>Figure 6.6-2</b> , Examination of the low-field (g ~ 6) region of HS Mb and Mb-nitrite spectra. ....	146
<b>Figure 6.6.1-1</b> , HYSCORE spectra of HS-Mb pH 6.3 and HS Mb-nitrite pH 9.5 .....	148
<b>Figure 6.7-1</b> , Pulse sequences for Davies ENDOR and Mims ENDOR.....	149
<b>Figure 6.7.1-1</b> , Mims ENDOR of Mb-nitrite at pH 7.5.....	150

---

---

**Chapter 7**

<b>Figure 7.7-1</b> , Results of web of science search “DFT calculations hemes” .....	158
<b>Figure 7.8-1</b> , Myoglobin-nitrite model schemes to be examined.....	159
<b>Figure 7.8-2</b> , Fragment construction for Mb-nitrite <i>O</i> -bound mode. ....	160
<b>Figure 7.8-3</b> , Initial and final geometries for unconstrained <i>N</i> -bound nitrite. ....	161
<b>Figure 7.8-4</b> , Rotation of distal histidine away from nitrite .....	162
<b>Figure 7.8-5</b> , Spin density plots of model geometries.....	163
<b>Figure 7.10-1</b> , Relaxed Surface scan of HS and LS nitrosyl-Mb.....	165
<b>Figure 7.10-2</b> , Spin Density of <i>O</i> -bound and <i>N</i> -bound Mb-nitrite. ....	166

**Appendix 1**

<b>Figure 1.2-1</b> , Structure of the hydrophilic domain of Complex I from <i>Thermus thermophilus</i> .....	179
<b>Figure 1.4-1</b> , Simulation of complex I S-band CW-EPR.....	185
<b>Figure 1.4-2</b> , S-band EPR spectra of -400 mV Complex I .....	186
<b>Figure 1.4-3</b> , -400 mV poised Complex I spectrum at 12 K .....	187
<b>Figure 1.4-4</b> , S-band EPR spectra of -300 mV potential complex I measured at 12 K .	188
<b>Figure 1.4-5</b> , S-band EPR spectra of -1000 mV poised complex I sample .....	189

**Appendix 2**

<b>Figure 2.2-1</b> , Structure of ferric binding protein (FbpA) from <i>N. gonorrhoea</i> 1D9Y .....	194
<b>Figure 2.3-1</b> , PELDOR pulse sequence. ....	195
<b>Figure 2.4-1</b> , Simulation of MTSL spin-labeled Cu(II) Fbp R48C.....	197
<b>Figure 2.4-2</b> , Two-dimensional two-pulse $t_2$ relaxation plot of Cu(II) Fbp at 10K. ....	198
<b>Figure 2.4-3</b> , Crystal structure 1D9Y and Cu(II) MTSL distance scheme. ....	199
<b>Figure 2.4-4</b> , Pump and observe positions for initial PELDOR experiment Fbp 10K....	200
<b>Figure 2.5-1</b> , PELDOR traces of FbpA.....	201
<b>Figure 2.6-1</b> , Data Analysis summary from DeerAnalysis 2011 of PELDOR trace.....	202

---

**Appendix 3**

<b>Figure 3.2-1</b> , Structure of yeast cyt $bc_1$ complex 1KB9 .....	208
<b>Figure 3.3-1</b> , X-band cw-EPR spectra of the reduced $bc_1$ -complex from yeast .....	212
<b>Figure 3.3-2</b> , Plot of the time traces observed using varying relaxation times .....	214

---

---

**List of Tables****Chapter 3**

<b>Table 3-1</b> , Nuclear quadrupole interaction parameters for the heme pyrrole $^{14}\text{N}$ in nitrosyl-hemoprotein .....	45
<b>Table 3-2</b> , Heme nitrogen hyperfine and quadrupole coupling parameters.....	60

**Chapter 4**

<b>Table 4-1</b> , Buffers used in the course of the investigation of nitrite binding to Mb. ....	75
<b>Table 4-2</b> , Extinction coefficients reported for Mb .....	85
<b>Table 4-3</b> , Calculated concentrations of Mb titration experiment .....	87
<b>Table 4-4</b> , Principle g-values for two species in Mb-OH <sup>-</sup> .....	90

**Chapter 5**

<b>Table 5-1</b> , Simulation parameters used in 5.2.. .....	100
<b>Table 5-2</b> , Effect on pH of 50 $\mu\text{M}$ Mb solution of addition of sodium nitrite.....	100
<b>Table 5-3</b> , MbOH $^{14}\text{N}$ nuclear parameters used for initial three-pulse ESEEM simulation.....	112
<b>Table 5-4</b> , MbOH $^{14}\text{N}$ nuclear parameters used for final three-pulse ESEEM simulation.....	113
<b>Table 5-5</b> , Approximate magnetic field positions of principle g-values for Mb-OH ....	115
<b>Table 5-6</b> , Nuclear coupling parameters for $^{14}\text{N}$ of nitrite in Mb-NO <sub>2</sub> <sup>-</sup> .....	120

**Chapter 7**

<b>Table 7-1</b> , Difference in energies of models using BP86/TZVP level of theory. ....	161
<b>Table 7-2</b> , Final single-point energies of models using B3LYP/SV(P) level of theory...	164

---

**Appendix 1****Table 1-1**, Simulation parameters for individual Fe-S clusters of Complex I at pH 7... 184

## Preface

I will inform the reader that I am not a chemist, nor am I a biologist and yet I found myself in the School of Chemistry at the University of East Anglia undertaking a PhD in Electron Paramagnetic (EPR) Spectroscopy. Nor did I necessarily follow the conventional route in to academia: Whilst working in industry after completing my undergraduate degree in physics I was offered the opportunity of continuing my studies. It can also be seen by glancing at my PhD timeline that I have been involved with a number of projects since I began in 2007. The main body of this thesis is concerned with one project in particular and is outlined in the abstract following. The initial investigation into whether different binding modes of nitrite to myoglobin could be resolved using pulsed-EPR originated from Dr Myles Cheesman as a proof-of-principle for application to hydroxylamine ligation to cytochrome *cd<sub>1</sub>* Nitrite reductase of *Paracoccus pantotrophus*. During background reading I discovered there was a biological significance to the myoglobin situation with regard to hypoxic conditions. I therefore expanded this question into a major research project, by using pH to simulate varying degrees of hypoxia. Computational chemistry was another area that I had been interested in since beginning my PhD and I decided to apply this to the project in March of 2011. From the beginning of this project I have, for better or worse, led and determined the course of the research. Thus explaining it as the focus of my thesis, I feel better able to defend work that I have had complete control over. I will include some of the background and results of my other projects as appendices but ultimately the initial research questions were generated by others and/or I had very little input in the overall research philosophy, although of course each helped me to develop as a researcher. I would like to take this opportunity to thank Dr Justin Bradley who has helped me by reading a great deal of the following work and for his helpful discussions during the course of my PhD. I would also like to thank Prof. Andrew Thomson for an important conversation that gave me confidence in this work. Ubiquitous thanks go to the EPSRC to providing the funding to undertake it. During the last year I have supervised two project students who contributed to aspects of the original work: Chris Stephens and Alex Morley. Also to Jess van Wonderen, Morgan Bye and James Tolchard for helpful discussions and moral support during the course of my PhD. Finally of course I would like to extend my gratitude to my supervisor Dr Fraser MacMillan for allowing me to work in his group and for

---

the generous use of EPR spectrometers throughout my studies, as well as introducing me to a number of projects during my time at UEA.

---

---

## Abbreviations

<b>1D</b>	One dimensional
<b>2D</b>	Two dimensional
<b>COSY</b>	Correlation Spectroscopy
<b>CW</b>	Continuous Wave
<b>Cyt</b>	Cytochrome
<b>DFT</b>	Density Functional Theory
<b>DONUT</b>	Double Nuclear Coherence Transfer
<b>DQ</b>	Double Quantum
<b>ENDOR</b>	Electron Nuclear Double Resonance
<b>EPR</b>	Electron Paramagnetic Resonance
<b>ESEEM</b>	Electron Spin Echo Envelope Modulation
<b>EZ</b>	Electron Zeeman
<b>Hb</b>	Hemoglobin
<b>HFI</b>	Hyperfine Interaction
<b>HFS</b>	Hyperfine Splitting
<b>His</b>	Histidine
<b>HS</b>	High-Spin
<b>HYSCORE</b>	Hyperfine sublevel Correlation Spectroscopy
<b>LS</b>	Low-Spin
<b>Mb</b>	Myoglobin
<b>Met</b>	Methionine
<b>MW</b>	Microwave
<b>NQI</b>	Nuclear Quadrupole Interaction
<b>NZ</b>	Nuclear Zeeman
<b>SQ</b>	Single Quantum
<b>TPP</b>	Tetraphenylporphyrin
<b>ZFS</b>	Zero Field Splitting

---

---

## List of Symbols

<b>A</b>	Hyperfine tensor
<b>A<sub>iso</sub> , a<sub>iso</sub></b>	Isotropic component of Hyperfine interaction
<b>B<sub>0</sub></b>	Static magnetic field
<b>B<sub>1</sub></b>	Applied magnetic field
<b>D</b>	Zero-field interaction tensor
<b>G</b>	g-factor
<b>H</b>	Planks constant $6.63 \times 10^{-34}$ J.s
<b>I</b>	Nuclear spin operator
<b>K</b>	Quadrupole coupling constant
<b>m<sub>I</sub></b>	Nuclear spin manifold
<b>m<sub>S</sub></b>	Electron spin manifold
<b>P</b>	Nuclear quadrupole tensor
<b>S</b>	Electron spin operator
<b>T</b>	Dipolar component of hyperfine Interaction
<b>T<sub>1</sub></b>	Longitudinal relaxation time
<b>T<sub>2</sub></b>	Transverse relaxation time
<b>T<sub>M</sub></b>	Phase-memory time
<b>η</b>	Quadrupole asymmetry parameter
<b>μ<sub>B</sub></b>	Bohr Magneton $9.274 \times 10^{-24}$ J.T <sup>-1</sup>
<b>N</b>	Frequency
<b>ω<sub>I</sub></b>	Nuclear Zeeman frequency

---

**PhD Timeline****2007**

- November Began PhD at UEA  
Tasked with S X Q-band CW-EPR spectrometer reassembly

**2008**

- March SXQ CW-EPR spectrometer calibration  
May S-band CW-EPR colicin (low-temperature)  
S-band Complex I (NADH dehydrogenase)  
June Q-band CW-EPR colicin (low-temperature)  
September Pulsed EPR training  
December Room temperature S and Q-band colicin

**2009**

- February Ferric binding protein (Fbp)  
March PELDOR  
May Super HQ CW-EPR  
December Tol C

**2010**

- April Tol C chromium compound  
June Cytochrome  $bc_1$  X-band CW-EPR  
December Nitrite binding in myoglobin

**2011**

- March Initial computational chemical calculations with *Orca*  
August End of EPR experimental research
-

**For Foxcat and Foxkitten**

**And for my Parents**

**Who have always believed in me**

---

---

---

# 1 CHAPTER **An Introduction to Electron Paramagnetic Resonance EPR**

---

## 1.1 Introduction

In general, spectroscopy may be considered as the measurement of the interaction of electromagnetic radiation with a material. Electron Paramagnetic Resonance (EPR) spectroscopy is no exception and utilizes microwave frequency electromagnetic radiation (typically in the region 2-280 GHz) to perturbate unpaired electrons within the sample of interest. As chemical binding is electron pairing, such unpaired electrons are relatively rare, however, they are usually reactive and/or catalytically active and so may be of great interest. Examples include transition metal [1] and rare earth ions [2], free radicals [3] and crystal defects [4]. Diamagnetic materials may also be studied using EPR by the addition of spin probes to the sample of interest [5]. Molecules or atoms have discrete states, each of which with a corresponding energy. The measurement and interpretation of the energy differences between these different states in atoms or molecules yields information relating to the identity, structure and dynamics of the sample under study and is known as spectroscopy. Planck's law describes the energy of electromagnetic radiation:

$$E = h\nu \quad (1.1)$$

Where  $h$  is Planck's constant:  $6.63 \times 10^{-34}$  J.s,  $\nu$  is the frequency of the radiation, and  $E$  is the energy.

The absorption of energy can cause a transition from the lower energy state to the higher. For conventional spectroscopy if the frequency  $\nu$  is swept the frequencies at which absorption occur correspond to the energy differences of the states.

---

## 1.2 The Static Spin Hamiltonian

The transition frequencies and transition probabilities between the different energy states of the electron or electrons under consideration may be found by considering all the interactions that lead to energy differences between states. The EPR spectrum of a paramagnetic species in an external magnetic field  $\mathbf{B}_0$  can be described by a Hamiltonian of the form of **(1.2)**[6] which contains the contributions of all these interactions.

$$H_0 = H_{EZ} + H_{ZFS} + H_{HFS} + H_{NZ} + H_Q \quad (1.2)$$

Where the above terms stand for Electronic Zeeman (EZ), Zero-Field Splitting (ZFS), Hyper-Fine Splitting (HFS), Nuclear Zeeman (NZ) and Quadrupolar (Q) respectively.

Equation (1.2) may be expanded as follows:

$$H_0 = \mu_B \tilde{\mathbf{B}}_0 \mathbf{g} \mathbf{S} / h + \tilde{\mathbf{S}} \mathbf{D} \mathbf{S} + \sum_{k=1}^m \tilde{\mathbf{S}} \mathbf{A}_k \mathbf{I}_k - \mu_B \sum_{k=1}^m \mathbf{g}_{n,k} \tilde{\mathbf{B}}_0 \mathbf{I}_k / h + \sum_{I_k > 1/2} \tilde{\mathbf{I}}_k \mathbf{P}_k \mathbf{I}_k \quad (1.3)$$

$\mu_B$  = Bohr magneton ( $9.27 \times 10^{-24}$  J. T<sup>-1</sup>)

$\mathbf{B}_0$  = Applied Magnetic field

$\mathbf{g}$  = g-tensor

$\mathbf{S}$  = Electron spin operator

$\mathbf{I}_k$  = Nuclear spin operator

$h$  = Planck's constant

$\mathbf{D}$  = symmetric zero-field interaction tensor

$\mathbf{A}$  = Hyperfine tensor

$\mathbf{P}$  = Nuclear quadrupole tensor

Non-scalar quantities are denoted with a bold type-face. And a  $\sim$  denotes the transpose of the vector.

The spin Hamiltonian above **(1.3)** is constructed to define the energy of the system under study solely by its spin state. Magnetism arises from a combination of charge and angular momentum, and an electron has charge and spin producing a magnetic moment. However a

bound electron may also have a contribution to its angular momentum from its orbital motion (giving rise to g-value anisotropy). It can be seen from the Hamiltonian that the Electronic Zeeman and Nuclear Zeeman terms are dependent on the applied magnetic field. This aspect can be used to resolve contributions in an EPR spectrum from these terms, by performing multi-frequency EPR. The other terms are independent of the field and so the spectral representation of their contributions will remain constant at different frequencies.

### 1.2.1 The Electronic Zeeman Effect

When an unpaired electron is placed into an external magnetic field,  $\mathbf{B}_0$ , its magnetic moment interacts with this field (Zeeman Interaction) and can adopt  $(2S+1)$  orientations relative to the direction of  $\mathbf{B}_0$  (see **Figure 1.2.1-1**).

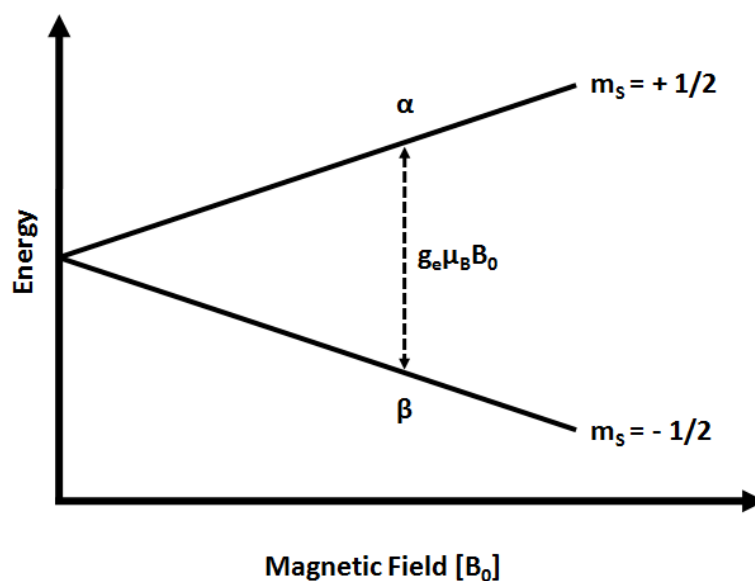


**Figure 1.2.1-1, Divergence of energy level of discrete spin states with application of magnetic field for an  $S = 1/2$  system**

A free electron,  $S = 1/2$ , is restricted to two positions, referred to as up and down. When in the presence of a magnetic field the electron will have a state of lowest energy when aligned in the same direction as the field, and highest energy when aligned against the magnetic field direction.

From the above Hamiltonian **(1.3)** the Electronic Zeeman interaction can be expressed by:

$$E = g\mu_B\mathbf{B}_0\mathbf{S} = \pm \frac{1}{2}g\mu_B\mathbf{B}_0 \quad (1.4)$$

Where  $g$  is the  $g$ -factor, a proportionality constant describing the divergence of the energy levels due to an applied magnetic field, and  $\mu_B$  is the Bohr magneton, the natural unit of electronic magnetic moment. From equation **(1.4)** it can be seen that the two spin states have the same energy in the absence of a magnetic field, and that the energy of the states diverges linearly with increasing magnetic field.

These facts have important consequences for EPR spectroscopy of an isotropic  $S = 1/2$  system, namely that without a magnetic field there is no measurable energy difference, and when there is a magnetic field the energy difference is linearly dependant on the field. As the energy differences between the two states can be varied by alteration of the magnetic field strength, one can obtain spectra by maintaining a constant electromagnetic radiation frequency and scanning the magnetic field (microwave frequency is kept constant due to stability of microwave source). When the magnetic field is equal to a value that tunes the spin states so that their difference in energy matches the energy of radiation, absorption occurs leading to an EPR spectrum. This magnetic field is known as the field for resonance. When the electron is in an atom the  $g$ -values may become anisotropic and the  $g$ -value must then be represented by a  $g$ -tensor as the electron now has orbital motion.

The field for resonance is not unique for a sample as spectra can be obtained at a range of frequencies. However, as the  $g$ -factor is usually independent of the microwave frequency it is more suitable to be used as a sample identifier.

$$g = \frac{h\nu}{\mu_B B_0} \quad (1.5)$$

The  $g$ -value yields information regarding the local symmetry of the paramagnetic site and its electronic state. **Figure 1.2.1-2** shows how the symmetry of the paramagnetic environment may be related to the  $g$ -tensor and the resulting EPR spectrum in both absorption and derivative modes.

---

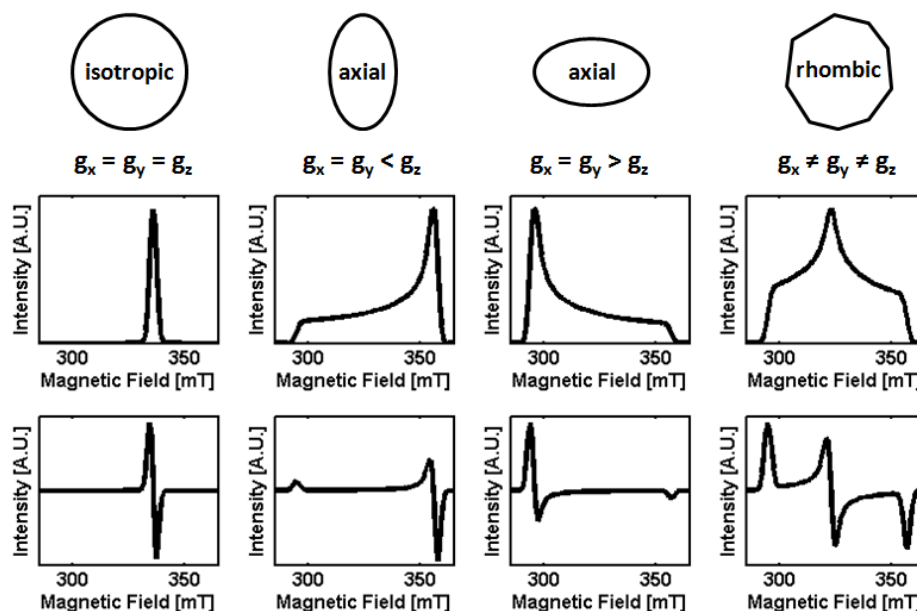


Figure 1.2.1-2, Effect of  $g$  anisotropy on the EPR spectrum of a sample.

### 1.2.2 Zero-Field splitting

For spin-systems with  $S > 1/2$  and lower than cubic symmetry, the  $(2S+1)$  fold degeneracy of the magnetic sublevels may be already (partially) removed in the absence of an applied magnetic field i.e. in the “zero-field” case. The zero-field interaction results from the dipole-dipole and/or spin-orbit coupling of the electron spins. It has been generally held that the first contribution is dominant in organic molecules, and the latter for transition metal ions, although work by Neese has cast doubt on this [7]. The interaction has the following term in the spin Hamiltonian:

$$H_{zfs} = \tilde{\mathbf{S}}\mathbf{D}\mathbf{S} \quad (1.6)$$

This term may be re-written in the principal axes system of the  $\mathbf{D}$ -tensor (which may not necessarily be coincident with that of the  $g$ -tensor) as:

$$H_{zfs} = D_x S_x^2 + D_y S_y^2 + D_z S_z^2 \quad (1.7)$$

For a traceless  $\mathbf{D}$ -tensor the interaction may be represented by two parameters. If we define the following conditions:

$$D \equiv 3D_z / 2$$

and

$$E \equiv (D_x - D_y) / 2$$

Equation (1.7) may be reformulated:

$$H_{zfs} = D[S_z^2 - \frac{1}{3}S(S+1)] + E(S_x^2 - S_y^2) \quad (1.8)$$

For cubic symmetry  $D = E = 0$ ; for axial symmetry  $D \neq 0$ ,  $E = 0$ ; and for lower symmetry  $D \neq E \neq 0$  and  $E \leq D/3$ . When  $D \gg h\nu$  an “effective” Hamiltonian approach may be utilized for Kramers systems.

### 1.2.3 The Hyperfine Interaction

Although g-factors may provide an indication to the species giving rise to a spectrum, they do not reveal much about the molecular structure of a sample. The unpaired electron is however sensitive to its local surroundings, a fact which can be reflected in the EPR spectrum. The nuclei of the atoms or molecules within the sample often have a magnetic moment, producing a magnetic field at the electron. The interaction with the electron and the nuclei is termed the hyperfine interaction (HFI) (**Figure 1.2.3-1**). Insight to the identity and number of atoms which compose the molecule as well as their distances from the unpaired electron can be gained by studying this interaction (although this is perhaps restricted to atoms relatively close to the unpaired electron). The magnetic moment of the nucleus can be thought of acting as a bar magnet. Thus a magnetic field  $\mathbf{B}_1$  is produced at the electron that either opposes or adds to the external magnetic field, depending on the alignment of the moment of the nucleus. When  $\mathbf{B}_1$  adds to the external magnetic field, less magnetic field from the magnet is needed for resonance to occur (i.e. the field for resonance is lowered by  $\mathbf{B}_1$ ). When  $\mathbf{B}_1$  subtracts from the external field the opposite is true. For an isotropic spin system if there is a second nucleus each of the two signals discussed above will further split into a pair, creating four signals in total when both nuclei have  $I = 1/2$ . Generally for  $N$  spin  $1/2$  nuclei, there are  $2^N$  EPR signals. This exponential increase in the number of signals leads to situations where the

signals overlap and only one broad signal is observed. If there are assumed to be  $n$  nuclear spins  $I_1, I_2, \dots, I_n$  to the electron spin, then the hyperfine interaction may be described by:

$$H_{HF} = \sum_{k=1}^n \mathbf{S} \mathbf{A}_k \mathbf{I}_k \quad (1.9)$$

Where  $\mathbf{A}_k$  are the HFI matrices and the  $\mathbf{I}_k$  are vector representations of nuclear spin.

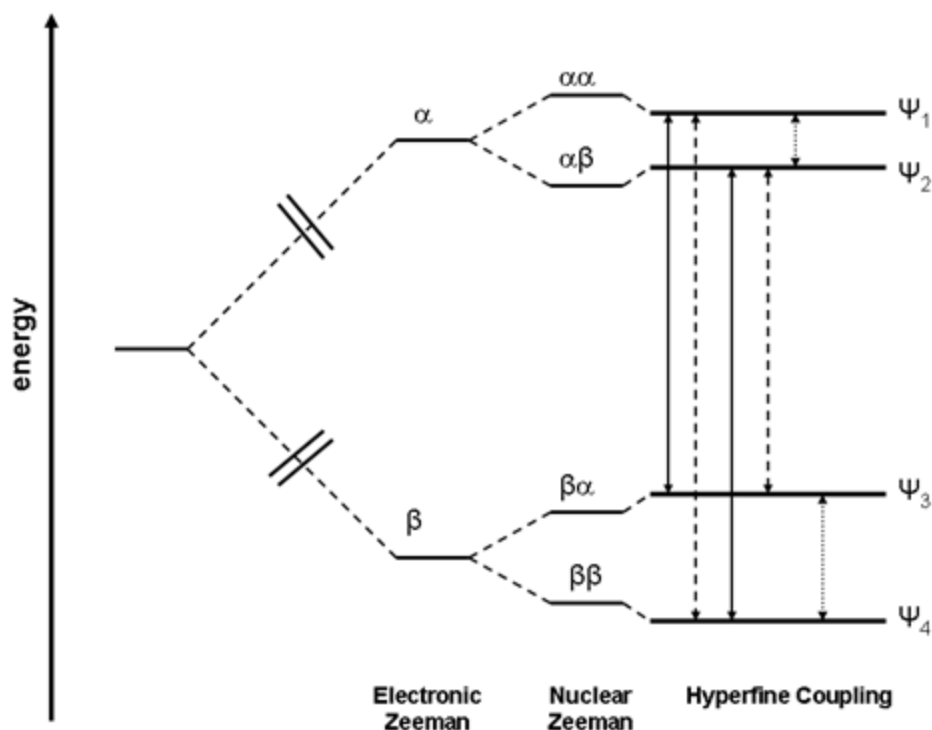


Figure 1.2.3-1, Energy level diagram for an electron spin  $S=1/2$  coupled to a nuclear spin  $I=1/2$ . Solid arrows represent allowed transitions, dashed lines forbidden transitions and dotted lines transitions associated with the radio-frequency (RF) pulse in ENDOR.

Furthermore the HFI may be considered to consist of two parts. Firstly there is a dipolar coupling that acts through space between the electron and nuclear spins. If it is assumed that each spin is approximated to a point dipole, the dipolar coupling may be described by the following equation:

$$H_{HFDD} = \frac{\hbar^2 \mu_0}{4\pi r_{en,k}^3} \gamma_e g_e \gamma_n g_{n,k} \left[ \mathbf{S} \mathbf{I}_k - \frac{3}{r_{en,k}^2} (\mathbf{S} \mathbf{r}_{en,k}) (\mathbf{I}_k \mathbf{r}_{en,k}) \right] \quad (1.10)$$

In this equation  $\mathbf{r}_{en,k}$  is a vector connecting the electron spin with the  $k$ -th nuclear spin.  $g_e$  and  $g_{n,k}$  are the  $g$ -values of the unpaired electron and  $k$ -th nucleus respectively and  $\gamma_e$  and  $\gamma_n$  the corresponding gyromagnetic ratios. There may also be, however, a contribution to the HFI if there is a finite probability that spin density from the electron overlaps with the spin density of the nucleus. This of course only holds true formally for  $s$ -orbital electrons as  $p$ -,  $d$ - or  $f$ -orbital electrons have no electron density at the nucleus, although hybridization of electron orbitals may give rise to an isotropic hyperfine interaction when an unpaired electron is “formally” in a non- $s$  orbital. This contribution to the HFI is known as the Fermi contact interaction and leads to an isotropic HFI.

#### 1.2.4 Nuclear Quadrupole Interaction

The Nuclear quadrupole interaction is formulaically analogous to the zero-field interaction. Nuclei with  $I \geq 1$  possess an electrical quadrupole moment  $Q$  arising from their non-spherical charge distribution. The interaction of this charge distribution with the electric-field gradient produced by the electrons in the close vicinity of the nucleus is described by:

$$H_{nq} = \tilde{\mathbf{I}} \mathbf{P} \mathbf{I} \quad (1.11)$$

Where  $\mathbf{P}$  is the nuclear quadrupole tensor. As in the case of the zero-field splitting, in the principal axes system this tensor may be represented in the following way:

$$H_{nq} = P_x I_x^2 + P_y I_y^2 + P_z I_z^2 \quad (1.12)$$

The tensor  $\mathbf{P}$  is again traceless and the two parameters used to represent the interaction are  $P \equiv 3P_z/2$  and an asymmetry parameter  $\eta \equiv (P_x - P_y)/P_z$  where ( $|P_z| \geq |P_y| \geq |P_x|$  and  $0 \leq \eta \leq 1$ ). This interaction is particularly significant in the case of interacting  $^{14}\text{N}$  nuclei, as is the case in myoglobin (Mb).

### 1.2.5 From the Hamiltonian to something Useful

In general the EPR spectroscopist has an array of different EPR techniques available to determine the set of parameters described above, and each of these parameters may provide an insight into a specific structural or dynamical situation. For example the  $g$ -tensor and zero-field interaction may be used to reveal important information regarding the ground state, oxidation state and local symmetry of the paramagnetic environment. In situations where  $I \geq 1/2$  measurement of the hyperfine interaction between the unpaired electron and the nucleus may confirm these elucidations. Moreover, this interaction may also be used to examine the spin-distribution in the system (via the Fermi contact term) as well as determining the distance to various nuclei via the dipole-dipole interaction. As the nuclear quadrupole interaction reflects an interaction with the electric-field gradient produced by the full electronic structure, it may be used to determine both the local geometric and electronic structure of the paramagnetic site. Also as most of the EPR parameters described above are tensors a measurement of the time-averaging of them yields direct information regarding the dynamics of the system under observation.

### 1.3 Relaxation

In the previous section the spin Hamiltonian was discussed. If the magnetic resonance spectra were to be viewed solely by this description one would observe (for a CW-EPR experiment) a series of perfectly sharp resonant transitions between energy levels. However useful this approach would be, it is however, unrealistic since every molecule interacts with its surroundings and these interactions have the effect of limiting the lifetime of the spin states. It is also worth remembering that in EPR it is the movement of electronic polarization between a non-Boltzmann population of energy levels that gives rise to the EPR spectrum, and that if no mechanism were to exist to allow a movement from the higher to lower energy levels the higher energy level would become saturated and no EPR spectrum would be able to be recorded. The concept of relaxation is also particularly important when discussing the field of pulsed-EPR [8].

---

### 1.3.1 General Introduction

The area of relaxation within magnetic resonance in general and EPR in particular has been widely covered by a number of treatises and monographs [9-13]. Most such examinations start from the foundations of the Bloch equations and while this method is extremely useful when discussing the origin of the different mechanisms of relaxation and their effect on the CW-EPR non-saturated line-widths and saturation conditions, they are not strictly necessary to understand the general workings of the various pulsed-EPR experiments to be described later in this work. As such, the following discussion of relaxation will limit itself to specific definitions of the processes as well as their relevance to specific applications. The section begins with a brief description of some associated concepts necessary for the discussion of relaxation.

### 1.3.2 The Rotating Frame

To describe the motion of the bulk magnetization during a pulse sequence the rotating frame formalism is employed, this is a way of simplifying these often quite complicated motions.

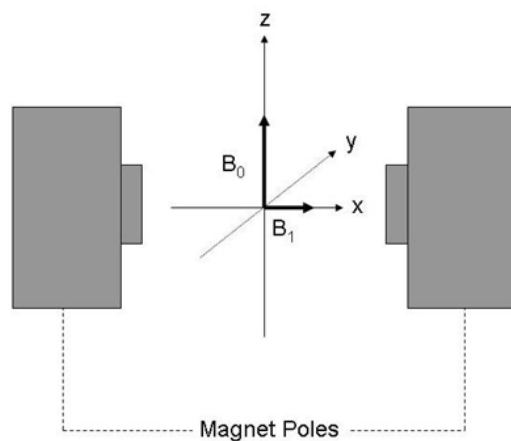


Figure 1.3.2-1, Definition of the lab-axes system

Initially it is assumed that the axis-system of reference is the lab frame **Figure 1.3.2-1**, which means to say a coordinate system of three stationary mutually perpendicular axes with the external magnetic field  $B_0$  defined as parallel to the z-axis. In this system the applied mw field

is parallel to the x-axis. If an electron spin is placed within the lab-frame it experiences the magnetic field which exerts a torque on it. This torque causes its magnetic moment to precess about the magnetic field at the Larmor frequency:

$$\omega_L = -\gamma \mathbf{B}_0 \quad (1.13)$$

Where  $\omega_L$  is the Larmor frequency,  $\gamma$  the gyromagnetic ratio of the electron and  $\mathbf{B}_0$  the magnetic field. However, within an EPR sample there is not just one electron spin but an ensemble of such spins. These spins may adopt one of two quantum states, either parallel or anti-parallel to the direction of the magnetic field (**Figure 1.3.2-2**).

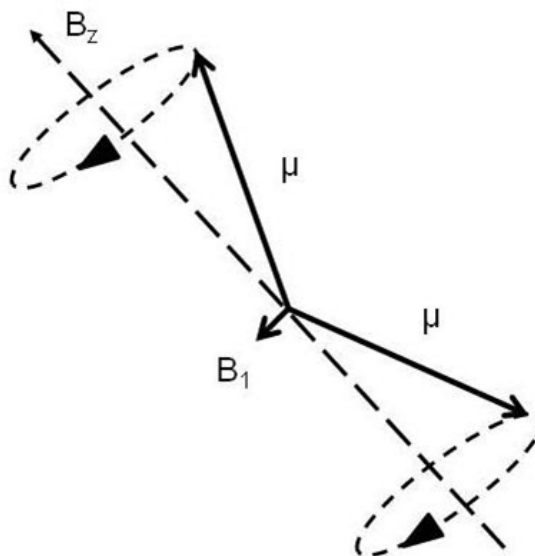


**Figure 1.3.2-2, Precession of vectors representing the magnetic moments ( $\mu$ ) of electrons in the two spin-states. To induce transitions between the two states  $B_1$  must be perpendicular to  $B_z$ .**

At thermal equilibrium there is a Boltzmann distribution between the two energy levels, with the parallel state having a higher population due to its lower energy. A vector sum of the net magnetization in this instance thus yields a bulk magnetization parallel to the z-axis. These electrons will still precess about the z-axis at the Larmor frequency but with random orientations in the transverse or x-y plane, for an ensemble of spins this magnetization sums to zero, resulting in a stationary magnetization  $\mathbf{M}_0$  aligned along  $\mathbf{B}_0$ .

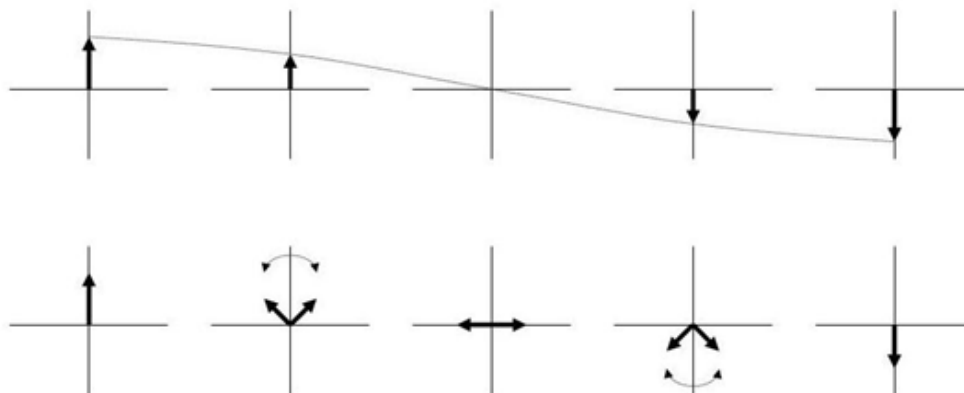


**Figure 1.3.2-3, The representation of linearly polarized microwaves (top) by two circularly polarized components (bottom).**

A microwave pulse is a linearly oscillating magnetic field  $\mathbf{B}_1$  applied in a direction (we may assume for now that this direction is along the x-axis of the laboratory frame). In general  $|\mathbf{B}_1| \ll |\mathbf{B}_0|$ . Linearly polarized mw may be viewed as a mw field oscillating at the mw frequency. When discussing the rotating-frame however, another useful way of regarding linearly polarized mw's is as the sum of two magnetic fields rotating in opposite directions at the mw frequency (**Figure 1.3.2-3**). When attempting to view the effect of  $\mathbf{B}_1$  on the bulk magnetization in the lab-frame the situation becomes rapidly complicated. If however, the rotating coordinate frame is used, in which the frame is rotated coincidentally with one of the rotating components of  $\mathbf{B}_1$  it may be seen that the situation becomes clearer. If the resonance condition is assumed so that the mw frequency is equal to the Larmor frequency of the electron, and the coordinate system rotated with the angular velocity of the mw radiation, then one of the two components of  $\mathbf{B}_1$  will appear to remain stationary. The other component will be seen to be rotating at twice the mw frequency. As this frequency is comparatively far from the resonance condition and has little effect on the electron spins it may be ignored. Another effect of the rotating frame is that the components of the magnetization precessing at the Larmor frequency will also appear stationary. Examination of **(1.13)** and the assumption that the bulk magnetization is not precessing in the rotating-frame shows that the magnetic

---

field  $\mathbf{B}_0$  may be neglected when describing the dynamics of the system, so that in the rotating-frame only the stationary  $\mathbf{B}_1$  and  $\mathbf{M}_1$  are of concern.

### 1.3.3 Polarization and Coherence

In the general case of an  $S = 1/2$  system there may be considered to be two energy level populations in the presence of an applied magnetic field. Without an irradiating mw field the populations of these levels may be described by a Boltzmann distribution. In all EPR experiments it is the difference between these populations that is measured which is known as the *polarization* of the transition. Often EPR experiments are performed at temperatures below RT in order to increase the degree of polarization and therefore increase the signal being measured in the EPR experiment. This is especially true in the case of pulsed EPR where other terms in the spin Hamiltonian may be desired to be determined and the pulse-sequence applied to the system of interest may act on the spin density matrix via one or more mixing and or evolution periods on the electron polarization before a subsequent detection. In this case the desired modulation of the EPR signal will be a fraction of the total polarization, and so it is desirable to maximize this as far as possible within the constraints of the experiment. In the discussion of the rotating frame above it was mentioned that in thermal equilibrium the distribution of the magnetization of the individual electron spins in the x-y plane was random, such that there was no bulk magnetization in this direction for the ensemble. It is worth remembering that this plane is also the detection plane for an EPR spectrometer such that in this condition for a pulse experiment no signal will be detected. Thus in order to detect an EPR signal the magnetization is moved using mw pulses. Each of the spins in the ensemble however, may be seen to experience slightly different magnetic fields due to their environments and will therefore precess at slightly different frequencies in the x-y-plane, so that the bulk magnetization in this plane will diminish with time (a process also known as de-phasing). *Coherence* therefore may be seen as the situation where the bulk magnetization is aligned in this plane in order to achieve a measurable signal. It should also be remembered that during de-phasing in the x-y plane, there is also a movement of the magnetization in the longitudinal direction such that the spins attempt to regain their thermal equilibrium state. Within a pulsed-EPR experiment the movement of the bulk magnetization

---

between polarization and coherence conditions is facilitated by mw pulses. **Figure 1.3.3-1** shows a representation of the creation of coherence for a spin ensemble.

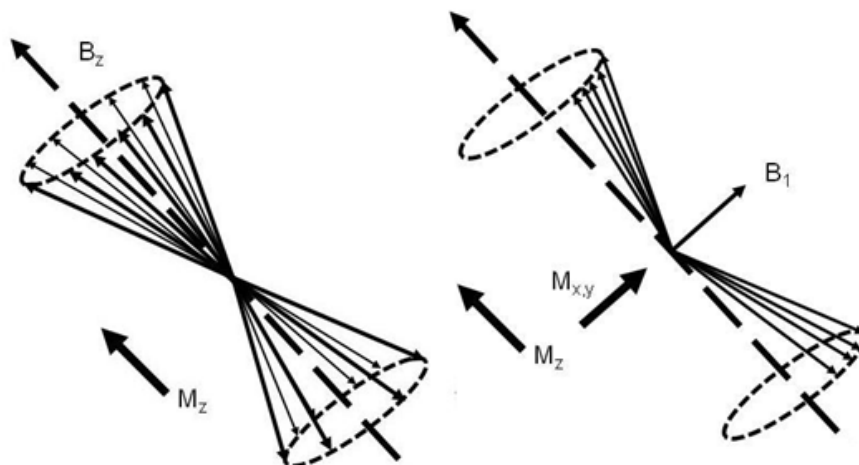


**Figure 1.3.3-1**, Precession of an ensemble of vectors with a random phase in the xy-plane results in a non-zero magnetization in the z-direction only (left). By applying a MW pulse ( $B_1$  field), rotating at the resonance frequency, the vectors attain phase-coherence leading to a magnetization in the xy-plane (right).

### 1.3.4 Longitudinal Relaxation

$T_1$  also known as the spin-lattice relaxation time may be characterized by the following equation:

$$\Delta n(t) = \Delta n_{eq} [1 - \exp(-t/T_1)] \quad (1.14)$$

Where  $\Delta n$  is the population difference between excited and ground state spins,  $\Delta n_{eq}$  is the equilibrium population difference and  $t$  is time.  $T_1$  relaxation can be viewed as the motion of the z-axis magnetic field component of the bulk magnetization from its excited state to ground state. The mechanism of this relaxation arises from magnetic interactions. In liquid samples dipolar coupling has the greatest effect on the relaxation; the dipolar coupling between two electrons depends on their distance and the angle between the inter-electron vector and the static magnetic field. As the molecules move in solution the distance and angle

vary in a complicated manner causing a rapid fluctuation of the interaction. This rapid fluctuation causes the electron spins to experience a time-dependant local magnetic field. If this field has a component at the electrons resonance frequency, transitions may be induced that return the electron to its ground state. In solid state or frozen solutions, where the molecular motion is restricted, the electron spin will be coupled to the crystal lattice vibration via spin-orbit coupling.

### 1.3.5 Transverse Relaxation

The transverse relaxation time  $T_2$ , also known as spin-spin relaxation, is a measure of the decay of the magnetization in the x-y plane. This phenomenon has two contributions both related to different line broadening mechanisms namely homogeneous and inhomogeneous broadening. In the homogeneous case; a system of spins that experience the same time-averaged magnetic field is said to be a spin-packet. Such spin-packets may experience fluctuating magnetic fields due to electron or nuclear spin-flips in their vicinity. As discussed above in terms of coherence, in the inhomogeneously broadened case each of the spins within the sample experience different magnetic fields that may act to decrease the transverse magnetization.

$$M_{xy}(t) = M_{xy}(0)e^{-t/T_2} \quad (1.15)$$

This equation describes the proportion of magnetization in the xy-plane  $M_{xy}$  at time t, in terms of the initial magnetization and the spin-spin relaxation time. Not only may the spins experience a varying magnetic field due to the chemical environment, but there may also be inhomogeneity of the magnetic field produced by the magnet itself. When this is taken into account a new variable describing the relaxation of the transverse magnetization may be constructed. This variable is known as  $T_2^*$ . It is related to  $T_2$  by the following equation:

$$\frac{1}{T_2^*} = \frac{1}{T_2} + \frac{1}{\gamma\Delta B} \quad (1.16)$$

Where  $\gamma$  is the gyro-magnetic constant for an electron and  $\Delta B$  is the inhomogeneity.

Comparing the lengths of the above relaxation times yields the following relationship:

$$T_1 > T_2 > T_2^*$$

### 1.3.6 Phase-Memory Time

The phase-memory time  $T_M$  is a general way of quantifying the transverse magnetization or coherence of the sample under investigation [14]. Using the definitions outlined above, the phase-memory time may be formulated thus:

$$\frac{1}{T_M} = \frac{1}{T_2} + \frac{1}{T_2^*} \quad (1.17)$$

This parameter may be measured relatively trivially experimentally and as such is often stated in literature. In pulsed-EPR experiments it is of particular importance as it provides an indication of which advanced pulsed methods may be applied to a system. If the  $T_M$  is shorter than an inter-pulse distance in a sequence then coherence will not survive throughout the duration of the experiment to make it successful. If the  $T_M$  of a sample is too short to perform a particular experiment it may be increased by the addition of glycerol in the case of frozen samples.

## 1.4 Orientation Selectivity

Frozen samples normally give rise to an isotropic absorption spectrum **Figure 1.2.1-2**. In transition-metal complexes this anisotropy is normally large and the case often arises where the excitation bandwidth of the mw pulse is less than the width of the absorption spectrum (50 MHz c.f. 1 GHz). In principle this effect allows for orientation selectivity i.e. magnetic interactions measured at specific points of the absorption spectrum may be related to the g-matrix coordinate system. Experiments may be performed at higher mw frequencies in order to enhance this phenomenon. **Figure 1.3.6-1** shows a simulated comparison of the orientation selectivity for a nitroxide spin label and low-spin myoglobin.

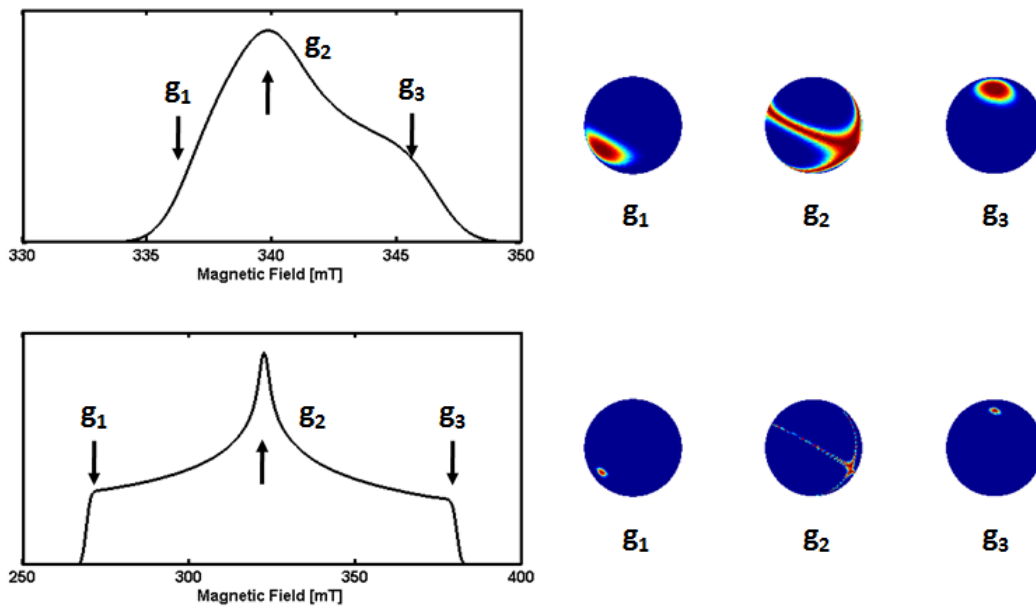


Figure 1.3.6-1, Calculated absorption spectra (left) and orientation selectivity (right) on a unit sphere For observer positions corresponding to principal  $g$ -values for a nitroxide spin-label  $g$ -values [2.08 2.06 2.02] (top) and low-spin myoglobin  $g$ -values [2.6 2.17 1.84] (bottom). MW pulses simulated with an excitation bandwidth of 50 MHz.

In this case simulation was performed at a frequency of 9.8 GHz using mw pulses with an excitation bandwidth of 50 MHz.

---

## References

1. Calle, C., et al., *Pulse EPR methods for studying chemical and biological samples containing transition metals*. Helvetica Chimica Acta, 2006. **89**(10): p. 2495-2521.
  2. Rudowicz, C. and P. Gnutek, *Modeling techniques for analysis and interpretation of electron magnetic resonance (EMR) data for transition ions at low symmetry sites in crystals-A primer for experimentalists*. Physica B-Condensed Matter, 2009. **404**(20): p. 3582-3593.
  3. Jeschke, G., *EPR techniques for studying radical enzymes*. Biochimica et Biophysica Acta (BBA) - Bioenergetics, 2005. **1707**(1): p. 91-102.
  4. Gehlhoff, W. and A. Hoffmann, *EPR identification of intrinsic and transition metal-related defects in ZnGeP(2) and other II-IV-V(2) compounds*. Physica B-Condensed Matter, 2009. **404**(23-24): p. 4942-4948.
  5. Steinhoff, H.J., et al., *Site-Directed Spin-Labeling Studies of Structure and Dynamics in Bacteriorhodopsin*. Biophysical Chemistry, 1995. **56**(1-2): p. 89-94.
  6. Schweiger, A. and G. Jeschke, *Principles of Pulsed Electron Paramagnetic resonance Spectroscopy*. 2001: Oxford University Press.
  7. Neese, F., *Importance of Direct Spin-Spin Coupling and Spin-Flip Excitations for the Zero-Field Splittings of Transition Metal Complexes: A Case Study*. Journal of the American Chemical Society, 2006. **128**(31): p. 10213-10222.
  8. Prisner, T., M. Rohrer, and F. MacMillan, *Pulsed EPR Spectroscopy: Biological Applications*. Annual Review of Physical Chemistry, 2001. **52**(1): p. 279-313.
  9. Poole, C.P. and H.A. Farach, *Relaxation in Magnetic Resonance*. 1971: Academic Press.
  10. Hore, P.J., J.A. Jones, and S. Wimperis, *NMR: The Toolkit*. 2000: Oxford University Press.
  11. Carrington, A. and A.D. McLachlan, *Introduction to Magnetic Resonance*. 1969: Harper and Row.
  12. Slichter, C.P., *Principles of Magnetic Resonance*. 1978: Springer Verlag.
  13. McLauchlan, K.A., *Magnetic Resonance*. 1972: Clarendon Press.
  14. Hilczer, W., et al., *Electron-Spin Echo Studies of Spin-Lattice and Spin-Spin Relaxation of SEO3- Radicals in (NH4)3H(SEO4)2 Crystal*. Solid State Communications, 1993. **85**(7): p. 585-587.
-

---

## **2 CHAPTER An Introduction to Heme Proteins**

---

### **2.1 Introduction**

A heme is a cofactor in which iron is held within a heterocyclic organic ring known as a porphyrin. Heme containing proteins are ubiquitous in nature and have been comprehensively studied by a variety of spectroscopic techniques [1]. The heme group in hemeproteins is perhaps amongst the most studied motifs in biochemistry, indeed one such protein, myoglobin (Mb), provided the first crystal structure [2]. These proteins may be further sub-divided into groups broadly relating to function e.g. cytochromes (cyt) *c* and electron transfer [3]. Despite the long period and intensity of study proteins are still being investigated and their roles and mechanisms of action revised. As for Chapter 1 the following Chapter aims to provide a background in the general characteristics of heme proteins with an emphasis on globins particularly myoglobin. Whilst the function of many heme proteins is well understood those of other closely structurally related proteins is less clear (e.g. hemoglobin and neuroglobin [4]). Indeed in some situations where the role of a particular protein is thought to have been conclusively determined new insights have led to the proposal of possible new roles, as is the case for the proposed nitrite reductase role for myoglobin which will be described in Chapter 4.

### **2.2 Structure**

It is a mantra of biochemistry that it is the structure and dynamics of a protein that determine its function. With hemeproteins this is no exception, and indeed may be seen to be a perfect example, where relatively minor structural differences are able to confer a vast array of differing function. Frausto da Silva and Williams [5] describe the association of the iron and porphyrin in a heme as almost creating a separate and unique element. From this it is perhaps

---

---

helpful to consider a heme protein initially in terms of its individual structural elements with a view to understanding how the subtle interactions of these factors lead to the proteins function.

### **2.2.1 Iron**

Iron is a transition metal and as such may exist in a range of oxidation states (specifically -2 to + 6). Biologically iron most commonly exists in the +2 and +3 oxidation states known as ferrous Fe(II) and ferric Fe(III) iron respectively. Within cells free iron is toxic as it may act as a catalyst in the production of free radicals [6], and so is stored in protein complexes such as ferritin [7].

#### **2.2.1.1 Spin States of d-electrons**

For transition metal coordination complexes the spin state refers to the spin configuration of the metal centres d-electrons. This is primarily determined by the field strength of the complex's ligands which act to split the energy levels of the d-orbitals. A strong field ligand will cause a large splitting  $\Delta$  which will lead to the lowest energy d-orbitals being filled and thus the low-spin (LS) case. Conversely a weak-field ligand will cause a small  $\Delta$ -splitting enabling all the d-orbitals to be energetically favourable for electron filling and the high-spin (HS) state will ensue. This is because in the HS case the electron-electron repulsion is lower, and it is this repulsion that has to be balanced. In general the charge of the metal ion will also have an effect on the field-splitting and all things being equal a greater charge will result in a larger ligand-field. Thus for the same geometrical and electrochemical state an Fe(III) complex is more likely to be LS than an Fe(II) complex. Iron porphyrins are no exception and may be qualitatively well understood with the ligand-field approach to the d-orbital splitting which states that the d-orbitals whose lobes are directed between the ligands ( $d_{xz}$ ,  $d_{xy}$ ,  $d_{yz}$ ) will cause less splitting than the d-orbitals pointing directly at the ligands ( $d_{x^2-y^2}$ ,  $d_{z^2}$ ). The latter sets are the stereo-chemically active orbitals (also known as the  $e_g$  set in group-theory nomenclature), their occupation in high-spin complexes always correlates with longer coordinate bond lengths compared to low-spin complexes [8].

---

A diagrammatical overview of the electron orbitals involved in ligand binding to the heme as well as the occupation of electron orbitals in the LS and HS case is shown in **Figure 2.2.1**.

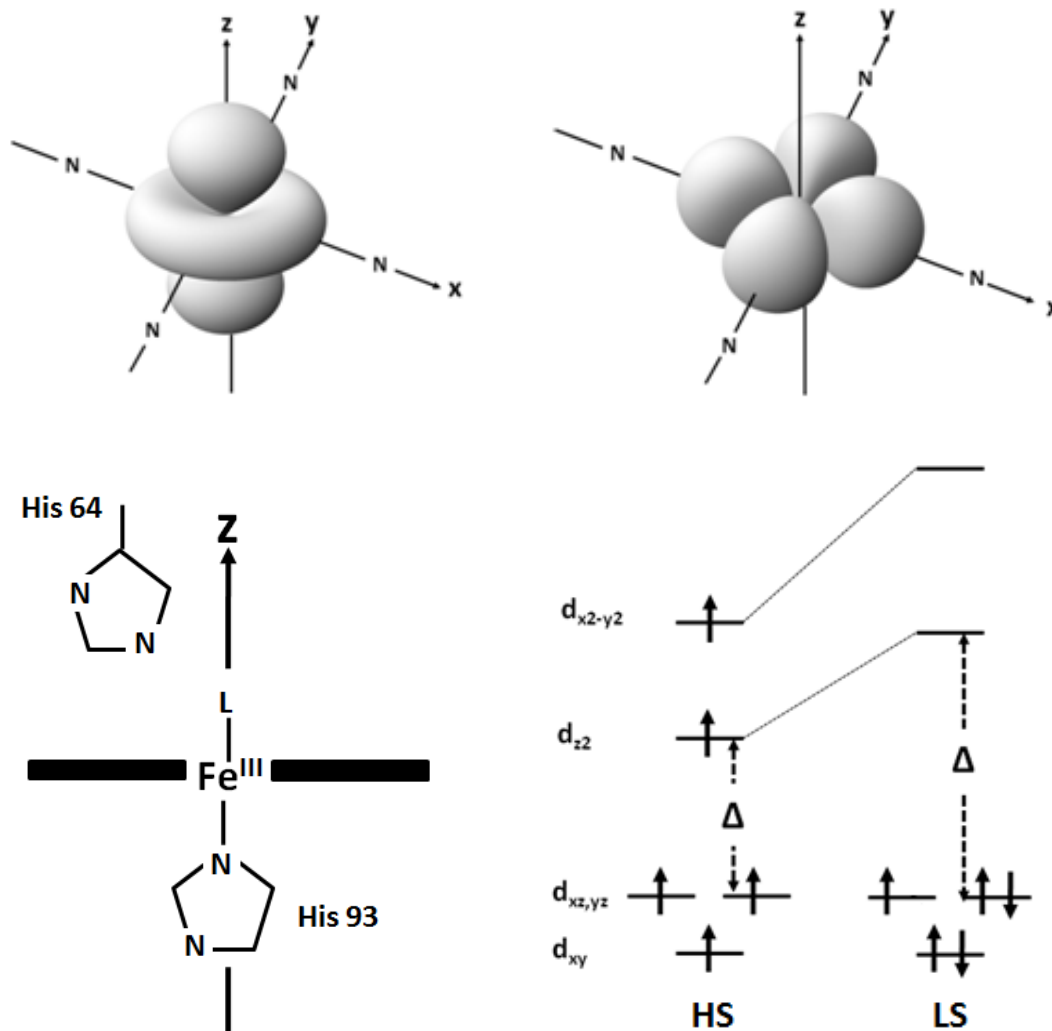


Figure 2.2.1,  $d(z^2, x^2-y^2)$  (top left and right respectively) electron orbitals. Schematic of heme centre in myoglobin (bottom-left) showing coordination to proximal histidine (His93) and defining the z-axis. The ligands on this axis primarily dictate the spin state of the complex (bottom-right). Strong-field ligands produce a large splitting  $\Delta$  and the low-spin Case (LS), Whilst weak-field ligands lead to the high-spin (HS) state.

The figure also defines the z-axis of a heme system, specifically that of myoglobin (Mb). It is the binding of a ligand to the heme along this axis that primarily determines the spin state of the iron.

### 2.2.2 Porphyrin

A porphyrin ring system consists of four pyrrole rings joined by one-carbon bridges [9]. It may be viewed as a di-anionic chelating agent able to bind a metal atom via the four pyrrole nitrogen atoms at the centre of the ring [Figure 2.2.2]. The porphyrin ring positions are also labelled with the conventional Fisher notation [10].

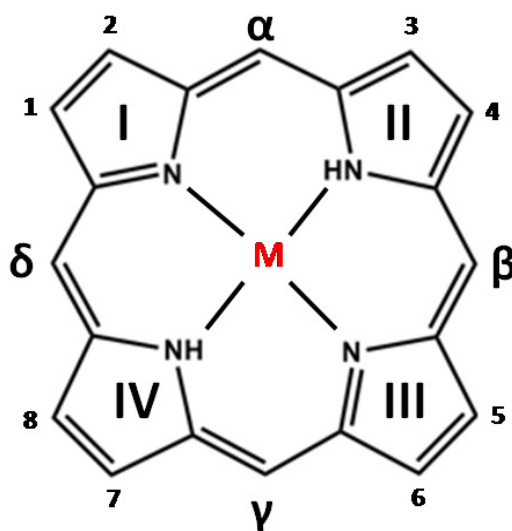


Figure 2.2.2, A Porphyrin macro-cycle (with positions labelled in conventional Fischer notation (defined by the relative positions of vinyl groups in pyrrolic rings I and II) in this case porphine. If the metal M becomes iron the System is known as a heme.

When Iron is bound in a porphyrin it is known as a heme. The iron-porphyrin complex has a number of interesting chemical properties which differ from those of iron which may explain the diversity of uses of heme-proteins [5] the most important of which for this work may be summarised as follows:

1. The motif has a limited solubility in water and may readily enter hydrophobic solvents, especially when the iron is screened by axial ligands.
2. The organic substituents of the outside of the porphyrin ring may be substituted leading to a variety of porphyrins with differing functions.
3. In both the ferrous and ferric (Fe(II) and Fe(III) respectively) forms the high, intermediate and low-spin states are energetically close to each other. This in

conjunction with the choice of axial ligands (commonly from the protein) can tune the metal to specific activity.

4. In the low-spin state Fe(II) is a strong  $\pi$ -donor which assists in the binding of O<sub>2</sub>, CO and NO.
5. The porphyrin surface is hydrophobic and is thus able to strongly interact with hydrophobic small molecules and protein surfaces.
6. The redox potentials of the heme may be readily adjusted by the protein environment around the binding site.

Much regarding the nature of heme proteins has been determined by the study of model iron-porphyrin complexes. These model complexes initially gave rise to expectations to structures and bond lengths in their biological counterparts. If these values are found to significantly differ it may be taken as an indication of potentially functionally important protein constraints upon the heme [8].

---

### 2.2.2.1 Heme Types

As mentioned in section 2.2.2, the porphyrin ring of the heme may accommodate a variety of organic substituents to tune the properties for specific functions. **Figure 2.2.3** shows the structures of some of the most commonly encountered (but not all) heme motifs taken from crystal structures.

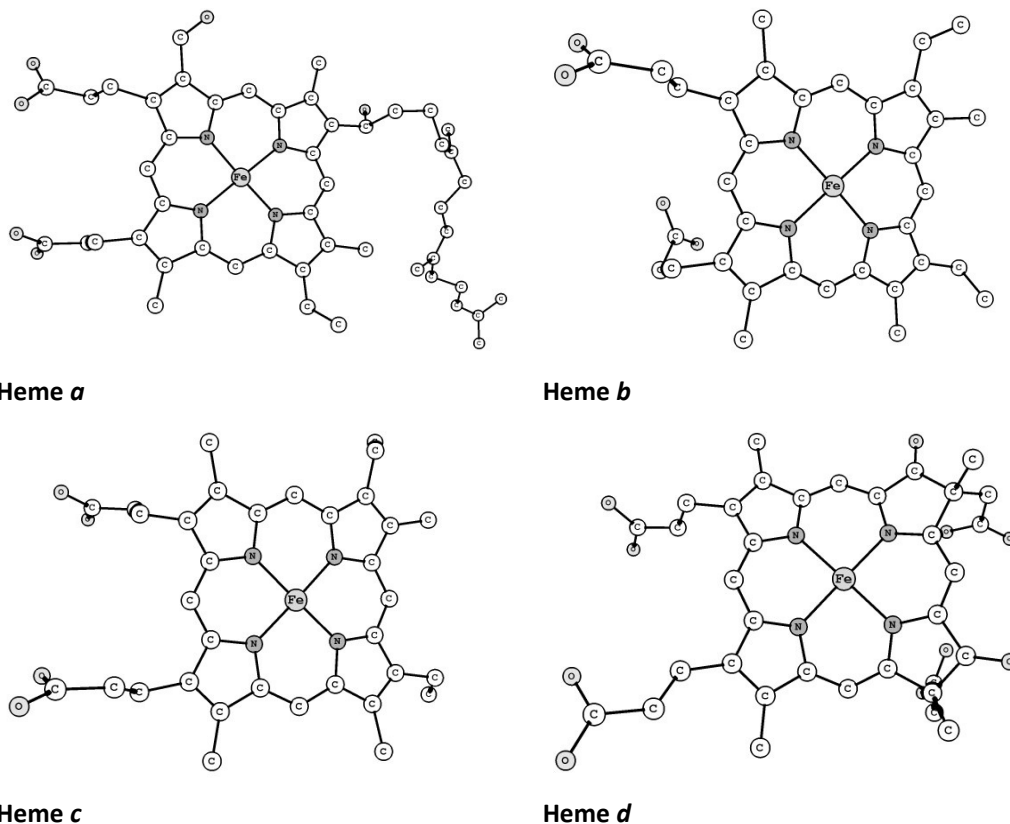


**Figure 2.2.3** Commonly encountered heme types. Heme *a* from 1QLE [11], heme *b* from 2FRF [12] and *c* and *d* from 1E2R [13].

Of the different heme types the most commonly encountered within proteins is Heme *b* and may to a certain extent be taken as a “standard” to compare other heme types against. It is also sometimes referred to as protoheme IX and is the motif found within the globin family of proteins (see § 2.3). In general the heme is covalently attached to the protein solely via the proximal ligand.

The second most common heme type is heme *c* which differs from heme *b* in that the vinyl groups (**Figure 2.2.4**) in the heme *b* are replaced by thioethers.

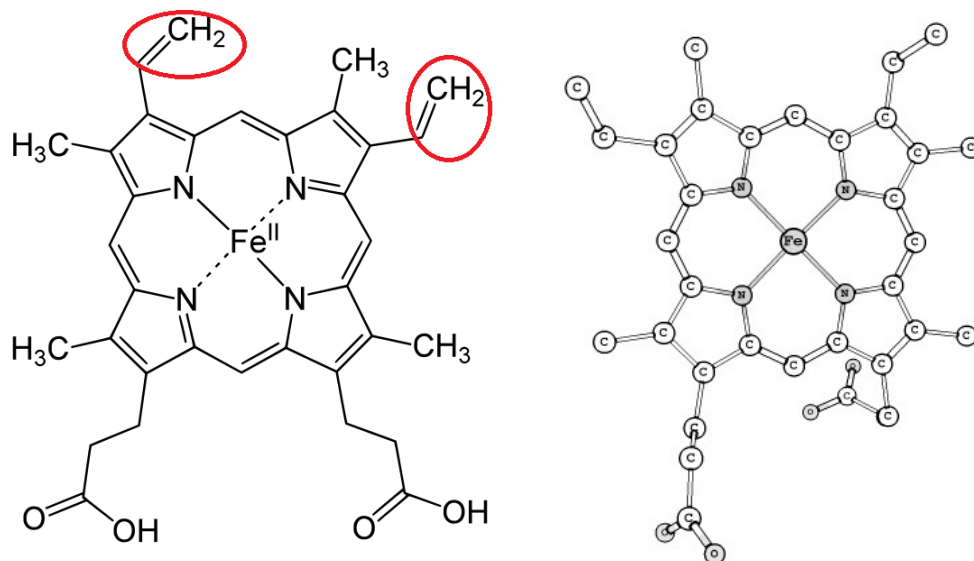


**Figure 2.2.4, Chemical (left) and crystal (right) structure of heme *b*. the crystal structure is again taken from 2FRF In the chemical structure the heme vinyl groups are circled (positions 2 and 4). In this case the macrocycles are orientated as in the labeling convention shown in Figure 2.2.2**

These are able to covalently bind to the protein if the sequence contains the CXXC binding motif. It is therefore difficult to dissociate heme *c* from its parent protein. Heme *a* is the most structurally different. According to Gibney and Dutton “ Heme *a* differs from heme *b* in peripheral porphyrin architecture; a formyl group replaces the methyl group at position 1 and a farnesyl side chain substitutes for the vinyl group at position 8” [14]. The formyl group is more electron-withdrawing than the vinyl group it replaces and so redox and ligand binding reactions will be altered. The farnesyl side chain apart from acting as a potential lipophilic anchor to the protein, may also facilitate long distance electron transfer reactions analogous to the case of ubisemiquinones [15]. Heme *d* is also derived from protoheme IX but contains a  $\gamma$ -spirolactone from hydroxylation of the propionic acid side chain. Another hydroxylated ring is found *Trans* to this lactone group [16]. It is frequently found in bacteria as the site of oxygen reduction at low oxygen levels. The electronic structure of this heme in the ferric state has been proposed to display the novel  $(d_{xz}, d_{yz})^4(d_{xy})^1$  ground state caused by a reordering of the energies of the ferric d-orbitals by the axial ligands for the porphyrinate [17].

### 2.2.2.2 Tetraphenylporphyrin (TPP)

The study of naturally occurring porphyrins is sometimes complicated by their low symmetry and the presence of polar substituents. This may be overcome as briefly mentioned above by the use of model compounds. One such compound is Tetraphenylporphyrin (TPP) **Figure 2.2.5.**

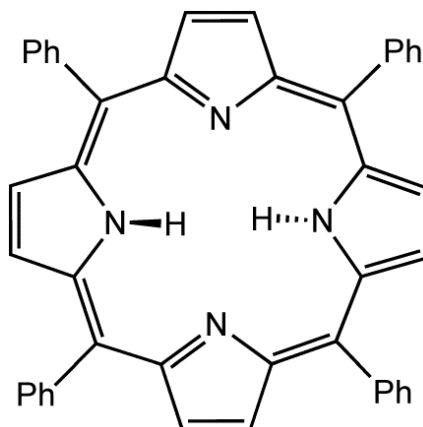


**Figure 2.2.5, the structure of tetraphenylporphyrin (TPP).**

It may be easily synthesized and is hydrophobic and symmetrically substituted. A number of the studies discussed in Chapter 3 utilize this compound.

### 2.2.3 Protein

A description heading such as protein for a hemeprotein includes by definition the iron and porphyrin that compose the heme, but this section is more concerned with the amino acid sequence that comprises the primary structure. Two separate aspects of this sequence should be considered as of great importance for this discussion: firstly the primary structure naturally determines the secondary, tertiary and if applicable, quaternary structure [18]. Secondly the active site, or binding pocket of the hemoprotein is the region where all three of the structural motifs mentioned in this section interact, and it is this interaction that ultimately drives the function of any particular hemoprotein, and allows small structural differences to be translated into the diverse functionality displayed within nature.

### 2.2.3.1 Secondary Structure

Myoglobin was the first protein for which the structure was determined using crystallography [2], followed by that of hemoglobin [19]. Analysis of these structures revealed both to be predominantly  $\alpha$ -helical (both  $\sim 70\%$ ). Coincidentally this figure also corresponds roughly to the overall percentage of heme proteins that exhibit predominantly  $\alpha$ -helical secondary structure. **Figure 2.2.6** shows the results of a structure search of the Heme Protein database [20] from where this percentage value was obtained. One may be able to infer from the general properties of an  $\alpha$ -helix that one reason for this large proportionality is the ability to align the helices in such a way as to create a hydrophobic pocket into which the heme motif may be inserted, as well as maintaining the structure and controlling the dynamics of the protein.



**Figure 2.2.6, CATH [21] assignment of hemoprotein secondary structure taken from a search of the Heme Protein Database [20] of 654 non-redundant structures.  $\alpha$ -helix (67%),  $\beta$ -sheet (12%), mixed  $\alpha/\beta$  (21%), low secondary structure (2 total).**

An example of a heme protein with a predominantly  $\beta$ -sheet secondary structure is Nitrophorin 4 (NP4) [22] which acts as a store and transporter of nitric oxide (NO) in the blood-feeding “kissing-bug” *Rhodius prolixus*. The protein contains a highly “ruffled” heme b, the iron of which exists in the ferric state *in vivo*. The  $\beta$ -sheets are able to combine and produce a  $\beta$ -barrel into which the heme binds. This dynamical study revealed that NP4 had a larger structural distribution than Mb which resulted in a greater flexibility for NP4. It was

theorised that this increased flexibility was needed for the protein to bind larger molecules such as histamine and nicotinamide not bound by the more rigid  $\alpha$ -helical heme proteins.

### 2.2.3.2 Binding Pocket

The binding pocket of a heme protein may be thought of as being divided into two halves by the heme plane. The side to which the heme is bound to the protein is termed the *proximal*, whilst the side which commonly binds molecules for transport or enzymatic activity is termed *distal*. **Figure 2.2.7** shows which amino acid residues are commonly found as proximal and distal ligands in heme proteins, again the source data is taken from the Heme Protein Database. From inspection of this data, by far the most common proximal amino acid is Histidine (His), with Methionine (Met) a distant second. His is also the most common residue encountered as a distal ligand.

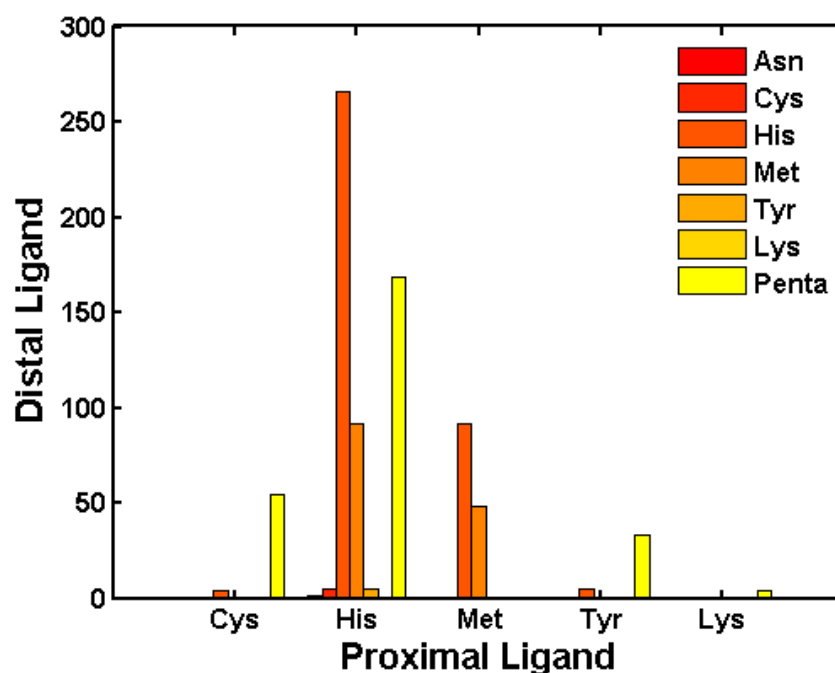


**Figure 2.2.7, Representation of frequency of amino acid residues commonly found in heme proteins as proximal and distal ligands data obtained from Heme Protein Database [20]. In this case "Penta" indicates no distal ligand (see section 2.3).**

An edge of the heme may be partially exposed and itself form part of the protein surface in many proteins. In Cytochrome  $b_5$ , one such protein, the organic substituents on this edge

were found to modify the overall reduction potential of the heme [23], an example of how the three individual structural motifs combine in a “cooperative” way to control the function of the protein. The secondary structure and a close-up of the binding pocket of nitrite-ligated Mb are shown in **Figure 2.2.8**. This structure (2FRF) and associated publication [24] form the starting point for the justification of the experimental section of this thesis. By inspection the clear dominance of the  $\alpha$ -helix in the secondary structure is obvious.

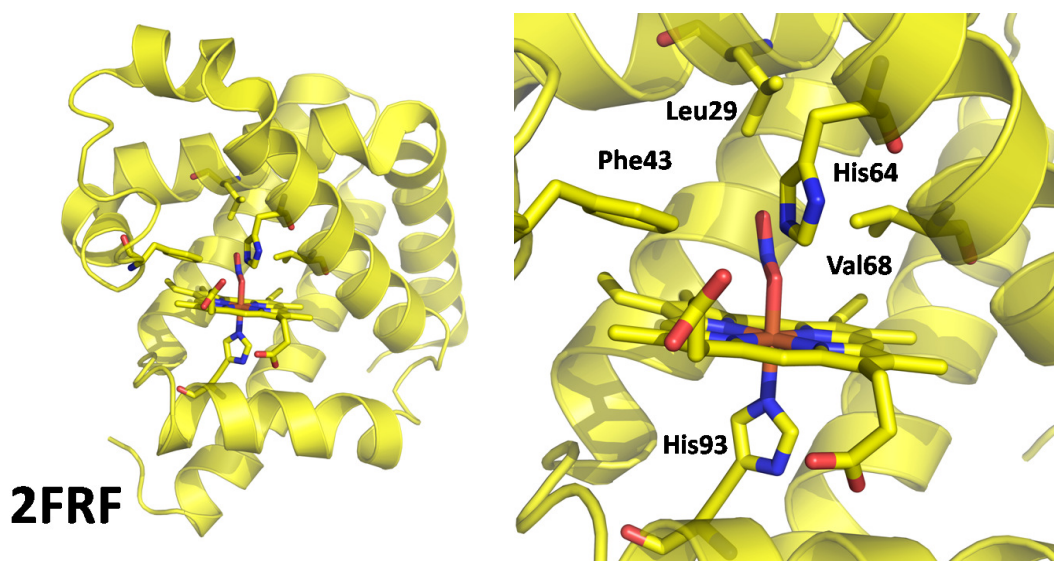


**Figure 2.2.8**, crystal structure of myoglobin nitrite complex showing secondary structure (left). Close-up of binding pocket residues (right) showing amino acid residues within 3.5 Å of nitrite anion. From structure 2FRF [24]

The close-up of the binding pocket also shows the proximal amino acid residue to be a histidine, in this case His93. The distal ligand is the nitrite anion, but amino acid residues within 3.5 Å of the nitrite anion are also shown. Clearly the His64 is in close proximity and is well within range to take part in any ligand-binding activity via hydrogen-bonding.

### 2.3 Globins

The protein at the centre of this work, myoglobin is a member of a family of structurally similar heme proteins known as globins [25]. Globins share a common secondary structure known as the *globin-fold*. This typically consists of eight  $\alpha$ -helices, normally labeled A-H. The labeling of these helices is shown for neuroglobin in **Figure 2.3-1**.

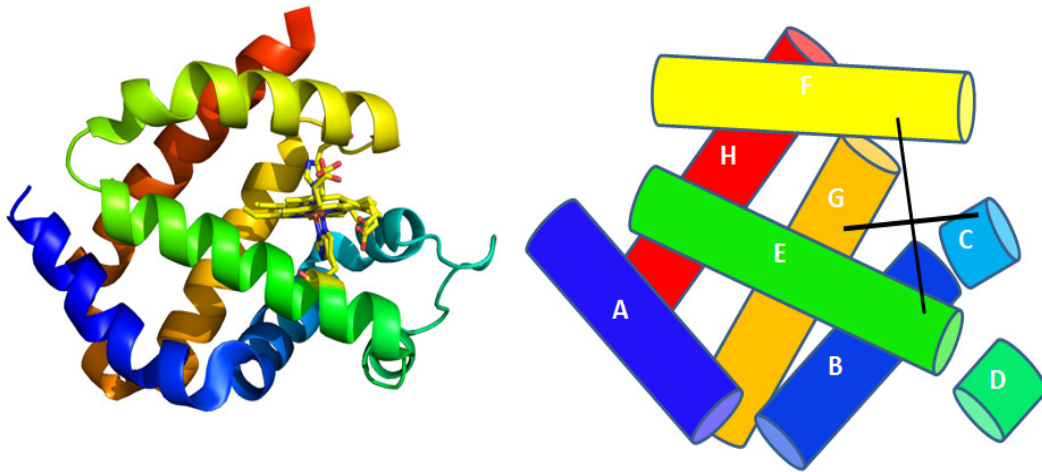
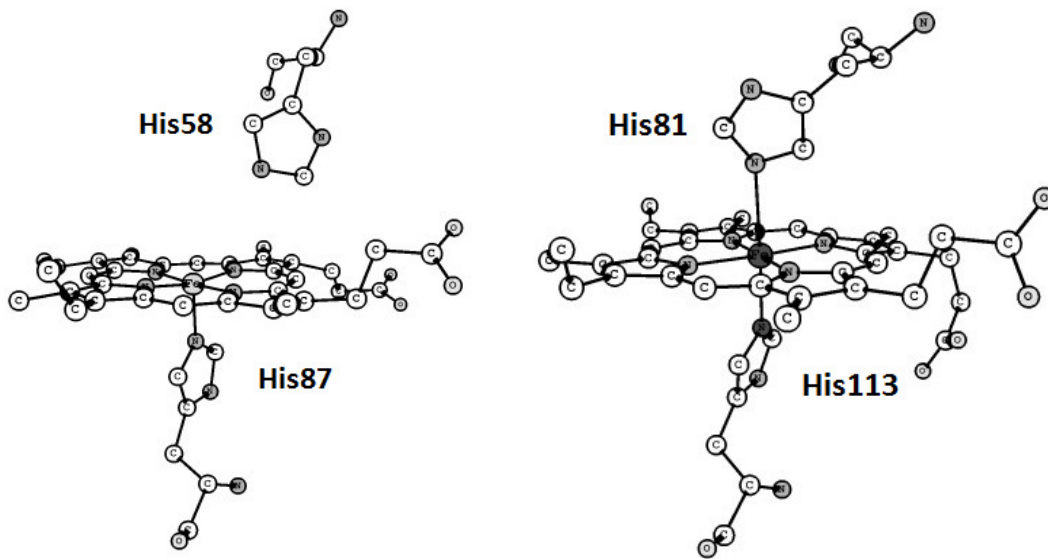


**Figure 2.3-1** crystal structure of mouse neuroglobin 2VRY (left) and schematic (right) indicating Labeling convention for helices in globins Black cross in left indicates heme.

Globin proteins also always incorporate heme *b*. Globin proteins were thought to be primarily concerned with oxygen storage and transport [26]. This was particularly the case for hemoglobin and myoglobin for the blood and muscle tissue respectively. Recently however the function of these proteins has started to be re-examined [27]. The main cause for this was the discovery of new globin proteins; neuroglobin in 2000 [28], and cytoglobin [29] in 2002. The high oxygen affinity of these proteins initially suggested this traditional role. There is however, a structural difference in the binding pocket of these two new globins; the hemes are hexa-coordinated (They are attached to the protein by both a proximal and distal amino acid), whereas hemoglobin and myoglobin are termed penta-coordinated attached to the protein only by the proximal residue, leaving the distal side free for exogenous ligand binding. It was this difference that led researchers to suggest more novel protein functions [29]. **Figure, 2.3.2** shows examples of penta and hexa-coordinated hemes from globins.



Figure, 2.3.2. Examples of penta (left hemoglobin 1HHO) and hexa (right cytoglobin 1UMO) coordinated hemes in globins.

---

## References

1. Walker, F.A., *Magnetic spectroscopic (EPR, ESEEM, Mossbauer, MCD and NMR) studies of low-spin ferriheme centers and their corresponding heme proteins*. Coordination Chemistry Reviews, 1999. **185-186**: p. 471-534.
  2. Kendrew, J.C., et al., *A Three-Dimensional Model of the Myoglobin Molecule Obtained by X-Ray Analysis*. Nature, 1958. **181**(4610): p. 662-666.
  3. Sharp, R.E. and S.K. Chapman, *Mechanisms for regulating electron transfer in multi-centre redox proteins*. Biochimica Et Biophysica Acta-Protein Structure and Molecular Enzymology, 1999. **1432**(2): p. 143-158.
  4. Burmester, T. and T. Hankeln, *What is the function of neuroglobin?* J Exp Biol, 2009. **212**(10): p. 1423-1428.
  5. Frausto da Silva, J.J.R. and R.J.P. Williams, *The Biological Chemistry of the Elements*. 2nd ed. 1991: Oxford University Press.
  6. Orino, K., et al., *Ferritin and the response to oxidative stress*. Biochem. J., 2001. **357**(1): p. 241-247.
  7. Aisen, P., C. Enns, and M. Wessling-Resnick, *Chemistry and biology of eukaryotic iron metabolism*. The International Journal of Biochemistry & Cell Biology, 2001. **33**(10): p. 940-959.
  8. Scheidt, W.R. and C.A. Reed, *Spin-state/stereochemical relationships in iron porphyrins: implications for the hemoproteins*. Chemical Reviews, 1981. **81**(6): p. 543-555.
  9. Bruice, P.Y., *Organic Chemistry*. 5th ed. 2007: Pearson Prentice Hall.
  10. James, M.F.M. and R.J. Hift, *Porphyrias*. British Journal of Anaesthesia, 2000. **85**(1): p. 143-153.
  11. Quenneville, J., D.M. Popovic, and A.A. Stuchebrukhov, *Combined DFT and electrostatics study of the proton pumping mechanism in cytochrome c oxidase*. Biochimica Et Biophysica Acta-Bioenergetics, 2006. **1757**(8): p. 1035-1046.
  12. Copeland, D.M., et al., *Crystal structures of the nitrite and nitric oxide complexes of horse heart myoglobin*. Journal of Inorganic Biochemistry, 2006. **100**(8): p. 1413-1425.
  13. Jafferji, A., et al., *X-ray Crystallographic Study of Cyanide Binding Provides Insights into the Structure-Function Relationship for Cytochromecd 1 Nitrite Reductase from Paracoccus pantotrophus*. Journal of Biological Chemistry, 2000. **275**(33): p. 25089-25094.
-

- 
14. Gibney, B.R., et al., *Self-Assembly of Heme A and Heme B in a Designed Four-Helix Bundle: Implications for a Cytochrome c Oxidase Maquette*<sup>†</sup>. *Biochemistry*, 2000. **39**(36): p. 11041-11049.
  15. Caughey, W.S., et al., *Heme A of cytochrome c oxidase. Structure and properties: comparisons with hemes B, C, and S and derivatives*. *Journal of Biological Chemistry*, 1975. **250**(19): p. 7602-7622.
  16. Murshudov, G.N., et al., *Structure of the Heme d of Penicillium vitale and Escherichia coli Catalases*. *Journal of Biological Chemistry*, 1996. **271**(15): p. 8863-8868.
  17. Cheesman, M.R. and F.A. Walker, *Low-Temperature MCD Studies of Low-Spin Ferric Complexes of Tetramesitylporphyrinate: Evidence for the Novel (dxz,dyz)<sub>4</sub>(dxy)<sub>1</sub> Ground State Which Models the Spectroscopic Properties of Heme d*. *Journal of the American Chemical Society*, 1996. **118**(31): p. 7373-7380.
  18. Sela, M., F.H. White, and C.B. Anfinsen, *Reductive Cleavage of Disulfide Bridges in Ribonuclease*. *Science*, 1957. **125**(3250): p. 691-692.
  19. Perutz, M.F., et al., *Structure of Haemoglobin: A Three-Dimensional Fourier Synthesis at 5.5- $\text{\AA}$  Resolution, Obtained by X-Ray Analysis*. *Nature*, 1960. **185**(4711): p. 416-422.
  20. Reedy, C.J., M.M. Elvekrog, and B.R. Gibney, *Development of a heme protein structure–electrochemical function database*. *Nucleic Acids Research*, 2008. **36**(suppl 1): p. D307-D313.
  21. Orengo, C.A., et al., *CATH – a hierarchic classification of protein domain structures*. *Structure*, 1997. **5**(8): p. 1093-1109.
  22. Schmidt, M., et al., *Protein dynamics of a  $\beta$ -sheet protein*. *European Biophysics Journal*, 2009. **38**(5): p. 687-700.
  23. Rivera, M., et al., *The Reduction Potential of Cytochrome b5 Is Modulated by Its Exposed Heme Edge*<sup>†</sup>. *Biochemistry*, 1998. **37**(6): p. 1485-1494.
  24. Yi, J., et al., *The Distal Pocket Histidine Residue in Horse Heart Myoglobin Directs the O-Binding Mode of Nitrite to the Heme Iron*. *Journal of the American Chemical Society*, 2009. **131**(50): p. 18119-18128.
  25. Vinogradov, S.N., et al., *A phylogenomic profile of globins*. *Bmc Evolutionary Biology*, 2006. **6**.
  26. Poole, R.K., *Oxygen Reactions with Bacterial Oxidases and Globins - Binding, Reduction and Regulation*. *Antonie Van Leeuwenhoek International Journal of General and Molecular Microbiology*, 1994. **65**(4): p. 289-310.
-

27. Kundu, S., J.T. Trent, and M.S. Hargrove, *Plants, humans and hemoglobins*. Trends in Plant Science, 2003. **8**(8): p. 387-393.
  28. Burmester, T., et al., *A vertebrate globin expressed in the brain*. Nature, 2000. **407**(6803): p. 520-523.
  29. Burmester, T., et al., *Cytoglobin: A novel globin type ubiquitously expressed in vertebrate tissues*. Molecular Biology and Evolution, 2002. **19**(4): p. 416-421.
-

---

---

## 3 CHAPTER HYSCORE EPR of Heme Proteins

---

### 3.1 Introduction

The following chapter was initially intended to be a literature review of how one specific electron paramagnetic resonance (EPR) experiment has been applied to heme-systems. However, a sequential critique of the literature proved unwieldy and possibly of little use to the reader. This section is now rather an overview of some key applications of this experiment and the specific difficulties encountered when performing EPR on high-spin (HS) heme systems. The HYSCORE: Hyperfine Sublevel correlation Spectroscopy [1] experiment, will be briefly introduced to an extent necessary for an understanding of the philosophy of its application. Subsequent sections of this work (Chapter 5) will describe the theoretical and practical aspects of this technique in more detail. At times references will be made to other types of EPR experiments (e.g. ENDOR) and they will be dealt with in the same manner.

### 3.2 Overview of the HYSCORE experiment

The HYSCORE experiment is a two-dimensional Electron-Spin Echo Envelope Modulation (ESEEM) [2] experiment (based upon the COSY (Correlation Spectroscopy) Nuclear magnetic Resonance (NMR) experiment [3]) that produces complimentary and comparable information to the perhaps more applied ENDOR (Electron-Nuclear Double Resonance) [4, 5] experiment. Both techniques in principle are able to detect nuclei coupled to a paramagnetic electron via the nuclear hyperfine and quadrupole interactions (see § 1.2). This enables the nuclear environment of many biologically important reaction centers to be investigated. For the purposes of this chapter the main difference between these two techniques may be considered the magnitude of the coupling that each may detect, with ESEEM generally described as being able to detect weakly coupled nuclei and ENDOR those that are strongly

---

coupled (although Mims ENDOR is more sensitive to weak couplings [4]). As a rough definition for this case, weak may be considered interactions less than 5 MHz and strong greater than 5 MHz (for a  $^{14}\text{N}$  nucleus). Having said this, the HYSCORE experiment possesses two distinct advantages over a standard one-dimensional ESEEM experiment. Firstly, the correlation patterns obtained from the introduction of a second dimension facilitate the assignment of the observed signal as is generally the case for two-dimensional experiments. An increase in spectral resolution is achieved by spreading overlapping peaks over two dimensions. Resulting in a simplification of the interpretation of one dimensional spectra that are otherwise visually indistinguishable from each others. Secondly, the HYSCORE experiment may show couplings of a higher magnitude than a one-dimensional ESEEM experiment. The pulse-sequence of the standard HYSCORE experiment is shown in **Figure 3.2-1**.



**Figure 3.2-1**, The standard HYSCORE pulse sequence

The actual HYSCORE experiment is measured in the time-domain (TD) with the inter-pulse times  $T_1$  and  $T_2$  varies independently along each axis. A two-dimensional (2D) Fourier transform is then carried to produce a 2D-frequency domain described by two frequency axes  $\nu_1$  and  $\nu_2$ . Within which is contained correlations between nuclear spin frequencies from opposite electron spin ( $m_s$ ) manifolds. Being a 2D experiment HYSCORE is understandably more time consuming than a one-dimensional (1D) ESEEM experiment. When considering its implementation it should be estimated to need at least four times the acquisition time compared to a comparable 1D experiment. Having said this correlation spectroscopy has the added advantage of being relatively noise-free compared to non-correlated experiments. This leads to the benefit that the success of the HYSCORE experiment may normally be evaluated after only one complete scan (of course increased measuring time still leads to better quality spectra). The spectra presented in subsequent sections of this work were typically acquired overnight.

In HYSCORE the frequency domain data is usually shown as two quadrants ((-,+) and (+,+)) with correlations in each quadrant being due to strong  $A_{iso} > 2\nu_l$  and weak  $A_{iso} < 2\nu_l$  isotropic hyperfine coupling ( $A_{iso}$ ) respectively [2] Figure 3.2-2.

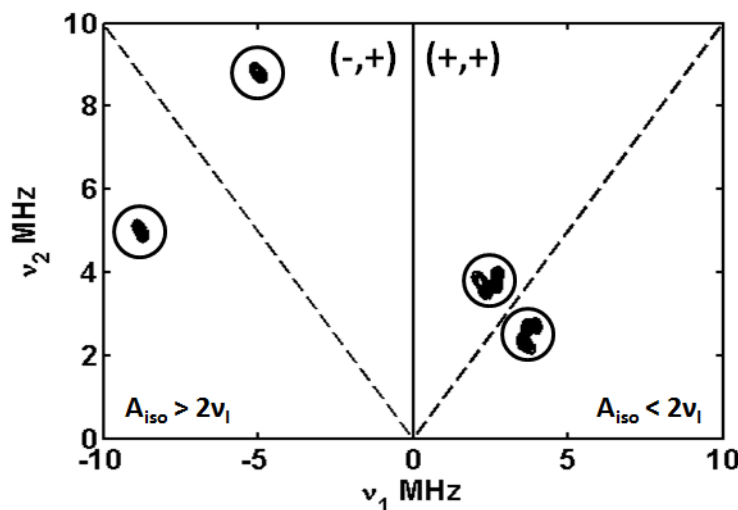


Figure 3.2-2, Simulated HYSCORE plot indicating weak ( $A=[0.8\ 0.8\ 1.1]$  MHz) and strong ( $A=[6.4\ 6.4\ 6.7]$  MHz) coupled signals (circled) in (+,+) and (-,+) quadrants respectively.

From the dipolar contribution to the hyperfine interaction it may be seen that the magnitude of this interaction depends in part to the distance between the unpaired electron and coupled nucleus. The nuclear spin of interacting nuclei will determine the Hamiltonian (§ 1.2) of the system and therefore the couplings potentially observed in the experiments. In the simplest case of  $S=1/2$ ,  $I = 1/2$  (e.g.  $^1\text{H}$ ) ESEEM and ENDOR spectra will only measure a hyperfine interaction. For the more complicated  $S = 1/2$ ,  $I=1$  case, as will be found for the interaction of  $^{14}\text{N}$  nuclei, the nuclear quadrupole interaction will also be present and may potentially frustrate the assignment of observed nuclear frequencies due the complicated nature of the spectra. In this case the  $^{14}\text{N}$  nucleus will be described by six nuclear frequencies. These frequencies can in principle cause up to nine pairs of correlations in the HYSCORE experiment, one DQ-DQ transition. (DQ=double-quantum), four DQ-SQ transitions (SQ= single quantum) and four SQ-SQ transitions [6]. The intensities of these transitions will be different in each quadrant for related features. The interpretation of the HYSCORE experiment in the two cases of  $S=1/2$  with  $I = 1/2$  [7] or 1 [8] have been investigated in some detail both theoretically and

experimentally and are at present reasonably well understood. **Figure 3.2-3** shows the energy-level diagrams for both cases.

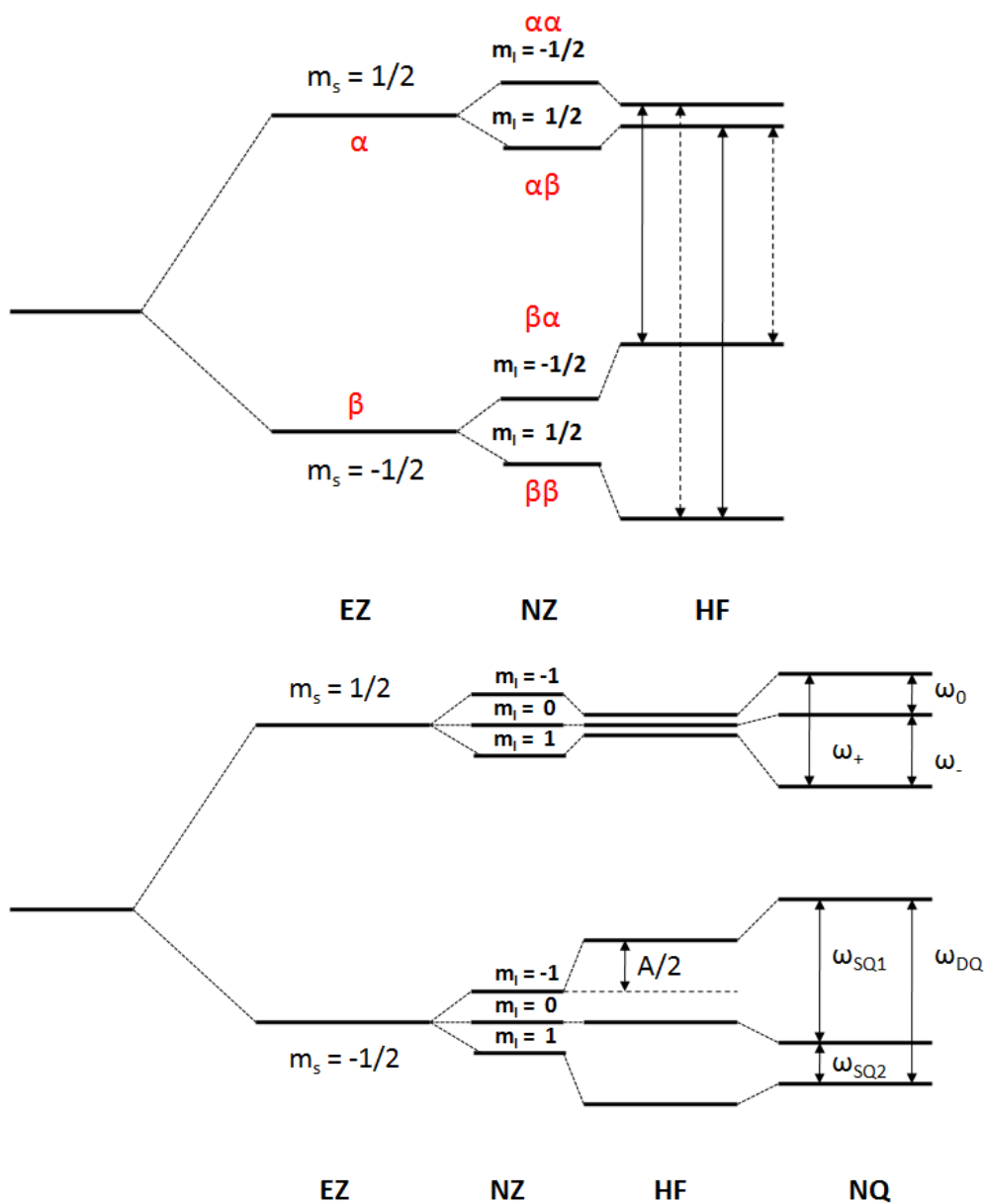


Figure 3.2-3, energy level diagrams for  $S = 1/2, I = 1/2$  (top), and  $S = 1/2, I = 1$  under cancellation condition (bottom). For the first case solid arrows represent allowed and dashed lines semi-forbidden transitions. EZ (Electron Zeeman), NZ (Nuclear Zeeman), HF (Hyperfine) and NQ (Nuclear Quadrupole).

---

For the  $S = 1/2$ ,  $I = 1$  case the energy level diagram for when the cancellation condition is met is shown. The cancellation condition is fulfilled when  $\omega_1 = |A/2|$  (where  $\omega_1$  is the nuclear Zeeman frequency). The effective field experienced by the nucleus in one of the  $m_s$  manifolds is removed and the resulting spectra are composed of the pure nuclear quadrupole resonance frequencies ( $\omega_0$ ,  $\omega_-$  and  $\omega_+$ ) from this manifold and are thus more readily interpreted. In ESEEM experiments it is advantageous that this condition is met to aid the interpretation of spectra. Experiments may also be performed at different microwave frequencies in order to effectively tune the system to this condition. The pulses used in experiments may also be tuned to enhance specific transitions and are known as *Matched*-pulses. Selective Isotope labeling may also be employed to aid the interpretation of hyperfine spectra. In this case differing isotopes will have differing nuclear spins and the resulting difference in spectra may be attributed to the species or molecule within the sample that was labeled. A successful example of the application of selective isotope labeling was the initial HYSCORE study of Garcia-Rubio to be described in § 3.3.5.

---

### 3.3 Low-Spin Systems

#### 3.3.1 Cobalt Model Complexes

Van Doorslaer and the Schweiger EPR group at ETH in Zurich began the investigation of systems using HYSCORE in 1999 with work on cobaltous tetraphenylporphyrin(pyridine) CoTPP(py) [9] ( $S=1/2$ ) **Figure 3.3-1** .

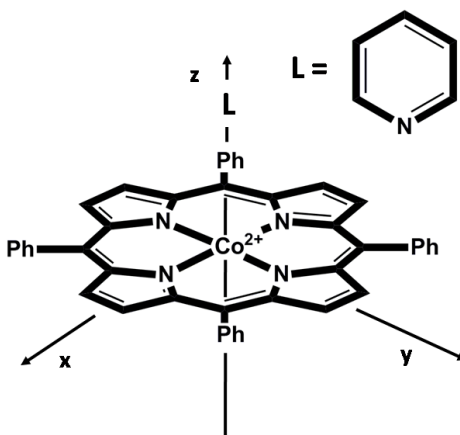


**Figure 3.3-1**, Structure of cobaltous Tetraphenylporphyrin (pyridine) CoTPP(py) from [9] and definition of axis-system used in work.

This compound was used as a model to study the heme group in deoxyferrous hemoglobin (Hb) and myoglobin (Mb) (adding to the initial work by Hoffman [10]) which are normally EPR silent due to their diamagnetic nature. In this initial work the weak hyperfine and nuclear quadrupole interactions of the porphyrin nitrogen's were able to be detected. The double nuclear coherence transfer (DONUT)-HYSCORE [11] experiment (Chapter 5) was found to be able to simplify the assignment of cross-peaks in HYSCORE spectra. This experiment provides complimentary information to the standard-HYSCORE experiment by correlating nuclear frequencies from the same electron manifold. For an  $S = 1/2$ ,  $I = 1$  system under exact cancellation this allows for the observation of cross-peaks due to nuclear quadrupole (NQ) frequencies. Davies and Mims ENDOR experiments (each more sensitive to strong and weak coupling respectively) as well as HYSCORE were also performed at S and X-band frequencies. Indeed this was the first paper to publish proton HYSCORE data at S-band. Deuterated pyridine was also used as an axial ligand to simplify the spectra and facilitate the assignment

of the observed couplings. This in conjunction with Davies-ENDOR allowed the determination of the hyperfine and nuclear quadrupole couplings of the pyridine nitrogen's. It should be noted however, that these values differed from earlier reported values determined by ESEEM [12, 13] Although prior to this paper, the observation of coupled protons had been reported [14], this was the first instance where the hyperfine parameters were able to be determined. The hyperfine data generated was thus used to calculate inter-nuclear distances and determine the distribution of the spin-density within the complex. The electron-spin density in the 3d and 4s orbitals of the cobalt atom was able to be calculated from a previously determined relationship [15]. The determined anisotropic component of the hyperfine interaction was used to estimate the spin density on the nitrogen nucleus. The anisotropic hyperfine interaction was also related to inter-nuclear distances by assuming a dipole-dipole interaction. Cobalt model complexes were further examined by this group with a similar methodology applied in each case [16, 17].

### 3.3.2 Iron Model Complexes

At the same time of Van Doorslaer *et al*s initial work on Co(TPP), Dikanov *et al* [18] applied HYSCORE to a  $^{15}\text{N}$ -Porphyrin-Fe(II)-NO model (TPP) complex in order to determine the position of the effective point electron-spin **Figure 3.3-2**.

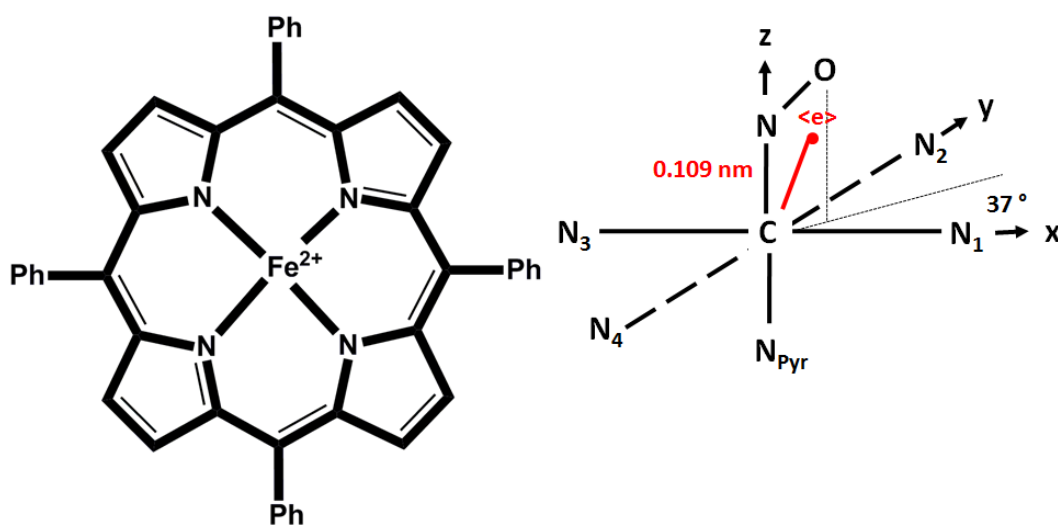


Figure 3.3-2, Model of  $^{15}\text{N}$ -porphyrin-Fe(II)-NO TPP complex (left) and location of calculated effective electron spin (C indicates centre of porphyrin ring system).

The  $^{15}\text{N}$  nucleus should theoretically facilitate the interpretation of ESEEM/HYSCORE data largely due to its larger magnetic moment, and it having a nuclear spin  $I = 1/2$  (no quadrupolar interaction). The couplings of the pyrrole nitrogens were again the focus of investigation. No evidence for the interaction with the  $^{14}\text{N}$  of pyridine was seen, which was suggested to be due to the hyperfine interaction being too large to be observable at X-band with ESEEM techniques. The HYSCORE data were analysed using the method of Dikanov and Bowman [19] to resolve the isotropic and anisotropic components of the hyperfine interaction. These values together with data from previous studies [20-22] were used to produce a model of the electron spin and the interaction of the pyrrole nitrogens.

### 3.3.3 Van Doorslaer Low-Spin Ferric Complexes Methodology

Using their previous experience with model heme complexes Van Doorslaer and Vinck proposed a complete methodology including the application of HYSCORE for the analysis of bis-imidazole low-spin ferric porphyrin complexes to determine the orientation of the heme's ligands with respect to the heme [23]. This work was partly based on the findings of Raitsimring and Walker relating the intensity of the combination peaks for distant protons in two-pulse ESEEM or combination peak experiments to the orientation of the g-tensor axes with respect to the molecular axis system [24, 25]. With this information it is, in principle, possible to infer the nature of the electronic orbital ground state of a low-spin ferric system and to determine whether the unpaired electron is mainly localized in one of the  $d_{\pi}$  orbitals ( $d_{yz}$  or  $d_{xz}$ ), or instead, in the  $d_{xy}$  orbital in the porphyrin plane. Van Doorslaer showed how the hyperfine and nuclear quadrupole tensors of the porphyrin nitrogens may be used to determine these axes in relation to the molecular frame. The g-values obtained from CW-EPR allow for an estimation of the angle between the projection of the imidazole ligand normal on the porphyrin plane and the nearest  $\text{N}_p\text{-Fe-N}_p$  ( $\text{N}_p = \text{porphyrin N}$ ) axis from a previous study on bis-imidazole porphyrin complexes [26]. From previous single-crystal studies of metallo-porphyrins [27, 28] it is known that the largest nuclear quadrupole principle value lies in the porphyrin plane perpendicular to the  $\text{Fe-N}_p$  bond. HYSCORE data measured at the principle g-values was simulated in order to determine complete nuclear coupling information and determine the orientation of the g-axes in the molecular frame, particularly the orientation of

the  $g_x$  and  $g_y$ -axes. The methodology relies heavily on the accurate simulation of the HYSCORE spectra for a complete determination of hyperfine and nuclear quadrupole couplings. Van Doorslaer *et al* applied this methodology to a series of heme proteins including non-symbiotic tomato hemoglobin [29], mouse neuroglobin [30], cytoglobin [31] and heme from the globin domain of the globin-coupled sensor protein [32]. At times the methodology was enhanced by the addition of ENDOR, DONUT-HYSCORE or other EPR techniques but still with the aim of a complete elucidation of the nuclear coupling parameters via effective simulation of spectroscopic data. For the investigation of the globin-coupled sensor however, the CW-EPR method of determining the axial ligand orientation was reviewed: Initially the CW-EPR spectrum of the protein was used to obtain the principal  $g$ -values and relate these to the possible orientations of the hemes axial ligands via the ligand-field parameters as previously mentioned. This method was applied more cautiously than had been previously as the authors point out a degree of controversy with its application [33], which was the first time that this possible shortcoming was mentioned in the EPR literature. Other sources were used to affirm however, that a  $g_z > 3$  for a bis-histidine heme, indicates the histidine planes being twisted and tilted [34]. It was also contended that the quadrupole asymmetry parameter  $\eta$  may be used for globins to elucidate the orientation of the different histidine side chain planes. It is stated that a small value for this parameter corresponds to cases where the planes are strongly tilted away from the  $g_{x,z}$  plane, as seen in human cytoglobin [35] and one orientation in mouse neuroglobin [30].

### 3.3.4 Nitrosyl-Hemoglobin

Concurrently to the initial model complex studies Tyryshkin, Dikanov and others were investigating nitrosyl (nitric oxide) heme complexes in what can be said to be the first application of the HYSCORE experiment to an actual biological system [6]. The aim of their study was again to elucidate the nature of oxygen binding to hemoglobin (Hb), this time however, nitrosyl-ligated Hemoglobin (HbNO) was used as a model for Oxy-Hb due to the similarities in its binding effects and the paramagnetic nature of the resulting complex. A series of nitrosyl heme proteins were employed in the investigation: The native Hb in both the R(relaxed) and T(tense) states (liganded and unliganded respectively), the isolated  $\alpha$  and  $\beta$

subunits of nitrosyl Hb, two hybrids of Hb with asymmetric cross-linked  $\alpha(\beta)$  chains, Mb-NO and Fe(TPP)-imidazole model complexes. The main EPR experimental methods utilised in this work were orientation-selected three-pulse ESSEM together with HYSCORE. The results from the ESEEM spectra were discussed in terms of the contribution from two conformations of the NO-heme group, known as state I and state II (**Figure 3.3-3**).

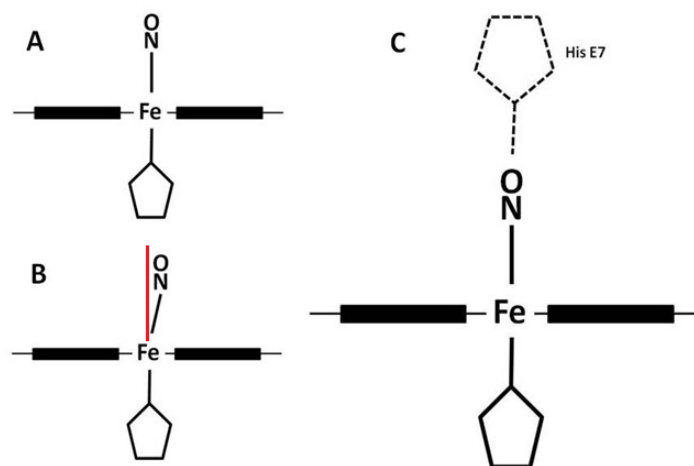


**Figure 3.3-3, Conformational state of nitrosyl (nitric oxide) ligated heme-complexes: A) State II (axial), B) State I (rhombic), C) Nitrosyl ligation to distal His E7 in state II.**

These two states were initially thought to be different displacements of the heme iron with respect to the porphyrin plane [20]. Subsequent EPR and ENDOR studies [36, 37] indicated however, that the two states comprised conformations in which the Fe-NO bond is not coincident with the heme plane normal, and another where it does (state I and state II also known as rhombic and axial respectively **Figure 3.3-3**). Prior to this the large hyperfine couplings of the directly coordinated  $^{14}\text{N}$  of the proximal histidine ( $A_{\text{max}} = 15\text{-}20$  MHz), and for the  $^{14}\text{N}$  and  $^{15}\text{N}$  of nitric oxide ( $A_{\text{max}} = 30\text{-}50$  MHz) had been determined using ENDOR [38, 39]. The small couplings to the pyrrole nitrogen's initially calculated [40] ( $\leq 5.5$  MHz), would be suitable for the application of ESEEM. Indeed this had previously been attempted using a similar series of nitrosyl-hemeproteins [12] with the conclusion that the ESEEM spectra indicated the contribution of only one type of pyrrole nitrogen. The magnetic interactions were found to be similar for all of the six complexes investigated. It should be noted however,

that this study failed to take orientation selectivity into account, which may have led them to inaccurate conclusions. Tyryshkin found that all the native nitrosyl complexes were characterised by the same nuclear quadrupole interaction (NQI) frequencies, these frequencies did none-the-less differ considerably from those of the NO-Fe<sup>2+</sup>(TPP)-Im model system. A comparison of the NQI values given in Table 3-1 shows the general consistency in quadrupole coupling constant K of the pyrrole nitrogen's.

Complex	$K = e^2Qq/4h$ (MHz)	$\eta$	Ref.
Hb-NO	0.45	0.37	[6]
Fe(TPP)	0.47	0.45	[6]
Cu(TPP)	0.463	0.377	[28]
Ag(TPP)	0.457	0.513	[28]
VO(TPP)	0.47	0.5-0.6	[41]
Co(TPP)	0.45	0.55	[9]

**Table 3-1 Nuclear quadrupole interaction parameters for the heme pyrrole <sup>14</sup>N in nitrosyl-hemoprotein and metal-complex models.**

The asymmetry parameter  $\eta$  demonstrates a wider variation via the chemical structure and local matrix. It is the difference in this asymmetry parameter that produces the difference in the NQI frequencies in the native and model systems. The values of these NQI frequencies were determined from the ESEEM data of what was termed the high-field region ( $g = 1.991$ ) which exhibited three narrow lines that satisfied an additive relationship, indicative of the cancellation condition for nitrogen nuclei [42]. These three lines correspond to the NQI transition frequencies. In addition a peak in the range  $\sim 5.3$ - $5.5$  MHz was seen both in this study and previously [12]. In the initial research [12] this was ascribed to a double-quantum ( $\nu_{dq+}$ ) transition, arising from the same species of pyrrole nitrogen that generate the NQI lines. Tyryshkin *et al* however thought this unlikely due to the uncorrelated variation of intensities between the NQI lines and the broad  $\nu_{dq+}$  line. They also observed that this line was not apparent in the model samples. These factors led them to the conclusion that the  $\nu_{dq+}$  line was generated by a different type of nitrogen to the pyrroles contributing to the NQI lines, which

was confirmed with HYSCORE. An analysis of the isolated  $\alpha$ NO and  $\beta$ NO chains having a largely state I and state II conformation respectively, aided the characterisation of the hyperfine couplings associated with each state. The interaction with the protein nitrogen assigned to the His-E7 (distal) residue was only seen for state II. This supported the assertion that variations in binding geometries between state I and state II are controlled by the heme's protein environment. They deemed the  $^{14}\text{N}$  hyperfine coupling values determined by this investigation to be consistent with earlier conformational models but were unable to further refine those models, as the complete analysis of the ESEEM data was hindered by the dominant contribution of the NQI. This resulted in only limited information regarding the hyperfine interactions with each of the pyrrole nitrogens being determined. It was suggested that this may be overcome by repeating the experiments with  $^{15}\text{N}$  substituted pyrrole nitrogens.

### 3.3.5 Cytochrome $b_{559}$

Perhaps the most successful initial application of the HYSCORE experiment to a heme containing system was the work led by Garcia-Rubio on cytochrome  $b_{559}$  in 2003 [43]. In a heme protein the paramagnetic spin is surrounded by several magnetically interacting nuclei (five or six N and numerous protons). Selective isotopic substitution of the nitrogen atoms of model heme compounds was employed in order to aid the assignment of the observed signals to specific nuclei. The hyperfine and quadrupole coupling tensors derived from the investigation were able to be interpreted in terms of the structure and electronic distribution of the heme. The work produced two main conclusions: from the hyperfine tensors the unpaired electron was seen to be confined in a non-bonding iron orbital with a negligible nitrogen p-orbital contribution. The quadrupolar coupling tensors indicated that the orientation of the semi-occupied orbital was driven by the orientation of the parallel proximal and distal histidine residues. In the simulation, as in the original data, the contributions from the DQ transitions of the heme and imidazole nitrogens can be resolved. Subsequent HYSCORE studies made use of this resolution in the assignment of their correlations. This was also the first study to solely use HYSCORE and ESEEM for the characterisation of the sample.

---

The dominant contributions to all spectra measured were assigned DQ transitions. **Figure 3.3-4** shows a simulation of the HYSCORE spectrum of cytochrome (Cyt)  $b_{559}$ .

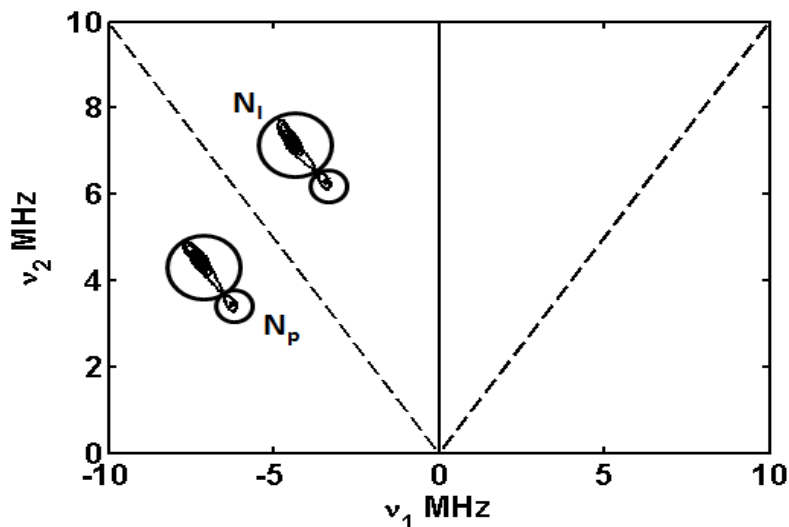


**Figure 3.3-4**, Simulation of HYSCORE spectrum measured in the heme-plane of Cyt  $b_{559}$  from [43].  $N_I$  and  $N_P$  indicate the Double-Quantum (DQ) correlations of the Imidazole (His) and heme nitrogens. Parameters used for simulation:  $N_I$ ,  $A = [5.6, 6.2, 5.1]$  MHz,  $Q = [1.6, 1]$  ( $e^2qQ/h, \eta$ ).  $N_P$ ,  $A = [4.7, 4.9, 5.8]$  MHz,  $Q = [-0.8, 1]$  ( $e^2qQ/h, \eta$ ).

The investigation was also able to resolve contributions to the spectra measured at the  $g_y$ -position and assign them to two inequivalent porphyrin nitrogens. Simulation of the data was not performed which possibly explains the contention from the authors that the observation of strong quadrupolar anisotropy in the  $g_y$ -spectra indicated that quadrupole tensor  $Q_{zz}$  was not the highest absolute value, which by definition it must be (§ 1.2.4).

### 3.3.6 Nitrosyl $cd_1$ Nitrite Reductase

The first work in this area from the Weizmann institute (Goldfarb) was a W-band ENDOR and HYSCORE investigation of the low  $g$ -anisotropy system,  $d_1$  heme-nitrosyl complex ( $Fe^{II}$ -NO) in  $cd_1$  nitrite reductase [44] in 2009. The aim of this study was to determine whether the tyrosine residue in the distal binding pocket affected the NO binding to the heme centre. Samples of wild-type (wt) protein and an Y10F mutant were examined to facilitate this. The hyperfine and quadrupole coupling parameters of the proximal histidine and nitrosyl nitrogens were able to be resolved. The study was undertaken using a high-power home-built

spectrometer [45], thus overcoming the problems mentioned in [46] for commercial spectrometers. The spectra measured at  $g = 2.0$  and  $1.99$  of the wt and Y10F mutant respectively, revealed correlations in both quadrants attributed to the coordinating nitrogen of the proximal histidine with reference to [47]. These peaks are also seen for Y10F at the  $g = 1.96$  and  $2.055$  positions. Additional correlations in the  $(-,+)$  quadrant were attributed to the NO nitrogen. To confirm the assignment of the correlations Davies ENDOR was performed, which revealed signals attributable to the heme and NO nitrogens, only one type of heme nitrogen was observed. The ENDOR frequencies were used to initially estimate the hyperfine and quadrupole coupling parameters which were then refined with simulation of the HYSCORE and ENDOR spectra. Small differences were found between the line positions of the two spectroscopic methods which led to small discrepancies between the calculated and experimental spectra. The hyperfine coupling parameters determined in this investigation were in good agreement for those previously found for nitrosyl complexes of Iron heme complexes **Figure 3.3-5**

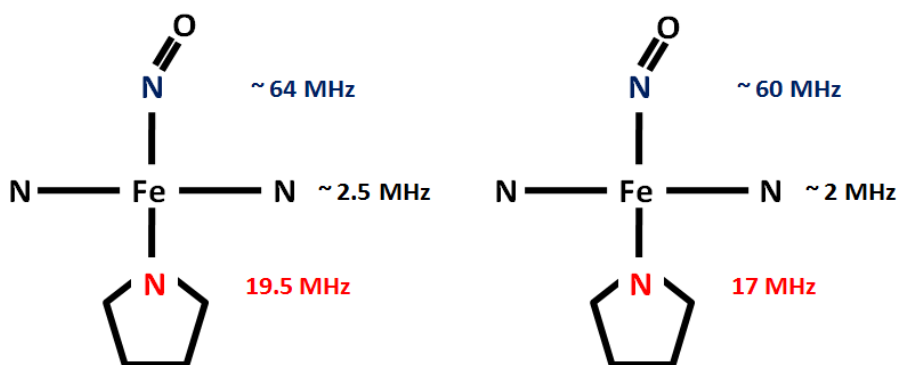


**Figure 3.3-5, Hyperfine couplings determined for coordinating nitrogens in nitrosyl cd<sub>1</sub> nitrite reductase (left) [44], and for heme-iron compound described in [2].**

The paper concludes that Tyr10 had little effect on the structure of the Fe-NO complex, in agreement with the crystal structure. W-band HYSCORE was presented as a tool to characterise nitrogen nuclei with  $A \sim 2\nu_N$  and its application to copper (II) containing proteins with histidine ligands is suggested. It is also remarked upon that the time taken to measure the HYSCORE spectra was significantly less than needed for the ENDOR spectra and that the HYSCORE provided more information overall. The paper claims to be the first application of

high-frequency HYSCORE and makes no reference to the previous published W-band HYSCORE spectrum [46]. Indeed most of the previous HYSCORE analysis of hemes is ignored. The low  $g$ -anisotropy of the system led to the application of W-band but it is not stated if X-band HYSCORE was attempted which may also have shown the interaction of the heme nitrogens. ESEEM may also have been advantageous in this work, as the appearance of correlations attributable to the same nuclei in both the weak and strong coupling quadrants indicate that the cancellation condition was met.

### 3.3.7 Cytochrome P450

A relatively qualitative application of the HYSCORE technique was performed to investigate the heme ligation in Cytochrome P450 [48]. In Cyt P450 the proximal ligand is cysteinate which is a strong ligand, therefore Cyt P450 exists in the low-spin state most of the time. The investigation utilised a variety of techniques other than EPR, the focus of interpretative data arising from molecular dynamics simulations. However the HYSCORE spectra measured at the  $g_z$  position of the wt, R108H mutant and wt with imidazole samples was able to determine that in the mutated form of the protein the heme was distally coordinated to the mutated histidine residue. Although the paper presents standard X-band HYSCORE spectra typical for heme proteins this is first example of HYSCORE difference spectra being shown for this area. The two spectra presented were produced by subtracting the normalised wt HYSCORE spectrum from the normalised spectra of the mutant and imidazole samples. Each difference spectra was shown in terms of the positive and negative peaks (i.e. additional and missing contributions to the spectra c.f. wt). The presence of a series of proton peaks in the wt sample and absent from the imidazole and mutant proteins was attributed to the protons of a coordinated water molecule to the heme. The similarity between the difference spectra of the imidazole and mutant proteins was used to support the hypothesis that the mutated histidine residue was coordinated to the heme centre in the R108H mutant protein.

## 3.4 Nitrosyl Myoglobin

The Weizmann group again applied high-field (W-band) HYSCORE was used to examine NO binding but this time to Mb [49], this study also utilised various quantum chemical

---

approaches to interpret the experimental HYSCORE data. The binding of NO to the reduced form of Mb was seen to lead to the formation of two complexes characterised by a rhombic and an axial g-tensor. The aim of the investigation was to determine which factors led to the formation of these two forms, with an emphasis on the role of H-bonding. The application of W-band standard HYSCORE allowed the detection of the rhombic form, for which a NO-H hydrogen bond was unambiguously assigned to the protonated nitrogen  $N_{\epsilon}$  in the His64 residue **Figure 3.4-1**.

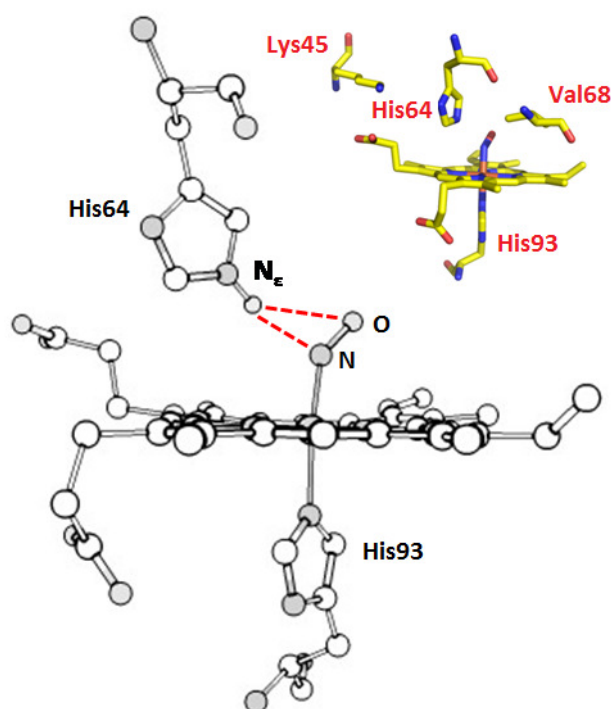


**Figure 3.4-1**, H-bonding in nitrosyl myoglobin (red lines). Insert shows residues included in computational calculations. Calculations based on structure 2FRJ [50].

The complete hyperfine and quadrupole parameters for the  $^{14}\text{N}$  of the His64 were also determined. One of the advantages stated for HYSCORE at this frequency was the facilitation of pseudo-crystal measurements due to the large g-anisotropy. Evidence for the origin of the axial form was, however, not conclusive.

### 3.5 High-spin hemes

#### 3.5.1 Problems associated with high-spin hemes for hyperfine EPR

Perhaps the greatest consequence of the spin-state of the paramagnetic centre to EPR for hyperfine spectroscopies is the lifting of  $2S + 1$  degeneracy of the spin-state caused by the application of a magnetic field. For the high-spin ( $S=5/2$ ) case this leads to the production of three Kramer's doublets only the lowest of which may be detected. Also due to the relaxation properties of high-spin systems pulsed experiments must usually be performed at extremely low temperature ( $\sim 4$  K). In the case of high-spin heme proteins where the hyperfine and  $g$ -tensors have the same principal axes the principal values of the hyperfine tensor may be described by an effective hyperfine tensor [51]:

$$A_{k,x}^{eff} = A_{k,x} \left( 3 - \frac{12E}{D} \right)$$

$$A_{k,y}^{eff} = A_{k,y} \left( 3 + \frac{12E}{D} \right)$$

$$A_{k,z}^{eff} = A_{k,z} - \frac{2A_{k,x}A_{k,y}}{D}$$

The main consequence of this being that the effective hyperfine components in the heme plane (i.e. the  $x$  and  $y$  directions) are increased by approximately a factor of three. For Mb this means effective hyperfine values of the order  $\sim 25$ - $30$  MHz, which is outside the range conventionally detectable by ESEEM experiments. There is also a large pseudo-nuclear contribution to the nuclear  $g_n$  tensor so that the nuclear Zeeman frequencies may no longer agree with tabulated values, complicating the interpretation of the ESEEM and ENDOR spectra. For these reasons the limited number of ESEEM studies have concentrated on the single-crystal like observer position  $g \approx g_z^{eff}$ .

### 3.5.2 Neuroglobin

Possibly the first HYSCORE study of high-spin ( $S=5/2$ ) globins was an investigation into the E7Q mutant (from E7H for WT) of human neuroglobin by Van Doorslaers group in 2007 [51]. In this study myoglobin was used experimentally as a model compound, and the seminal work of Scoles [27] used as a basis for understanding the experimental findings. Matched-pulse HYSCORE was used on the high-spin systems in order to resolve the spectral contributions from the nitrogens. (matched-Pulsed techniques are a method for increasing the sensitivity of the experiment to particular nuclei and will be discussed further in Chapter 5) The study also undertook to evaluate the validity of approximating the high-spin system as an effective  $S = 1/2$  system, the implications of which were discussed with reference to the effect on HYSCORE simulations. In conjunction with deuterium exchange experiments the overall findings of this work were that in the neuroglobin mutant, the heme iron was penta-coordinated, with no distal water ligated as in the myoglobin system. CW-EPR experiments indicated that at high pH the E10K residue in the neuroglobin coordinated to the iron. The paper provides a good theoretical discussion of the treatment of the system as an effective  $S = 1/2$ , as found in Abragam and Bleaney [52], it also discusses the general difficulties in performing ESEEM experiments on an  $S = 5/2$  system. However, the main findings of this work may be disputed: The HYSCORE spectra of neuroglobin presented clearly show a proton ridge, albeit with a different apparent value for the isotropic hyperfine interaction. The hypothesis that at high pH the iron coordinates to a lysine is based on the appearance of a low-spin EPR signal with  $g_z = 3.33$  in the CW-EPR. This signal, known as a Highly Anisotropic Low-Spin (HALS) or type I signal, may however, also be due to a bis-histidine coordination where the histidine planes are perpendicular [34]. An examination of the crystal structure for murine neuroglobin [53] shows that this is indeed the case. The authors also did not follow the correct convention for the assignment of the principal nuclear quadrupole values.

---

### 3.5.3 Aquometmyoglobin

The following two sections describe two papers that in effect may be considered a single study of weak and strong nuclear couplings in high-spin aquometmyoglobin. The results of the hyperfine experiments performed at X-band are summarised in **Figure 3.5-1**.

#### 3.5.3.1 Strongly Coupled Nuclei

The groups of ETH Zurich and Antwerp combined to create a work aimed at providing a definitive procedure for the analysis of high-spin heme proteins [46]. Aquometmyoglobin was used as a standard so the values determined experimentally in this work could be compared to the single crystal ENDOR data determined previously [27].

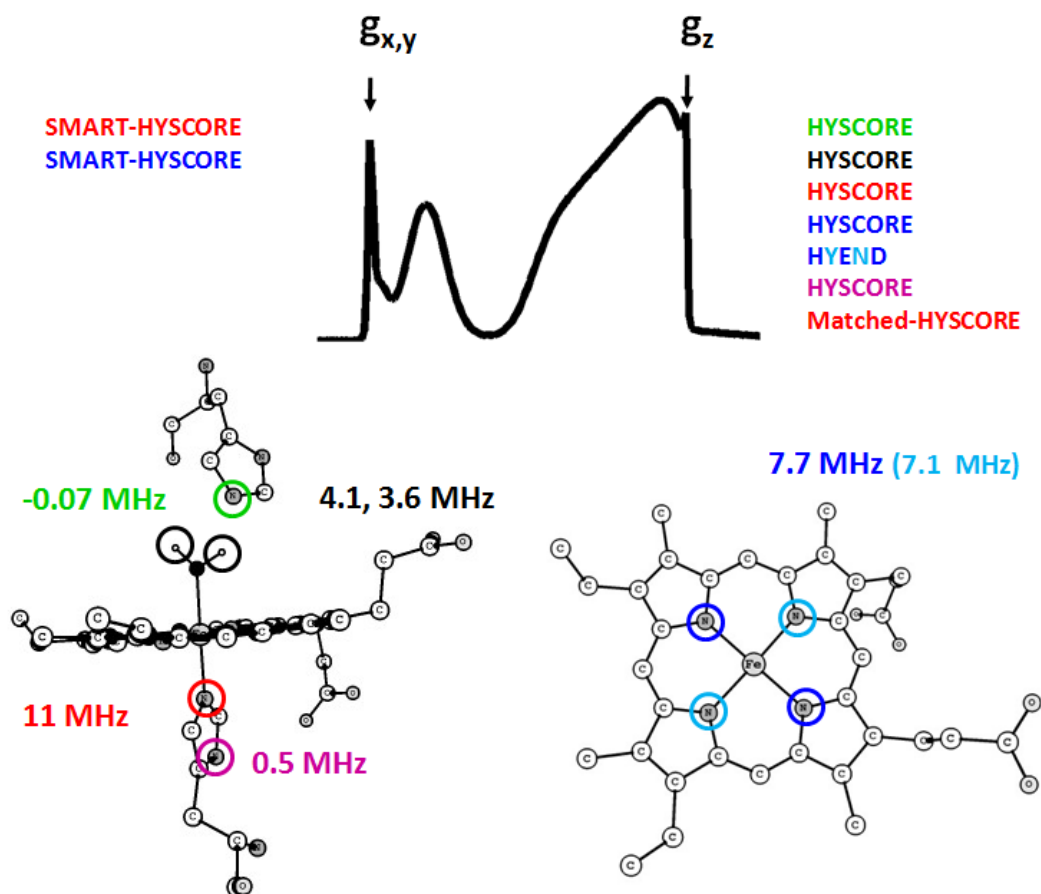


Figure 3.5-1, Summary of experiments used to determine hyperfine couplings in aquomet-Mb at X-band. For different nuclei at different g-value positions, summarized from [46, 54]. The dual blue colors used for HYEND indicate that it was able to resolve the inequivalency in the porphyrin nitrogens.

A large variety of pulsed experiments were used in this investigation including several variations of the standard HYSCORE experiment (Matched-Pulse HYSCORE and SMART HYSCORE) the standard HYSCORE experiment was also performed at Q and W-band. Standard X-band HYSCORE was first employed to determine the nuclear frequencies of the directly coordinated nitrogens. The sample was investigated at the  $g \approx g_z^{\text{eff}}$  position. For the heme nitrogens the spectrum contained correlations consistent with those found for the low-spin systems previously described ((+,+) quadrant), suggesting a hyperfine coupling of  $\sim 7.7$  MHz. Weaker correlations in this quadrant were associated, by comparison to Scholes findings, to the sq transitions of the histidine nitrogen with an effective hyperfine coupling of  $\sim 11$  MHz. The dq transitions for this nitrogen were not detected in this case. A number of the correlations in the spectrum showed a doubling of peaks, indicative of the two inequivalent but similar heme nitrogens. X-band HYEND (a two-dimensional ENDOR experiment) [55] at the  $g \approx g_z^{\text{eff}}$  position was also employed and was able to separate the contributions of the two inequivalent heme nitrogens (with couplings of 7.1 and 7.7 MHz) and the histidine nitrogen. This experiment was also able to determine the nuclear quadruple couplings along the heme normal (see table). This technique was however, unable to produce useful data at lower field positions due to the significant broadening out of the hyperfine lines at non single crystal like field positions. Matched pulse X-band HYSCORE increased the resolution of the standard experiment at the single-crystal position allowing the DQ frequencies of the histidine nitrogen to be detected. More combination frequencies were also seen allowing the determination of the sign of the coordinated water proton and heme nitrogen hyperfine coupling, information unobtainable from ENDOR data. Matched HYSCORE was still however, unable to measure signals at positions near  $g \approx g_{x,y}^{\text{eff}}$ . This was not the case for the SMART HYSCORE [56] experiment, which allowed the signals of the coordinating nitrogens to be detected near this position. The experiment also corroborated the assignment of the signs of the hyperfine values. The spectra presented were recorded with protein in deuterated buffer; the authors note that this enhanced the detection of the DQ peaks. This is accounted for by an increase in the phase memory time by a factor of 13 and by cross suppression effects [57] in which echo modulations associated with protons are responsible for the suppression of those associated with nitrogens. The authors' simulations led them to theorise that this

---

suppression effect should be less evident for Q-band HYSCORE due to the decreased proton modulation depth at this frequency. This was also observed experimentally as the detection of nitrogen signals was facilitated by the use of higher mw frequencies even away from the  $g \approx g_z^{\text{eff}}$  position. The increase in the Boltzmann populations afforded by the increased mw frequency also enabled spectra to be recorded at higher temperatures (5.5 K c.f. 3.8 K). W-band HYSCORE was also performed. The problems of obtaining enough power to generate hard  $\pi$ -pulses with commercial spectrometers at this frequency are somewhat overcome in the high-spin case due to the spin-system dependence on the pulse flip-angle. So that in comparison to an  $S = 1/2$  system a  $\pi/2$ -pulse can be obtained with a shorter pulse length. The spectrum was recorded at the  $g \approx g_{x,y}^{\text{eff}}$  position, and recorded the sq correlation of the heme nitrogens, with the shape of the correlation ridges reflecting the inequivalence of the two sets of porphyrin nitrogens. W-band ELDOR detected NMR [58] revealed information consistent with the findings described above but with less resolution than the multi-frequency HYSCORE approach. It was able however, to obtain this information in one scan and so was far quicker than the previous methods employed.

As mentioned above, this investigation was performed on a model system so that the findings of the series of experiments could be compared with data already obtained from the single-crystal ENDOR study of Scholes. The paper therefore clearly sets out exactly what information may be obtained for previously unstudied frozen solutions. The interactions of the distal ligand (water) were also measured in this investigation with the aid of  $^{17}\text{O}$ -labelled water.

### 3.5.3.2 Weakly Coupled Nuclei

Furthering the analysis of high-spin globins was a follow on from the above ETH/Antwerp groups, but this time looking at the nuclear couplings of remote magnetic nuclei again in met-Mb [54]. In this work standard and SMART HYSCORE experiments were undertaken at both X and Q-band. This investigation reported the detection of correlations associated to protons of the proximal histidine, mesoprotons of the heme and the two separate protons of the coordinated water molecule. Correlation peaks from naturally abundant  $^{13}\text{C}$  in the heme were also reported. The work implies that signals detected in the (+,+) quadrant (weak-coupling)

would be due to remote nuclei. This investigation aimed to place HYSCORE in a position to compete with NMR for the determination of the hyperfine interactions of remote nuclei. From a theoretical point the investigation took the position that the effective  $g$ -values and principal hyperfine values would deviate from the electronic spin 5/2 Hamiltonian by a multiplicity of three as discussed in § 3.5.1.

### Protons

The standard X-band HYSCORE spectrum was a gain measured at the  $g \approx g_z^{\text{eff}}$  position, for which it is stated, only molecules for which the heme normal lay  $\sim 10^\circ$  away from the magnetic-field direction would contribute to the spectrum. This spectrum revealed several correlations in the (+,+) quadrant, particularly those of protons centred at  $\nu_H$ , but also several in the low-frequency region centred at  $2\nu_N$  and  $\nu_C$  indicating the detection of remote nitrogens and natural abundance  $^{13}\text{C}$  near the iron centre. As documented in their previous studies the proton ridges were assigned to the coordinated water molecule. As spectra were measured at lower field positions the correlations due to the weakly coupled nuclei became less intense and at the  $g \approx g_{x,y}^{\text{eff}}$  position no signal is observable with either ENDOR or HYSCORE. For a complete characterisation of the proton hyperfine interaction it is however, necessary to measure correlations away from the  $g \approx g_z^{\text{eff}}$  position. To this end SMART HYSCORE was again employed. For the  $g \approx g_{x,y}^{\text{eff}}$  position the spectrum revealed proton correlation peaks in both the (+,+) and (-,+) quadrants, suggesting that some protons were approaching the cancellation condition  $|A^{\text{eff}}|/2 \approx |\nu_H|$ . To increase the measurable signal, protein samples were prepared in deuterated buffers as in the previous study. To facilitate the assignment of the proton ridges data from X-ray diffraction and NMR studies were used as simulation starting values. This enables the assignment of the proton ridges to the heme mesoprotons and to the  $C_\delta$  and  $C_\epsilon$  protons of the directly coordinated histidine. It is mentioned that as expected the correlation patterns obtained were asymmetric and that a number of peaks were apparent at  $2\nu_H$ , although this is not commented on further. Q-band SMART HYSCORE was employed to obtain more information about the coordinated water molecule at the  $g \approx g_{x,y}^{\text{eff}}$  position. These spectra also revealed well defined correlation ridges centred on  $\nu_H$ . These correlations were assigned to mesoprotons based on the X-band

data and to the water protons from a combination of simulation and deuterium exchange. In order to obtain a good fit between the simulated and experimental data an isotropic hyperfine interaction of -0.3 MHz was needed. The paper reinforces the point that good quality Q-band data may be obtained without the need for deuterated solvents and references their previous work [46] to corroborate this. The X-band standard HYSCORE spectrum near  $g \approx g_z^{\text{eff}}$ , and the Q-band SMART HYSCORE spectrum at  $g \approx g_{x,y}^{\text{eff}}$  both revealed a separate set of proton correlations that disappeared with deuteration. It was theorised that this was most likely due to distinguishing between the two water protons, although the possibility of the water molecule being detected in two slightly different coordinations in the frozen powder sample could not be ruled out.

### Weakly coupled Nitrogens

The standard X-band HYSCORE spectrum at  $g \approx g_z^{\text{eff}}$  showed a number of correlations in the low-frequency region of the spectrum that had been previously unseen with other EPR techniques in high-spin hemes. These correlations were centred around  $2\nu_N$  and  $\nu_C$ , and disappeared below 300 mT. They were however, observable in standard Q-band spectra in the region  $g^{\text{eff}} = 4-6$ . The enhancement of the Zeeman splitting at this frequency also separated the contributions to the spectra from these two nuclei. The most intense correlations in the X-band data were assigned to dq transitions and lay at an average frequency of  $\sim 0.5$  MHz above  $2\nu_N$ . These correlation peaks were also observable in the Q-band spectra. Simulation of this correlation led to hyperfine values greatly different from those of the directly coordinating nitrogens previously reported and to a nuclear quadrupole value  $K = 0.4$  MHz. This value is typical for protonated nitrogens of imidazoles (unreferenced) and so was assigned to the  $N_\delta$  of the proximal histidine. The hyperfine parameters measured for this work may be seen in.

These correlations were also visible in the spectrum of E7Q-neuroglobin [51], but not in the model cyt P450 complex in which the axial ligand is a sulphonyl group [59]. The most intense peaks in the Q-band spectra however, were attributed to another nitrogen nucleus, and were centred  $\sim 1$  MHz above the  $2\nu_N$  frequency. This indicated that the nucleus had a larger quadrupole value and suggesting the  $N_\epsilon$  of the distal histidine. Due to the large distance of

this atom from the iron centre of the heme the hyperfine coupling was initially estimated with the point-dipole approximation, and a value of  $T = 0.07$  MHz was obtained, an isotropic contribution of  $-0.2$  MHz was also needed to fit the data. This ultimately led to the determination of  $K = 0.77$  MHz, similar to values reported for non-protonated nitrogens of imidazole rings [60] [61].

### **<sup>13</sup>C signals**

To determine whether the proposed <sup>13</sup>C correlations arose from the heme or protein carbons, X-band HYSCORE was performed on a model heme solution, the signals were still present and so were assigned to the heme carbons. These signals were also apparent in the cyt P450 spectrum [ref 34] but not interpreted as such. The point dipole approach was again employed to assign the correlations to specific types of heme carbons.

The hyperfine and nuclear quadrupole parameters determined for the heme nitrogens in the work discussed may be found in **Table 3-2**

---

Complex	Spin	$A_x$	$A_y$	$A_z$	$K = e^2Qq/4h$	$\eta$	Ref.
			(MHz)		(MHz)		
Fe(TPP)	LS	-	-	-	0.47	0.45	[6]
Fe(TPP) (Melm) <sub>2</sub>	LS	4.8	4.8	5.8	0.46	0.1	[30]
Co(TPP)	LS	2.43	2.85	4.07	0.45	0.55	[9]
Co <sup>II</sup> DiMelm-O <sub>2</sub> 1	LS	2.7	2.7	3.9	0.53	0.1	[17]
Co <sup>II</sup> DiMelm-O <sub>2</sub> 2	LS	3.1	3.1	3.7	0.56	0.1	[17]
Co <sup>II</sup> py-O <sub>2</sub>	LS	2.7	2.7	4.0	0.73	0.18	[17]
MetMb	HS	6.7	6.9	8.3	0.61	0.51	[62]
AquometMb	HS	9.86	6.89	7.11	0.52	0.48	[27]
MbOH	LS	4.9	5.1	5.3	0.55	0.1	[63]
Hb-NO	LS	1.75 – 2.92	1.75 – 2.92	1.75 - 2.92	0.45	0.37	[6]
mNgb	LS	4.2	4.2	5.7	0.48	0.1	[30]
E7Q-NGB	HS	9.4	6.85	7.25	0.48	0.52	[51]

---

CyGb	LS	4.0	4.1	5.45	0.46	0.1	[31]
Ns tHb	LS	4.5	3.6	5.4	0.44	0.55	[29]
GsGCS	LS	4.5	5.0	5.4	0.49	0.05	[32]
Cytochrome-d		6.5	7.0	8.2	0.65	0.49	[62]
Cytochrome b <sub>559</sub>	LS	4.7	4.9	5.8	0.4 – 0.55	0 – 0.27	[43]
Hemin		6.1	6.8	7.7	0.56	0.51	[62]
		6.7	6.7	8.6	0.58	0.51	

---

**Table 3-2 Heme nitrogen hyperfine and quadrupole coupling parameters taken from reported work.**

---

---

## References

1. Hofer, P., et al., *Hyperfine Sublevel Correlation (HYSCORE) Spectroscopy - A 2D Electron-Spin-Resonance Investigation of the Squaric Acid Radical*. Chemical Physics Letters, 1986. **132**(3): p. 279-282.
  2. Deligiannakis, Y., M. Louloudi, and N. Hadjiliadis, *Electron spin echo envelope modulation (ESEEM) spectroscopy as a tool to investigate the coordination environment of metal centers*. Coordination Chemistry Reviews, 2000. **204**(1): p. 1-112.
  3. Bernstein, M.A., L.D. Hall, and S. Sukumar, *Assignment of Proton NMR-Spectra of Carbohydrates, Using Two-Dimensional Techniques - COSY AND SECSY*. Carbohydrate Research, 1982. **103**(1): p. C1-C16.
  4. Mims, W.B., *Pulsed ENDOR Experiments*. Proceedings of the Royal Society of London. Series A, Mathematical and Physical Sciences (1934-1990), 1965. **283**(1395): p. 452-457.
  5. Davies, E.R., *A new pulse endor technique*. Physics Letters A, 1974. **47**(1): p. 1-2.
  6. Tyryshkin, A.M., et al., *Characterization of bimodal coordination structure in nitrosyl heme complexes through hyperfine couplings with pyrrole and protein nitrogens*. Journal of the American Chemical Society, 1999. **121**(14): p. 3396-3406.
  7. Dikanov, S.A., A.M. Tyryshkin, and M.K. Bowman, *Intensity of Cross-Peaks in Hyscore Spectra of  $S = 1/2$ ,  $I = 1/2$  Spin Systems*. Journal of Magnetic Resonance, 2000. **144**(2): p. 228-242.
  8. Dikanov, S.A., et al., *Two-dimensional ESEEM spectroscopy of nitrogen hyperfine couplings in methemerythrin and azidomethemerythrin*. Journal of the American Chemical Society, 1998. **120**(27): p. 6797-6805.
  9. Van Doorslaer, S., R. Bachmann, and A. Schweiger, *A pulse EPR and ENDOR investigation of the electronic and geometric structure of cobaltous tetraphenylporphyrin(pyridine)*. Journal of Physical Chemistry A, 1999. **103**(28): p. 5446-5455.
  10. Hoffman, B.M. and D.H. Petering, *Coboglobins - Oxygen-Carrying Cobalt-Reconstituted Hemoglobin and Myoglobin*. Proceedings of the National Academy of Sciences of the United States of America, 1970. **67**(2): p. 637-&.
  11. Goldfarb, D., et al., *Double Nuclear Coherence Transfer (DONUT)-HYSCORE: A New Tool for the Assignment of Nuclear Frequencies in Pulsed EPR Experiments*. J. Am. Chem. Soc., 1998. **120**(28): p. 7020-7029.
-

12. Magliozzo, R.S., J. McCracken, and J. Peisach, *Electron-Nuclear Coupling in Nitrosyl Heme-Proteins and in Nitrosyl Ferrous and Oxy Cobaltous Tetraphenylporphyrin Complexes*. *Biochemistry*, 1987. **26**(24): p. 7923-7931.
  13. Lee, H.C., et al., *Electron spin echo envelope modulation and extended X-ray absorption fine structure studies of active site models of oxygenated cobalt-substituted hemoproteins: Correlating electron-nuclear couplings and metal-ligand bond lengths*. *Journal of the American Chemical Society*, 1997. **119**(50): p. 12201-12209.
  14. Dages, G.P. and J. Huttermann, *ESR and ENDOR of Pentacoordinated Cobalt(II) Porphyrins*. *Journal of Physical Chemistry*, 1992. **96**(12): p. 4787-4794.
  15. Wayland, B.B., Minkiewi.Jv, and Abdelmag.Me, *Spectroscopic Studies for Tetraphenylporphyrincobalt(II) Complexes of CO, NO, O2, RNC, and (RO)3P, And a Bonding Model for Complexes OF CO, NO, and O2 withCobalt(II) and Iron(II) Porphyrins*. *Journal of the American Chemical Society*, 1974. **96**(9): p. 2795-2801.
  16. Van Doorslaer, S. and A. Schweiger, *Continuous Wave and Pulse EPR and ENDOR Study of Oxygenated Cobalt(II) Heme Model Systems*. *J. Phys. Chem. B*, 2000. **104**(13): p. 2919-2927.
  17. Van Doorslaer, S., et al., *Effects of the dendrimer cage on O-2 binding of dendritic cobalt(II) porphyrins*. *ChemPhysChem*, 2002. **3**(8): p. 659-667.
  18. Gilbert, D.C., et al., *A study of pyridyl nitrosyl iron(II) tetraphenyl 15N4-porphyrin. NO geometry and spin coupling to the pyrrole nitrogens*. *Chemical Physics Letters*, 1999. **315**(1-2): p. 43-48.
  19. Dikanov, S.A. and M.K. Bowman, *Cross-Peak Lineshape of Two-Dimensional ESEEM Spectra in Disordered S = , I = Spin Systems*. *Journal of Magnetic Resonance, Series A*, 1995. **116**(1): p. 125-128.
  20. Morse, R.H. and S.I. Chan, *Electron paramagnetic resonance studies of nitrosyl ferrous heme complexes. Determination of an equilibrium between two conformations*. *Journal of Biological Chemistry*, 1980. **255**(16): p. 7876-7882.
  21. Fukui, K., H. OhyaNishiguchi, and H. Kamada, *N-14 coupling parameters in oxovanadium(IV)-amine, -imine, and -isothiocyanate complexes studied by electron spin echo envelope modulation spectroscopy*. *Inorganic Chemistry*, 1997. **36**(24): p. 5518-5529.
  22. Piciulo, P.L., Rupprech.G, and W.R. Scheidt, *Stereochemistry of Nitrosyl-Metalloporphyrins - Nitrosyl-Alpha, Beta Gamma, Delta-tetraphenylporphinato(1-Methylimidazole)Iron and Nitrosyl-Alpha, Beta Gamma, Delta-tetraphenylporphinato(4-Methylpiperidine)Manganese*. *Journal of the American Chemical Society*, 1974. **96**(16): p. 5293-5295.
-

- 
23. Vinck, E. and S. Van Doorslaer, *Analysing low-spin ferric complexes using pulse EPR techniques: a structure determination of bis (4-methylimidazole) (tetraphenylporphyrinato)iron(III)*. Physical Chemistry Chemical Physics, 2004. **6**(23): p. 5324-5330.
  24. Astashkin, A.V., A.M. Raitsimring, and F.A. Walker, *H-1 pulsed ENDOR and ESEEM evidence that the bis-imidazole complexes of iron(III) tetraphenylchlorin and tetraphenylporphyrin have the same order of g values, and the same electronic ground state*. Journal of the American Chemical Society, 2001. **123**(9): p. 1905-1913.
  25. Raitsimring, A.M. and F.A. Walker, *Porphyrin and ligand protons as internal labels for determination of ligand orientation in ESEEMS of low-spin d(5) complexes in glassy media: ESEEM studies of the orientation of the g tensor with respect to the planes of axial ligands and porphyrin nitrogens of low-spin ferriheme systems*. Journal of the American Chemical Society, 1998. **120**(5): p. 991-1002.
  26. Quinn, R., et al., *Electronic structure of low-spin ferric porphyrins: a single-crystal EPR and structural investigation of the influence of axial ligand orientation and the effects of pseudo-Jahn-Teller distortion*. Journal of the American Chemical Society, 1987. **109**(11): p. 3301-3308.
  27. Scholes, C.P., et al., *Electron Nuclear Double-Resonance (ENDOR) from Heme and Histidine Nitrogens in Single-Crystals of Aquometmyoglobin*. Journal of the American Chemical Society, 1982. **104**(10): p. 2724-2735.
  28. Brown, T.G. and B.M. Hoffman, *N-14, H-1 and Metal ENDOR of Single-Crystal Ag(II)(TPP) and Cu(II)(TPP)*. Molecular Physics, 1980. **39**(5): p. 1073-1109.
  29. Ioanitescu, A.I., et al., *Characterization of Nonsymbiotic Tomato Hemoglobin*. Biophys. J., 2005. **89**(4): p. 2628-2639.
  30. Vinck, E., et al., *Analyzing heme proteins using EPR techniques: the heme-pocket structure of ferric mouse neuroglobin*. Journal of Biological Inorganic Chemistry, 2006. **11**(4): p. 467-475.
  31. Ioanitescu, A.I., et al., *Probing the heme-pocket structure of the paramagnetic forms of cytoglobin and a distal histidine mutant using electron paramagnetic resonance*. Molecular Physics, 2007. **105**(15/16): p. 2073-2086.
  32. Desmet, F., et al., *The heme pocket of the globin domain of the globin-coupled sensor of Geobacter sulfurreducens -- An EPR study*. Journal of Inorganic Biochemistry. **104**(10): p. 1022-1028.
  33. Teixeira, M., et al., *Pitfalls in assigning heme axial coordination by EPR: c-Type cytochromes with atypical Met-His ligation*. FEBS Letters, 1993. **317**(3): p. 233-236.
-

- 
34. Walker, F.A., *Magnetic spectroscopic (EPR, ESEEM, Mossbauer, MCD and NMR) studies of low-spin ferriheme centers and their corresponding heme proteins*. Coordination Chemistry Reviews, 1999. **185-186**: p. 471-534.
  35. Ioanitescu, A.I., et al., *Probing the heme-pocket structure of the paramagnetic forms of cytoglobin and a distal histidine mutant using electron paramagnetic resonance*, in *Molecular Physics*. 2007, Taylor & Francis Ltd. p. 2073-2086.
  36. Huttermann, J., C. Burgard, and R. Kappl, *Proton ENDOR from Randomly Orientated NO-Ligated Hemoglobin - Approaching the Structural Basis for the R-T Transition*. Journal of the Chemical Society-Faraday Transactions, 1994. **90**(20): p. 3077-3087.
  37. Hori, H., M. Ikedasaito, and T. Yonetani, *Electromagnetic Properties of Hemoproteins .6. Single-Crystal EPR of Myoglobin Nitroxide - Freezing-Induced Reversible Changes in the Molecular-Orientation of the Ligand*. Journal of Biological Chemistry, 1981. **256**(15): p. 7849-7855.
  38. Lobrutto, R., et al., *ENDOR and EPR Study on the Structure of the NO-Ligated Heme Alpha-3 in Cytochrome-C Oxidase*. Journal of Biological Chemistry, 1983. **258**(12): p. 7437-7448.
  39. Hohn, M., et al., *N-14 AND H-1 ENDOR OF Nitrosyl-Hemoglobin*. Journal of the American Chemical Society, 1983. **105**(1): p. 109-115.
  40. Mun, S.K., J.C. Chang, and T.P. Das, *Origin of Observed Changes in N-14 Hyperfine Interaction Accompanying R-T Transition in Nitrosyl-Hemoglobin*. Proceedings of the National Academy of Sciences of the United States of America, 1979. **76**(10): p. 4842-4846.
  41. Fukui, K., H. Ohyanishiguchi, and H. Kamada, *Electron-Spin Echo Envelope Modulation Study on Oxovanadium(IV)-Porphrin Complexes - Reinvestigation of Hyperfine and Quadrupole Couplings of Pyrrole Nitrogen*. Journal of Physical Chemistry, 1993. **97**(46): p. 11858-11860.
  42. Lee, H.-I., P.E. Doan, and B.M. Hoffman, *General Analysis of  $^{14}\text{N}$  ( $I = 1$ ) Electron Spin Echo Envelope Modulation*. Journal of Magnetic Resonance, 1999. **140**(1): p. 91-107.
  43. Garcia-Rubio, I., et al., *HYSCORE Spectroscopy in the Cytochrome b559 of the Photosystem II Reaction Center*. Journal of the American Chemical Society, 2003. **125**(51): p. 15846-15854.
  44. Radoul, M., et al., *Heme d(1) Nitrosyl Complex of cd(1) Nitrite Reductase Studied by High-Field-Pulse Electron Paramagnetic Resonance Spectroscopy*. Inorganic Chemistry, 2009. **48**(9): p. 3913-3915.
  45. Goldfarb, D., et al., *HYSCORE and DEER with an upgraded 95 GHz pulse EPR spectrometer*. Journal of Magnetic Resonance, 2008. **194**(1): p. 8-15.
-

- 
46. Fittipaldi, M., et al., *A multi-frequency pulse EPR and ENDOR approach to study strongly coupled nuclei in frozen solutions of high-spin ferric heme proteins*. Journal of Physical Chemistry B, 2008. **112**(12): p. 3859-3870.
  47. Johnson, M.K., et al., *Electron paramagnetic resonance studies on Pseudomonas nitrosyl nitrite reductase. Evidence for multiple species in the electron paramagnetic resonance spectra of nitrosyl haemoproteins*. Biochem. J., 1980. **189**(2): p. 285-294.
  48. Roberts, A.G., et al., *Intramolecular Heme Ligation of the Cytochrome P450 2C9 R108H Mutant Demonstrates Pronounced Conformational Flexibility of the B-C Loop Region: Implications for Substrate Binding*. Biochemistry, 2010. **49**(40): p. 8700-8708.
  49. Radoul, M., et al., *Revisiting the nitrosyl complex of myoglobin by high-field pulse EPR spectroscopy and quantum mechanical calculations*. Physical Chemistry Chemical Physics, 2011. **12**(26): p. 7276-7289.
  50. Copeland, D.M., et al., *Crystal structures of the nitrite and nitric oxide complexes of horse heart myoglobin*. Journal of Inorganic Biochemistry, 2006. **100**(8): p. 1413-1425.
  51. Trandafir, F., et al., *Studying high-spin ferric heme proteins by pulsed EPR spectroscopy: Analysis of the ferric form of the E7Q mutant of human neuroglobin*. Applied Magnetic Resonance, 2007. **31**(3-4): p. 553-572.
  52. Abragam, A. and B. Bleaney, *Electron Paramagnetic Resonance of Transition Ions*. 1970: Clarendon Press.
  53. Vallone, B., et al., *The structure of murine neuroglobin: Novel pathways for ligand migration and binding*. 2004, Wiley Subscription Services, Inc., A Wiley Company. p. 85-92.
  54. Garcia-Rubio, I., et al., *A Multifrequency HYSCORE Study of Weakly Coupled Nuclei in Frozen Solutions of High-Spin Aquometmyoglobin*. Inorganic Chemistry, 2008. **47**(23): p. 11294-11304.
  55. Jeschke, G. and A. Schweiger, *Hyperfine-correlated electron nuclear double resonance spectroscopy*. Chemical Physics Letters, 1995. **246**(4-5): p. 431-438.
  56. Liesum, L. and A. Schweiger, *Multiple quantum coherence in HYSCORE spectra*. Journal of Chemical Physics, 2001. **114**(21).
  57. Stoll, S., et al., *Peak suppression in ESEEM spectra of multinuclear spin systems*. Journal of Magnetic Resonance, 2005. **177**(1): p. 93-101.
  58. Schosseler, P., T. Wacker, and A. Schweiger, *Pulsed ELDOR detected NMR*. Chemical Physics Letters, 1994. **224**(3-4): p. 319-324.
-

- 
59. Bachmann, R.S., A. Aissaoui, H. Woggon, W. D. . in *Joint 29th AMPERE 13th ISMAR International Conference*. 1998. TU Berlin.
  60. Hunt, M.J., A.L. Mackay, and D.T. Edmonds, *Nuclear quadrupole resonance of  $^{14}\text{N}$  in imidazole and related compounds*. *Chemical Physics Letters*, 1975. **34**(3): p. 473-475.
  61. Ashby, C.I.H., C.P. Cheng, and T.L. Brown, *Nitrogen-14 nuclear quadrupole resonance spectra of coordinated imidazole*. *Journal of the American Chemical Society*, 1978. **100**(19): p. 6057-6063.
  62. Jiang, F.S., et al., *Nitrogen and proton ENDOR of cytochrome d, hemin, and metmyoglobin in frozen solutions*. *Journal of the American Chemical Society*, 1993. **115**(22): p. 10293-10299.
  63. Magliozzo, R.S. and J. Peisach, *Electron spin echo envelope modulation spectroscopic study of iron-nitrogen interactions in myoglobin hydroxide and iron(III) tetraphenylporphyrin models*. *Biochemistry*, 1992. **31**(1): p. 189-199.
-

---

---

## 4 CHAPTER Myoglobin and Nitrite

---

### 4.1 Research Motivation

The primary function of myoglobin (Mb) has long been considered to be the cellular storage and supply of oxygen [1]. Recently, however, a role has been suggested for Mb as a nitrite reductase [2], where the nitrite anion is reduced to nitric oxide ( $\text{NO}^\bullet$ ). Under hypoxic conditions  $\text{NO}^\bullet$  is able to regulate cardiac energy consumption and reduce myocardial oxygen consumption thereby reducing the risk of ischemic-reperfusion injury [3], a major source of tissue damage after periods of vasoconstriction as may be experienced after a stroke or heart attack.

To understand the mechanism of nitrite reduction by Mb it is necessary to examine the binding of the anion to the protein substrate, which is the iron centre of a heme moiety. Crystal structures of horse-heart Mb [4] and human hemoglobin (Hb) [5] (hypothesized to be functionally related to Mb), suggest that the anion adopts the uncommon *O*-nitrito binding mode, in which the heme iron is directly coordinated to an oxygen of nitrite **§ 4.2.3**.

In order to determine whether this binding mode occurs in protein unconstrained by crystallization, electron paramagnetic resonance (EPR) spectroscopy has been employed. To better understand the behavior of Mb under varying physiological conditions the protein was examined over a range of pH values [pH 5.0-10.8]. Optical and Continuous-wave (CW) EPR measured at X-band spectroscopies initially provide insights into the local heme environment which will be covered in this chapter. These findings are complimented and expanded by the application of hyperfine spectroscopic techniques (ESEEM [6], HYSCORE [7], and ENDOR [8, 9]) to resolve the mode of nitrite binding which will be the subject of Chapters 5 and 6.

## 4.2 Biological background

### 4.2.1 Introduction

It has been established that many mammalian heme proteins react with various nitrogen oxide species and that these reactions are biologically relevant to mammalian physiology. Recent studies have indicated a role for nitrite as an endocrine storage pool of  $\text{NO}^\bullet$  that can be bio-activated along the physiological oxygen gradient in order to mediate a number of responses, including hypoxic vasodilatation, [10] cyto-protection following cardiac ischemia/reperfusion and  $\text{NO}^\bullet$ -dependent and independent signalling. It is generally believed that nitrite reduction by heme-containing nitrite reductase (NiR) enzymes begins by the ligation of the nitrite anion to the heme iron centre within these proteins. As such a determination of the binding mode adopted by the nitrite anion within the heme protein is an important step in the elucidation of the mechanism of NiR activity.

### 4.2.2 Role of Myoglobin in Nitrite Reduction

It has been widely accepted for some time that the primary source of nitric oxide within biological tissues is the metabolism of L-arginine by  $\text{NO}^\bullet$  synthase (NOS) [11]. There is however, an increasing amount of evidence for alternative NOS-independent mechanisms for  $\text{NO}^\bullet$  synthesis. It is also believed that these mechanisms may function in situations where conventional  $\text{NO}^\bullet$  production is impaired [10, 12]. Inorganic nitrite is an endogenous anion produced by the oxidation of  $\text{NO}^\bullet$  under aerobic conditions [13]. Conversely  $\text{NO}^\bullet$  can be produced in acidic conditions from the reduction of nitrite. Within blood, nitrite derived  $\text{NO}^\bullet$  is thought to be generated via deoxyhemoglobin and to have vasodilatory properties [10]. This alternative mechanism for  $\text{NO}^\bullet$  production may be of particular importance under ischemic conditions, as the generation of  $\text{NO}^\bullet$  from L-arginine by NOS is dependent on oxygen, which is rapidly depleted under ischemic conditions. A study of the rat myocardium using EPR spectroscopy previously demonstrated NOS-independent synthesis of  $\text{NO}^\bullet$  [12]. In this case the  $\text{NO}^\bullet$  generation was attributed to the chemical reduction of nitrite during ischemic conditions. It has been suggested that this reduction is derived simply from an acidification reaction [14, 15], as ischemia-induced acidosis lowers the pH of blood from  $\sim$  pH

7.4 to ~ pH 5.5. There is however, further evidence that this reaction may be dependent on enzymatic catalysis [16].

### 4.2.3 Nitrite Anion Binding to Globins *N-nitro* versus *O-nitrito*

As a consequence of the renewed interest in nitrite ligation to Mb Copeland and Richter-Addo [4] investigated the crystal structure of the horse heart variant of Mb using X-ray crystallography to determine how nitrite interacts with the heme centre. Several binding modes were known for nitrite to metals previous to this study **Figure 4.2.3-1** [17], however, the coordination to hemes [18-20] had always exhibited the *N-nitro* mode (**Figure 4.2.3-2**). Indeed the structures of synthetic iron-porphyrin compounds with both ferric and ferrous centres [21, 22] had also revealed this mode.

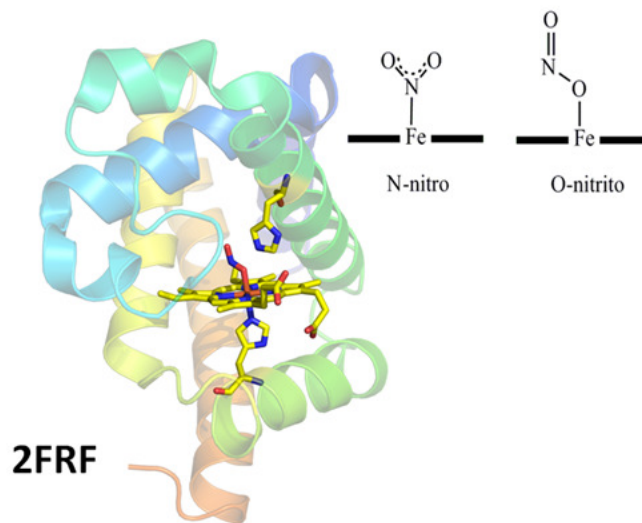


**Figure 4.2.3-1, N-nitro versus O-nitrito binding modes of the nitrite anion to a heme centre. The crystal structure shown is of wild-type Mb and nitrite [4], with the heme centre and the proximal and distal histidines highlighted. The nitrite clearly exhibits O-nitrito binding**

It is however, pertinent to discuss the methods by which binding modes obtained for these heme proteins were obtained in order to relate the findings to Mb and to a possible mechanism for nitrite binding. In particular the conditions under which the crystals were grown i.e. the method by which and the stage at which the nitrite anion was added to the protein.

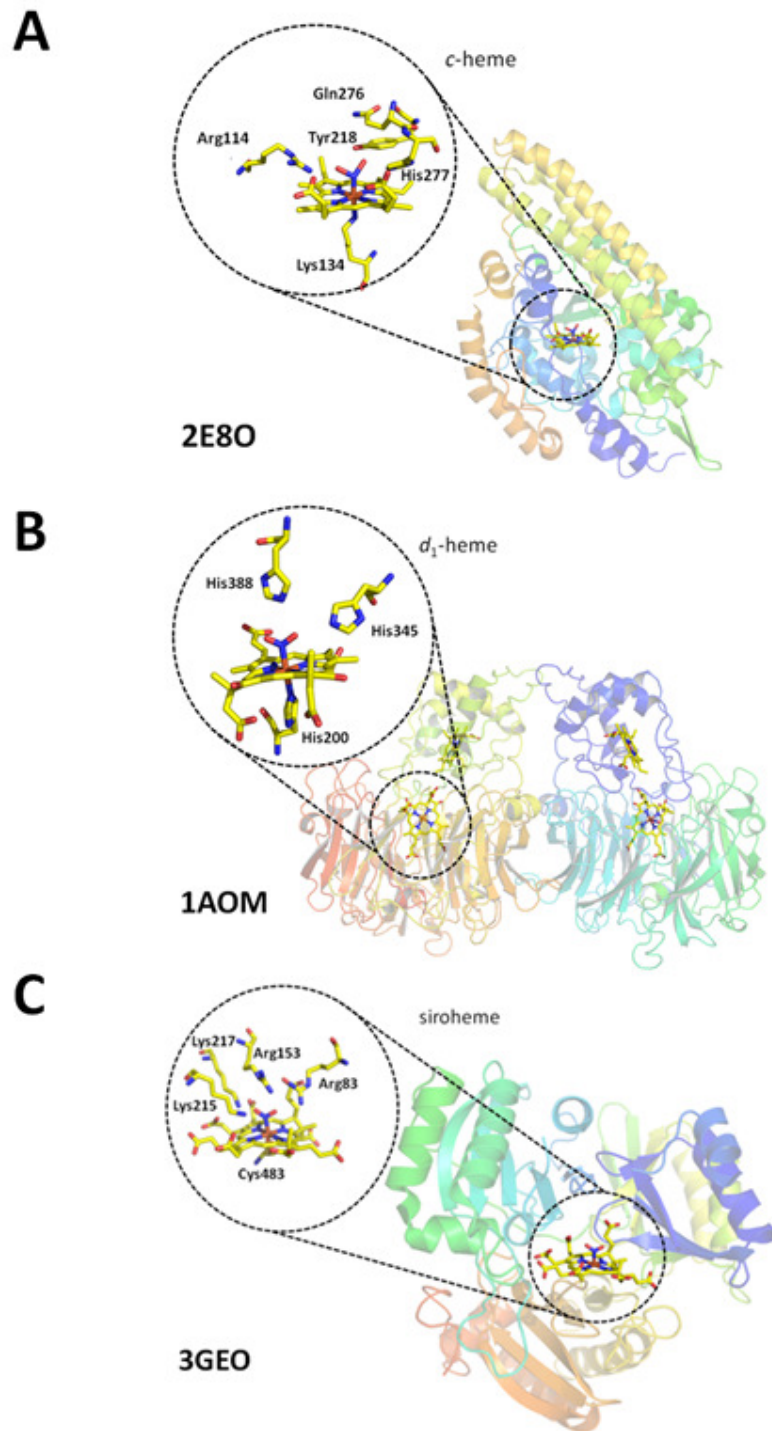


Figure 4.2.3-2, N-nitro nitrate binding to heme centre in A) Cytochrome *c* nitrite reductase, B) Cytochrome *cd*<sub>1</sub> nitrate reductase, C) Sulphite reductase. Protein data bank file references are given below each structure. Amino acid residues theorized to have a role in ligand binding shown and labeled.

The first crystal structure of N-bound nitrite to a heme was determined by Crane and coworkers in the sulphite reductase hemoprotein (SiRHP) [20] (**Figure 4.2.3-2-C**). In this case the proximal ligand is a cysteine. Two Arg and two Lys residues are available in the binding pocket on the distal side for direct H-bonding to the oxygen atoms of bound anions. Complexed crystals were obtained by soaking the initial protein crystals in 100 mM NaNO<sub>2</sub>, in this case in HEPES buffer at pH 7.7. Analysis of the crystal structure revealed the N-bound form and the researchers state the electron density was not consistent with an O-bound form. The paper also cites an EPR study [23] in which the hyperfine splitting of the nitrosyl-ferriheme changes from a triplet to a doublet on substitution of <sup>14</sup>NO<sub>2</sub><sup>-</sup> for <sup>15</sup>NO<sub>2</sub><sup>-</sup> as a confirmation of the N-bound nitrite form.

The second heme moiety found to exhibit the N-bound nitrite form was the *d*<sub>1</sub>-heme of cytochrome *cd*<sub>1</sub> from *Thiosphaera pantotropha* [19] (now known as *Paracoccus pantotrophus*) (**Figure 4.2.3-2-B**). Again nitrite ligated forms of the crystals were obtained by soaking the crystals with nitrite, but this time the crystals were first reduced with dithionite, as the affinity of NO for a heme iron is known to increase dramatically under this condition [24]. This heme displays the usual histidine proximal ligand but has a tyrosine distal ligand which is released upon reduction to allow substrate binding. Nitrite was seen bound by its nitrogen to the *d*<sub>1</sub> heme in two separate crystals. Both crystals also showed one of the nitrite oxygen's to be suitably positioned for H-bonding to His345 and His388 residues (2.9-3.2 Å). This finding was used to support a previous proposal [25] that the two histidines provide protons to the nitrite oxygen atom that will eventually become part of the product water molecule. It should be noted that upon reduction of nitrite the nitrite oxide anion was found to bind in a bent confirmation to the *d*<sub>1</sub> heme in a similar fashion to the observed ligation in Fe(II) hemoglobin [26]. Also of note is the observation that in one subunit of the second crystal, the *d*<sub>1</sub> heme was clearly found to have a ligand, the density of which however, could be modeled in more than one way. It was hypothesized that this probably represented a mixture of various species.

Crystallization of Cytochrome *c* nitrite reductase from *Wolinella succinogenes* [18] was combined with density functional calculations to propose a mechanism for the reduction of

nitrite to ammonia by this enzyme. Firstly it should be noted that atypically, the proximal ligand to the heme is a lysine and not the usual histidine (**Figure 4.2.3-2-A**). Crystals were grown in sodium acetate buffer pH 5.7 [27] and complexed with nitrite by soaking the crystals with 100 mM sodium nitrite 1 hour before measurement. Although it is stated in the work that it was possible to produce this complex by co-crystallization with 25 mM sodium nitrite it is not explicitly stated whether this was done or investigated further. Indeed in the results section it is stated that in order to obtain the Fe(III)-nitrite structure, nitrite had to be soaked into the Cytochrome *c* crystals in high excess. It is further remarked that this is a surprising phenomenon as the enzyme should have a high substrate binding constant especially in the Fe(III) form. Crystal structures for the complex could only be obtained for the oxidized Fe(III) form due to the high activity of the enzyme in the Fe(II) case. For the density functional calculation of this case the nitrite was modeled in both the *N*-bound and *O*-bound forms. It was assumed however, that the *N*-bound form would lead to a low-spin configuration, whereas the *O*-bound form would produce the high-spin form. While at first glance this might appear a valid assumption the situation may in fact be more complicated if hydrogen bonding were to be involved in the binding mode, as this may have an influence on the electron density in the coordination environment.

#### **4.2.4 Richter-Addo H-bonding residue mutant investigation**

To determine how the binding mode of the nitrite anion was directed by the amino acid residues in the binding pocket of Mb, Richter-Addo and colleagues performed crystallographic studies on a series of Mb-Mutants [28]. In conjunction with the wild-type (WT) protein two mutants were investigated: H64V and the double mutant H64V V67R. In the WT protein the H64 residue was theorized to dictate the binding mode of the nitrite anion through H-bonding. The H64V mutant then replaced this histidine with a valine residue incapable of forming H-bonds. The double mutant whilst still having the histidine residue removed, added another residue with a potential for H-bond formation. It again should be emphasized that the nitrite bound crystals were formed with the crystal soak method. In summary Richter-Addo found that when H-bonding residues were present the nitrite was ligated via the *O*-

nitrito mode, and when these were absent the *N*-nitro mode was favored. **Figure 4.2.4-1** shows the nitrite binding found within crystals of the mutated proteins.

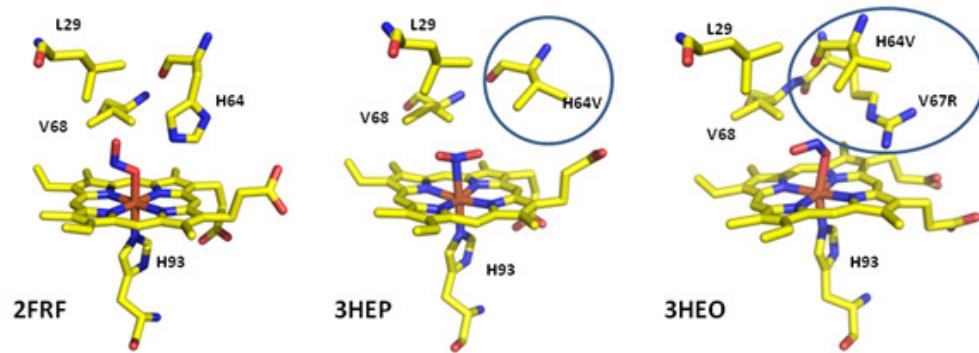


**Figure 4.2.4-1, Heme centre from crystal structures of Mb with ligated nitrite anion. (2FRF) native Mb, (3HEP) Mb with H64V mutation and (3HEO) Mb with H64V and V67R mutation.**

It is clear the method by which nitrite bound crystals were obtained, by soaking already crystallized protein in nitrite solutions may yield structures different to the actual *in-vivo* protein conformations.

### 4.3 Experimental Characterization of Myoglobin and Nitrite-Myoglobin

From the above discussion it is clear there is scope to investigate the conformation of nitrite binding to myoglobin by a non-crystallographic method. EPR is ideally suited to this and will be the main technique applied in the course of the experimental investigation. During this electron paramagnetic resonance (EPR) led investigation samples were also characterized by electronic absorbance using an Hitachi U2900 photospectrometer.

#### 4.3.1 Reagents and Chemicals

Samples of 98% purity lyophilized horse heart myoglobin were purchased from Sigma-Aldrich. The protein was stated to have a molecular weight of 17.6 kDa [29]. The extinction coefficient for ferric Mb is  $3.3 \text{ mM}^{-1}\text{cm}^{-1}$  at 632 nm at pH 6.5 [30] see § 4.3.7. Nitrite was added in the form of sodium nitrite also purchased from Sigma Aldrich.  $\text{Na}^{14}\text{NO}_2$  was of at least 97% purity with sulphite and chloride anion contributions of less than 0.01% and 0.05% respectively.  $\text{Na}^{15}\text{NO}_2$  contained 98%  $^{15}\text{N}$  atoms and was 95% complete product isotope labeled nitrite. Moisture content of nitrite was stated to be less than 2% by weight. It is possible that trace amounts of nitrate were present but there is no evidence that nitrate may bind to Mb (It is likely that the molecule is too large to fit in the binding pocket). Indeed nitrate is hypothesized to be a biological source for the production of nitrite [31]. Nitric oxide was present and bound to Mb at low pH but was able to be resolved spectroscopically and will be discussed separately where pertinent. Mb was examined throughout as met-Mb, as such samples were made in an aerobic environment.

### 4.3.2 Buffers

The following buffers were used during the course of the investigation:

Buffer		pH	pH range	pKa (at 20°C)
<b>Sodium Citrate</b>		5.0	3.0-6.2	
<b>MES</b>	4-Morpholineethanesulfonic acid	6.5	5.5–6.7	6.16
<b>HEPES</b>	4-(2-Hydroxyethyl)piperazine -1-ethanesulfonic acid	7.5	6.8–8.2	7.55
<b>TAPS</b>	<i>N</i> -Tris(hydroxymethyl)methyl -3-aminopropanesulfonic acid	8.5	7.7-9.1	8.49
<b>CHES</b>	<i>N</i> -Cyclohexyl-2-aminoethanesulfonic acid	9.5	8.6–10.0	9.55
<b>CAPS</b>	<i>N</i> -Cyclohexyl-3-aminopropanesulfonic acid	10.8	9.7–11.1	10.56

**Table 4-1 Buffers used in the course of the investigation of nitrite binding to Mb at differing pH values.**

Buffer solutions were made up to 50 or 100 mM standards and were adjusted to the correct pH using a Precisa pH900 pH meter calibrated to known standards. Phosphate buffers were not used for any experiments due to the known pH artifacts associated with freezing [32].

### 4.3.3 Optical spectroscopy of ferric myoglobin

One of the most distinctive properties of heme complexes is their absorption of visible and ultra-violet light. **Figure 4.3.3-1** shows the optical spectrum of LS and HS Mb (bottom) and a depiction of the contribution to the Soret peak from LS and HS species (top right).

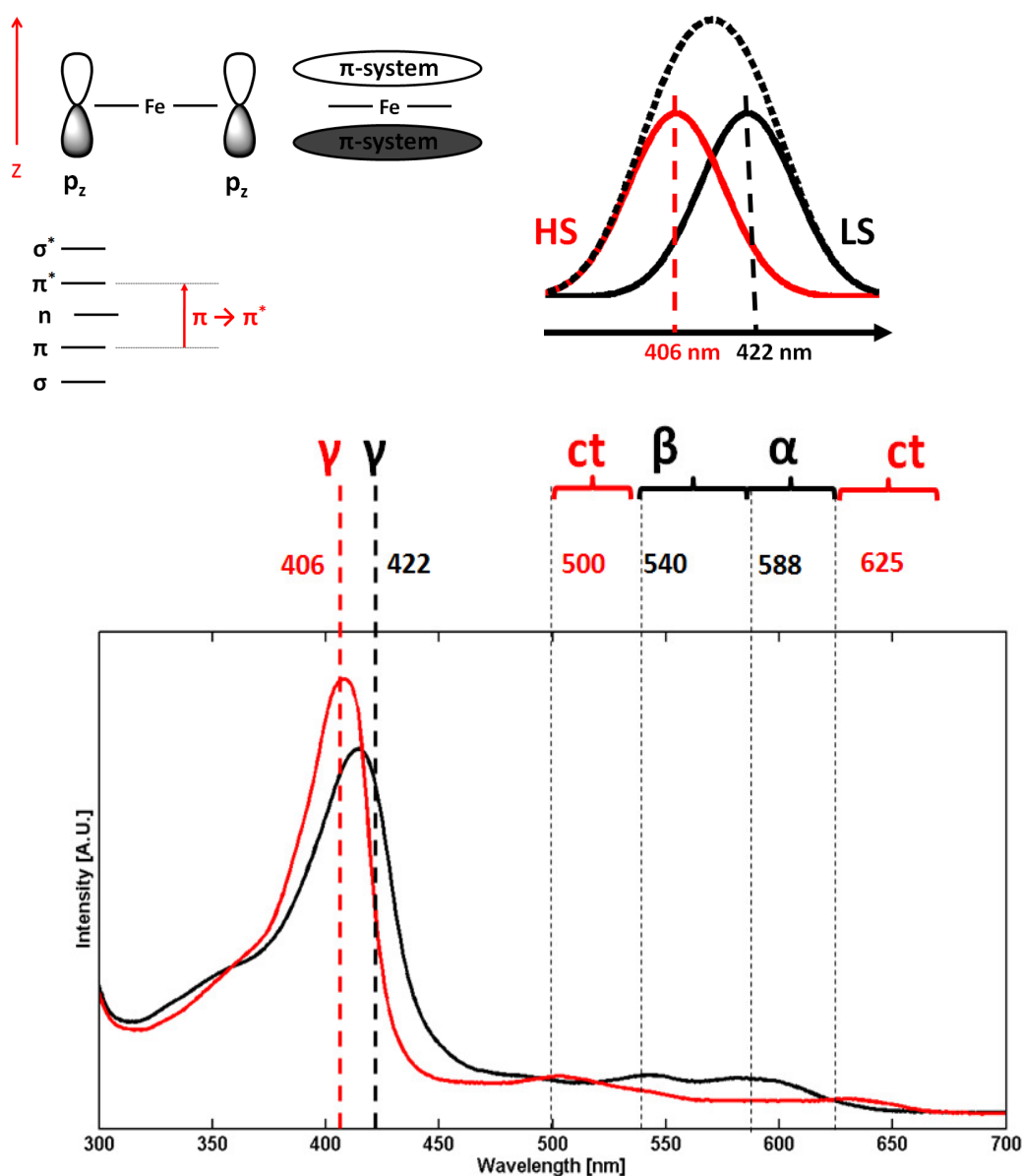


Figure 4.3.3-1, optical spectrum of high-spin (pH 5) and low-spin (pH 11) met-myoglobin (red and black respectively). Numbers to the side of dashed lines indicate positions of band peaks from [33]. ct (charge transfer).

The dominant contribution to these spectra arises from the  $\pi \rightarrow \pi^*$  transitions of the conjugated porphyrin macro-cycle leading to the Soret band ( $\gamma$ -band or B-band). It is widely known that the position of the Soret band is related to the magnetic susceptibility of the heme ligand [34]. The direct cause of the position of the Soret band is however, perhaps less well known and arises from individual contributions to the Soret band envelope from high-spin (HS) and low-spin (LS) states each having a specific and different transition energy **Figure 4.3.3-1**. The resulting position of the Soret peak is therefore more correctly an indication of the HS/LS character of the bulk sample [33]. By measuring the optical spectra of a series of myoglobin samples with ligands of differing magnetic susceptibilities the peaks for 100% HS ( $F^-$ ) and 100% LS ( $CN^-$ ) were determined to be located at 406 and 422 nm respectively, the higher energy of the HS Soret band possibly resulting from mixing with the charge-transfer band in the visible region.

Less well understood in general however, are the ligand-field ( $d \rightarrow d$ ) transitions of the heme ligands that are, in principle, able to provide direct information regarding the electronic and structural basis for heme iron reactivity. The peaks displayed at around 540 and 588 nm are the  $\beta$  and  $\alpha$ -bands of the low-spin complex, also sometimes referred to as the  $Q_0$  and  $Q_v$  bands. The intensity of the  $\alpha$ -band is strongly dependant on the identity of the axial ligand [33]. The bands at 500 and 625 nm are the charge-transfer (ct) bands of the high-spin species.

Nonetheless several past studies have described key features attributed to nitrite binding in heme proteins including Mb and a pertinent step in the overall investigation by EPR of the binding mode is a characterization by optical spectroscopy.

#### **4.3.4 Optical characterization of myoglobin at differing pH**

It is known that ferric myoglobin in aqueous solution changes spin-state depending on the pH of the solution. This is due to the relative ligand strengths of the coordinated hydroxide molecule at high pH (relatively strong ligand) and water molecule at low pH (relatively weak ligand),  $pK_a$  water coordinated to ferric Mb = 8.9 [35]. In order to characterize this behavior of Mb a titration experiment was performed whereby 200 ml of 25  $\mu$ M Mb solution (by weight) at pH 11.0 was reduced in pH by increments of 0.2 pH units. A buffer mixture comprised of

equal parts of 50 mM sodium citrate, HEPES, CHES and CAPS was used to obtain this range. The optical spectrum was measured between 300 and 800 nm for each incremental change. 6 M HCl was used to effect the change in pH in order to minimize dilution of the Mb sample. For each optical measurement 1 ml of the total sample solution was transferred into 1.4 ml plastic cuvettes. **Figure 4.3.4-1** shows the results of this experiment.

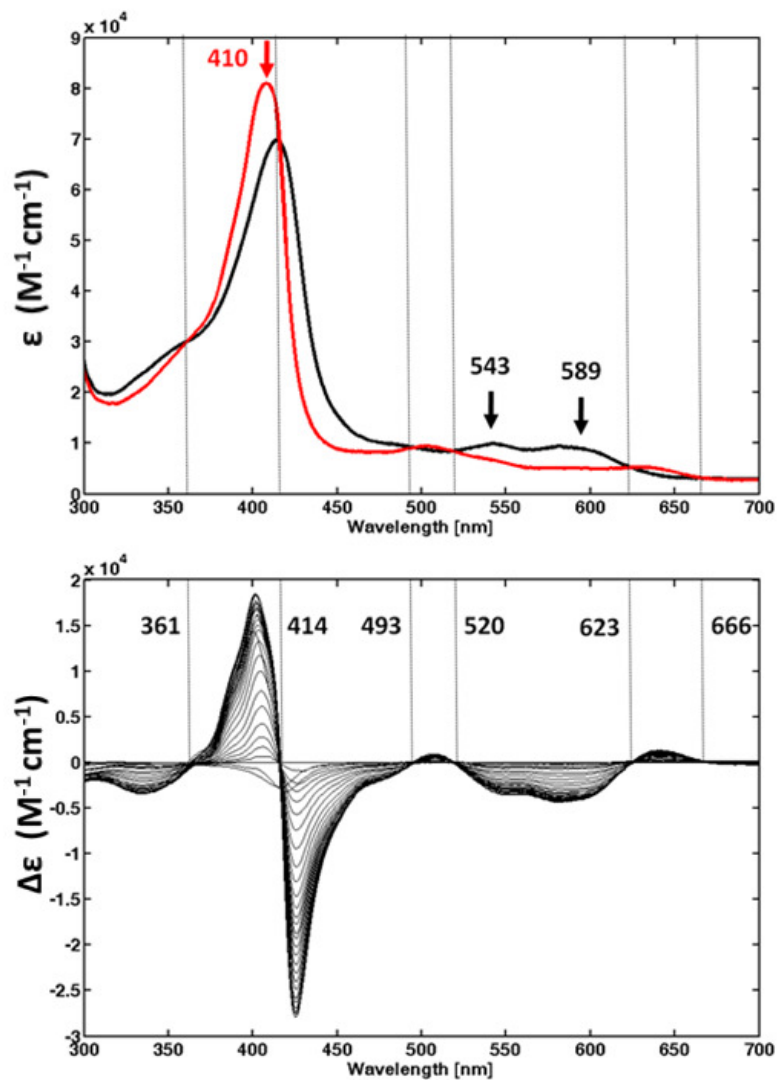
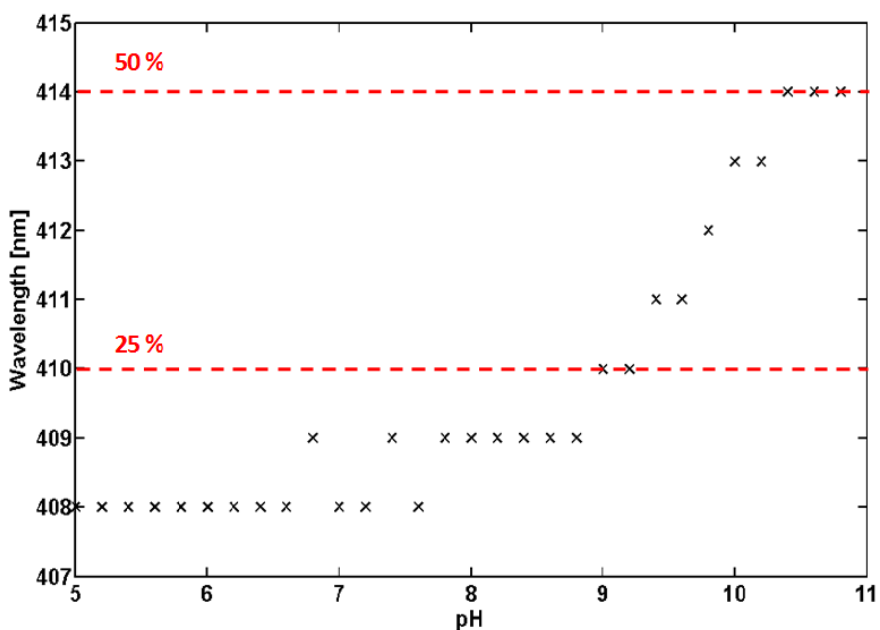


Figure 4.3.4-1, results from pH titration of Mb. Top: high-spin (pH 5.0) and low-spin (pH 11.0) Mb spectra (red and black respectively). Bottom: difference spectrum starting from high pH. Positions of isosbestic points indicated.

The salient points of the upper panel may be clearly seen as described in § 4.3.3. The red spectrum is that of Mb at pH 5.0 and the black of Mb at pH 11.0 and may be viewed as

demonstrating predominantly high-spin and low-spin characteristics respectively. The lower panel is the difference spectrum of the complete data range of the experiment, starting from pH 11.0. The isobestic points may also be clearly observed with the data displayed in this way. The contributions to the spectrum of features associated with the high-spin and low spin states may also be resolved with this method. In this case negative features are associated with low-spin and positive with high-spin heme.

An estimate of the percentage of HS and LS population may be obtained if the position of the Soret band is plotted as a function of the pH at which the spectrum was recorded. **Figure 4.3.4-2** shows such a plot for Mb. It is clear from this that for the pH range of the experiment the sample is always in an admixed spin-state with  $\sim 80\%$  HS at pH 5.0 (408 nm) falling to 50% HS above pH 10.4 (414 nm).



Plotting the maximum intensity of the  $\alpha$  and  $\beta$ -bands of LS-Mb (589 and 543 nm respectively) as a function of pH (**Figure 4.3.4-3**) provides an estimate of the  $pK_a$  of the Mb-H<sub>2</sub>O complex water molecule.

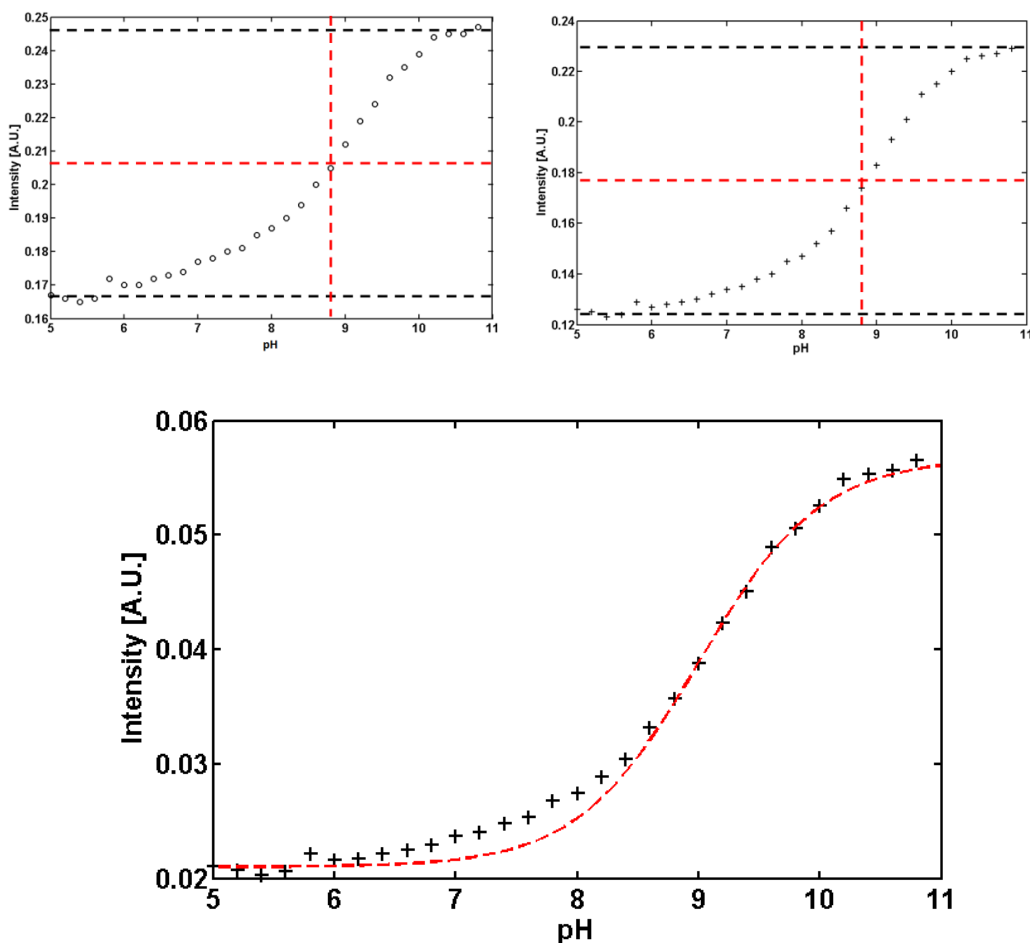


**Figure 4.3.4-3, Intensity profile of LS bands of Mb as a function of pH. Top left:  $\beta$ -band (543 nm), Top right:  $\alpha$ -band (589 nm). Bottom: ratio of  $\alpha$  and  $\beta$  -bands with data fitted to Henderson-Hasselbalch equation. Dashed vertical line in each case indicates approximate  $pK_a$ . (~8.8-9.0).**

In this case a value of between 8.8 and 9.0 is indicated. Which is in agreement with the value quoted above in this section [35]. In the bottom panel of this figure the data are fitted to the Henderson-Hasselbalch equation [36] with a  $pK_a$  of 9.0. It may be seen that there is a slight deviation in the experimental data from the equation at lower pH. This may be explained by changes in protein tertiary structure over the course of the titration experiment and results in titration curves of a modified Henderson-Hasselbalch character [37].

### 4.3.5 pH Titration of Myoglobin-Nitrite

Nitrite was added in the form of sodium nitrite. A previous method for the addition of nitrite to a globin was followed [38] whereby a 20-fold excess over the heme of  $\text{NaNO}_2$  in aqueous solution was added to MetMb but found to be insufficient. CW-EPR Experiments indicated a larger value of around 240 fold excess to be optimum (c.f. 20 to 1000 excess in another study [39]) The experiment described in § 4.3.4 was then repeated with the addition of nitrite. Figure 4.3.5-1 shows an overview of the results.

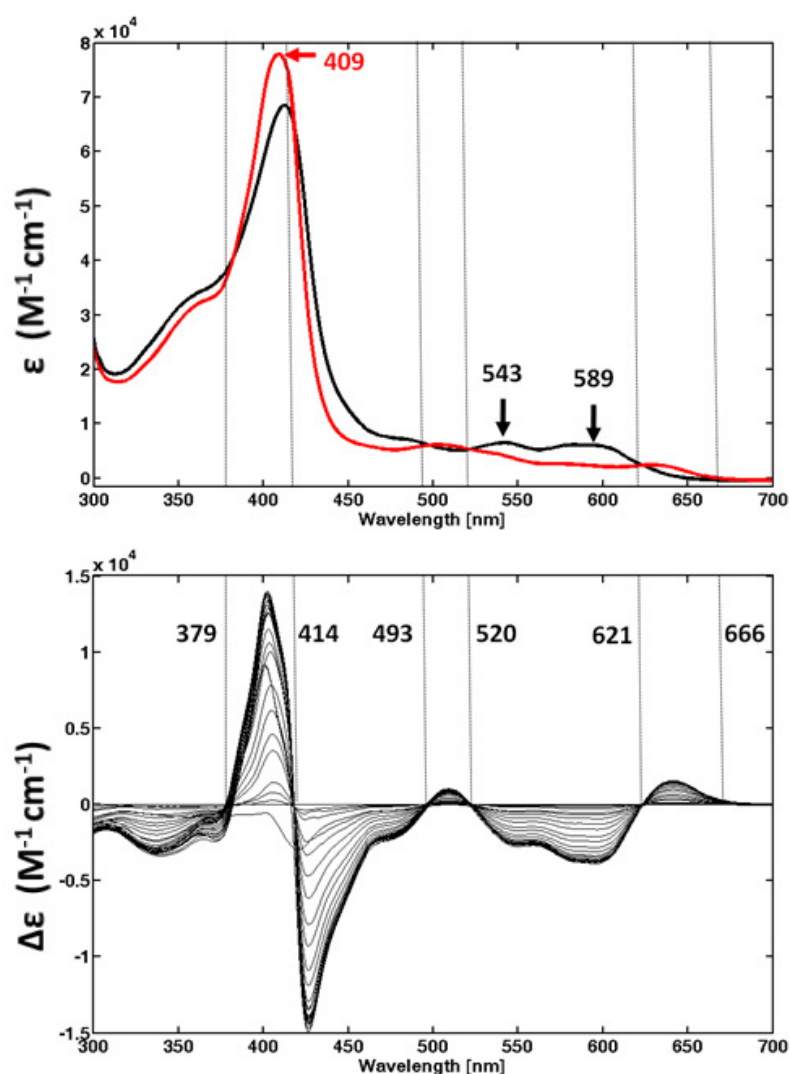
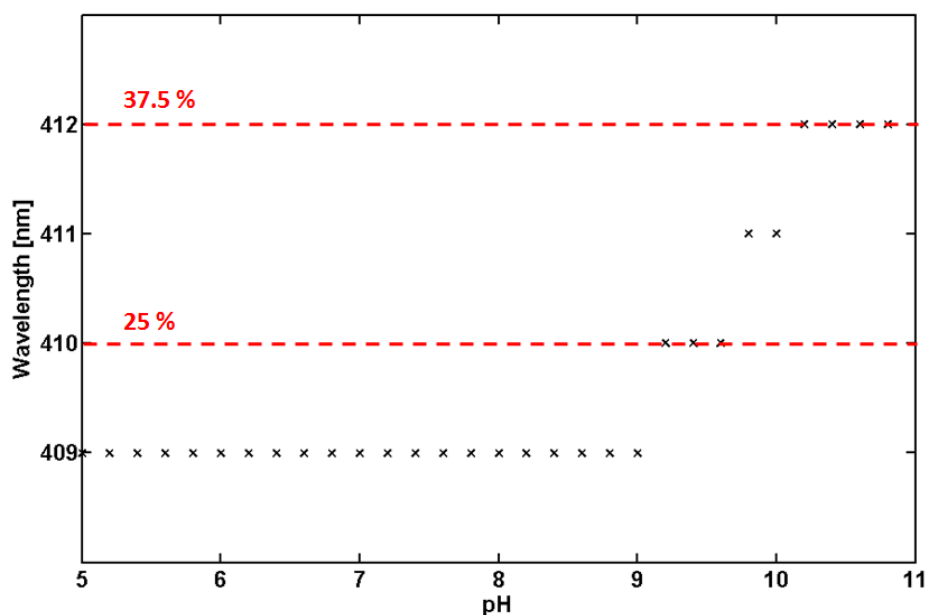


Figure 4.3.5-1, results from pH titration of Mb in the presence of 240-fold excess nitrite. Top: high-spin (pH 5.0) and low-spin (pH 11.0) Mb spectra (red and black respectively). Bottom: difference spectrum starting from high pH. Positions of isosbestic points indicated.

Again the salient points may be understood with reference to **Figure 4.3.3-1**. In all there is a great similarity to the spectra of the Mb only titration, with the small differences more apparent in the lower panel: the first isosbestic point is shifted from 361 nm for the Mb only case to 379 nm for the Mb-NO<sub>2</sub><sup>-</sup>. This is due to the influence of free nitrite contributing to the spectrum at this point. The relative contributions of the HS and LS components of the Soret band may also be seen to be more equal than in the Mb only case, suggesting less overall contribution from a LS species. Indeed using the same approach as in the preceding section an estimate of the spin state can be made (**Figure 4.3.5-2**), and the persistence of the HS state as a function of the pH may be clearly seen.



**Figure 4.3.5-2, wavelength of Soret Band maximum versus pH for myoglobin with nitrite. Red dashed lines indicate estimate of LS population.**

However, it may surely be seen that a definitive indication of the presence of coordinated nitrite within the Mb sample is lacking, once the underlying behavior of the Mb spectra as a function of the pH is taken into account. Previous authors have nonetheless reported values for the position and the extinction coefficients associated with the main features of nitrite ligated Mb [30]. In this case for sperm-whale Mb the Soret band was found to move from 409 nm for Mb to 411 nm for Mb-NO<sub>2</sub><sup>-</sup> (pH 7.7). Further the  $\alpha$ -band peak was reported to move

from 502 nm (Mb) to 570 nm (Mb-NO<sub>2</sub><sup>-</sup>), this clearly seems improbable from the description of the origin of the ferric heme bands given previously § 4.3.3, and it should be noted that the authors in this study defined the  $\alpha$ -band as the wavelength of maximum intensity in the 500-700 nm range.

#### 4.3.6 Spectral changes with the addition of nitrite

A previous study had documented the spectral changes observed in Mb with the addition of nitrite at pH 5.5 [40], albeit in the presence of NADH. A general procedure was therefore adopted from this study to obtain similar spectra at pH 5.0, 6.5, 7.5, 8.5, 9.5 and 10.8. Samples of 25  $\mu$ M metMb were made (by weight) at each of the pH values indicated using 50 mM solutions of the buffers described in § 4.3.2. 240-fold molar excess of aqueous NaNO<sub>2</sub><sup>-</sup> (also at the pH of the Mb sample in each case) was added after the Mb had equilibrated. Spectral changes of Mb were recorded in the region 500-600 nm. Spectra were taken of the Mb before the addition of nitrite, immediately following the addition and at 15, 60 and 90 minutes after the addition. The results of these experiments are shown in **Figure 4.3.6-1**. The larger spectra in the figure show the results at the extreme pH values, the trends of the experiment are shown in the bottom spectrum of Mb at pH 10.8 in CAPS buffer. In general it may be said that the intensity of the  $\alpha$ -band and  $\beta$ -band peaks increases with the addition of nitrite, this trend is seen for all of the pH values measured, although at pH 5.0 this increase is only slight. The intensity of the HS charge-transfer band at around 500 nm also generally decreases with the addition of nitrite, the exception again being at pH 5.0. If the two extreme cases are ignored (i.e pH 5.0 and pH 10.8) it may be said that the LS  $\alpha$  and  $\beta$ -band peaks become better resolved from each other as the pH is increased. It should be noted that in the previous study that inspired the experimental procedure described in this section [40], it was this resolution between the two bands that was ascertained to indicate the presence and absence of nitrite, with the absent case leading to greater resolution between the peaks. A more universal and therefore useful trend observed in the spectra with the addition of nitrite was that the position of the  $\alpha$ -band peak blue-shifted by 3 nm. It was previously stated in § 4.3.3 that the intensity of this peak was strongly dependent on the axial ligand. It is therefore suggested that this shift may be deemed the most reliable indication of nitrite bound Mb.

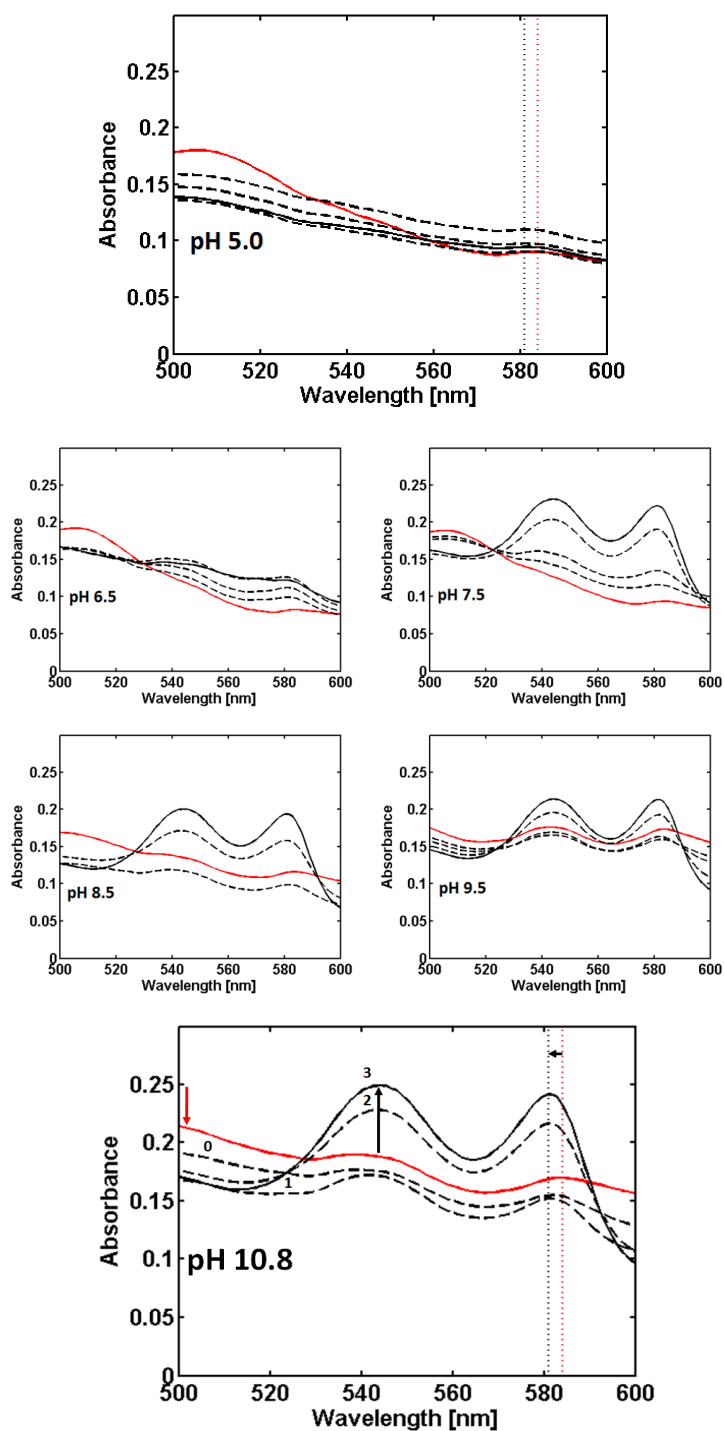


Figure 4.3.6-1, Spectral changes during the reaction of metmyoglobin with nitrite: Top pH 5.0  
 Quadrants: top left pH 6.5, top right pH 7.5, bottom left pH 8.5, bottom right pH 9.5  
 Bottom pH 10.8, showing spectra of initial Mb (red) then with the addition of nitrite (0) bottom,  
 then at 15 mins (1), 60 mins (2) and 90 mins (3). The  $\alpha$ -band peak shift with nitrite addition is  
 shown.

### 4.3.7 Evaluation of reported extinction coefficients

One of the major uses of optical spectroscopy is for the determination of protein concentrations via the Beer-Lambert Law. To achieve this extinction coefficients are often quoted in the literature at specific wavelengths for specific forms of proteins. It may be noted that hereto the quoted concentrations of Mb solutions have been via the molecular weight of the protein. This method of course assumes that all of the weight of the lyophilized protein used will be incorporated into the final protein solution (i.e. there will be no loss), which is not usually the case. However, there are many reported extinction coefficients for Mb at various wavelengths and pH values and many differ from each other quite considerably. This section therefore uses the data outlined in § 4.3.4 to evaluate the accuracy of a number of reported extinction coefficients of MetMb. **Table 4-2** lists the extinction coefficients to be evaluated.

$\epsilon \text{ mM}^{-1}\text{cm}^{-1}$	Wavelength (nm)	pH	Ref.
9.7	505	N.S.	[40]
12.92	555	6.9	[41]
3.0	637	6.4 (H <sub>2</sub> O)	[33]
2.2	594	-	
1.19	546	-	
9.62	502	-	
4.16	596	OH <sup>-</sup>	
3.17	580	-	
3.66	540	-	
8.01	484	-	

**Table 4-2, Extinction coefficients reported for Mb to be evaluated. N.S. (Not Stated)**

It is possible to make some initial assumptions to aid the evaluation process. Firstly the protein concentration calculated via these extinction coefficients should not exceed 25  $\mu\text{M}$ . This would indicate the unlikely 100% weight to protein incorporation. However, as there are also a number of differing reported molecular weights for horse-heart Mb a small error should be assumed for this figure and the maximum concentration therefore increased to 30  $\mu\text{M}$ . (allowing for a 20% error in the molecular weight). It may also be assumed that as the

same sample was used throughout the titration experiment described in 4.3.4 the concentration of the sample should remain approximately constant (the dilution due to altering the pH was minimized, each sample required around 20  $\mu\text{l}$  of 2M HCL acid to alter the pH 0.2 units in initial volume of 200 ml) or slightly decrease during the experiment from high pH to low pH. It seems reasonable to assume therefore that an accurate position for the location (in terms of the wavelength associated with the extinction coefficient) should be near an isosbestic point. With these factors in mind we can evaluate the coefficients with reference to **Figure 4.3.7-1**.

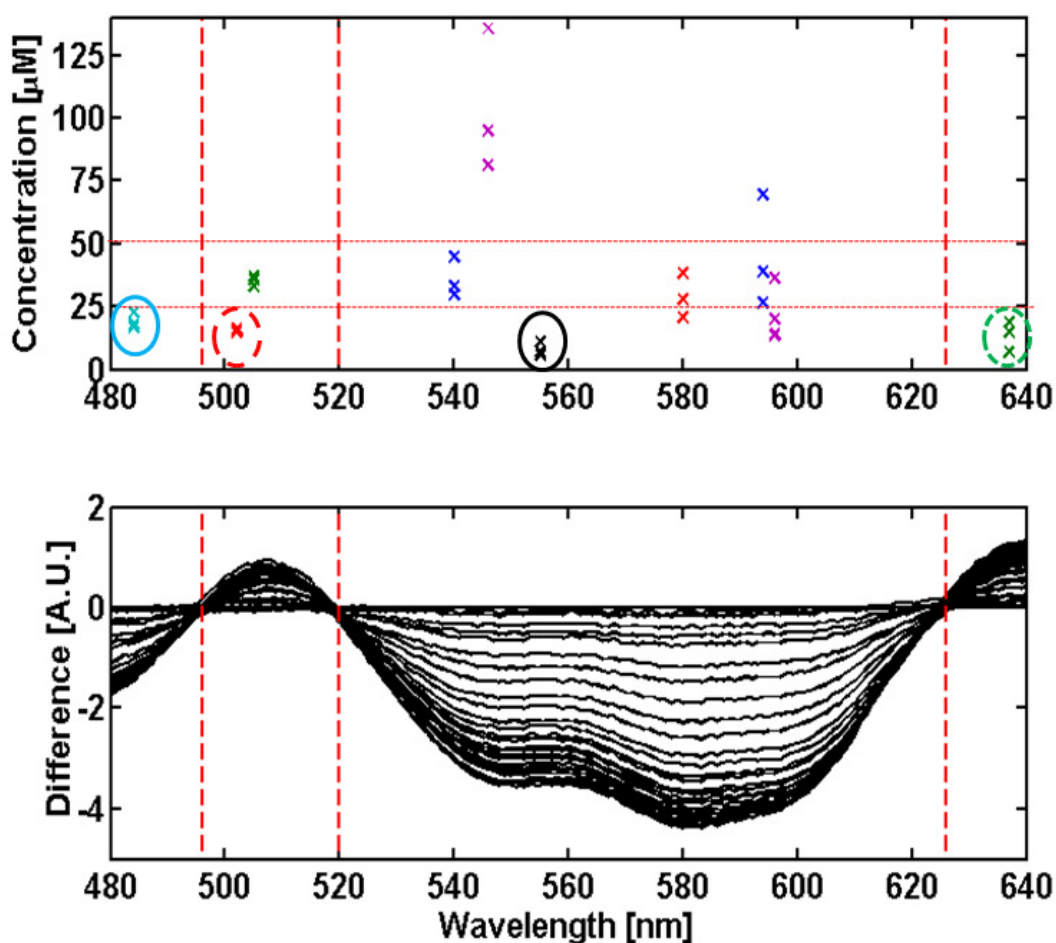


Figure 4.3.7-1, Mb titration difference spectrum (bottom) and calculated concentrations of solution using extinction coefficients listed in Table 4-2. Circled data indicate calculated concentrations near or below 25  $\mu\text{M}$ . Dashed circles indicate a larger concentration calculated for the end of the titration than the beginning.

The bottom spectrum of which shows the Mb titration experiment between the range 480-640 nm. And the top spectrum shows the concentrations calculated using the extinction coefficients listed in **Table 4-2**. Three concentrations are plotted for each extinction coefficient: the initial, final (pH 11.0 and pH 5.0) and the mean value. The positions of the isosbestic points for this wavelength range are also indicated. Data that suggest reasonable values for the calculated concentrations are circled. Solid circles indicate the concentration was calculated to decrease during the titration whilst dashed circles indicate the calculated concentration rose. It should however be noted that the data indicated by dashed circles are located in the HS charge-transfer band region and thus the intensity at this point may be expected to increase with decreasing pH. The values of the calculated concentrations for the circled data are given in **Table 4-3**.

$\epsilon \text{ mM}^{-1}\text{cm}^{-1}$	Wavelength (nm)	Initial Conc.	Final Conc.	Mean Conc.	Colour
12.92	555	11.0	6.0	7.2	Black
9.62	502	15.0	16.1	15.6	red
3.0	637	6.8	18.0	14.7	green
8.01	484	22.5	17.0	18.3	Blue

**Table 4-3, Calculated concentrations of Mb titration experiment indicated in Figure 4.3.7-1.**

In terms of proximity to an isosbestic point and a small range for the calculated concentration the extinction coefficient of  $9.62 \text{ mM}^{-1}\text{cm}^{-1}$  at 502 nm provides reasonable and consistent values. The indication that 64% of the protein by weight becomes protein in solution is also a realistic figure. Indeed when this same coefficient is used for the Mb-nitrite titration experiment in **§ 4.3.5** a mean value of  $16.2 \mu\text{M}$  is calculated with initial and final concentrations of 15 and  $16.1 \mu\text{M}$ . which may also be thought a reasonable series of values.

### 4.3.8 CW-EPR Investigation of Myoglobin

As an initial step in characterization Mb without nitrite added was initially examined with continuous-wave (CW) EPR. A Bruker E500 CW X-band spectrometer was used in conjunction with a Bruker Super High-Q resonator. Initial sample concentrations of Mb were 100  $\mu\text{M}$  (by weight). Spectra were measured at 20 K. Mb was dissolved in buffers mentioned above (§ 4.3.2) covering the range pH 10.8 to pH 5.0. Spectra were recorded at 9.4 GHz with an optimized CW-microwave (MW) power of 5 mW with a modulation frequency of 100 KHz and amplitude of 1 G. The MW frequency was measure using a Marconi Instruments 2440 MW counter. Magnetic field values were calibrated against a DPPH standard.

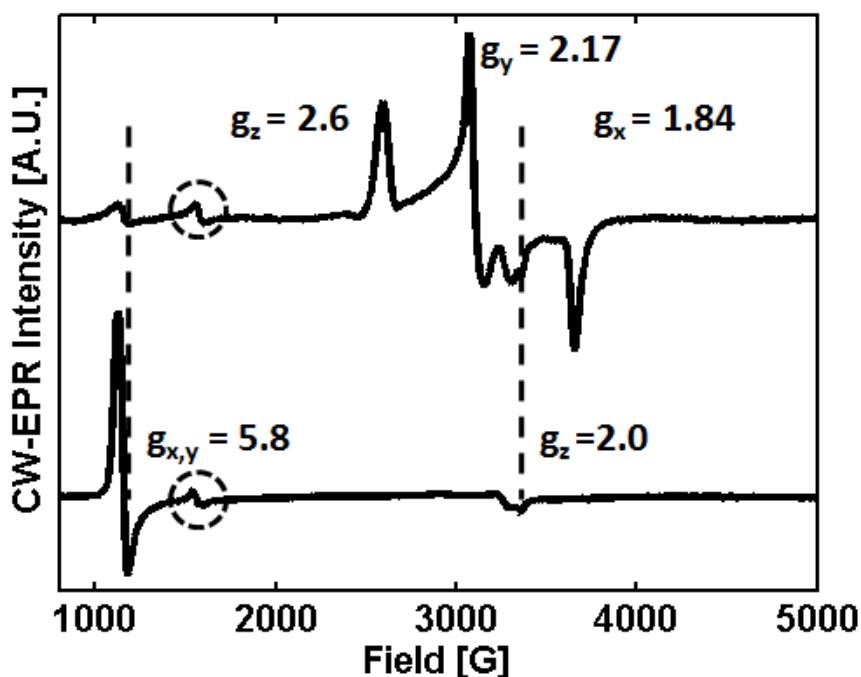


Figure 4.3.8-1, CW-EPR spectrum of 100  $\mu\text{M}$  horse heart myoglobin measured at 20 K at pH 10.8 (i) and pH 5.0 (ii).

Figure 4.3.8-1 Shows the CW EPR spectrum of Mb measured at pH 10.8 (top) and pH 5.0 (bottom). At these extreme pH values the spectra almost entirely demonstrate the low-spin and high-spin forms of Mb respectively. It can be seen that the low-spin form exhibits a rhombic spectrum with principle g-tensor values [ $g_z = 2.6$ ,  $g_y = 2.17$ ,  $g_x = 1.84$ ] typical for Mb

at this pH [42]. The high-spin form is also typical revealing an axial spectrum with  $g$ -values  $g_{x,y} = 5.8$  and  $g_z = 2.0$ . The small signal at  $g = 4.3$  (circled) may be attributed to adventitiously bound iron. It is clear to see from this figure that CW-EPR may easily distinguish between the low and high-spin forms of Mb **Figure 4.3.8-2**.

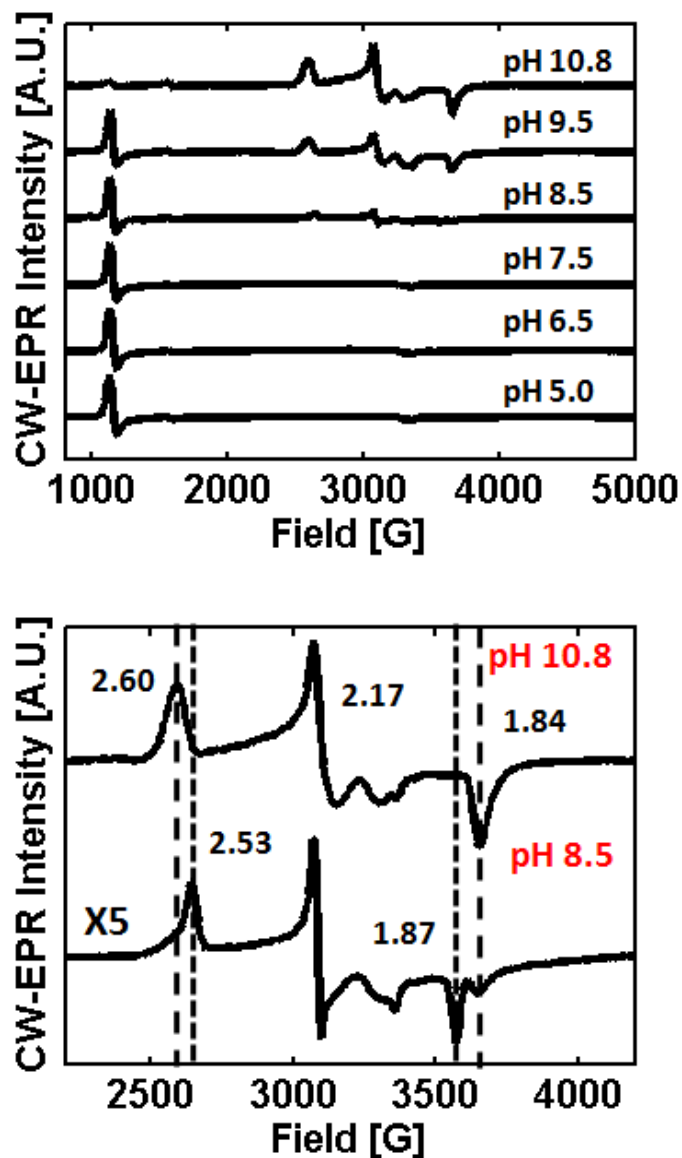


Figure 4.3.8-2, CW-EPR spectrum of 100  $\mu$ M horse heart myoglobin measured at 20 K at range of pH values from pH 10.8 to pH 5.0 (top). Bottom panel shows a comparison of the low-spin region of the spectrum for Mb at pH 10.8 and pH 8.5. The pH 8.5 spectrum shows a contribution from two low-spin species.

It is clear to see that as the pH is lowered the spectrum moves from a dominant low-spin contribution (pH 10.8) to a mixture of spin-states (pH 9.5-8.5) before becoming solely dominated by the high-spin contribution (pH 7.5-5.0). The lower panel shows the spectra of the Mb samples at pH 10.8 and pH 8.5 in greater detail (top and bottom respectively). The pH 8.5 spectrum although indicating a significantly smaller proportion of low-spin contribution, reveals the presence of a second rhombic spectrum with values [ $g_z = 2.53$ ,  $g_y = 2.17$ ,  $g_x = 1.87$ ], whilst also maintaining a contribution from the species predominant at pH 10.8. The species with g-values [ $g_z = 2.6$ ,  $g_y = 2.17$ ,  $g_x = 1.84$ ] will be referred to as species I and that associated with g-values [ $g_z = 2.53$ ,  $g_y = 2.17$ ,  $g_x = 1.87$ ] as species II. This phenomenon has been previously reported for Mb at pH 7, measured at 77 K [43] **Table 4-4**.

Species	$g_z$	$g_y$	$g_x$	Ref
I	2.6	2.17	1.84	This work
II	2.53	2.17	1.87	This work
I	2.59	2.15	1.84	[43]
II	2.55	2.17	1.85	[43]

**Table 4-4, Principle g-values for two species in Mb-OH<sup>-</sup>**

The work does not however, offer an explanation of the origin of these two species. Initially it is tempting to assume that each species may be due to different binding conformations of the coordinated hydroxide anion. The fact that this is so clearly resolved at pH 8.5 perhaps suggests that species II is Mb-OH<sup>-</sup> with the hydroxide hydrogen bonded to the distal histidine [44] (§ 5.2). However, it is known that Mb-OH<sup>-</sup> whilst chemically pure, can exist as a HS/LS mix [45], so it should be not ruled out that one of the LS species could be due to a similar situation for aquomet Mb i.e. LS Mb-H<sub>2</sub>O.

### 4.3.9 Investigation of Nitrite Ligated Myoglobin

Figure 4.3.9-1 shows spectra recorded over the same range of pH values as in § 4.3.8 but with nitrite added to the Mb solutions.

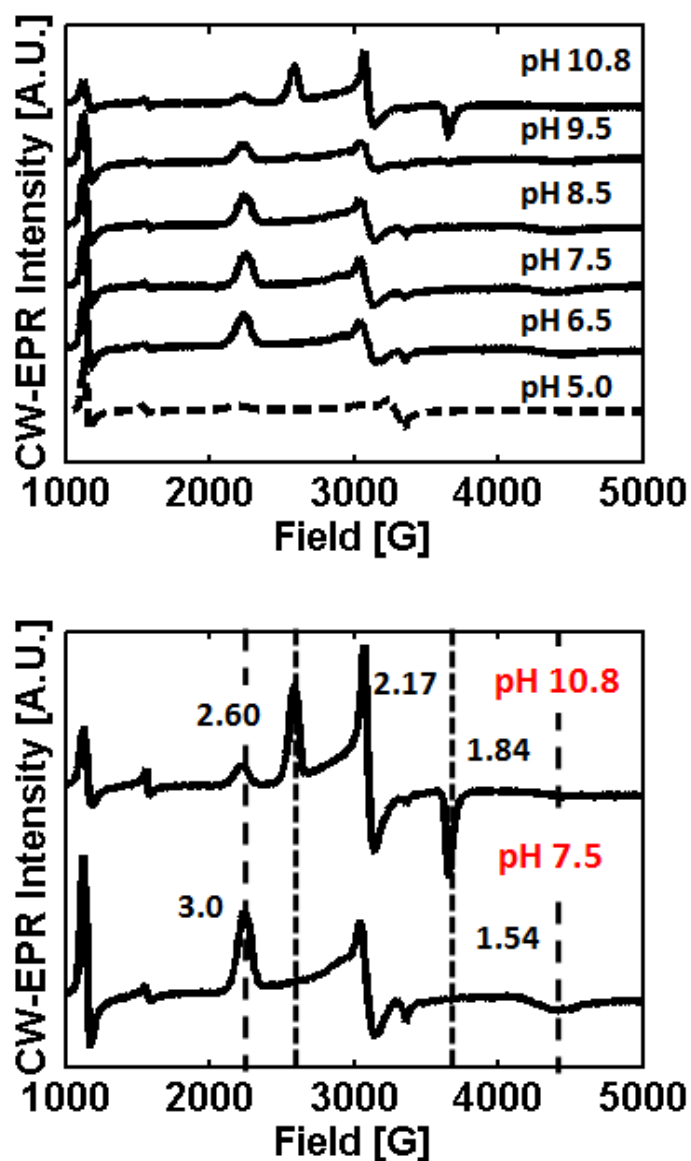


Figure 4.3.9-1, Top: CW-EPR spectrum of 100  $\mu\text{M}$  horse heart myoglobin and 20 fold excess  $\text{NaNO}_2^-$  measured at 20 K at range of pH values from pH 10.8 to pH 5.0. Dashed vertical lines demonstrate contributions to spectra from LS-species I (short)  $\text{Mb-NO}_2^-$  (long). Bottom: Shows a comparison of the low-spin region of the spectrum for  $\text{Mb-NO}_2^-$  at pH 10.8 and pH 7.5.

Samples of nitrite-ligated Mb were prepared by adding 240-fold excess of sodium nitrite ( $\text{NaNO}_2$ ) to  $100 \mu\text{M}$  Mb at each of the measured pH values.  $100 \mu\text{l}$  of the  $\text{Mb-NO}_2^-$  sample was then added to an X-band EPR tube and frozen in liquid nitrogen. Samples were stored at 77 K when not in use. Spectra were recorded at 20 K using the same EPR parameters as for the characterization of Mb in § 4.3.8. From the upper panel it is apparent that there is the contribution to the spectra of a species with g-values [ $g_z = 3.0$ ,  $g_y = 2.19$ ,  $g_x = 1.54$ ] consistent for values previously reported for  $\text{Mb-NO}_2^-$ . For the spectrum of  $\text{Mb-NO}_2^-$  at pH 10.8 the spectrum contains a significant contribution from LS-species I. This contribution persists, but to a much smaller extent at pH 9.5 and is no longer present by pH 8.5. From then on the spectra contain only the contribution of  $\text{Mb-NO}_2^-$  until pH 5.0, the spectrum of which may be attributed to  $\text{Mb-NO}^*$  [46]. The lower panel shows a comparison of the spectra of  $\text{Mb-NO}_2^-$  at pH 10.8 and pH 7.5. The pH 7.5 sample was found to indicate the maximum contribution to the EPR spectrum of the nitrite bound signal.

In conclusion, it is apparent that where optical spectroscopy fails or is only partially able to do so; CW-EPR may unambiguously resolve the contributions from Mb in the native low spin and high-spin states i.e. with hydroxide and water respectively bound, and  $\text{Mb-NO}_2^-$ . It is also clear that many authors fail to consider the effect that pH has upon many of the data used for characterization of Mb. This last fact is perhaps indicative of a broader inconsideration of the effect that pH has on the action and behavior of proteins in general.

## References

1. Wittenberg, B.A., J.B. Wittenberg, and P.R. Caldwell, *Role of myoglobin in the oxygen supply to red skeletal muscle*. Journal of Biological Chemistry, 1975. **250**(23): p. 9038-9043.
2. Rassaf, T., et al., *Nitrite Reductase Function of Deoxymyoglobin: Oxygen Sensor and Regulator of Cardiac Energetics and Function*. Circ Res, 2007. **100**(12): p. 1749-1754.
3. Hess, M.L. and N.H. Manson, *Molecular oxygen: Friend and foe: The role of the oxygen free radical system in the calcium paradox, the oxygen paradox and ischemia/reperfusion injury*. Journal of Molecular and Cellular Cardiology, 1984. **16**(11): p. 969-985.
4. Copeland, D.M., et al., *Crystal structures of the nitrite and nitric oxide complexes of horse heart myoglobin*. Journal of Inorganic Biochemistry, 2006. **100**(8): p. 1413-1425.
5. Yi, J., M.K. Safo, and G.B. Richter-Addo, *The Nitrite Anion Binds to Human Hemoglobin via the Uncommon O-Nitrito Mode*. Biochemistry, 2008. **47**(32): p. 8247-8249.
6. Deligiannakis, Y., M. Louloudi, and N. Hadjiliadis, *Electron spin echo envelope modulation (ESEEM) spectroscopy as a tool to investigate the coordination environment of metal centers*. Coordination Chemistry Reviews, 2000. **204**(1): p. 1-112.
7. Hofer, P., et al., *Hyperfine Sublevel Correlation (HYSCORE) Spectroscopy - A 2D Electron-Spin-Resonance Investigation of the Squaric Acid Radical*. Chemical Physics Letters, 1986. **132**(3): p. 279-282.
8. Mims, W.B., *Pulsed ENDOR Experiments*. Proceedings of the Royal Society of London. Series A, Mathematical and Physical Sciences (1934-1990), 1965. **283**(1395): p. 452-457.
9. Davies, E.R., *A new pulse endor technique*. Physics Letters A, 1974. **47**(1): p. 1-2.
10. Cosby, K., et al., *Nitrite reduction to nitric oxide by deoxyhemoglobin vasodilates the human circulation*. Nature Medicine, 2003. **9**(12): p. 1498-1505.
11. Bredt, D.S., et al., *Cloned and Expressed Nitric-Oxide Synthase Structurally Resembles Cytochrome-P-450 Reductase*. Nature, 1991. **351**(6329): p. 714-718.
12. Zweier, J.L., et al., *Enzyme-Independent Formation of Nitric-Oxide in Biological Tissues*. Nature Medicine, 1995. **1**(8): p. 804-809.
13. Lauer, T., et al., *Plasma nitrite rather than nitrate reflects regional endothelial nitric oxide synthase activity but lacks intrinsic vasodilator action*. Proceedings of the

- National Academy of Sciences of the United States of America, 2001. **98**(22): p. 12814-12819.
14. Ferrari, R., et al., *Metabolic adaptation during a sequence of no-flow and low-flow ischemia - A possible trigger for hibernation*. *Circulation*, 1996. **94**(10): p. 2587-2596.
  15. Gabel, S.A., et al., *Decreased intracellular pH is not due to increased H<sup>+</sup> extrusion in preconditioned rat hearts*. *American Journal of Physiology-Heart and Circulatory Physiology*, 1997. **273**(5): p. H2257-H2262.
  16. van Faassen, E.E., et al., *Nitrite as Regulator of Hypoxic Signaling in Mammalian Physiology*. *Medicinal Research Reviews*, 2009. **29**(5): p. 683-741.
  17. Hitchman, M.A. and G.L. Rowbottom, *Transition-Metal Nitrite Complexes*. *Coordination Chemistry Reviews*, 1982. **42**(1): p. 55-132.
  18. Einsle, O., et al., *Mechanism of the six-electron reduction of nitrite to ammonia by cytochrome c nitrite reductase*. *Journal of the American Chemical Society*, 2002. **124**(39): p. 11737-11745.
  19. Williams, P.A., et al., *Haem-ligand switching during catalysis in crystals of a nitrogen-cycle enzyme*. *Nature*, 1997. **389**(6649): p. 406-412.
  20. Crane, B.R., L.M. Siegel, and E.D. Getzoff, *Probing the catalytic mechanism of sulfite reductase by x-ray crystallography: Structures of the Escherichia coli hemoprotein in complex with substrates, inhibitors, intermediates, and products*. *Biochemistry*, 1997. **36**(40): p. 12120-12137.
  21. Wyllie, G.R.A. and W.R. Scheidt, *Solid-state structures of metalloporphyrin NO<sub>x</sub> compounds*. *Chemical Reviews*, 2002. **102**(4): p. 1067-1089.
  22. Nasri, H., et al., *Variable pi-bonding in iron(II) porphyrinates with nitrite, CO, and tert-butyl isocyanide: Characterization of [Fe(TpivPP)(NO<sub>2</sub>)(CO)](-)*. *Inorganic Chemistry*, 2004. **43**(9): p. 2932-2942.
  23. Janick, P.A. and L.M. Siegel, *EPR and Optical Spectroscopic Evidence for Interaction Between Siroheme and Fe4S4 Prosthetic Groups in Escherichia-Coli Sulfite Reductase Hemoprotein Subunit*. *Biochemistry*, 1982. **21**(15): p. 3538-3547.
  24. Ribeiro, J.M.C., et al., *Reversible Binding of Nitric-Oxide by a Salivary Heme Protein from a Bloodsucking Insect*. *Science*, 1993. **260**(5107): p. 539-541.
  25. Fulop, V., et al., *The Anatomy of a Bifunctional Enzyme - Structural Basis for Reduction of Oxygen to Water and Synthesis of Nitric-Oxide by Cytochrome cd<sub>1</sub>*. *Cell*, 1995. **81**(3): p. 369-377.

26. Harutyunyan, E.H., et al., *The Binding of Carbon Monoxide and Nitric Oxide to Leghaemoglobin in Comparison with Other Haemoglobins*. Journal of Molecular Biology, 1996. **264**(1): p. 152-161.
27. Einsle, O., et al., *Cytochrome c nitrite reductase from Wolinella succinogenes - Structure at 1.6 angstrom resolution, inhibitor binding, and heme-packing motifs*. Journal of Biological Chemistry, 2000. **275**(50): p. 39608-39616.
28. Yi, J., et al., *The Distal Pocket Histidine Residue in Horse Heart Myoglobin Directs the O-Binding Mode of Nitrite to the Heme Iron*. Journal of the American Chemical Society, 2009. **131**(50): p. 18119-18128.
29. Darbre, P.D., A.E. Romeroherrera, and H. Lehmann, *Comparisson of Myoglobin of Zebra (Equus-Burchelli) with that of Horse (Equus-Caballus)*. Biochimica Et Biophysica Acta, 1975. **393**(1): p. 201-204.
30. Young, L.J. and L.M. Siegel, *On The Reaction of Ferric Heme-Proteins with Nitrite and Sulfite*. Biochemistry, 1988. **27**(8): p. 2790-2800.
31. Hendgen-Cotta, U.B., M. Kelm, and T. Rassaf, *A highlight of myoglobin diversity: The nitrite reductase activity during myocardial ischemia-reperfusion*. Nitric Oxide-Biology and Chemistry. **22**(2): p. 75-82.
32. Williams-Smith, D.L., et al., *Changes in Apparent pH on Freezing Aqueous Buffer Solutions and Their Relevance to Biochemical EPR Spectroscopy*. Biochemical Journal, 1977. **167**(3): p. 593-600.
33. Smith, D.W. and R.J.P. Williams, *Analysis of Visible Spectra of Some Sperm-Whale Ferrimyoglobin Derivatives*. Biochemical Journal, 1968. **110**(2): p. 297-+.
34. Scheler, W., G. Schoffa, and F. Jung, *Lichtabsorbtion und Paramagnetische Suszeptibilitat bei Derivativen des Pferde-Methamoglobins und Chironimus-Methamoglobins Sowie des Pferde-Metmaoglobins*. Biochemische Zeitschrift, 1957. **329**(3): p. 232-246.
35. Lin, J., et al., *Metmyoglobin/Azide: The Effect of Heme-Linked Ionizations on the Rate of Complex Formation*. Archives of Biochemistry and Biophysics, 1999. **362**(1): p. 148-158.
36. Henderson, L.J., *Concerning The Relationship Between the Strength of Acids and Their Capacity to Preserve Neutrality*. American Journal of Physiology -- Legacy Content, 1908. **21**(4): p. 465.
37. Markley, J.L., *Observation of Histidine Residues in Proteins by Means of Nuclear Magnetic-Resonance Spectroscopy*. Accounts of Chemical Research, 1975. **8**(2): p. 70-80.

38. Schwab, D.E., J.S. Stamler, and D.J. Singel, *EPR Spectroscopy of Nitrite Complexes of Methemoglobin*. Inorganic Chemistry, 2010. **49**(14): p. 6330-6337.
39. Doeller, J.E. and B.A. Wittenberg, *Myoglobin Function and Energy-Metabolism of Isolated Cardiac Myocytes - Effect of Sodium-Nitrite*. American Journal of Physiology, 1991. **261**(1): p. H53-H62.
40. Nakamura, M. and S. Nakamura, *Conversion of metmyoglobin to NO myoglobin in the presence of nitrite and reductants*. Biochimica et Biophysica Acta (BBA) - General Subjects, 1996. **1289**(3): p. 329-335.
41. Bowen, W.J., *The Absorption Spectra and Extinction Coefficients of Myoglobin*. Journal of Biological Chemistry, 1949. **179**(1): p. 235-245.
42. Sono, M. and J.H. Dawson, *Formation of low spin complexes of ferric cytochrome P-450-CAM with anionic ligands. Spin state and ligand affinity comparison to myoglobin*. Journal of Biological Chemistry, 1982. **257**(10): p. 5496-5502.
43. Sono, M. and J.H. Dawson, *Formation of low spin complexes of ferric cytochrome P-450-CAM with anionic ligands. Spin state and ligand affinity comparison to myoglobin*. J. Biol. Chem., 1982. **257**(10): p. 5496-5502.
44. Bashford, D., et al., *Electrostatic calculations of side-chain pKa values in myoglobin and comparison with NMR data for histidines*. Biochemistry, 1993. **32**(31): p. 8045-8056.
45. Della Longa, S., et al., *Fe-heme conformations in ferric myoglobin*. Biophysical Journal, 1998. **75**(6): p. 3154-3162.
46. Hori, H., M. Ikeda-saito, and T. Yonetani, *Electromagnetic Properties of Hemoproteins .6. Single-Crystal EPR of Myoglobin Nitroxide - Freezing-Induced Reversible Changes in the Molecular-Orientation of the Ligand*. Journal of Biological Chemistry, 1981. **256**(15): p. 7849-7855.

---

---

## 5 CHAPTER EPR Investigation of Nitrite Binding Mode

---

### 5.1 Introduction

It was seen in the previous chapter how continuous wave (CW)-EPR was able to determine whether  $\text{H}_2\text{O}$ ,  $\text{OH}^-$  or  $\text{NO}_2^-$  was bound to myoglobin (Mb), at any of the pH values to be considered in this investigation. This was in contrast to the application of optical spectroscopy. The following chapter now applies CW-EPR and some more advanced pulsed-EPR methods to investigate and resolve the nitrite binding mode ambiguity described in the introduction to Chapter 4.

### 5.2 Nitrite Binding to Myoglobin over Time Using CW-EPR

It is clear that if Mb does indeed have a nitrate reductase role then it may be expected that the EPR signal of  $\text{Mb-NO}_2^-$  would not remain constant after the initial addition of nitrite to Mb. Indeed the initial CW-EPR experiments performed with Mb and  $\text{Mb-NO}_2^-$  described in Chapter 4 suggested this. It was therefore decided to examine the behavior of Mb after the addition of nitrite with time using CW-EPR spectroscopy. 1 ml of 2 mM Mb stock solution (by weight) was made to pH 10.8 (using CAPS buffer). 100  $\mu\text{l}$  of this solution was removed to a suprasil quartz X-band EPR tube and frozen in liquid nitrogen. 240-fold molar excess of aqueous  $\text{NaNO}_2^-$  solution was then added to the Mb stock solution. A further 100  $\mu\text{l}$  were removed to EPR tubes and frozen after periods of 1, 2, 5, 10, 20, 60 and 120 minutes after the addition of nitrite. The X-band EPR spectra of the samples were then measured at a temperature of 10 K using a Bruker E500 spectrometer with a Super High-Q cavity fitted. Spectra were recorded at 9.4 GHz with a CW-microwave (MW) power of 0.1 mW with a modulation frequency of 100 KHz and amplitude of 5 G. The MW frequency was measured using a Marconi Instruments 2440 MW counter. Magnetic field values were calibrated against

---

a DPPH standard. The effect over time of nitrite addition on the EPR spectrum of Mb is shown in **Figure 5.3.1-1**. The intensities of spectra are normalized to the intensity of the unincorporated iron signal (black dashed circle).

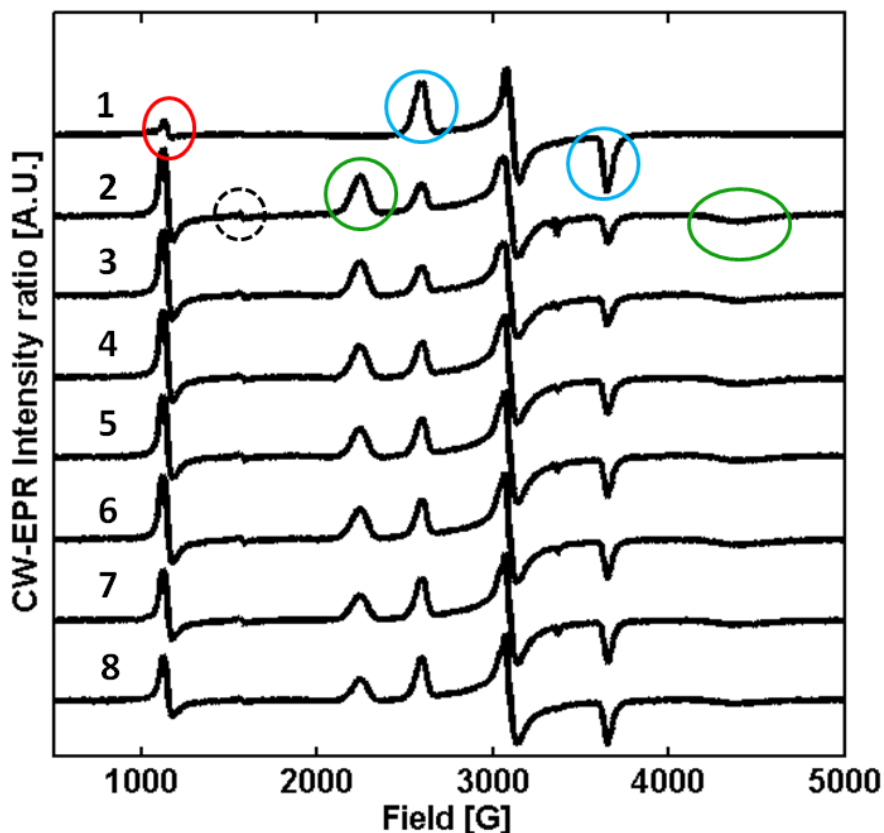


**Figure 5.3.1-1**, X-band CW-EPR spectra at 10 K of 2 mM Mb pH 10.8 (1), and then after the addition of 240-fold excess of nitrite after 1 minute (2), 2, 5, 10, 20, 60 and 120 minutes (3-8) respectively. The red circle in (1) indicates the contribution to the spectra of the high-spin (HS) signal. The blue of the low-spin (LS) Mb ( $\text{Mb-OH}^-$ ) and the green of the LS-nitrite. The dashed black circle indicates the unincorporated iron signal at  $\sim g = 4.3$  to which the intensity of spectra were normalized.

Also indicated are the signals attributed to the high-spin and low-spin (HS and LS) Mb signal (i.e. water/hydroxide coordinated red and blue circles respectively) and the LS-nitrite signal (green circles). Spectrum 1 is that of as prepared Mb whilst those below show the spectra at increasing times after the addition of nitrite. As in the experiments described in the previous chapter, the spectral contribution  $\text{NO}_2^-$  bound heme is clear. Another feature that is apparent in this figure is the increase in the intensity of the HS peak at  $\sim g = 6$  with the addition of

nitrite. The EPR spectral simulation package EasySpin [1] was used in order to quantify this as well as the change in the intensities associated with the other species. **Figure 5.3.1-2** shows the simulations obtained as well as the variation in individual species contribution to the simulated spectra.

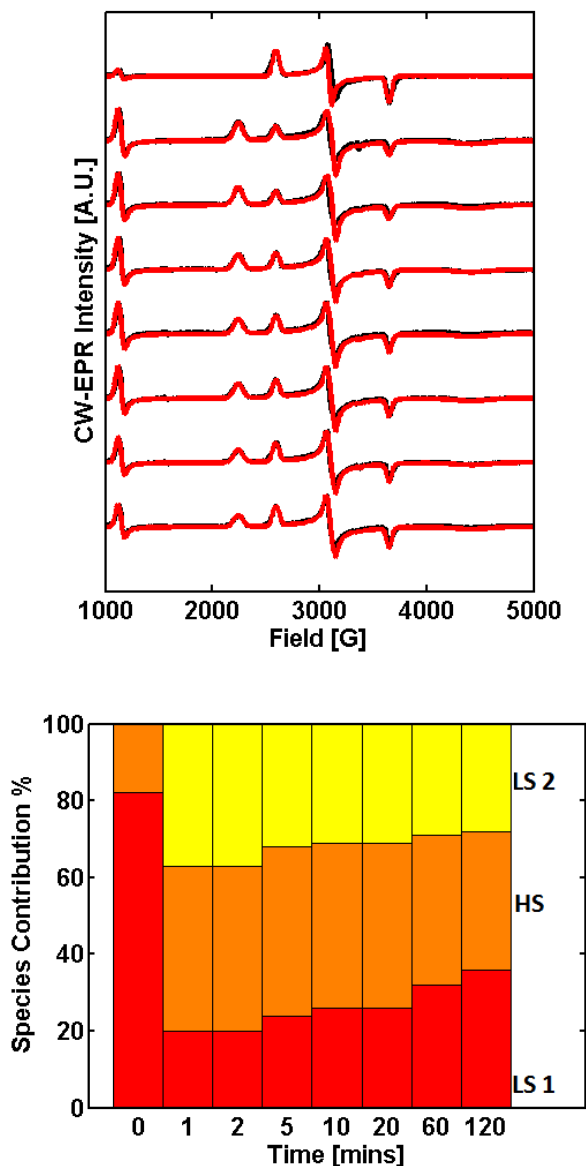


Figure 5.3.1-2, Simulation of data in Figure 5.3.1-1 pH 10.8 (red simulated, black real data) (top), graph to show variation in species spectral contribution (bottom). Mb only simulation parameters positioned at origin. LS1 ( $\text{Mb-OH}^-$ ), LS2 ( $\text{Mb-NO}_2^-$ ) and HS = high-spin.

The parameters used for the simulations are listed below in **Table 5-1**. It is clear from the spectral contributions to the simulations that the intensity of the HS signal increases by a factor of 2.3 after the addition of nitrite. Followed by a much slower reduction in the HS contribution.

Species	g-value			Line-Broadening (MHz)			LWPP (mT)
	$g_1$	$g_2$	$g_3$	$B_1$	$B_2$	$B_3$	
Mb-H <sub>2</sub> O	-	2	5.99	-	-	-	5.5
Mb-OH <sup>-</sup>	2.62	2.2	1.86	250	150	150	0.5
Mb-NO <sub>2</sub> <sup>-</sup>	3.03	2.17	1.53	400	150	800	0.5

**Table 5-1, Simulation parameters used in 5.2. LWPP (line-width peak-to-peak).**

It is unlikely that this increased HS contribution would be due to increased water ligation to Mb as the spectra were measured at pH 10.8. However, it may have been possible that the addition of nitrite lowered the pH such as to favor the coordination of a water molecule. It was therefore pertinent to verify the effect nitrite had on the pH of the sample. A 15 ml sample of 50  $\mu$ M Mb at pH 10.8 (50 mM CAPS) had a dry mass of NaNO<sub>2</sub><sup>-</sup> added in increasing amounts whilst the pH was monitored, the results are shown in **Table 5-2**.

pH	Total NaNO <sub>2</sub> (mg)	Resulting Nitrite concentration (mM)
10.37	0	0
10.37	1.5	1.45
10.39	6.5	6.28
10.42	16.5	15.9
10.48	31.5	30.4
10.50	51.5	49.7
10.63	551.5	530
10.65	1051.5	1000

**Table 5-2, Effect on pH of 50  $\mu$ M Mb solution (pH 10.37) of solid mass addition of sodium nitrite**

It can be seen that actually nitrite slightly increased the pH of the Mb sample therefore the increased HS signal cannot be due to the effect of nitrite on pH. It is therefore tempting to speculate that the increased HS intensity associated with the addition of nitrite could be due to the two proposed binding modes existing in the sample (the LS-NO<sub>2</sub><sup>-</sup> characterized by g-

---

values [3.03 2.17 1.53] and a HS species). Indeed there is perhaps evidence that nitrite may coordinate in both modes within a single sample from a previous study on a porphyrin derivative [2], although it is stated that iron was in the Fe(II) state. This study included crystallographic structures of the complex stated to have NO<sub>2</sub> and NO axial ligands. The structure apparently showing two binding modes is stated to show the disorder that resulted from the linkage isomerism of binding the nitrite anion. Whilst this work describes the bond lengths found for the two binding modes to be similar to other low-spin type Fe-porphyrin complexes it should be kept in mind that an analogous situation in Mb or indeed another protein may be more complex and possibly result in a higher spin state. A view also taken into consideration in a crystallographic and computational chemical investigation of the nitrite reduction to ammonia in cytochrome c nitrite reductase [3] in which various spin-states and nitrite binding modes were considered (in this case N-bound low-spin was found to be energetically favorable).

It is clear therefore that it is possible that the two binding modes may co-exist, but that further investigation is necessary to strengthen the argument for this case.

The increased HS signal above was found at a pH of 10.8. The effect of pH on the distribution of HS/LS species formed by addition of nitrite to Mb was investigated by repeating the above measurements with Mb in solutions of pH 9.5, 8.5, 7.5 and 6.5. At pH 5 the nitrite was found to rapidly reduce to NO<sup>•</sup>, and for the protein to be unstable (the instability will be discussed further in Chapter 6). A similar procedure was followed as above wherein 250 μl of 2 mM samples of Mb were prepared using 50 mM buffer solutions (for different pH values 6.5–10.8). 100 μl of each sample was then placed in an X-band suprasil quartz EPR tube and frozen in liquid nitrogen. 240-fold excess nitrite was then added in solution (at each corresponding pH value) to each of the Mb samples. After 1 minute 100 μl of the Mb-NO<sub>2</sub><sup>-</sup> solution was removed to an EPR tube and also frozen. The X-band CW-EPR spectra of each sample before and after the addition of nitrite were measured at 10 K using the parameters stated above. The results of the experiment may be seen in **Figure 5.3.1-3**. The top panel indicates the CW-EPR spectra of the Mb (red) and Mb-NO<sub>2</sub><sup>-</sup> (black) samples. For this experiment the spectra

---

were unable to be corrected to the unincorporated iron signal due to the large intensity of the HS signal obscuring it in the pH range 6.5–8.5.

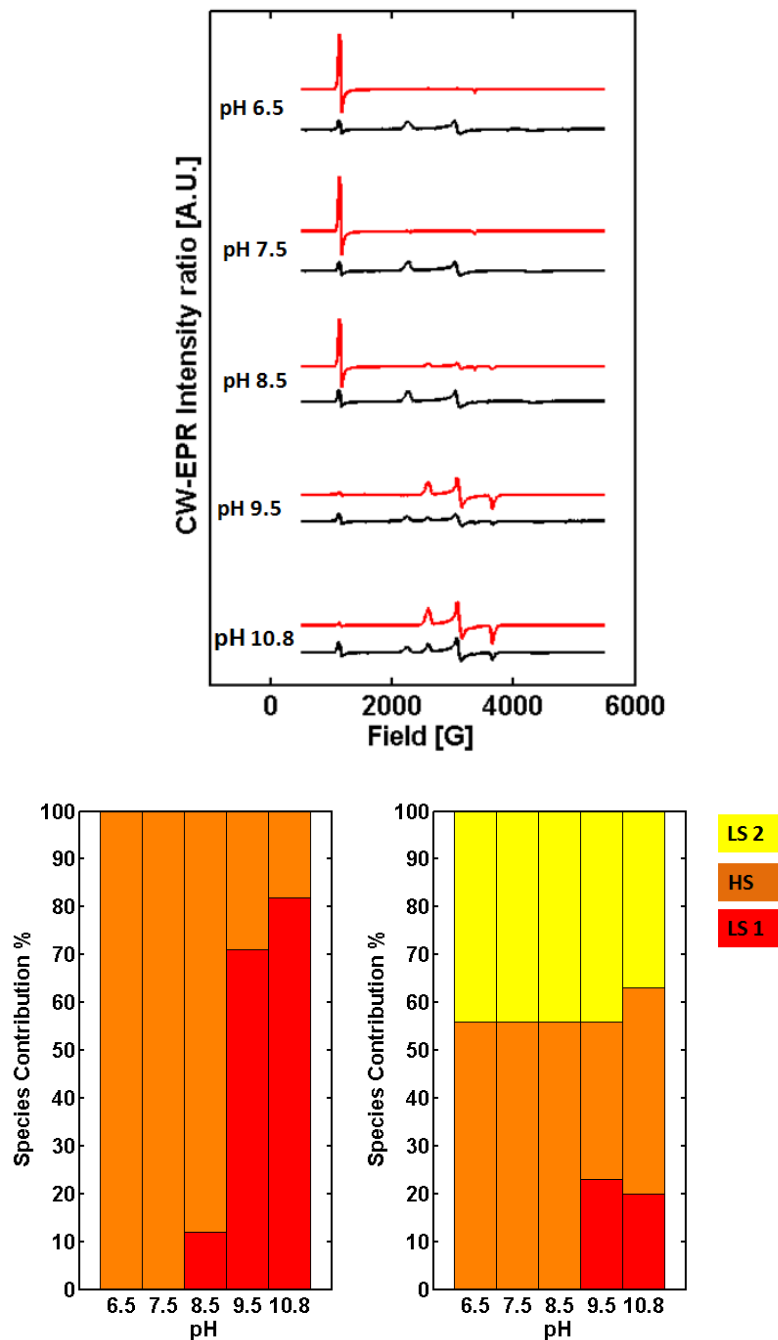


Figure 5.3.1-3, CW-EPR showing spectra of Mb before (red) and after (black) the addition of nitrite (top) At pH values indicated. Bottom chart shows contribution to spectra from simulation, associated with HS and LS-NO<sub>2</sub><sup>-</sup> (LS2) and LS-OH<sup>-</sup> (LS1).

---

The bottom panel displays a graph showing the contribution to the spectra from the different species: HS, LS Mb-OH<sup>-</sup> and LS Mb-NO<sub>2</sub><sup>-</sup>. The percentages indicated were determined by simulation. It may be observed that above pH 8.5 the HS intensity increases with the addition of nitrite. It is interesting that the transition between the HS signal decreasing and increasing with the addition of nitrite is between pH 8.5 and 9.5. In Chapter 4 it was stated that the pK<sub>a</sub> water coordinated to ferric Mb = 8.9 [4] and above this pH Mb would be more likely to bind hydroxide. If we however recall the study Richter-Addo and colleagues on a series of Mb-Mutants [5] (§ 4.2.4) it was found that when H-bonding residues were present the nitrite was ligated via the *O*-nitrito mode, and when these were absent the *N*-nitro mode was favored. It will also be recalled that the most significant H-bonding residue in the binding pocket of Mb was the His64 amino acid. The pK<sub>a</sub> of the protonation of histidine is typically around 6 [6], and above pH 8 the residue will be almost completely unprotonated and so unlikely to be involved in hydrogen bonding. It may therefore be inferred that the increased HS signal observable above pH 8.5 may be due to the *N*-nitro mode the LS signal associated with the addition of nitrite would therefore likely be due to the *O*-nitrito form. The remainder of this chapter will describe the application of pulsed-EPR techniques to test this hypothesis.

---

### 5.3 Pulsed-EPR Investigation of nitrite binding Mode

The following describes the more advanced pulsed-EPR experiments applied to test the above hypothesis. The techniques will be introduced in turn before a description of their application and findings.

#### 5.3.1 Introduction to Field-Swept Echo (FSE)

One of the most simple and useful pulsed EPR experiments is that of the Field-Swept Echo (FSE) also known as the two-pulse Hahn Echo experiment [7]. This experiment is performed before the more-advanced techniques in order to determine the field-values of the canonical positions and to characterize the signal intensity **Figure 5.3.1-1** shows the pulse sequence of the FSE and how its appearance relates to that commonly found in CW-EPR.

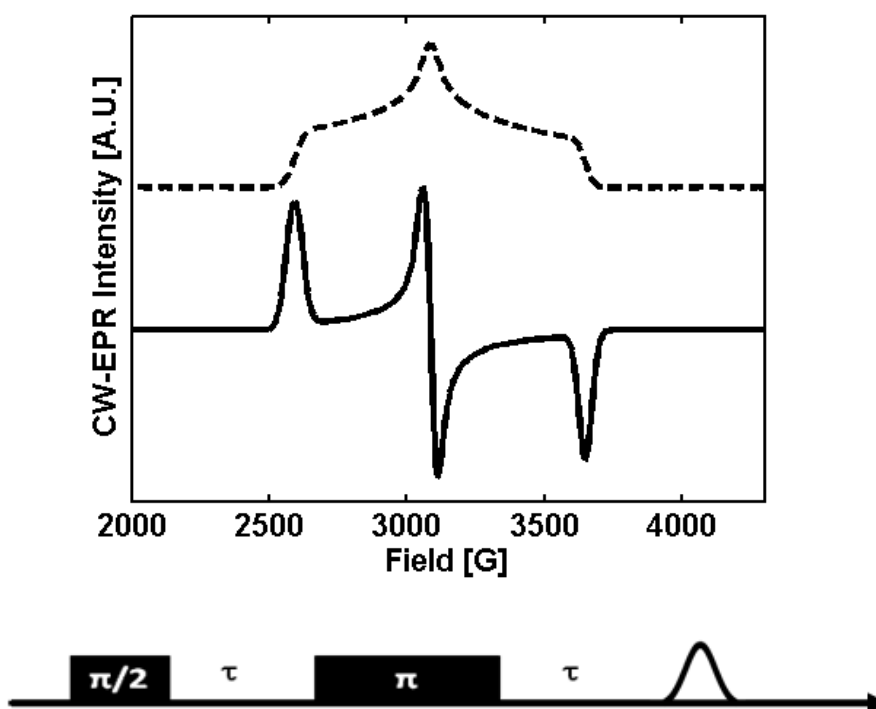


Figure 5.3.1-1, Simulated spectrum of LS-Mb (top) shown in absorbance (dashed) and derivative (solid) mode. Pulsed sequence for Field-Swept-Echo (bottom).

In this experiment a  $\pi/2$  ( $90^\circ$ ) pulse first induces electronic coherence which then begins to de-phase, after a time ( $\tau$ ) a  $\pi$ -pulse is applied that inverts the de-phasing spins such that they

regain coherence after a further time period  $\tau$ , which manifests itself as an echo that is recorded, and is known as the primary echo. The resulting signal is usually obtained as an absorbance spectrum as opposed to the derivative spectrum usually obtained for CW-EPR. The Intensity of the FSE may be subject to a  $\tau$ -value dependence as is seen in the top panel of **Figure 5.3.2-1**.

### 5.3.2 Orientation of g-value Axes within Molecular Frame

It is convenient to relate the field-position at which hyperfine EPR experiments are carried out on frozen or powder-like samples to the geometry of the spin-system. For low-spin ferriheme systems the g-values are related to the heme as depicted in **Figure 5.3.2-1** [8].

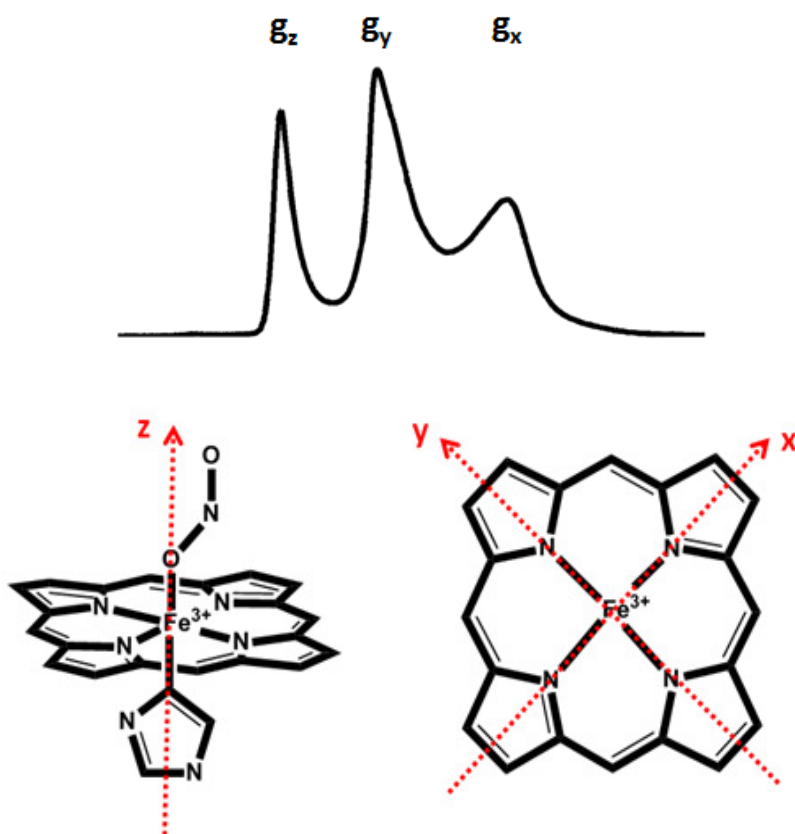


**Figure 5.3.2-1, g-value definition of FSE (top) and relation to geometry of Heme in Mb (bottom)**

Thus the contribution of an exogenous ligand to the heme would be detected by performing an experiment at the field-position corresponding to  $g_z$ .

---

### 5.3.3 Introduction to Electron Spin Echo Envelope Modulation (ESEEM)

Electron-Spin Echo Envelope Modulation (ESEEM) experiments [9] are performed by measuring the echo intensity generated by a series of resonant MW pulses separated by a series of evolution times (periods when MW power is off). In the presence of nuclear spins weakly coupled with the electron spin, the echo is modulated at the nuclear transition frequencies of the interacting nucleus. The modulation of the echo intensity by the interaction of the nuclear spin is known as the modulation envelope. Fourier Transform (FT) of the time-domain echo envelope produces a frequency spectrum similar to the corresponding ENDOR spectrum. 1D and 2D ESEEM experiments may be applied to nuclei that are coupled to the electron spin via an anisotropic hyperfine interaction (the interaction between nuclear and electronic dipoles, averaged to zero in liquid samples), especially for weak hyperfine couplings e.g. of the order of the nuclear Larmor frequency.

ESEEM differs from ENDOR in that no RF is needed, as the nuclear spins are observed due to a mixing of the frequencies of the semi-forbidden and allowed EPR transitions. Strong modulation effects are only observable with the following conditions:

- a) Anisotropic hyperfine or quadrupolar interaction.
- b) MW pulses strong enough to drive an allowed and semi-forbidden EPR transition simultaneously.
- c) Cancellation of nuclear splitting for one electronic manifold.

Due to a) ESEEM effects cannot be directly observed in liquid samples of small molecules. b) Dictates that at least one MW pulse must be sufficiently strong to simultaneously drive a forbidden and an allowed transition. The ESEEM effect will be more pronounced when the probabilities of these two transitions are similar. This can be achieved by alteration of the external magnetic field to tune the nuclear level splitting of one electronic manifold (see **Figure 5.3.3.2.**)

In a 1D ESEEM experiment the two-pulse Hahn echo - primary echo, (**Figure 5.3.1-1**) intensity is monitored as a function of the pulse separation time **Figure 5.3.3-1**. The echo intensity

---

oscillation is caused by spins evolving on different electronic coherences before and after the re-focusing pulse. In this experiment the modulation can only be observed for the time scale of the transverse electron relaxation time. In many cases this is too short to obtain sufficient resolution in complex spectra with several coupled nuclei.

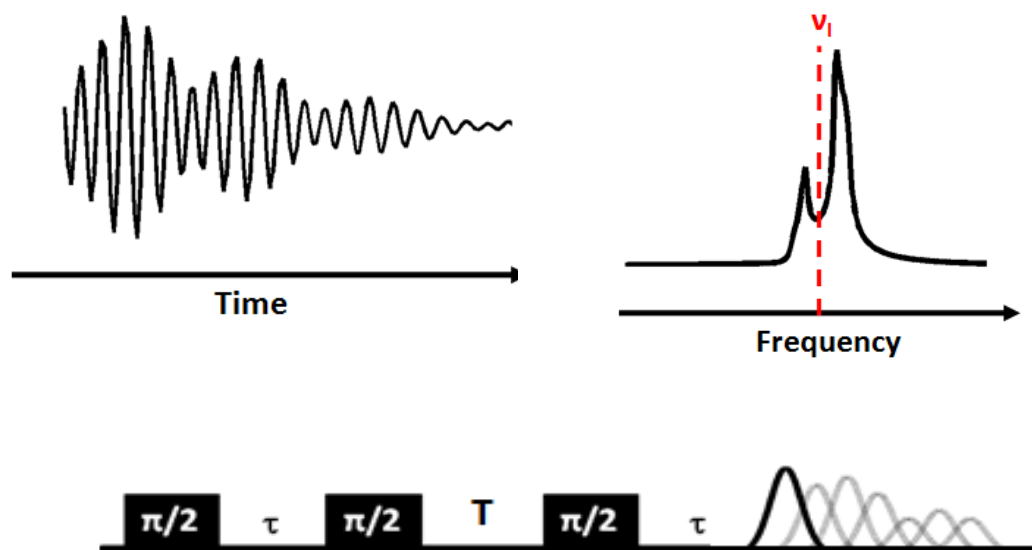


Figure 5.3.3-1, Pulse sequence for three-pulse ESEEM (bottom) including depiction of echo envelope as a modulation as a function of moving the pulse distance  $T$  to produce the time-domain spectrum (top left), which may be Fourier-transformed to obtain the nuclear frequencies (top right), which in the  $S=1/2$   $I=1/2$  case has the features centered around the nuclear Larmor frequency.

### 5.3.3.1 Two-Pulse and Three-Pulse ESEEM

The most common forms of the one-dimensional ESEEM experiment are the two-pulse and three-pulse experiments based on the modulation of the primary and stimulated (generated by three  $\pi/2$ -pulses and  $T_1$  dependant) echo respectively. The two-pulse experiment has two major shortcomings over the three-pulse experiment. Firstly: the two-pulse ESEEM line-width is related to the phase memory time of the electron spins which usually results in poor frequency domain resolution. Secondly the frequency domain spectrum contains sum and difference combination peaks of the nuclear frequencies which can make interpretation difficult. For these reasons only three-pulse ESEEM (pulse sequence shown in **Figure 5.3.3-1**) will be applied experimentally in this work.

### 5.3.3.2 Cancellation condition

In practice for a powder sample the interpretation of the frequency domain is often complicated due to the superposition of the spectra of different orientations. This problem is alleviated under the particular condition when the hyperfine coupling matches the nuclear Zeeman interaction such that:

$$A_{\text{iso}} = 2\nu_I$$

Under these conditions the frequency domain ESEEM spectra include a series of characteristic frequencies depending on the nuclear spin  $I$  of the coupled nucleus. In general the larger the value of  $I$  the more complicated the spectrum in both the matching and non-matching conditions. For the purposes of this work the  $I = 1$ ,  $^{14}\text{N}$  nucleus shall be the only case to be discussed in detail. **Figure 5.3.3-2** shows the energy level diagram and corresponding example of a three-pulse ESEEM spectrum under the cancellation condition.

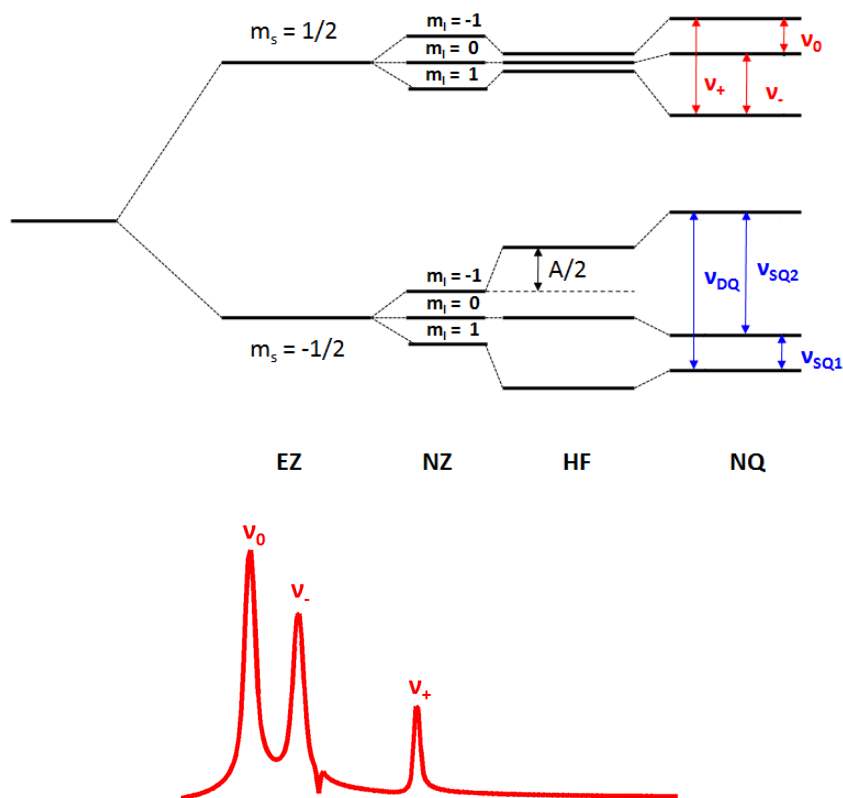


Figure 5.3.3-2, Energy level diagram for  $S=1/2$ ,  $I=1$  under cancellation condition (top). Resulting frequency domain three-pulse ESEEM spectrum showing principal nuclear frequencies.

At this condition the frequency spectrum is dominated by three narrow low-frequency lines (red lines) dependant on the nuclear quadrupole parameters. The three observed frequencies are:

$$\nu_+ = 3K(1 + \eta)$$

$$\nu_- = 3K(1 - \eta)$$

$$\nu_0 = 2\kappa\eta$$

With  $K = e^2qQ/4h$ . The intensities of the lines being determined by the relative orientation of the NQ and hyperfine axes systems and the  $\tau$ -value used in the experiment [10]. It can be seen from the diagram that in the other electron spin manifold the nuclear frequencies arise from an addition of the nuclear Zeeman and hyperfine interactions (blue lines). The observed transitions are therefore much broader and the only transition that may be resolved is a double quantum (DQ) transition line with the approximate maximum intensity frequency position of [10]:

$$\nu_{DQ} \sim 2\left[\left(\nu_I + \frac{A}{2}\right)^2 + K(3 + \eta^2)\right]^{1/2}$$

In this case  $A$  is the secular component of the hyperfine coupling and is mainly determined by  $a_{iso}$ . The above condition is robust for small dipolar contributions which tend to affect the shape but not the position of the observed DQ frequencies in the frequency domain spectrum. When there is no significant dipolar contribution and  $|\nu_I - A_{iso}/2| < 2K/3$  the spectrum will still exhibit similar features to the cancellation condition even with slight deviations from  $A_{iso} = 2\nu_I$ . However, in this case there will be a decrease in the modulation depth of the time-domain signal.

If there is a strong dipolar contribution or  $A_{iso} \ll 2\nu_I$  the observed ESEEM features will degrade. For strong isotropic hyperfine couplings ( $A_{iso} > 2\nu_I$ ) sharp DQ frequencies are observed corresponding to the contributions for each electron spin manifold.

### 5.3.4 Initial characterization of low-spin myoglobin

As a starting point for the pulsed-EPR investigation of Mb-NO<sub>2</sub><sup>-</sup> the characterization of LS Mb (pH 10.8) was deemed pertinent. This form of the protein has been previously investigated using a variety of spectroscopic techniques including pulsed-EPR. The characteristic features associated with the heme motif are therefore reasonably well understood and facilitate the effective simulation of the following experiments from initial starting parameters.

For this characterization 100  $\mu$ l of 1 mM Mb at pH 10.8 (CAPS) was frozen in a suprasil quartz X-band EPR tube.

#### 5.3.4.1 Field-Swept-Echo of Low-Spin Myoglobin

The Field-Swept-Echo (FSE) spectra of LS-Mb measured at 10 K are shown in **Figure 5.3.4-1**. Two spectra with  $\tau$ -values of 120 and 240 ns (black and red respectively) are presented.

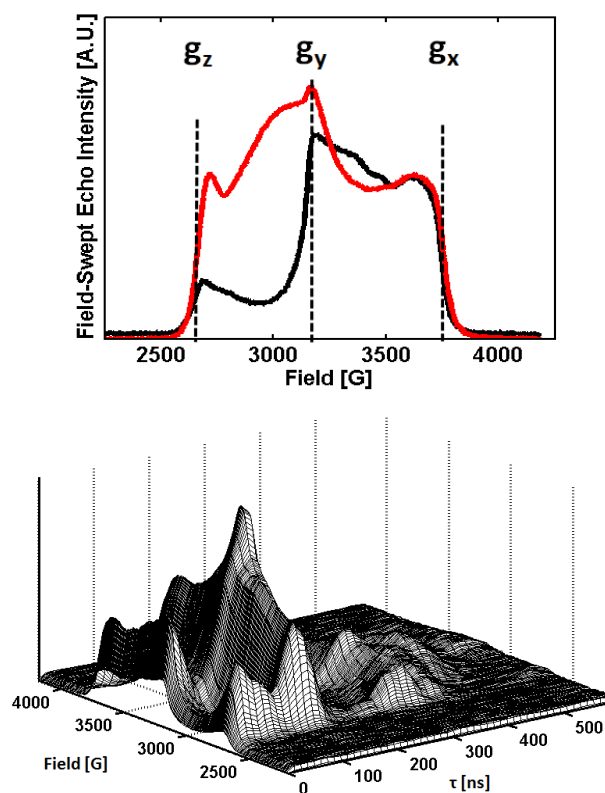


**Figure 5.3.4-1, Top:** FSE spectra of LS-Mb measured with  $\tau$ -values of 120 and 240 ns (black and red). **Bottom:** FSE versus  $\tau$ -value (zero on time axis corresponds to initial  $\tau$ -value of 120 ns).

A 16 ns  $\pi$ -pulse was used and the echo optimized with 3 dB High Power Attenuation (HPA) and a shot-repetition time (SRT) of 1000  $\mu$ s. The subsequent spectra are the sum of 16 scans. It may be seen that as expected the  $g$ -values are comparable to those determined through CW-EPR. Field positions corresponding to approximate canonical  $g$ -values are indicated where subsequent advanced pulsed-EPR experiments were conducted. Actual canonical positions were not used due to insufficient signal intensity at extreme  $g$ -values ( $g_z$  and  $g_x$ ). It may be seen that the spectra reveal a  $\tau$ -dependent intensity previously reported [11] due to strong echo-modulation effects. The bottom portion of the figure shows the 2D field-swept-echo versus  $\tau$ -value spectrum of LS-Mb to further illustrate this point.

#### 5.3.4.2 Three-Pulse ESEEM of Low-Spin Myoglobin

Figure 5.3.4-2 shows the three-pulse ESEEM frequency domain spectra of LS-Mb measured near the three canonical positions as a sum of two  $\tau$ -values (120 ns and 240 ns). 8 ns  $\pi/2$ -pulses were used with a T of 16 ns and the spectra were recorded at 10 K.

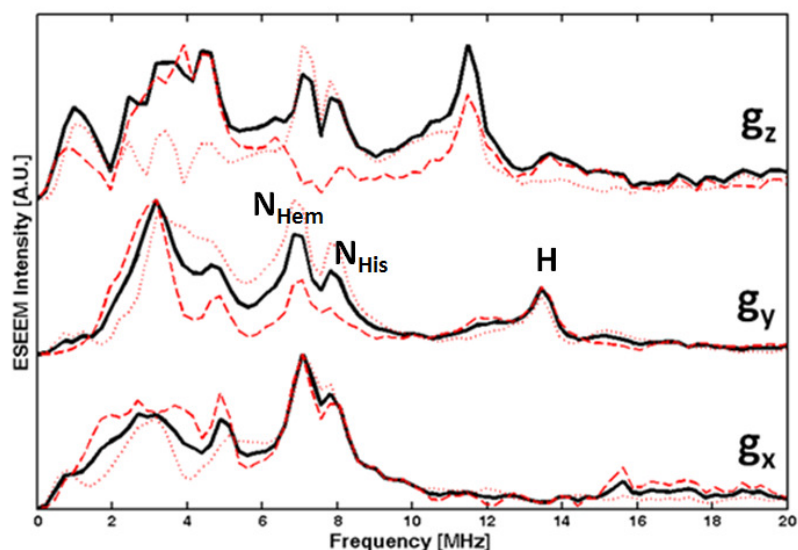


Figure 5.3.4-2, Frequency domain three-pulse ESEEM of 1mM Myoglobin measured at 10K showing spectra obtained at canonical field positions ( $g_z = 2718$  G,  $g_y = 3171$  G and  $g_x = 3650$  G). Spectra measured at MW frequency of 9.68 GHz, using an 8 ns  $\pi/2$ -pulse. Black lines indicate the Summed spectra of  $\tau = 120$  ns (red dotted lines) and  $\tau = 240$  ns (red dashed lines). The positions of the DQ peaks associated with two types of  $^{14}\text{N}$  are indicated in the middle spectra.

To understand the principal features of the spectra the simulation package EasySpin [1] was used. Initially the hyperfine and quadrupole coupling parameters for the pyrrole and

imidazole nitrogens of Mb-OH were taken from data reported from Magliozzo and Peisach [12, 13] (Table 5-3).

$^{14}\text{N}$	$A_1$	$A_2$	$A_3$	$e^2qQ$	$\eta$	Ref
		MHz		MHz		
Porphyrin	4.9	5.1	5.3	2.2	0.1	[12]
Imidazole	5.5	5.5	4.2	2.3	0.1	[13]

Table 5-3, MbOH  $^{14}\text{N}$  nuclear parameters used for initial three-pulse ESEEM simulation

The results of the simulations are plotted against the experimental spectra in Figure 5.3.4-3. Although many of the features do indeed correlate, only one peak [7-8 MHz] is seen in the simulations whereas this is resolved as a splitting in the experimental data. As stated in Chapter 4, this study failed to take orientation selectivity into account which possibly contributes to this observation via a slight miss-assignment of the principal hyperfine parameters by the authors.

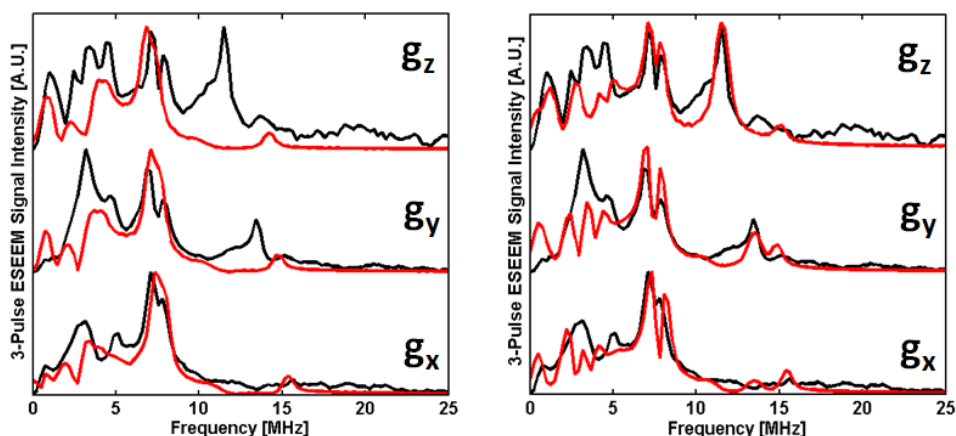


Figure 5.3.4-3, Simulated three-pulse ESEEM spectra (red) and experimental data (black) of LS-Mb Near canonical positions measured at 10 K, using values from Magliozzo and Peisach (left) Table 5-3, and refined parameters Table 5-4.

The simulation values were therefore refined to fit the experimental data Figure 5.3.4-3 right (including proton coupling). The resulting parameters are presented in Table 5-4.

$^{14}\text{N}$	$A_1$	$A_2$	$A_3$	$e^2qQ/h$	$\eta$
		MHz		MHz	
Porphyrin	5.5	5.5	4.2	2.2	0.1
Imidazole	5.9	5.9	6.1	2.3	0.1

Table 5-4, MbOH  $^{14}\text{N}$  nuclear parameters used for final three-pulse ESEEM simulation

### 5.3.5 Pulsed-EPR Investigation of Low-Spin Myoglobin Nitrite

2 mM Mb samples were prepared using the buffers described in Chapter 4 to make samples at pH 6.5, 7.5, 8.5, 9.5 and 10.8. As previously 240-fold excess of sodium nitrite was then added and the samples placed in EPR-tubes previously described and frozen in liquid nitrogen. Pulsed experiments were performed on a Bruker E-680 spectrometer using a Bruker dielectric ring resonator ER 4118X-MD5. As a first step in the characterization the FSE's of each sample were measured at 10 K and at  $\tau$ -values of 120 and 260 ns. The remainder of the experimental parameters were as described in § 5.3.4.1. The spectra measured with a  $\tau$ -value of 120 ns are shown in **Figure 5.3.5-1**.

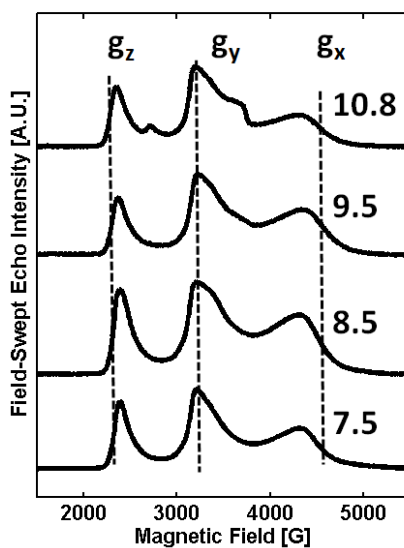
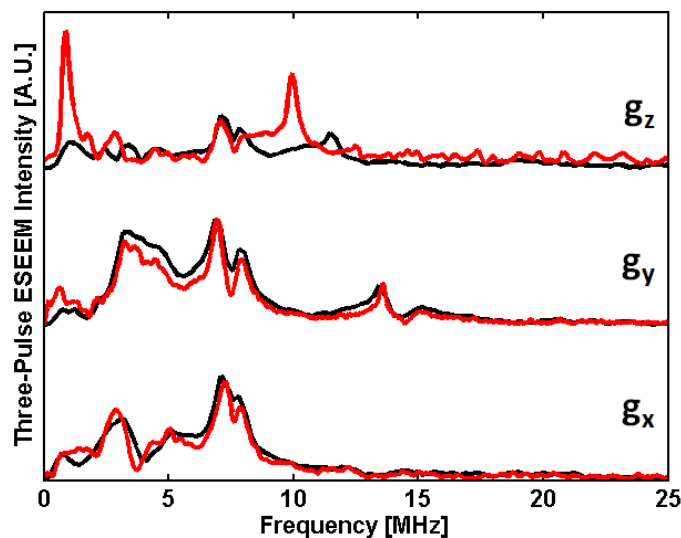


Figure 5.3.5-1, FSE spectra measured at 10 K of Mb-NO<sub>2</sub><sup>-</sup>. Values on the right of spectra indicate the pH Of the samples.

The principal  $g$ -values of the nitrite ligated Mb (LS signal) are indicated and are the same as those measured by CW-EPR in the previous chapter: [ $g_z = 3.0$ ,  $g_y = 2.19$ ,  $g_x = 1.54$ ]. The spectra also indicate a similar contribution from LS Mb-OH at high pH. The spectra do not however, show a contribution from a HS signal. This is due to the relaxation properties of such a species which may normally only be measured at very low temperatures (less than 5 K) and will be examined later. The spectra also exhibited similar  $\tau$ -dependant intensity as reported in § 5.3.4.1 for Mb.

### 5.3.6 Three-Pulse ESEEM of Myoglobin Nitrite

The Three-Pulse ESEEM frequency-domain spectra of Mb and Mb-NO<sub>2</sub><sup>-</sup> at pH 10.8 measured with a  $\tau$ -value of 120 ns and at 10 K are shown in **Figure 5.3.6-1**. The other experimental parameters were as in § 5.3.4.2.



**Figure 5.3.6-1**, Three-Pulse ESEEM frequency domain spectra of Mb pH 10.8 (black) and Mb-NO<sub>2</sub><sup>-</sup> At pH 10.8 (red) measured near  $g$ -value canonical positions at 10 K.

It is clear from this figure that the spectra measured at the  $g_x$  and  $g_y$  positions (contribution from the heme-plane) exhibit similar frequencies in both cases, whereas the spectra at the  $g_z$  position (contribution from heme axial ligands) show distinct differences with the addition of nitrite. It should be kept in mind that the field-positions corresponding to the  $g_z$ -position are significantly different in each sample. **Table 5-5** indicates the approximate field-positions for

the principal  $g$ -values in each case. This has a marked effect on the position of the proton coupling peak that may be seen at around 10 MHz in the Mb-NO<sub>2</sub><sup>-</sup> case. ( $\nu_H = 11.6$  and 9.9 MHz for 2720 and 2330 G respectively).

	$g_z$	$g_y$	$g_x$
	Field Value [G]		
<b>Mb-OH</b>	2720	3170	3650
<b>Mb-NO<sub>2</sub><sup>-</sup></b>	2330	3190	3750

**Table 5-5, Approximate magnetic field positions of principle  $g$ -values for Mb-OH and Mb-NO<sub>2</sub><sup>-</sup>**

The dominant feature in the spectrum for the  $g_z$ -position in the Mb-NO<sub>2</sub><sup>-</sup> case is a strong sharp peak at  $\sim 0.8$  MHz. It should be expected, that the nuclear couplings due to the <sup>14</sup>N of coordinated nitrite should be apparent at this position. At pH 10.8 however, there is still a significant amount of Mb-OH species as may be seen in **Figure 5.3.5-1**. To better resolve the couplings due to coordinated nitrite the three-pulse ESEEM technique was also applied to samples at a lower pH. The pH 7.5 situation was chosen to maximize the proportion of coordinated nitrite to Mb.

Figure 5.3.6-2 shows the three-pulse ESEEM time-domain and frequency domain spectra of Mb-OH and Mb-NO<sub>2</sub><sup>-</sup> at pH 10.8 and Mb-NO<sub>2</sub><sup>-</sup> at pH 7.5 measured near the  $g_z$  position at 10 K. An examination of the time-domain data reveals a strong modulation depth with a large periodicity for the nitrite ligated sample that is not present in the low-spin Mb spectrum.

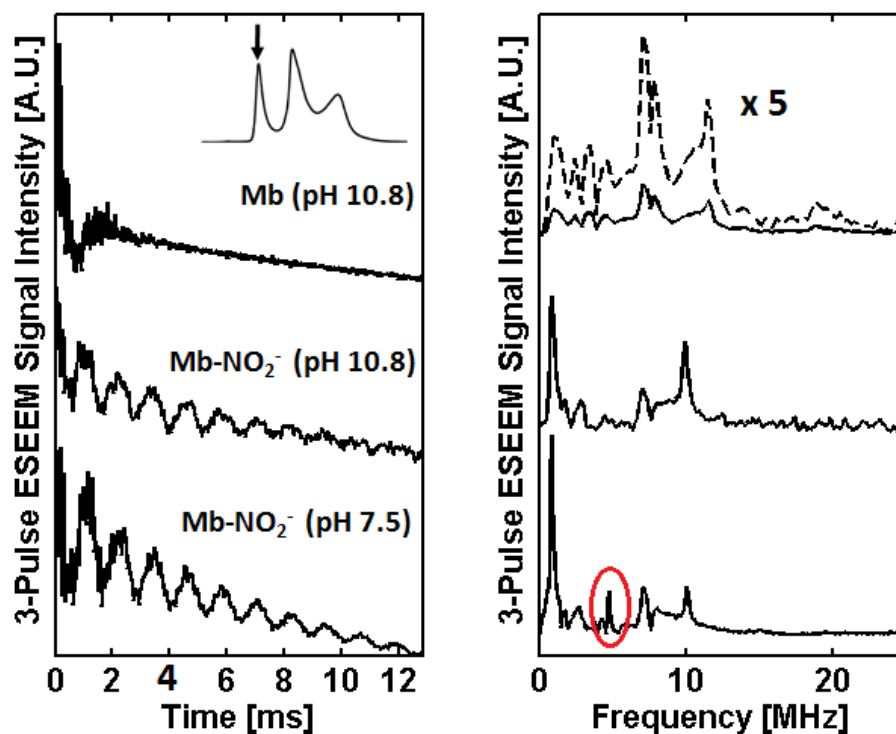


Figure 5.3.6-2, Three-Pulse ESEEM time domain (left) and frequency domain (right) spectra of Mb species indicated in left panel measured at the  $g_z$ -position and at 10 K. FSE insert in left panel indicates position at which ESEEM Experiments were performed.

Fourier transform of these spectra indicates that this periodicity gives rise to the strong sharp peak at  $\sim 0.81$  MHz. As the pH is lowered to 7.5 these key features increase in intensity, a second sharp peak although less intense than that at 0.81 MHz is seen at  $\sim 4.9$  MHz (red circle lower plot in left panel). The three-pulse ESEEM of isotope labeled nitrite was performed in order to verify that the extra features described were indeed due to the coupling from the  $^{14}\text{N}$  of the bound nitrite and to aid in the determination of the nuclear coupling parameters and will be the subject of the following section.

### 5.3.7 Isotope labeled nitrite

Isotope labeling may prove useful in the determination of nuclear parameters from hyperfine spectroscopy. In the case of nitrogen the quadruple coupling of the  $^{14}\text{N}$  nucleus ( $I=1$ ) often leads to complicated spectra.  $^{15}\text{N}$  has a nuclear spin  $I=1/2$ , and therefore no quadrupole interaction. If the nuclei coupled to the electron spin are replaced with  $^{15}\text{N}$  nuclei the resulting spectra may be more readily interpreted.  $^{15}\text{N}$  labeled nitrite was donated by Dr Myles Cheesman and added to Mb to a 240-fold excess. The FSE was then measured to ensure the  $^{15}\text{N}$  labeled nitrite had bound to the Mb and that the spectra of both complexes were comparable. The FSE spectra with a  $\tau$ -value of 120 ns, measured at 10 K for both isotopes of nitrite bound to Mb at pH 7.5 is shown below in **Figure 5.3.7-1**.

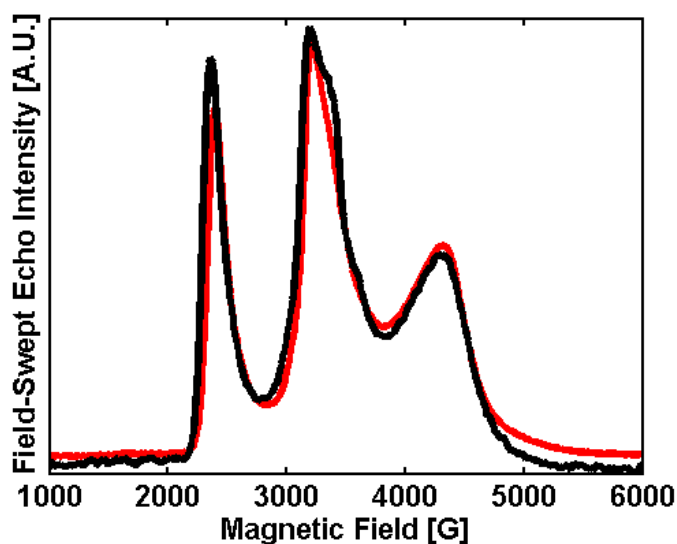


Figure 5.3.7-1, FSE of Mb- $^{14}\text{NO}_2$  (black) and Mb- $^{15}\text{NO}_2$  (red) measured at 10 K with a  $\tau$ -value of 120 ns

It may be seen that as expected the spectra were comparable with the principal g-values coinciding in both cases indicating that the labeled nitrite had indeed bound to the Mb in a similar geometry to the  $^{14}\text{N}$  nitrite. The samples could therefore be further characterized with hyperfine spectroscopic techniques. The three-pulse ESEEM of  $^{15}\text{N}$  and  $^{14}\text{N}$  nitrite ligated to Mb at pH 7.5 is shown in **Figure 5.3.7-2**.

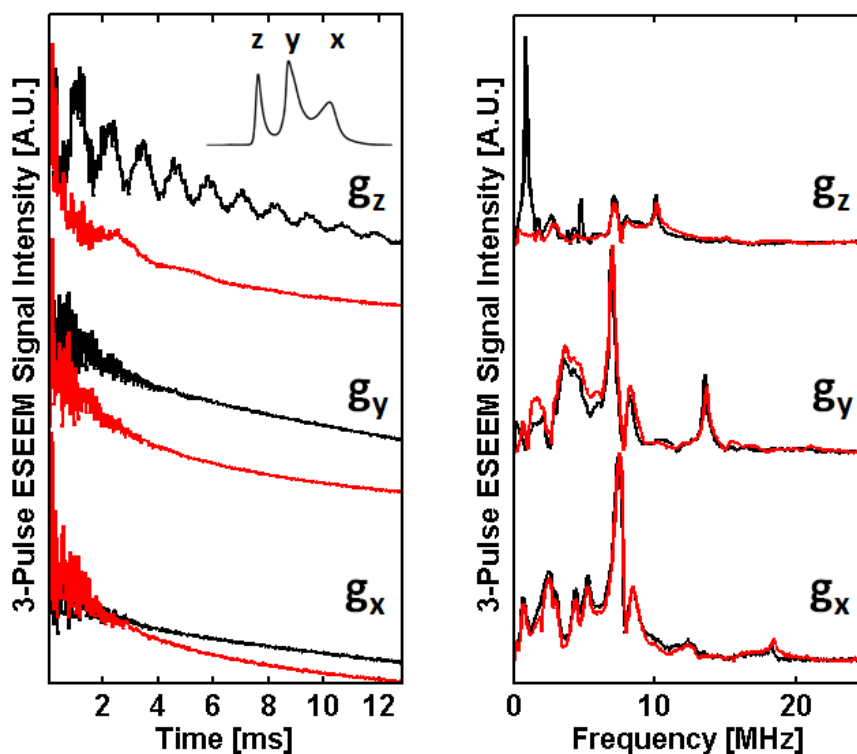


Figure 5.3.7-2, Three-Pulse ESEEM time domain (left) and frequency domain (right) spectra of pH 7.5 Mb Complexed with  $^{14}\text{N}$  and  $^{15}\text{N}$  labeled nitrite (red and black respectively) measured near canonical Positions and at 10 K. FSE insert in left panel indicates position at which at which ESEEM Experiments Were performed.

The spectra were measured at 10 K using the experimental parameters previously described. It is only at the  $g_z$ -position that a difference is observed between the two nitrogen isotopes, which again is as expected from the discussion of the heme geometry in § 5.3. Whilst the data serve to prove the contribution to the spectra from the  $^{14}\text{N}$  nucleus of the nitrite they do not show the contribution expected from the  $^{15}\text{N}$  nucleus. This may be attributed to a suppression effect found in three-pulse ESEEM and HYSCORE spectra for systems with more than one nucleus coupled to the electron spin [14]. For such systems, the ESEEM signal contains internuclear combination peaks of varying intensity. At the same time, the peaks at the basic ESEEM frequencies are reduced in intensity, up to the point of complete cancellation. For both three-pulse ESEEM and HYSCORE, the amplitude of a peak of a given nucleus depends not only on its modulation depth parameter but also those of all other nuclei. Leading to the

observation that peaks of nuclei with shallow modulations can be strongly suppressed by nuclei with deep modulations.

### 5.3.8 Simulation of Nitrite Nuclear Couplings

The data determined in the preceding section at the  $g_z$ -position was then used to determine the nuclear parameters for the  $^{14}\text{N}$  nucleus of nitrite via simulation of the time and frequency-domain spectra using EasySpin. The results of the simulation are shown below in **Figure 5.3.8-1**.

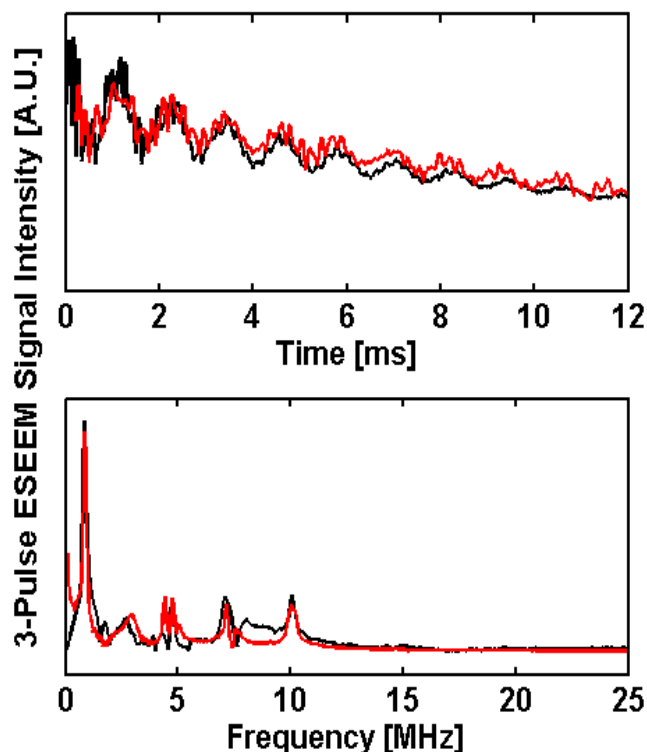


Figure 5.3.8-1, Simulation of  $\text{Mb-NO}_2^-$  three-pulse ESEEM spectrum using parameters from Table 5-4 for Heme  $^{14}\text{N}$ 's

For the time-domain it may be seen that the general periodicity of the long period oscillation corresponding to the frequency domain peak at 0.81 MHz and modulation depth correspond well to those observed experimentally. For the frequency domain the nitrite peaks are also well reproduced and the heme and histidine peaks reproduced using the values from § 5.3.4.2

weighted to fit the experimental data. The nuclear coupling parameters used for the simulation of the  $^{14}\text{N}$  of nitrite are given in **Table 5-6**.

$A_{\text{iso}}$	T	$e^2qQ/h$	$\eta$
	MHz		
1.31	1.36	0.5	0.01

**Table 5-6, Nuclear coupling parameters for  $^{14}\text{N}$  of nitrite in  $\text{Mb-NO}_2^-$  determined by simulation**

Initial insights into the value of the isotropic hyperfine coupling ( $A_{\text{iso}}$ ) came from the large modulation depth of the spectra measured at the  $g_z$ -position which resembled that expected near the cancellation condition § 5.3.3.2. At this field position (2360 G) the Larmor frequency of a  $^{14}\text{N}$  nucleus is 0.72 MHz, suggesting an  $A_{\text{iso}}$  near 1.44 MHz. It was found that the nuclear frequencies could be reproduced reasonably well using two different sets of simulation parameters with different hyperfine coupling regimes. The second discarded set of parameters [ $A_{\text{iso}} = 3.3$ ,  $T = 0.07$ ] MHz was, however, unable to reproduce the large modulation depth observed in the experimental time-domain data.

From the Pulsed Electron-Electron Double Resonance (PELDOR) [15] experiment the equation relating the dipole interaction to the distance between two electron spins is:

$$\omega_{dd}(\theta, r) = \frac{2\pi g_1 g_2}{g_e^2} (3\cos^2 \theta - 1) \frac{52.04}{r^3} [\text{MHz} / \text{nm}^3]$$

Collecting the constants in the equation leads to the following simplification for an electron-electron dipole interaction:

$$r = \sqrt[3]{\frac{52.04}{\nu_{\text{perp}} \text{MHz}}} \text{nm}$$

If the magnetic moment of a nucleus is taken to be 1000 times smaller than that of an electron, and the nuclear  $g$ -value of  $^{14}\text{N}$  to be 0.4 then the simplification may be adapted to provide an estimate of the distance between the unpaired electron and coupled nucleus from

---

the anisotropic hyperfine coupling (from a point-dipole model). This simplified relationship therefore becomes:

$$r = \sqrt[3]{\frac{0.021}{T}} \text{ (nm)}$$

Which leads to an estimated distance of 0.25 nm (2.5 Å) for the T value given in **Table 5-6** of 1.36 MHz. This compares favorably to the distance of 2.78 Å found in the crystal structure of O-bound nitrite [5], corroborating the value of the anisotropic hyperfine interaction determined from simulation. The corresponding Fe-N (nitrite) distance in the N-bound case (3HEP) [5] is 2.6 Å, however this is rather long for a Fe-ligand bond in a LS heme which are typically 1.9-2.1 Å [16] and so may be a crystallization effect. Energy optimized structures determined by computational methods to be described in Chapter 7 reduce this bond length to ~ 2 Å.

Both sets of parameters had similar quadrupole coupling values (discarded [ $e^2qQ/h = 0.3$ ,  $\eta = 0.4$ ]), which may be described as a weak quadrupole interaction for which the spectrum becomes dominated by the hyperfine interaction [10].

The complexes were then examined using the HYSORE technique to confirm the assignment of nuclear frequencies. The next section will introduce the technique before describing its application to Mb and Mb-nitrite

---

### 5.3.9 HYSCORE

#### 5.3.9.1 Introduction

The HYSCORE (Hyperfine Sublevel Correlation) Experiment was first proposed by Höffer [17] as an application of the COSY (Correlation Spectroscopy) [18] NMR experimental approach to EPR. It is often stated that the HYSCORE experiment is a version of the standard ESEEM experiment but that the shifting of the experiment in to two-dimensions increases the spectral resolution and allows correlations of nuclear frequencies between electron spins from opposite manifolds. Whilst this is indeed true, the advantages of this experiment may be said to surpass these as an indication is usually gained in the experiment from both weakly and strongly coupled nuclear interactions which normally may only be achieved by the application of both ESEEM and ENDOR separately. The standard HYSCORE pulse sequence is shown in **Figure 5.3.9-1**.



**Figure 5.3.9-1**, the standard HYSCORE pulse sequence

The experiment is essentially a three-pulse ESEEM experiment with a  $\pi$ -pulse between the second and third  $\pi/2$  pulses. The experiment consists of four periods: The time between the first two pulses, the preparation period,  $T_1$  during which time the nuclear coherence is able to freely evolve. The  $\pi$ -pulse then acts as a mixer transferring the nuclear coherence between the two opposite electron spin manifolds  $\alpha$  and  $\beta$  [19], after which the nuclear coherence again evolves in the evolution period  $T_2$  before the last pulse initiates the detection period. Fourier transform of the corrected time domain data in both dimensions then leads to a frequency domain spectrum where correlated nuclear frequency transitions are located with respect to the diagonal. Usually the frequency domain data is shown as two quadrants ((-,+) and (+,+)) with correlations in each quadrant being due to strong  $A_{iso} > 2\nu_1$  and weak  $A_{iso} < 2\nu_1$  hyperfine coupling respectively [9]. Often in experimental situations a significant proportion of the signal is found located along the diagonal, this is due to the  $\pi$ -pulse being unable to

achieve a complete inversion of the nuclear coherence for all spin packets in the system. In effect these diagonal peaks indicate the ESEEM frequencies and may in fact be useful. For small hyperfine couplings however, the diagonal and correlated peaks may near each other making interpretation of the spectrum difficult, this is especially true for disordered systems. Consequently a number of experimental techniques have been developed to try and achieve greater degrees of correlation. These techniques will be discussed later.

### 5.3.9.2 Common Features of HYSCORE Spectra

The theoretical background for the appearance of HYSCORE correlation ridges and peaks for a number of different spin situations has been discussed in detail elsewhere [20-23], however a brief discussion of the appearance of ridges under a certain number of key conditions is useful for the interpretation of experimental data and so will be discussed here.

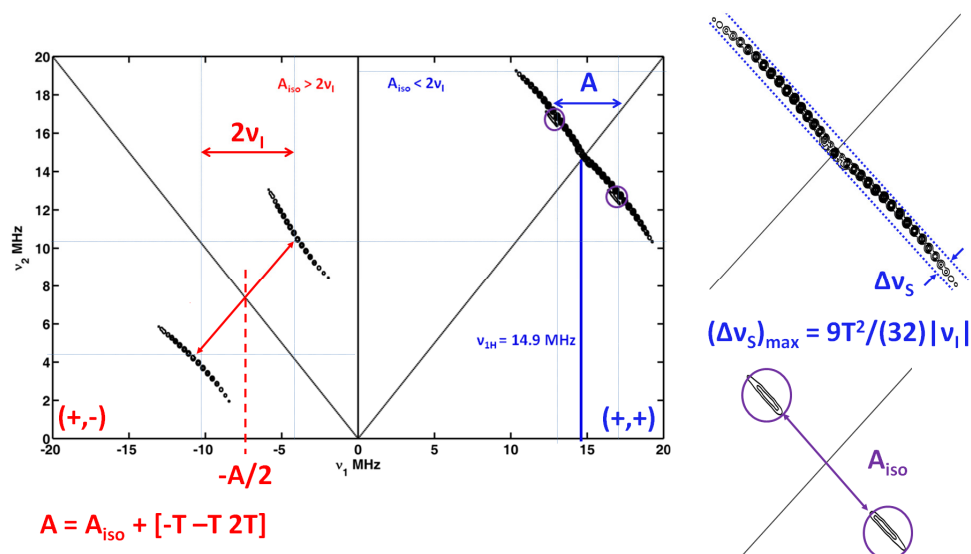


Figure 5.3.9-2, Simulation of two  $^1\text{H}$  and one  $^{13}\text{C}$  nuclei demonstrating the key interpretative aspects for a HYSCORE spectrum for the  $S = 1/2$ ,  $I = 1/2$  case. The simulation used a MW frequency of 9.8 GHz and a field position of 3456 G. The hyperfine tensors for each nucleus were:  $^{13}\text{C}$  [20 20 8],  $^1\text{H}_1$  [-1 -1 10] and  $^1\text{H}_2$  [3 3 6] (values in MHz). The contribution of the  $^{13}\text{C}$  nucleus is found in the (+,-) quadrant, whilst those of the two  $^1\text{H}$  are in the (+,+) quadrant with the contribution of  $^1\text{H}_2$  highlighted with purple circles.

A HYSCORE spectrum is normally presented as two quadrants [(+,-) (+,+)] representing the strong and weak hyperfine coupling condition respectively with the relations for strong of  $A_{\text{iso}}$

$> 2\nu_I$  and weak  $A_{iso} < 2\nu_I$  **Figure 5.3.9-2**. The interpretation of correlations in each quadrant is somewhat different however, and care must be taken to make sure these are applied correctly. These features for an  $S = 1/2, I = 1/2$  are depicted above in **Figure 5.3.9-2**

Typically in HYSCORE spectra correlated features appear either parallel or perpendicular to the diagonal in each quadrant. The first stage of interpretation of the data is to determine which type of nucleus is responsible for the observed correlation. This may be achieved by determining the  $\nu_I$  associated with it. In the (+,+) quadrant this the point on the x-axis ( $\nu_I$  MHz) at which the correlations bisect the diagonal. For the example in **Figure 5.3.9-2** the two inequivalent proton correlations are thus found centered around 14.9 MHz, the  $\nu_H$  for this field value and microwave frequency. In the (-,+) quadrant for the strongly coupled  $^{13}\text{C}$  nucleus however, the separation of the correlations with-respect-to the diagonal yields this information, such that the peaks are separated by a value of  $2\nu_I$ . In this quadrant the hyperfine coupling (A) may be determined from the position on the x-axis at which the correlations bisect the diagonal. In the (+,+) quadrant the both the isotropic ( $A_{iso}$ ) and dipolar (T) contributions to the hyperfine may, in principle be determined. In this example the (+,+) quadrant contains the contributions from two inequivalent protons  $^1\text{H}_1$  and  $^1\text{H}_2$  possessing a hyperfine coupling dominated by the dipolar and isotropic contributions to this interaction respectively. For the first case it may be seen that the dipolar coupling causes the correlation peaks to bow such that they have a width of arc proportional to T, indicated by the blue arrows on the top right insert of the figure, from the relationship:

$$(\Delta\nu_S)_{max} = 9T^2 / (32|\nu_I|)$$

For the case of a dominant isotropic interaction the correlations become separated by a value proportional to the strength of this interaction.

Whilst it is theoretically possible to determine the nuclear coupling parameters from a HYSCORE spectrum in this way it is generally impractical in disordered systems with many magnetically interacting nuclei. In this case parameters are usually obtained through accurate simulation of the data (§ 3.3.3), and comparison to previously investigated systems.

---

### 5.3.9.3 Nitrogen HYSCORE

The case of an  $S = 1/2$ ,  $I = 1/2$  system described above is however, not the case when examining heme proteins as will be the focus of this work. Nitrogen nuclei have a nuclear spin  $I = 1$  which leads to a nuclear quadrupole interaction contributing to the nuclear frequencies. This in general complicates the observed correlations in HYSCORE spectra as in ESEEM but to the extent that generally depending on the type of nucleus only double quantum (DQ) or single quantum (SQ) transitions are observed (e.g. for  $^{14}\text{N}$  and  $^2\text{H}$  nuclei respectively).

### 5.3.10 HYSCORE of LS Mb

As for the case of three-pulse ESEEM the HYSCORE technique was first applied to LS-Mb to characterize the nuclear couplings. Again a 1 mM sample of Mb at pH 10.8 was used. The HYSCORE spectra of LS Mb measured near the canonical positions (§ 5.3.4.1) and at 10 K are shown in **Figure 5.3.10-1**. A  $\tau$ -value of 120 ns was used in conjunction with 8 ns  $\pi/2$  pulses and a 14 ns  $\pi$ -pulse. The values  $T_1$  and  $T_2$  were incremented in steps of 24 ns. The time-domain spectra were baseline corrected in each dimension using a third-order polynomial then fitted with a Hamming window function and zero-filled. The real part of the two-dimensional data was then Fourier transformed and the absolute value of the data presented. By inspection certain features are immediately apparent: Each of the positions shows prominent correlations in the strong coupling quadrant suggestive of DQ transitions. The  $g_z$ -position clearly contains the DQ peaks from two inequivalent  $^{14}\text{N}$  nuclei. The spectrum taken at the  $g_y$ -position contains significant signal in both the weak and strong coupling quadrants centered along the same principal frequencies indicating a near cancellation condition situation.

---

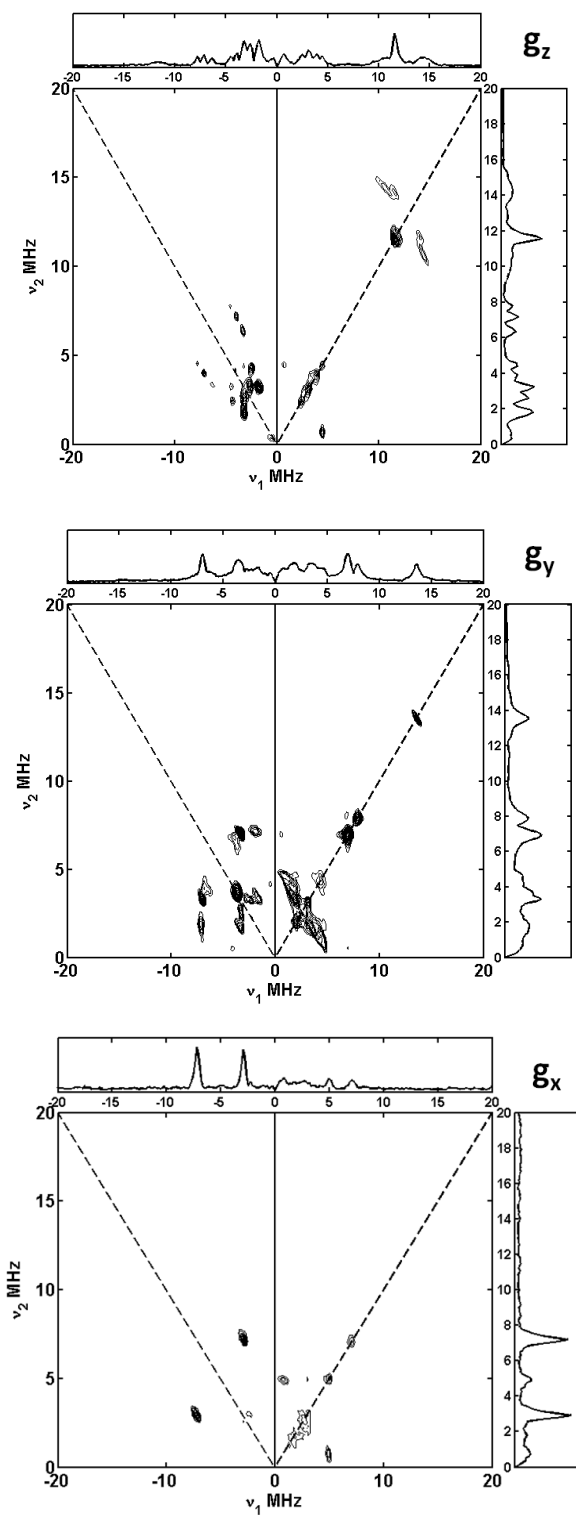
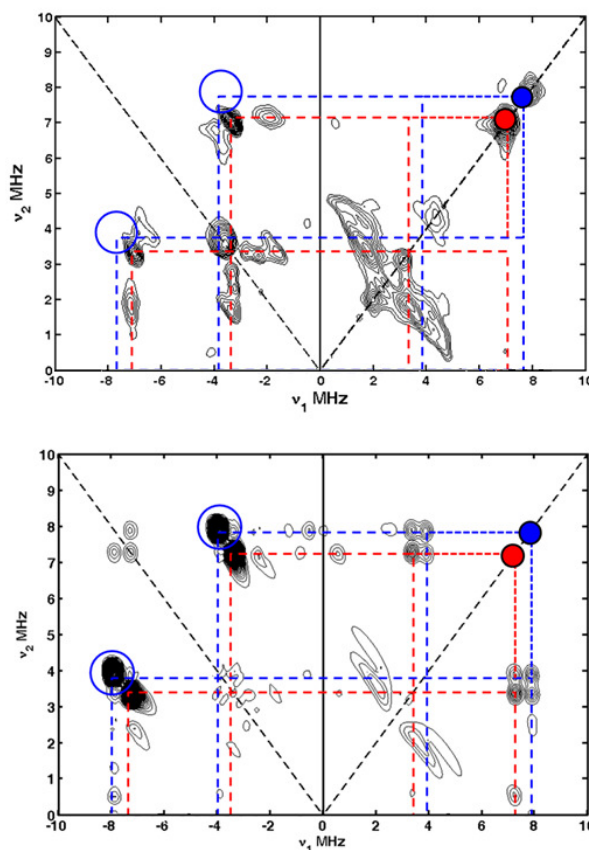


Figure 5.3.10-1, HYSCORE of LS-Mb measured at 10 K near canonical positions.  $\tau$ -value 120 ns, 8 ns  $\pi/2$ -pulse 14 ns  $\pi$ -pulse.

The HSCORE spectrum of the  $g_y$ -position was simulated using the nuclear parameters determined in § 5.3.4.2 for the  $^{14}\text{N}$  couplings from the heme and the histidine **Figure 5.3.10-2**.



**Figure 5.3.10-2, Easypin simulation (bottom) of HSCORE spectrum of LS-Mb for the  $g_y$ -position (top) Using  $^{14}\text{N}$  parameters from Table 5-4. Red and blue dashed lines indicate contributions of heme and Histidine nitrogens respectively).**

This position was chosen as it appeared to display the cancellation condition enabling a better resolution of the nuclear parameters. The simulation is able to demonstrate the contributions to the spectrum from both nitrogens. The simulation assumes a “perfect” inversion pulse able to move the correlations of the spectrum off the diagonal. In the experimental case this is not always the case and so the positions of the  $\text{DQ}_+$  and  $\text{DQ}_-$  transitions for the heme and histidine nitrogens (red and blue) are also indicated. The simulation was able to confirm the assignment of the  $\text{DQ}$  transitions previously observed in another heme protein [24]. The

contributions to the spectra measured at the other field-positions were also able to be assigned from simulation and are shown in **Figure 5.3.10-3**.

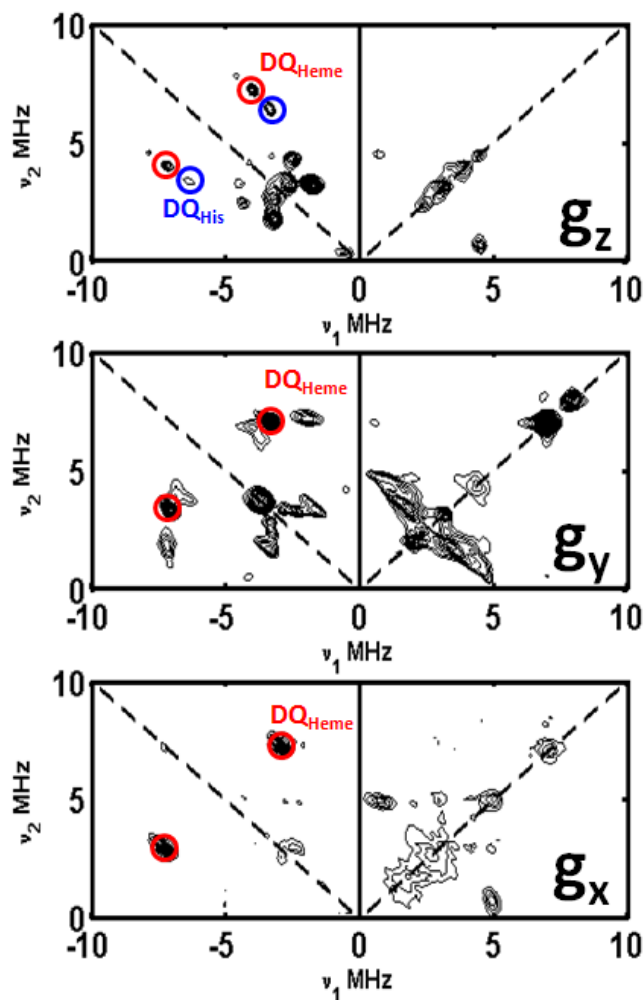
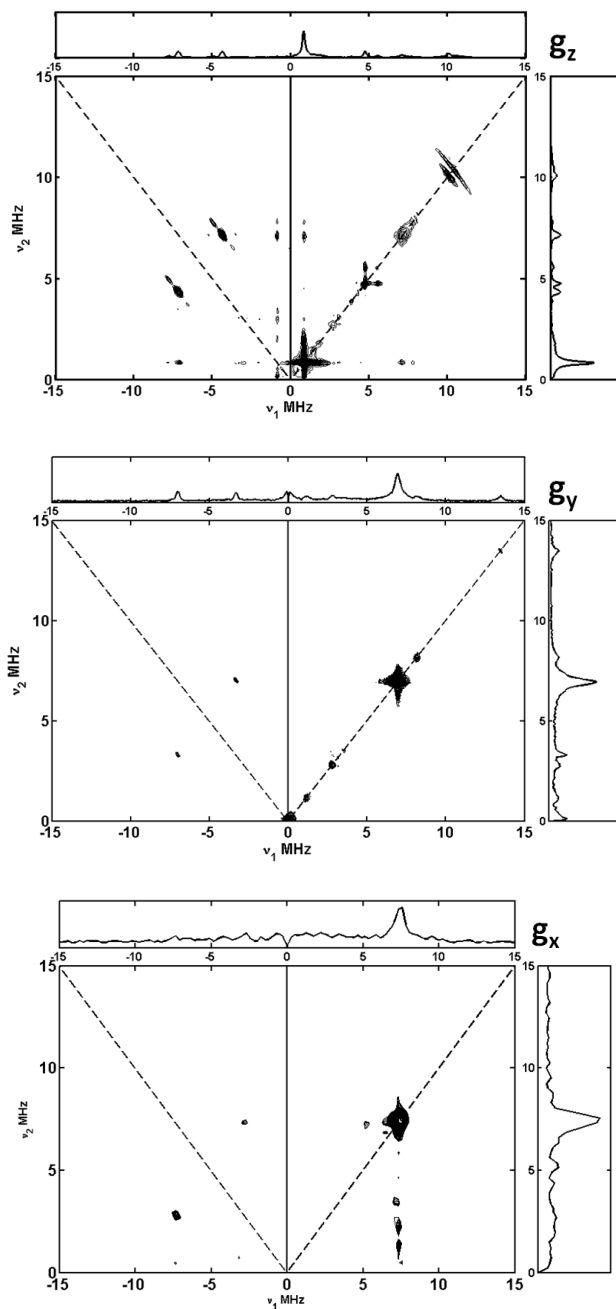


Figure 5.3.10-3, HSCORE spectra of LS-Mb near canonical positions at 10 K showing contributions from Heme and histidine  $^{14}\text{N}$  couplings.

As expected the contribution from the histidine residue is better resolved at the  $g_z$ -position corroborating the assignment from the simulation.

### 5.3.11 HYSCORE of Mb-NO<sub>2</sub><sup>-</sup>

Mb-NO<sub>2</sub><sup>-</sup> at pH 7.5 was examined using the HYSCORE technique. The spectra measured near the canonical positions and at 10 K are shown below in **Figure 5.3.11-1**.



**Figure 5.3.11-1**, HYSCORE spectra of Mb-NO<sub>2</sub><sup>-</sup> at pH 7.5 at 10 K, measured near canonical positions. T-value of 120 ns, 8 ns  $\pi/2$ -pulse and 14 ns  $\pi$ -pulse.

The remainder of the experimental parameters were as those described in § 5.3.10. The main correlations may be assigned to nuclei from the simulation of the LS-Mb HYSCORE spectra outlined in the preceding section. An overview of this assignment is shown in **Figure 5.3.11-2**.

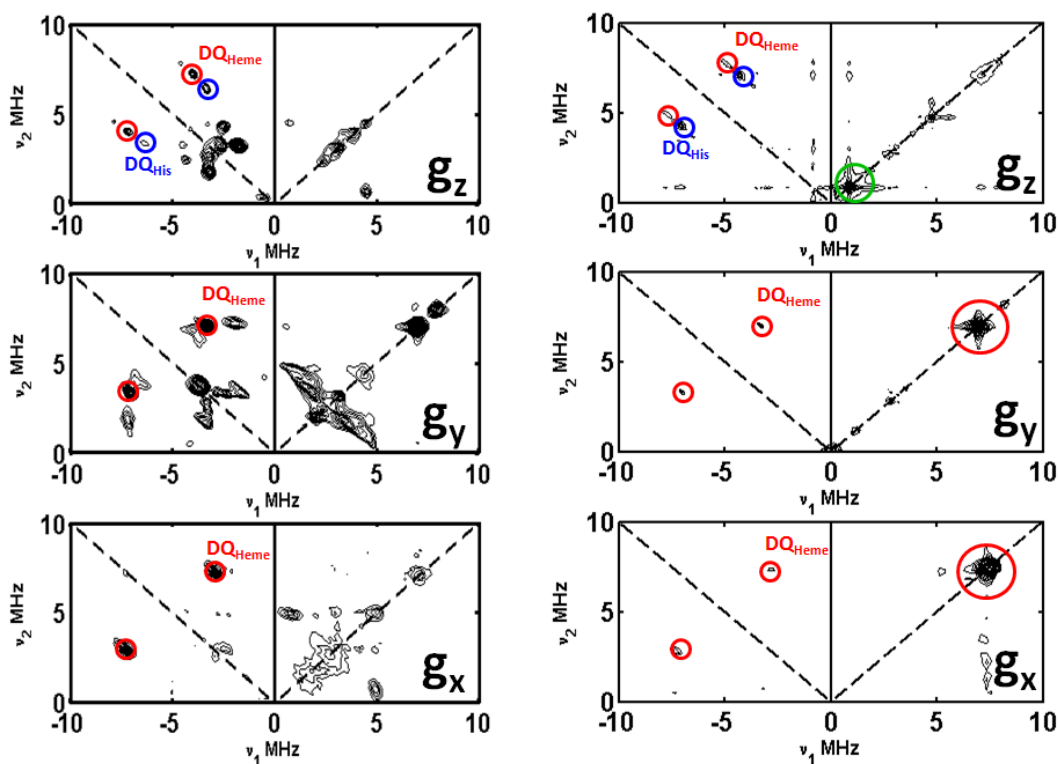


**Figure 5.3.11-2**, HYSCORE spectra of LS-Mb (left) and Mb-NO<sub>2</sub><sup>-</sup> (right) near canonical positions at 10 K showing contributions from heme and histidine <sup>14</sup>N couplings (red and blue circles). The correlation attributed to the <sup>14</sup>N of nitrite is highlighted with a green circle.

As in the ESEEM experiment the contribution to the spectrum from the nitrite coupling is only apparent at the  $g_z$ -position (highlighted by a green circle) appearing at 0.81 MHz. The histidine and heme correlations are also visible at this field-value. At the  $g_y$  and  $g_x$ -positions the correlations may be wholly attributed to the heme nitrogen coupling. It may also be seen that the correlations appear in both quadrants again suggesting a near cancellation condition. The data support the assignment from the ESEEM data, and allow the correlations associated with different <sup>14</sup>N nuclei to be more readily resolved. Overall the HYSCORE data reinforce the assignment of the LS Mb-nitrite signal to the *O*-bound case. The appearance of the nitrogen

couplings associated with the addition of nitrite measured at the  $g_z$ -position always appearing in the (+,+) weak coupling quadrant suggests a nitrogen not directly coordinated to the heme iron.

---

---

## References

1. Stoll, S. and A. Schweiger, *EasySpin, a comprehensive software package for spectral simulation and analysis in EPR*. Journal of Magnetic Resonance, 2006. **178**(1): p. 42-55.
  2. Nasri, H., et al., *Sharing the pi-bonding. An iron porphyrin derivative with trans,pi-accepting axial ligands. Synthesis, EPR and Mossbauer spectra, and molecular structure of two forms of the complex nitronitrosyl(alpha,alpha,alpha,alpha-tetrakis(o-pivalamidophenyl)porphyrinato)ferrate(II)*. Journal of the American Chemical Society, 1997. **119**(27): p. 6274-6283.
  3. Einsle, O., et al., *Mechanism of the six-electron reduction of nitrite to ammonia by cytochrome c nitrite reductase*. Journal of the American Chemical Society, 2002. **124**(39): p. 11737-11745.
  4. Lin, J., et al., *Metmyoglobin/Azide: The Effect of Heme-Linked Ionizations on the Rate of Complex Formation*. Archives of Biochemistry and Biophysics, 1999. **362**(1): p. 148-158.
  5. Yi, J., et al., *The Distal Pocket Histidine Residue in Horse Heart Myoglobin Directs the O-Binding Mode of Nitrite to the Heme Iron*. Journal of the American Chemical Society, 2009. **131**(50): p. 18119-18128.
  6. Bashford, D., et al., *Electrostatic calculations of side-chain pKa values in myoglobin and comparison with NMR data for histidines*. Biochemistry, 1993. **32**(31): p. 8045-8056.
  7. Hahn, E.L. and D.E. Maxwell, *Spin Echo Measurements of Nuclear Spin Coupling in Molecules*. Physical Review, 1952. **88**(5): p. 1070.
  8. Walker, F.A., *Magnetic spectroscopic (EPR, ESEEM, Mossbauer, MCD and NMR) studies of low-spin ferriheme centers and their corresponding heme proteins*. Coordination Chemistry Reviews, 1999. **185-186**: p. 471-534.
  9. Deligiannakis, Y., M. Louloudi, and N. Hadjiliadis, *Electron spin echo envelope modulation (ESEEM) spectroscopy as a tool to investigate the coordination environment of metal centers*. Coordination Chemistry Reviews, 2000. **204**(1): p. 1-112.
  10. Flanagan, H.L. and D.J. Singel, *Analysis of <sup>14</sup>N ESEEM patterns of randomly oriented solids*. Journal of Chemical Physics, 1987. **87**(10): p. 5606.
  11. Fittipaldi, M., et al., *A multi-frequency pulse EPR and ENDOR approach to study strongly coupled nuclei in frozen solutions of high-spin ferric heme proteins*. Journal of Physical Chemistry B, 2008. **112**(12): p. 3859-3870.
-

- 
12. Magliozzo, R.S. and J. Peisach, *Electron spin echo envelope modulation spectroscopic study of iron-nitrogen interactions in myoglobin hydroxide and iron(III) tetraphenylporphyrin models*. *Biochemistry*, 1992. **31**(1): p. 189-199.
  13. Magliozzo, R.S. and J. Peisach, *Evaluation of nitrogen nuclear hyperfine and quadrupole coupling parameters for the proximal imidazole in myoglobin-azide, -cyanide, and -mercaptoethanol complexes by electron spin echo envelope modulation spectroscopy*. *Biochemistry*, 1993. **32**(33): p. 8446-8456.
  14. Stoll, S., et al., *Peak suppression in ESEEM spectra of multinuclear spin systems*. *Journal of Magnetic Resonance*, 2005. **177**(1): p. 93-101.
  15. Schiemann, O. and T.F. Prisner, *Long-range distance determinations in biomacromolecules by EPR spectroscopy*. *Quarterly Reviews of Biophysics*, 2007. **40**(01): p. 1-53.
  16. Scheidt, W.R. and C.A. Reed, *Spin-state/stereochemical relationships in iron porphyrins: implications for the hemoproteins*. *Chemical Reviews*, 1981. **81**(6): p. 543-555.
  17. Hofer, P., et al., *Hyperfine Sublevel Correlation (HYSCORE) Spectroscopy - A 2D Electron-Spin-Resonance Investigation of the Squaric Acid Radical*. *Chemical Physics Letters*, 1986. **132**(3): p. 279-282.
  18. Bernstein, M.A., L.D. Hall, and S. Sukumar, *Assignment of Proton NMR-Spectra of Carbohydrates, Using Two-Dimensional Techniques - COSY AND SECSY*. *Carbohydrate Research*, 1982. **103**(1): p. C1-C16.
  19. Ponti, A. and A. Schweiger, *Nuclear coherence-transfer echoes in pulsed EPR*. *The Journal of Chemical Physics*, 1995. **102**(13): p. 5207-5219.
  20. Dikanov, S.A., et al., *Two-dimensional ESEEM spectroscopy of nitrogen hyperfine couplings in methemerythrin and azidomethemerythrin*. *Journal of the American Chemical Society*, 1998. **120**(27): p. 6797-6805.
  21. Dikanov, S.A., et al., *Orientationally-Selected Two-Dimensional ESEEM Spectroscopy of the Rieske-Type Iron-Sulfur Cluster in 2,4,5-Trichlorophenoxyacetate Monooxygenase from Burkholderia cepacia AC1100*. *J. Am. Chem. Soc.*, 1996. **118**(35): p. 8408-8416.
  22. Poppl, A. and L. Kevan, *A practical strategy for determination of proton hyperfine interaction parameters in paramagnetic transition metal ion complexes by two-dimensional HYSCORE electron spin resonance spectroscopy in disordered systems*. *Journal of Physical Chemistry*, 1996. **100**(9): p. 3387-3394.
  23. Astashkin, A.V. and A.M. Raitsimring, *Properties of the HYSCORE Spin Echo Signal*. *Journal of Magnetic Resonance*, 2001. **148**(2): p. 379-387.
-

24. Garcia-Rubio, I., et al., *HSCORE Spectroscopy in the Cytochrome b559 of the Photosystem II Reaction Center*. *Journal of the American Chemical Society*, 2003. **125**(51): p. 15846-15854.
-

---

---

## 6 CHAPTER Further Elucidations for Myoglobin

---

### 6.1 Introduction

Whilst the experiments outlined in the previous chapter sought to answer the specific question of the nitrite binding mode those in this section provide an insight to the broader activity of myoglobin (Mb) and Mb-NO<sub>2</sub><sup>-</sup> or an example of the application of other EPR spectroscopic methods.

### 6.2 Myoglobin at a low pH

It may be seen by the reader that although the initial pH range of this investigation was stated as being from pH 5.0 to pH 10.8 the actual lower limit of EPR experiments discussed was pH 6.5. It was also mentioned earlier in Chapter 4 that the case of low-pH Mb would be discussed separately. The Continuous-Wave (CW) Electron Paramagnetic Resonance (EPR) spectrum of Mb-NO<sub>2</sub><sup>-</sup> at this pH invariably showed that the nitrite had reduced rapidly to nitric oxide (NO). It was observed that when such a sample was left unfrozen overnight the colour of the solution would go from a red/brown normal for low-spin (LS) Mb, to a greenish solution. It was found that the transition between the two solutions was reversible and that the green solution could be returned to its original colour by increasing the pH (in this case adding concentrated NaOH). It is known that in Mb binding of NO and the lowering of the solution pH work together to weaken the bond between the heme iron and proximal histidine, leading ultimately to a rupturing of the bond [1]. This is due to the NO exerting a repulsive trans effect on the proximal histidine [2]. This transition may be observed spectrally using both EPR and optical spectroscopy. In EPR the shift in coordination is demonstrated by a change from a nine line signal for the six-coordinate system to a three line signal for the five-coordinate system. In the optical spectra a shift from 420 to 388 nm is also observed for the same transition.

---

Figure 6.2-1 shows these spectral changes as well as schemes for both coordination environments.

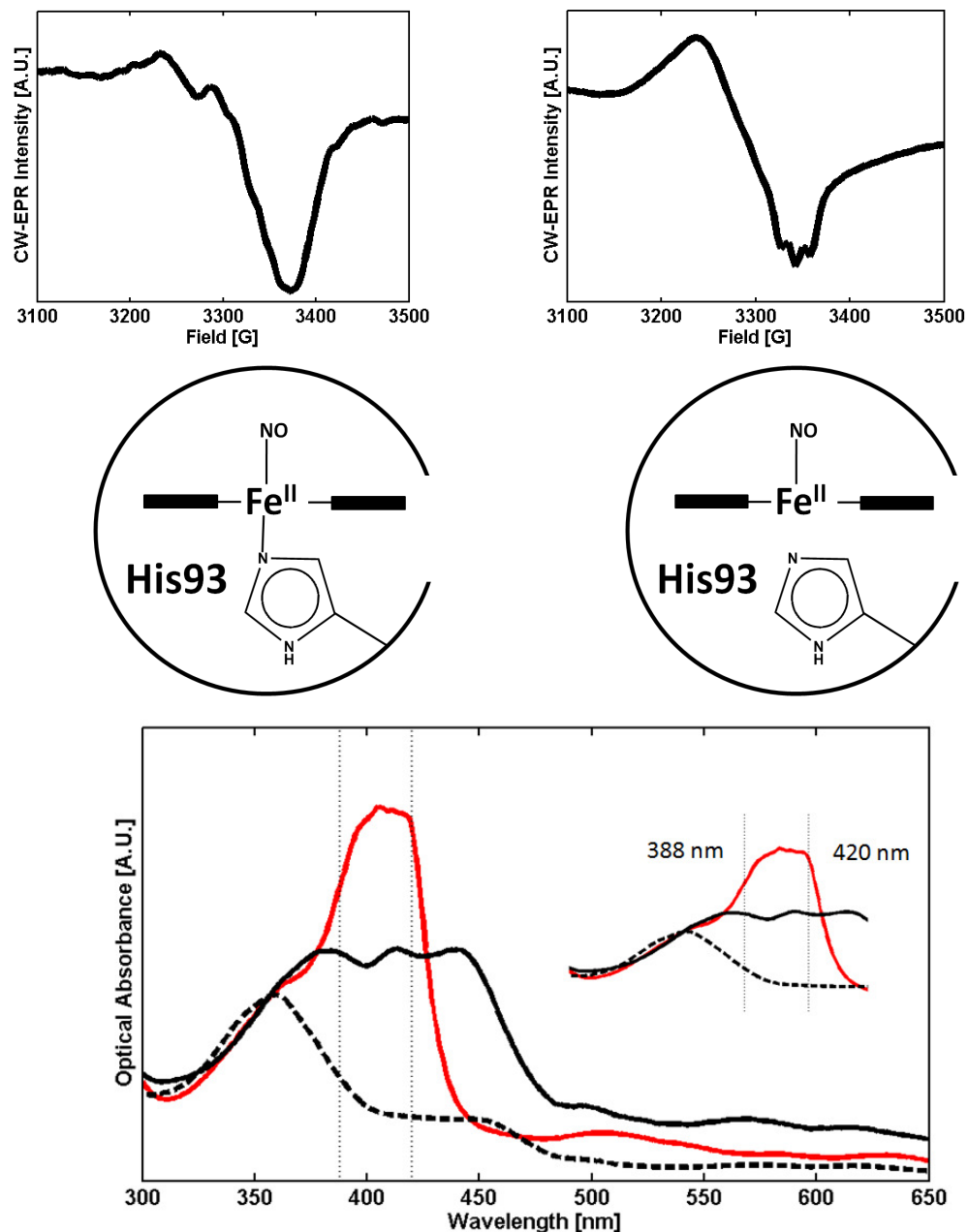


Figure 6.2-1, Spectral changes observed for Mb-NO in five and six coordinate environments. Top: EPR spectra at 20K of six coordinate environment with characteristic nine line (weak) signal (left) And the five coordinate environment with a three line signal (right). The corresponding coordination scheme is shown immediately below each EPR spectrum. The bottom panel shows the optical spectra of six coordinate “red” Mb (red-line) as the pH is lowered in the presence of nitrite. The solid black line shows the five coordinate “green” Mb solution. The spectral shift from around 420 to 388 nm can be observed.

The EPR spectra were measured at 20 K using a microwave (mw) power of 5 mW a modulation frequency of 100 KHz and a modulation amplitude of 1 G. 1 mM protein solutions were used with 240-fold excess of nitrite in the form of aqueous sodium nitrite. The six-coordinate ferrous system was obtained by reducing this solution with dithiothreitol (DTT) to a two-fold molar excess. The EPR spectrum of the five coordinate system was measured at pH 5.5. The optical spectra were measured using 25  $\mu$ M solutions. In the literature it is stated that although the reaction is reversible the transition is cooperative and involves six protons for pH lowering but only two as the pH is raised. The pK is stated as being 4.7 [1].

### 6.3 Multi-frequency continuous-Wave EPR

Performing EPR experiments at more than one mw frequency may aid in the resolution of *g*-values due to the magnetic field dependence on the Zeeman Effect (§ 1.2.1). A previous EPR study on nitrite binding to methemoglobin revealed signals consistent with two low-spin species, with *g*-values of [3.018 2.122 1.45] and [2.870 2.304 1.45] [3]. This study utilized CW-EPR at S and X-band frequencies ( $\sim$  4 and 9.2 GHz respectively) as well a range of pH's to assert that the signals were consistent with two-forms of *N*-bound nitrite. To determine whether this was also the case for Mb experiments on a series of Mb and Mb-NO<sub>2</sub><sup>-</sup> samples were carried out on an S and Q-band ( $\sim$  34GHz) CW EPR spectrometer assembled by the author using components from Bruker E200 and E300 EPR spectrometers and run by software also written by the author using the fsc2 spectrometer control program developed by Jens Törring currently at the FU Berlin. Bruker S and Q-band resonators and mw bridges were also used. The EPR spectra of Mb at pH 10.8 and Mb-NO<sub>2</sub><sup>-</sup> at pH 10.8 and 7.5 measured at S and Q-band is shown in **Figure 6.3-1**, along with the corresponding X-band data discussed in Chapter 4 for comparison. For the S-band situation 2 mM samples were used with nitrite as before in 240-fold excess. The spectra were measured at a frequency of 4.02 GHz, 10 mW power a modulation frequency of 100 KHz and a modulation amplitude of 5 G. For Q-band the spectra were measured at 40 K also using 2 mM samples. The spectra were measured at a frequency of 34.03 GHz, 1 mW power a modulation frequency of 12.5 KHz and a modulation amplitude of 5 G. In the spectra from the methemoglobin study the presence of the two species was particularly visible by a splitting in the *g*<sub>z</sub>-peak.

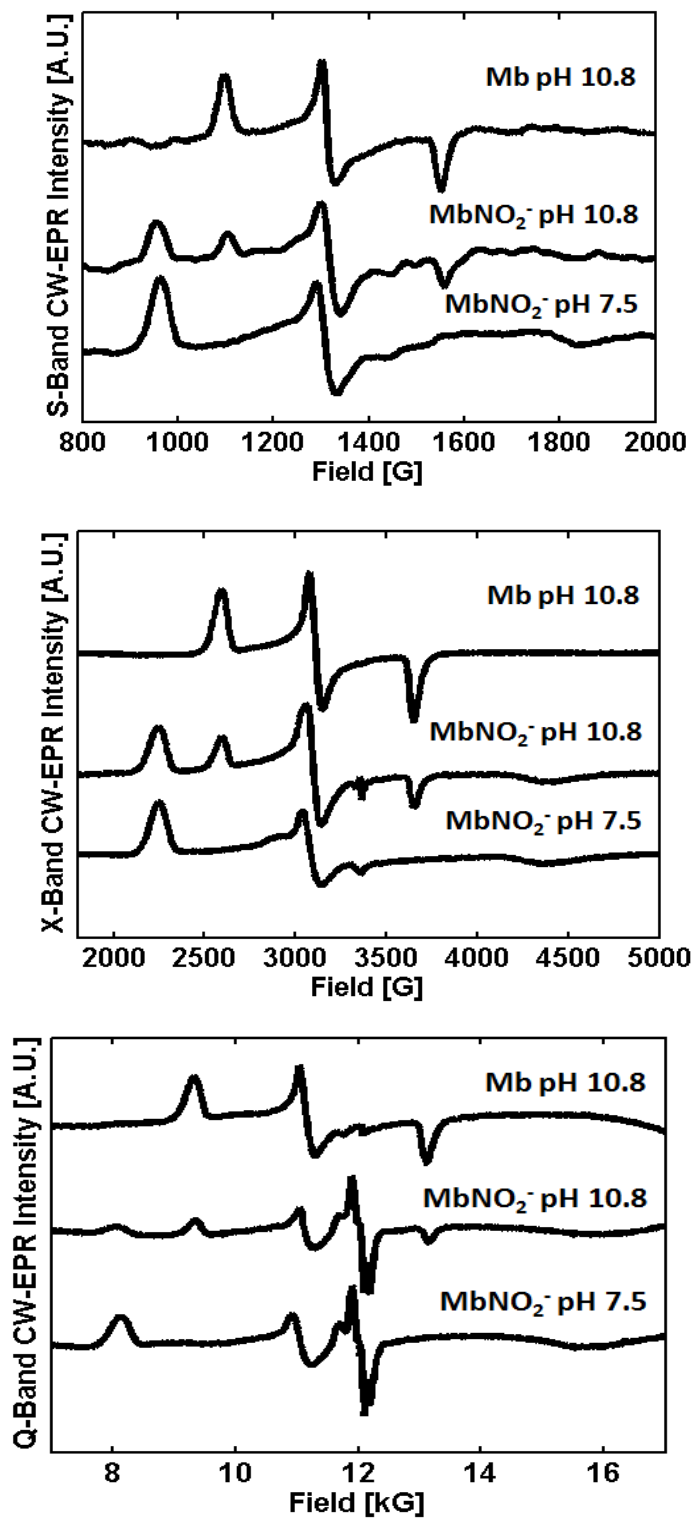


Figure 6.3-1, EPR spectra of Mb and Mb-NO<sub>2</sub><sup>-</sup> complexes measured at S, X and Q-band frequencies (top, middle and bottom panels respectively). S and X-band measured at 20 K and Q-band at 40 K.

It may be seen in the figure that no such splitting is observed at this position at any of the three mw frequencies used. It seems likely therefore, that the two sets of  $g$ -values correspond to slightly different nitrite ligation geometries in the two subunits of hemoglobin (further discussed in § 8.1.1). The three sets of data presented above may be seen to be consistent with each other and demonstrate the same spectral features seen previously at X-band. The Q-band spectra of Mb in the presence of nitrite also show additional features around the  $g = 2$  position that may be attributed the presence and resolution of Mb-NO. The Q-band Mb spectrum also displays a high-field baseline artifact which may be ignored.

## 6.4 Matched-Pulse HYSCORE of Low-Spin Myoglobin-Nitrite

### 6.4.1 Matched HYSCORE

Several techniques have been developed to obtain more information from the standard HYSCORE (Hyperfine Sublevel Correlation) experiment. One of these methods termed matched-HYSCORE [4] incorporates matched pulses [5] into the HYSCORE sequence. A matched also known as a high-turning angle (HTA) pulse increases the efficiency of the forbidden transfers within the experiment in order to achieve larger signal intensities in both ESEEM (Electron Spin-Echo Envelope Modulation) and HYSCORE experiments. The pulse sequence for a typical matched-HYSCORE experiment is shown in **Figure 6.4.1-1**.



**Figure 6.4.1-1, Pulse Sequence used for matched-HYSCORE experiments. For the pulse sequence shown the first transfer is an allowed transition, as is the detected transition. HTA indicates High Turning Angle.**

The application of matched pulses to the HYSCORE experiment has been shown to increase the signal-to-noise ratio for strongly coupled nitrogens significantly. The sequence has also facilitated the application of the HYSCORE technique to  $S > 1/2$  systems [6]. The matched HYSCORE spectra of Mb- $^{15}\text{NO}_2^-$  at pH 7.5 measured at the  $g_z$ -position at 10 K using a range of matched-pulse lengths is shown in **Figure 6.4.1-2**.

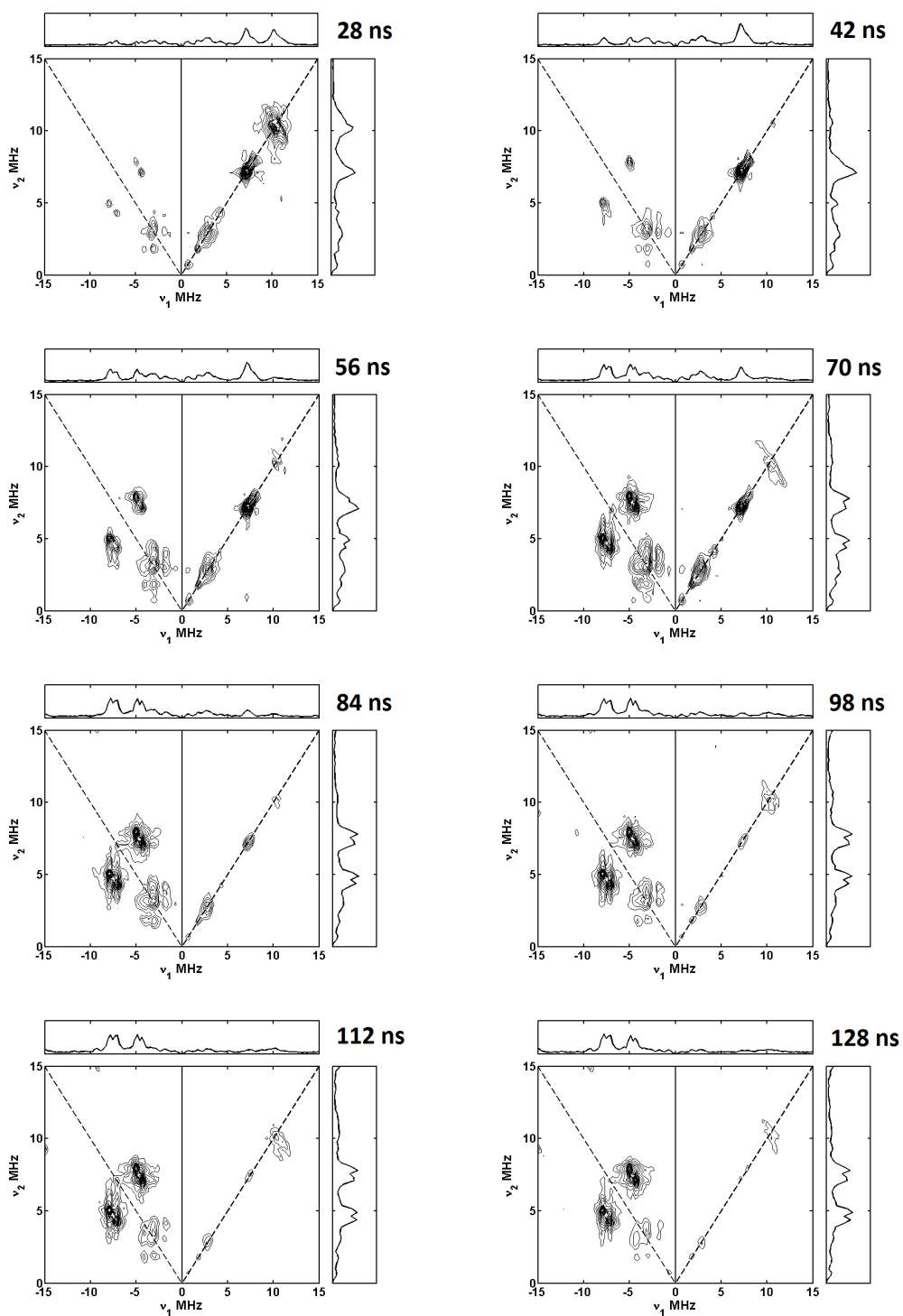
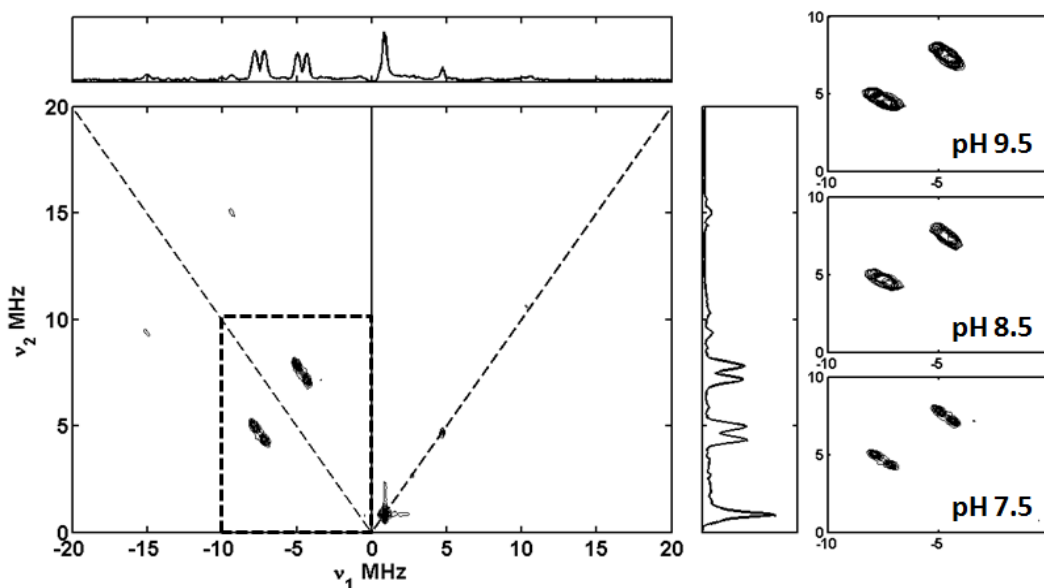


Figure 6.4.1-2, Matched-HYSCORE frequency-domain spectra of Mb-<sup>15</sup>NO<sub>2</sub><sup>-</sup> at pH 7.5 measured at 10 K And at the g<sub>z</sub>-position. 12 ns  $\pi/2$ -pulse, 120 ns  $\tau$ -value. Matched pulse length indicated in top-right of Each Spectrum.

12 ns  $\pi/2$ -pulses and a  $\tau$ -value of 120 ns were used. It may be seen that the contribution to the spectra from the double-quantum (DQ) transitions of the heme and histidine  $^{14}\text{N}$ s as well as the proton contribution is significantly dependant on the length of the matched-pulse chosen for the experiment. As a technical note: the bracketed pulse channels of the E680 spectrometer were used for the matched-pulses as they allowed the power of these pulses to be altered independently. Maximum spectrometer power for these pulses was used in all experiments. It was also necessary to ensure that the two bracketed channels (positive and negative) were orthogonal to each other. **Figure 6.4.1-3** shows the full matched-pulse HYSORE spectrum of Mb-NO<sub>2</sub><sup>-</sup> at pH 7.5 and the heme and histidine DQ transition region of the same complex at pH values 9.5, 8.5 and 7.5. Spectra were measured at 10 K using a matched pulse length of 128 ns,  $\pi/2$  pulse lengths of 8 ns and  $\pi$ -pulse length 14 ns. A  $\tau$ -value of 120 ns was used.



**Figure 6.4.1-3, Matched-pulse HYSORE of the  $g_z$ -position of Mb-NO<sub>2</sub><sup>-</sup> at pH 7.5 (full spectrum) and The DQ region of Mb-NO<sub>2</sub><sup>-</sup> at pH 9.5, 8.5 and 7.5. spectra measured at 10 K with a 128 ns Matched-pulse length.**

This matched-pulse length clearly enhances the contribution to the spectra from  $^{14}\text{N}$  nuclei. The DQ-transitions shown in the inserts show more defined correlations between the heme and histidine contributions as the pH is lowered. This suggests the nitrite being bound in a more rigid conformation from high to low pH as would be the case if hydrogen bonding were

involved. This further supports the case that the low-spin nitrite bound form is indeed the *O*-bound form from the findings of the Mb mutant study by Richter-Addo and coworkers that this form is directed by H-bonding [7]. Additional correlations in the strong-coupling quadrant may be attributed to natural abundance  $^{13}\text{C}$  contributions.

### 6.4.2 DONUT-HYSCORE

Whereas the standard HYSCORE and matched-HYSCORE experiments obtain correlations between opposite electron spin manifolds the DONUT (Double Nuclear Transfer) HYSCORE experiment was designed to detect the correlations between the same spin manifold [8]. The DONUT-HYSCORE pulse sequence is shown in **Figure 6.4.2-1**.

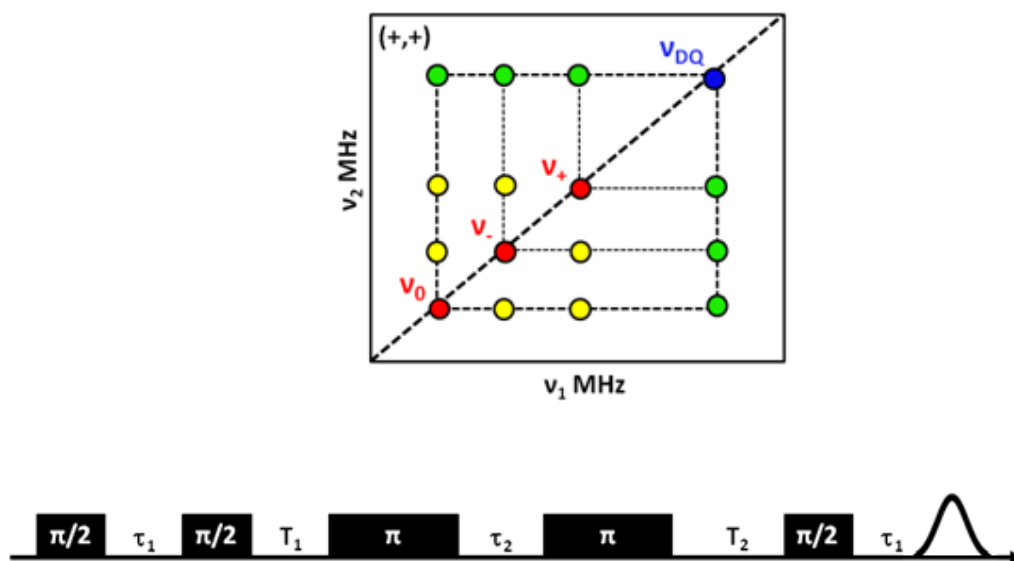


**Figure 6.4.2-1**, DONUT-HYSCORE pulse sequence (bottom-panel) and comparison of correlation features Between: HYSCORE (green) and DONUT-HYSCORE (yellow) correlation patterns in the (+,+) quadrant. The diagonal features are the associated ESEEM frequencies (top-panel).

The experiment is complimentary to the standard and matched HYSCORE experiments and is useful in obtaining a full set of nuclear parameters for the case  $I = 1$  as in that for the  $^{14}\text{N}$  nucleus. **Figure 6.4.2-1** also demonstrates the pattern of correlation features that would be seen in the standard HYSCORE and DONUT-HYSCORE experiments in the weak coupling quadrant of the experiments. It may be expected that the additional pulse in the DONUT-

HYSCORE experiment would lead to lower signal-to-noise level spectra, in practice however, the quality of spectra measured for both experiments may be expected to be comparable [8].

**Figure 6.4.2-2** shows the HYSCORE and DONUT-HYSCORE spectra of Mb- $^{15}\text{NO}_2^-$  at pH 7.5 measured at 10 K and at the  $g_z$ -position. 8 ns  $\pi/2$ -pulses, 12 ns  $\pi$ -pulses and a  $\tau$ -value of 120 ns were used. For the DONUT experiment a  $\tau_2$ -value of 800 ns was chosen. Matched-pulse versions of these experiments are also shown in which case matched-pulse lengths of 128 ns were used. For matched-pulse DONUT-HYSCORE the second and third  $\pi/2$ -pulses were replaced with matched-pulses.

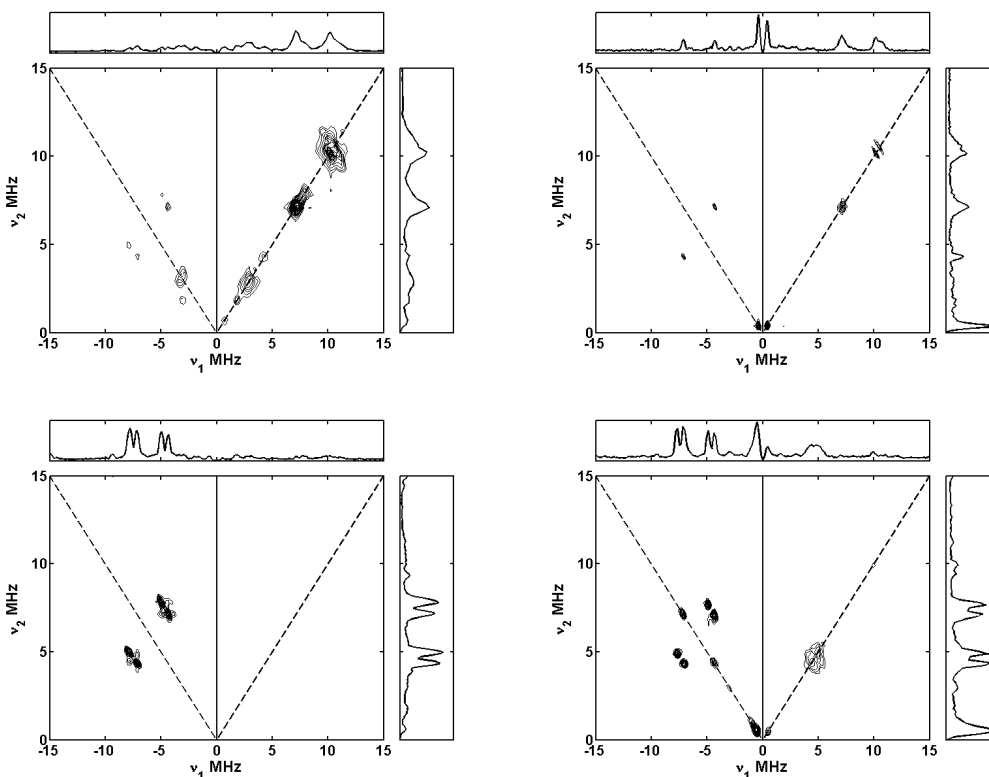


**Figure 6.4.2-2, Comparison of HYSCORE (left) and DONUT-HYSCORE (right) Spectra of Mb- $^{15}\text{NO}_2^-$  at pH 7.5 and 10 K. Top panels show standard experiments and bottom panels matched experiments.**

In terms of the contribution to the spectra from  $^{14}\text{N}$  couplings the HYSCORE experiments both standard and matched display contributions from the DQ transitions, with the matched-pulse experiment enhancing this contribution. The DONUT-HYSCORE spectra reveal an additional contribution attributable to the  $^{15}\text{N}$  of nitrite which was previously unseen in both three-

pulse ESEEM and HYSCORE experiments due to a peak-suppression effect [9], a hitherto unreported benefit of the experiment.

## 6.5 Two-Dimensional Three-Pulse ESEEM

A method for attributing the peaks in a three-pulse ESEEM to specific types of nuclear interaction is a two-dimensional three-pulse ESEEM experiment in which a three-pulse ESEEM experiment with a fixed  $\tau$ -value comprises one dimension and the magnetic field-value comprises the second. This experiment is particularly useful in a disordered,  $I = 1$  case [10] as is found for frozen samples of Mb and Mb-nitrite. The frequency-domain spectrum of this experiment applied to Mb-NO<sub>2</sub><sup>-</sup> at pH 7.5 and measured at 10 K is shown in **Figure 6.5-1**.

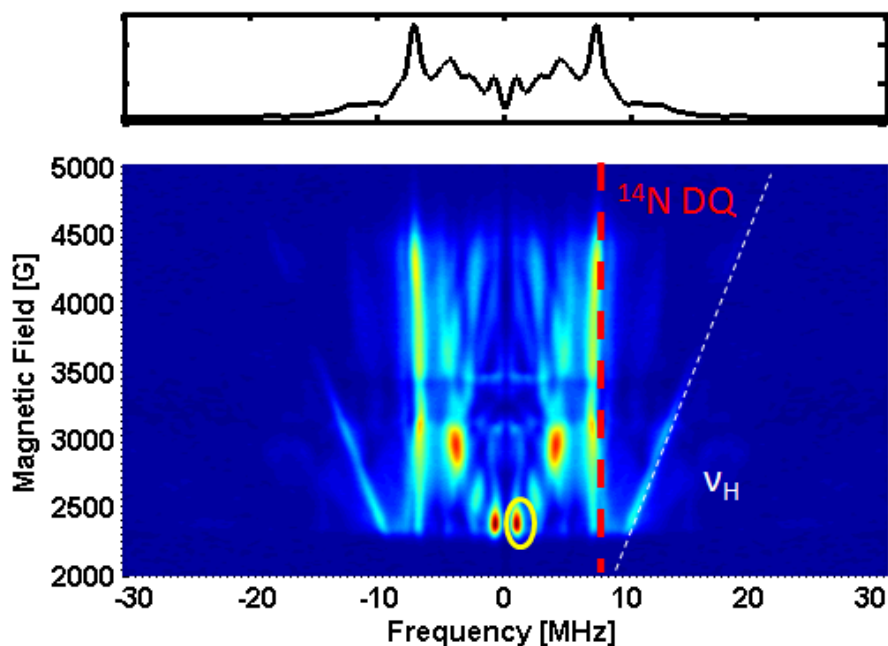
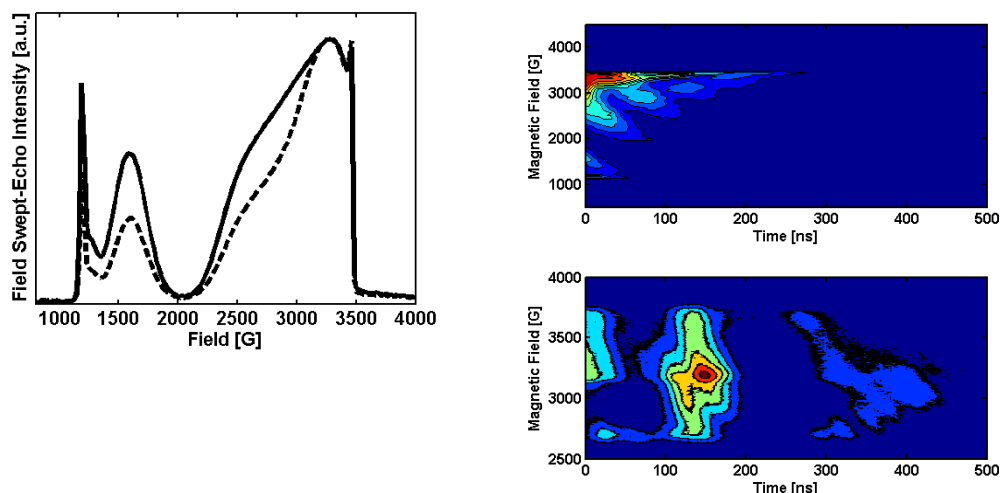


Figure 6.5-1, Two-dimensional three-pulse ESEEM spectra of Mb-NO<sub>2</sub><sup>-</sup> at pH 7.5 measured at 10 K.

$\pi/2$ -pulse lengths of 8ns and a  $\tau$ -value of 120 ns were used with field steps of 5 G. In this spectrum the contribution from an  $I=1/2$  <sup>1</sup>H nucleus may be observed as a straight line at the proton Larmor frequency. As this frequency is field-dependant it may be readily seen to diverge linearly with the field-position. The DQ transitions of the <sup>14</sup>N nuclei dominate the spectrum due to their lack of orientation dependence, and will display a near constant frequency in the spectrum.

## 6.6 High-Spin Myoglobin

A 2 mM Mb sample at pH 6.3 was used to investigate the high-spin HS state of Mb. **Figure 6.6-1** shows the field-swept echo (FSE) spectrum of this sample measured at 4 and 3.5 K (left). a  $\tau$ -value of 160 ns,  $\pi/2$ -pulse of 16 ns and a  $\pi$ -pulse of 32 ns were used. Low microwave (mw) power (0.2  $\mu$ W c.f. 0.6 mW for LS experiments) was also used.



**Figure 6.6-1, Left:** Field-swept echo spectrum of high-spin Mb (pH 6.3) measured at 4 K (dashed line) and 3.5 K (Solid-line). T-value 160 ns,  $\pi/2$ -pulse 16 ns and  $\pi$ -pulse 32 ns. **Right:** two-dimensional FSE spectra of HS (top) and LS (bottom) Mb.

The spectrum is comparable to one of the few examples of a FSE from a HS heme protein [6], specifically Mb. In order to measure the spectrum extremely low temperatures are necessary (4 K). The spectrum was also found to be particularly sensitive to the mw power and  $\tau$ -value (more so than in the LS case). The right colour-figures show a two dimensional FSE experiment with the magnetic-field position comprising the y-axis. The top panel shows the spectrum resulting from HS Mb and the bottom from LS Mb. These spectra depict a measure of the T2 time and therefore phase-memory time for each sample. It is clear from these spectra that for HS Mb the phase memory time for field positions away from the  $g = 2$  position are short which hinders the measurement pulsed-EPR spectra. For HS Mb the FSE is generally axial with the  $g = 6$  position corresponding to the effective perpendicular  $g$ -values  $g_x^{\text{eff}}$  and  $g_y^{\text{eff}}$ , whilst  $g = 2$  corresponds to the effective parallel position  $g_z^{\text{eff}}$  [6].

It is known that the low-field region of the CW-EPR spectrum of a HS heme may be used as a conformation probe of the heme environment [11]. The characteristics of this region may be used to determine the symmetry of the heme. Constraints upon the heme within a protein may cause a departure from a tetragonal to a rhombic EPR spectrum in which the CW derivative in the low-field region is broadened and may contain to resolvable g-values. This effect will be more pronounced when the constraint upon the heme is large. **Figure 6.6-2** contains a series of panels focusing on the low-field peak of several HS Mb and Mb-nitrite samples.

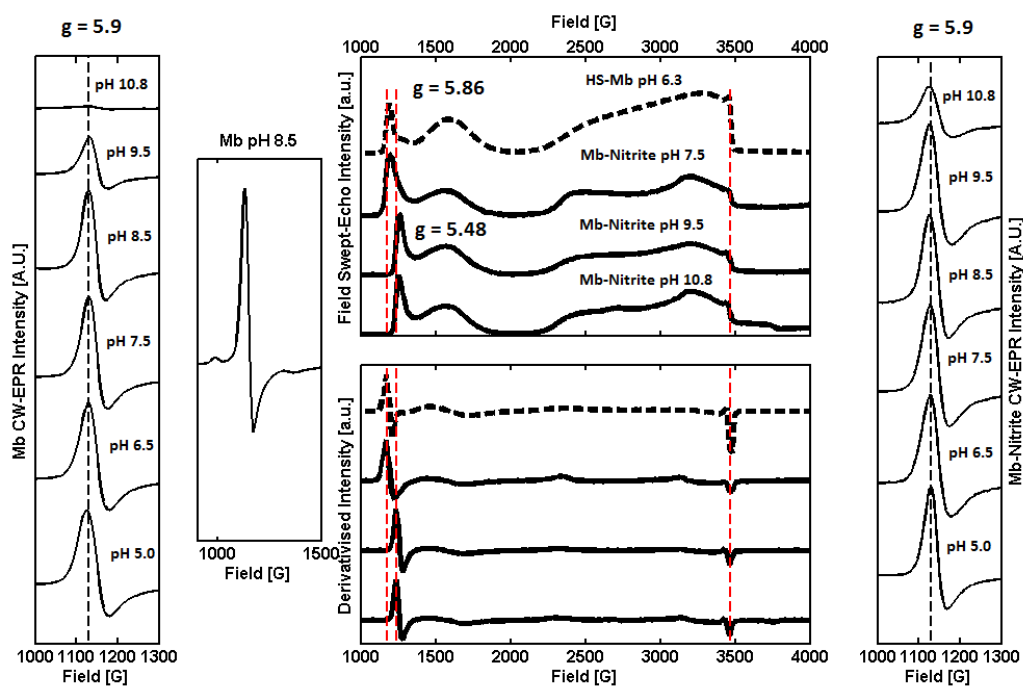


**Figure 6.6-2, Examination of the low-field ( $g \sim 6$ ) region of HS Mb and Mb-nitrite spectra.**

The furthest left and right show the  $g \sim 6$  peaks for Mb and Mb-nitrite respectively at pH values from 10.8 to 5.0. It may be seen that the peak maxima occur at a g-value of 5.9 consistently in all samples. The panel to the right of the Mb pH-range data shows an expansion of the Mb at pH 8.5 peak in which may be seen to show a divergence from the tetragonality seen at other pH values. This suggests a particular constraint upon the heme at this pH possibly due to the ionization of water to hydroxide at the heme that is also likely to involve protonation of the distal histidine residue. The larger central panels show the FSE

---

(top) and derivatised FSE spectra of HS Mb and Mb-nitrite at pH 7.5, 9.5 and 10.8 measured with experimental parameters necessary for HS heme centres described above. For these spectra measured using pulsed-EPR the position of the low-field  $g$ -value appears at different positions for the samples examined. The HS Mb and Mb-nitrite at pH 7.5 have the peak at around  $g = 5.86$  whilst the Mb-nitrite samples at pH 9.5 and 10.8 have this peak at a visibly lower  $g$ -value of 5.48. It may also be seen that the other spectral features are located at the same positions in each sample (e.g. the  $g=2$  peak) which rules out a field-offset between the spectra being responsible for the  $g$ -value difference. The fact that the same lower  $g$ -value is seen for nitrite ligated samples at a higher pH where hydrogen bonding from the distal histidine residue should be less pronounced again fits with the assignment of the HS case being the  $N$ -bound form. It is perhaps surprising, however, that the CW-EPR data do not reveal a deviation from a  $g$ -value of 5.9 and may indicate that FSE method is more suited to the acquisition of spectra in this case. If this were due to over-modulation of the EPR signal then the averaged peak position from a powder sample would still be expected to assume different values. This may be due to the dependence of the acquired spectrum the  $T_2$  value (with a CW-EPR spectrum being influenced also by  $T_1$  but not being relaxation dependant below 150 K [12]).

---

### 6.6.1 Proton HSCORE

Until now the discussion of the findings of EPR hyperfine techniques has focused on determining the coupling parameters of nitrogen nuclei in this section it is the weakly coupled proton interactions that are of interest. **Figure 6.6.1-1** shows the standard HSCORE spectra of HS-Mb (pH 6.3) and the HS contribution from Mb-nitrite (pH 9.5) top and bottom respectively. Both spectra were measured at 4 K at the  $g_z^{\text{eff}}$  position ( $\sim 3440$  G).

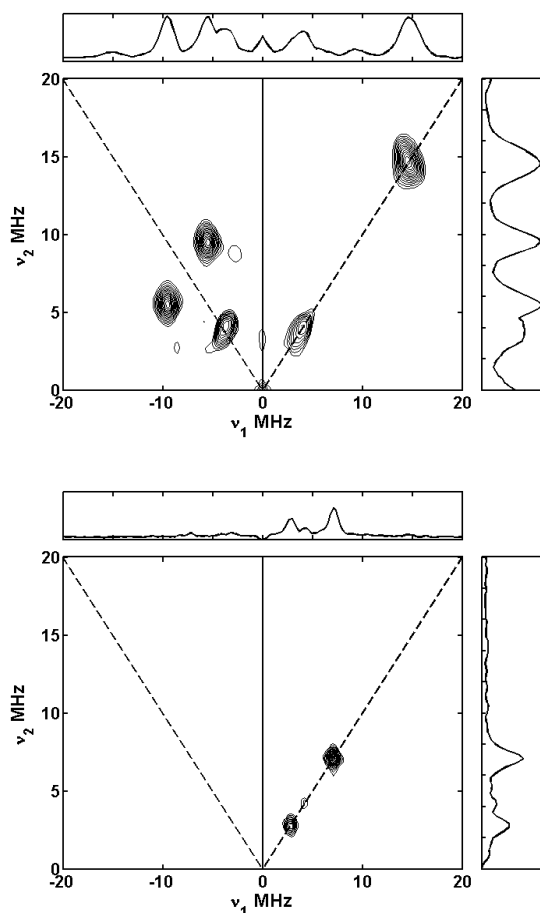


**Figure 6.6.1-1, HSCORE spectra of HS-Mb pH 6.3 (top) and HS Mb-nitrite pH 9.5 (bottom) Measured at 4 K near the  $g_z^{\text{eff}}$  field-position.**

A  $\tau$ -value of 160 ns,  $\pi/2$ -pulse lengths of 16 ns and inversion pulse length of 32 ns were used as well as low mw power. In the HS-Mb spectrum the correlation associated with a weakly coupled proton is seen centered at the proton Larmor frequency ( $\sim 14.65$  MHz). this correlation has been previously reported and assigned to the protons of a coordinated water

molecule with a hyperfine coupling at this position of  $\sim 5.9$  MHz [13], this value also agreed with the seminal single-crystal ENDOR study of Scholes [14]. The figure also shows the HYSORE spectrum of Mb-nitrite at pH 9.5 measured with the same experimental parameters and conditions that favor the measurement of the HS signal. The spectrum was also measured at the  $g_z^{\text{eff}}$  position. In this spectrum proton contributions are absent suggesting that the HS species does not have a coordinated water or even hydroxide molecule. This is further support for the HS signal being due to *N*-bound nitrite. The spectrum in this case consists of purely diagonal signal indicating that the inversion pulse was too weak to induce correlations. As this was not the case for the HS Mb spectrum measured with the same pulse lengths and power it may be inferred that the nitrogen nuclei contributing to the spectrum are differently coupled which in turn suggests a markedly different geometry in each case.

## 6.7 ENDOR

ESEEM techniques rely on the excitation of both allowed and forbidden transitions by the application of mw pulses. Electron Nuclear Double Resonance (ENDOR) techniques on the other hand directly excite nuclear transitions using radio frequency (r.f.) radiation to produce nuclear frequency spectra. There are two types of pulsed-ENDOR experiments commonly used: Mims-ENDOR [15] and Davies-ENDOR [16], both of which rely on the transfer of polarization between electron and nuclear transitions. The pulse sequences for these experiments are depicted in **Figure 6.7-1**.

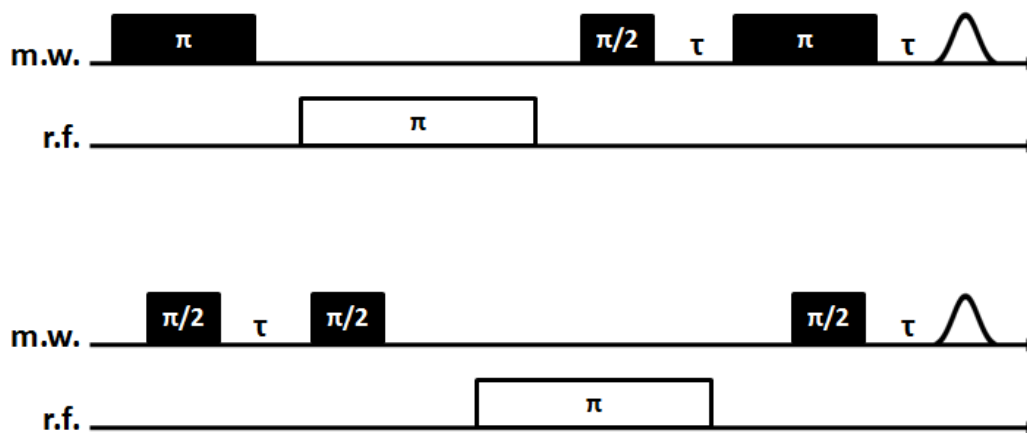


Figure 6.7-1, Pulse sequences for Davies ENDOR (top) and Mims ENDOR (bottom). The r.f. pulse length is incremented.

In general Davies-ENDOR is used for the measurement of large hyperfine couplings whilst Mims is more sensitive to smaller couplings. In Davies-ENDOR the spectrum is recorded by monitoring the primary echo intensity as the r.f. is incremented over the desired frequency range. In Mims-ENDOR three non-selective  $\pi/2$ -pulses lead the measurement of the stimulated echo which increases the sensitivity of the experiment but also leads to a similar blind-spot behavior encountered in the three-pulse ESEEM experiment.

### 6.7.1 ENDOR of Low-Spin Species

The Mims-ENDOR spectra of the  $^{14}\text{N}$  region (1-6 MHz) of LS Mb and Mb-nitrite are shown in **Figure 6.7.1-1**. Spectra were measured at 10K, 8 ns mw  $\pi/2$ -pulses and a 20  $\mu\text{s}$  r.f. pulse of variable frequency were used with an inter-pulse time  $\tau$ , of 112 ns.

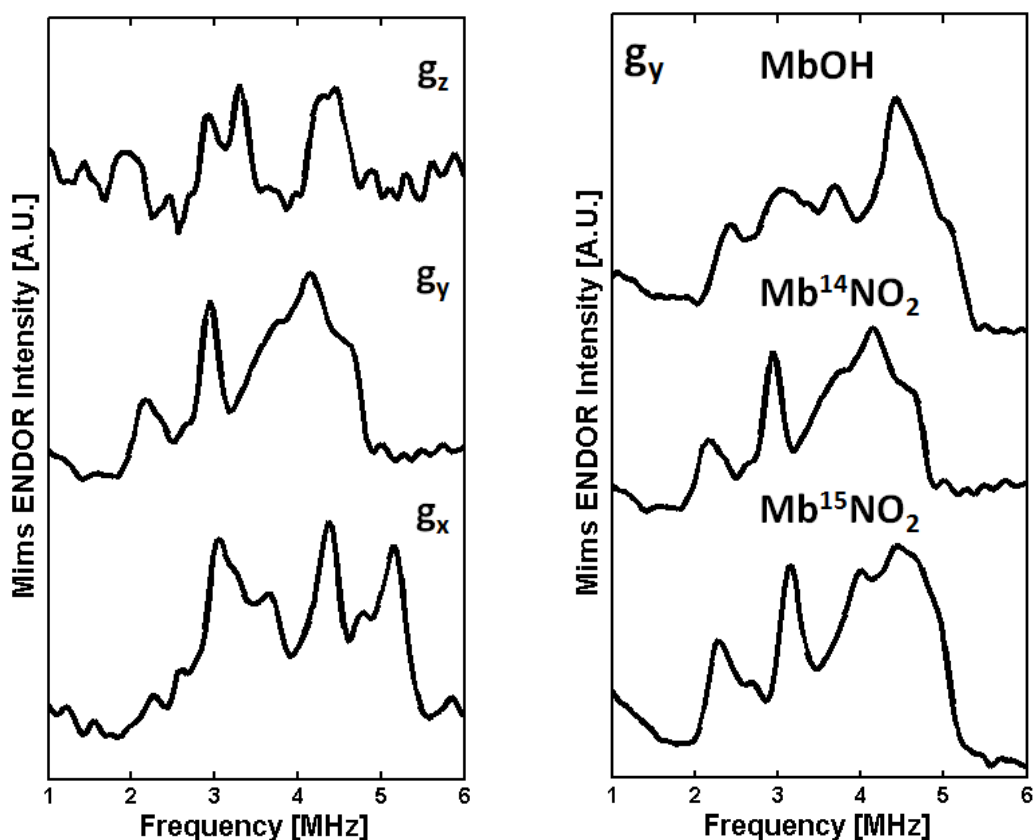


Figure 6.7.1-1, Left: Mims ENDOR of Mb-nitrite at pH 7.5 measured near canonical positions at 10 K. Right: Mims ENDOR of MbOH (pH 10.8)  $\text{Mb}^{14}\text{NO}_2$  (pH 7.5) and  $\text{Mb}^{15}\text{NO}_2$  (pH 7.5) top, middle and bottom respectively also measured at 10 K.

---

The panel on the right shows the spectra measured at canonical positions of Mb<sup>14</sup>NO<sub>2</sub>. The spectra are comparable with previously published LS ferric heme ENDOR data [17] and do not contain extra features at the g<sub>z</sub>-position attributable to the nitrogen of bound nitrite. This apparent absence of a strongly-coupled nitrogen interaction again supports the hypothesis that the LS nitrite signal is caused by *N*-bound nitrite. The right panel shows the g<sub>y</sub>-position ENDOR spectra of Mb and Mb-nitrite samples measured under the same conditions.

---

---

## References

1. Duprat, A.F., et al., *Myoglobin-NO at Low pH: Free Four-Coordinated Heme in the Protein Pocket*. *Biochemistry*, 1995. **34**(8): p. 2634-2644.
  2. Decatur, S.M., et al., *Trans Effects in Nitric Oxide Binding to Myoglobin Cavity Mutant H93G*. *Biochemistry*, 1996. **35**(15): p. 4939-4944.
  3. Schwab, D.E., J.S. Stamler, and D.J. Singel, *EPR Spectroscopy of Nitrite Complexes of Methemoglobin*. *Inorganic Chemistry*, 2010. **49**(14): p. 6330-6337.
  4. Jeschke, G., R. Rakhmatullin, and A. Schweiger, *Sensitivity enhancement by matched microwave pulses in one- and two-dimensional electron spin echo envelope modulation spectroscopy*. *Journal of Magnetic Resonance*, 1998. **131**(2): p. 261-271.
  5. Jeschke, G. and A. Schweiger, *Matched two-pulse electron spin echo envelope modulation spectroscopy*. *Journal of Chemical Physics*, 1996. **105**(6): p. 2199-2211.
  6. Fittipaldi, M., et al., *A multi-frequency pulse EPR and ENDOR approach to study strongly coupled nuclei in frozen solutions of high-spin ferric heme proteins*. *Journal of Physical Chemistry B*, 2008. **112**(12): p. 3859-3870.
  7. Yi, J., et al., *The Distal Pocket Histidine Residue in Horse Heart Myoglobin Directs the O-Binding Mode of Nitrite to the Heme Iron*. *Journal of the American Chemical Society*, 2009. **131**(50): p. 18119-18128.
  8. Goldfarb, D., et al., *Double Nuclear Coherence Transfer (DONUT)-HYSCORE: A New Tool for the Assignment of Nuclear Frequencies in Pulsed EPR Experiments*. *J. Am. Chem. Soc.*, 1998. **120**(28): p. 7020-7029.
  9. Stoll, S., et al., *Peak suppression in ESEEM spectra of multinuclear spin systems*. *Journal of Magnetic Resonance*, 2005. **177**(1): p. 93-101.
  10. Lee, H.-I., P.E. Doan, and B.M. Hoffman, *General Analysis of  $^{14}\text{N}$  ( $I = 1$ ) Electron Spin Echo Envelope Modulation*. *Journal of Magnetic Resonance*, 1999. **140**(1): p. 91-107.
  11. Peisach, J., et al., *The Effects of Protein Conformation on the Heme Symmetry in High Spin Ferric Heme Proteins as Studied by Electron Paramagnetic Resonance*. *Journal of Biological Chemistry*, 1971. **246**(10): p. 3342-3355.
  12. Gaffney, B.J., G.R. Eaton, and S.S. Eaton, *Electron Spin Relaxation Rates for High-Spin Fe(III) in Iron Transferrin Carbonate and Iron Transferrin Oxalate*. *The Journal of Physical Chemistry B*, 1998. **102**(28): p. 5536-5541.
  13. Garcia-Rubio, I., et al., *A Multifrequency HYSCORE Study of Weakly Coupled Nuclei in Frozen Solutions of High-Spin Aquometmyoglobin*. *Inorganic Chemistry*, 2008. **47**(23): p. 11294-11304.
-

14. Scholes, C.P., et al., *Electron Nuclear Double-Resonance (ENDOR) from Heme and Histidine Nitrogens in Single-Crystals of Aquometmyoglobin*. Journal of the American Chemical Society, 1982. **104**(10): p. 2724-2735.
  15. Mims, W.B., *Pulsed ENDOR Experiments*. Proceedings of the Royal Society of London. Series A, Mathematical and Physical Sciences (1934-1990), 1965. **283**(1395): p. 452-457.
  16. Davies, E.R., *A new pulse endor technique*. Physics Letters A, 1974. **47**(1): p. 1-2.
  17. Vinck, E., et al., *Analyzing heme proteins using EPR techniques: the heme-pocket structure of ferric mouse neuroglobin*. Journal of Biological Inorganic Chemistry, 2006. **11**(4): p. 467-475.
-

---

---

## 7 CHAPTER Computational Investigation

---

### 7.1 Computational Chemistry

Computational chemistry is a rapidly expanding area within theoretical chemistry, the focus of which is the examination of chemically related problems using calculations. As the only systems that may be solved exactly (with regards to the Schrödinger equation) are very small and consist of a very few number of particles, theoretical chemistry and thus computational chemistry rely on a series of approximations to determine quantitative and qualitative answers to questions posed by computational experiments. The success of the method therefore relies heavily on selected simplifications which should be based on valid physical assumptions and considerations of the system of interest. An excellent text in this field describes how the method may be applied to a variety of systems and the intricacies of the computational method [1]. This text contains the following definitions in relation to the potential energy of a molecule which this author found to be particularly insightful:

Chemistry is knowing the energy as a function of the nuclear coordinates.

Which leads to a further definition for molecular properties:

Properties are knowing how the energy changes upon adding a perturbation.

The following describes the application of computational chemistry to provide insight into the nature of nitrite binding in myoglobin (Mb). A brief introduction to the methods used will be complemented by an explanation of the common terms encountered overall the discussion will be presented in a predominantly qualitative manner. The computational experiments performed by this author will then be presented with justification as to the methods and approximations employed.

---

## 7.2 Hartree-Fock

The Hartree-Fock (HF) approximation [2] in essence attempts to solve the Schrödinger equation to determine the ground-state wave-function by replacing the complicated multi-electron problem by a one-electron situation in which the electron-electron repulsion is treated in an average way. The multi-electron system is described by a Slater determinant [3], a matrix in which the columns are single electron wave-functions and the rows contain the electron coordinates. Importantly the Slater determinant also satisfies the Pauli Exclusion Principle. The Method by which the Hartree-Fock approximation is solved is called the Self-Consistent Field (SCF) method. This method calculates the average field experienced by the  $i^{\text{th}}$  electron (Hartree-Fock Potential) from an initial guess of the spin orbitals. This potential is then used to solve the eigenvalue equation for a new set of spin orbitals, which in turn may be used to determine new potentials. The procedure is repeated until the generated fields no longer change (i.e. they are self-consistent) and the spin orbitals used to construct the Fock operator are the same as its eigenfunctions.

## 7.3 Electron Correlation

Electron correlation [4] is a quantum mechanical effect related to the correlated motion of electrons. This phenomenon is particularly significant in both paramagnetic systems and those containing first-row transition metals. The computational method applied to determine the energy of such a system should therefore take this correlation into account. The Hartree-Fock method provides no account for this interaction and so is limited in its application to the Myoglobin-nitrite system.

## 7.4 Density Functional Theory

Density functional theory (DFT) [5] uses the spatially dependant electron-density of a system to determine its ground state wave-function. As the electron density is solely dependent on three coordinates and not the number of electrons (c.f. the Hartree-Fock method in which the Slater determinant will naturally be scaled to the size of the system) the size of the calculation may be reduced. It is the purpose of DFT methods therefore to produce functionals that connect the electron density with the system energy. To perform a DFT calculation both a

---

basis set and a density functional must be chosen. The combination of these choices determines the level of theory and therefore the computational expense of the calculation.

### 7.4.1 Quantum Chemistry Basis Sets

A basis set is a set of functions used to create the molecular orbitals. Basis sets are mathematical constructs that describe the position and motion of electrons and are expanded as a linear combination of such functions with the weights or coefficients to be determined. Usually these functions are atomic orbitals, in that they are centered on atoms. Otherwise, the functions are centered on bonds or lone pairs. The larger the basis set the greater its completeness and naturally the computational expense of the experiment.

All energy optimised basis sets primarily depend on the wave-function of the inner core of electrons however; chemistry is mostly concerned with the interaction of the valence electrons. Many properties of a molecule are dependent on the wave-function a significant distance from the nucleus. If this were to be accurately described by such a basis set the basis set would have to be very large which is computationally inefficient. Contracted basis sets use Gaussian functions to overcome this inefficiency. A Gaussian function has the advantage of being a computationally efficient way of describing two-electron integrals; they however suffer from not being optimum basis functions and are known to have different functional behaviour from actual molecular orbitals. If the full set of primitive (initial) Gaussian Type Orbitals (GTO) are combined into a smaller set of functions by forming fixed linear combinations the basis set is said to be contracted. The linear combinations are called contractions and the functions as contracted Gaussian functional (CGF).

Split-Valence Polarization SV(P) [6] is the smallest basis set that may be expected to reliably account for changes in the valence shell electrons due to bonding under the SCF method are of the split valence polarisation type. Within which the inner shell atomic orbitals (AO) are described by one basis function and two are provided for each valence shell AO, augmented by a set of polarisation functions. Polarisation functions allow for the description of atomic orbitals that have been distorted by participation in chemical bonding. They have higher angular momentum than a normal occupied orbital.

---

Triple Zeta Valence (TZV) [7] basis sets are contracted Gaussian type sets characterised by the inclusion of a single basis function for the inner shells and three basis functions for the valence shells. TZVP or Triple Zeta Valence Polarised functions are the same but include a polarisation function.

## 7.5 Functionals

Two functionals will be used in this investigation; the functionals are most widely applied to organo-metallic systems, namely the BP86 and B3LYP functionals. Functionals may be broadly viewed as representing approximations to the actual physical wave-function. The 1986 J.P. Perdew functional (BP86) [8] is perhaps the most widely used functional for initial heme system geometry optimization. It is reported that this functional predicts accurate geometries for transition-metal complexes [9]. Also commonly encountered is the B3LYP functional. This is a hybrid functional which includes HF exchange as well as DFT exchange and correlation functionals [10, 11]. The functional also contains three parameters that modify the extent of correlation and exchange mixing.

## 7.6 Orca

Computations were performed using the electronic structure program package Orca (version 2.8) [12-14]. The package contains many modules for quantum chemistry calculations including HF and DFT and is focused towards determination of the spectroscopic properties of open-shell molecules. For DFT calculations a reasonably large number of exchange and correlation functionals are included (including BP86 and B3LYP) as well as a large number of basis sets. Calculations were performed in parallel on the University of East Anglia (UEA) High-Power Computing (HPC) cluster: ESCluster.

## 7.7 Choice of Functional

It was stated in § 7.5 that the BP86 and B3LYP functionals were the most commonly used in DFT calculations applied to organo-metallic systems. To qualify this statement a literature search was performed on web of science on 20/06/11 using the keywords DFT calculations

---

and hemes. The search returned 50 records, 34 of which were accessible and stated the functional used in calculations. A summary of the functionals used is shown in **Figure 7.7-1**.

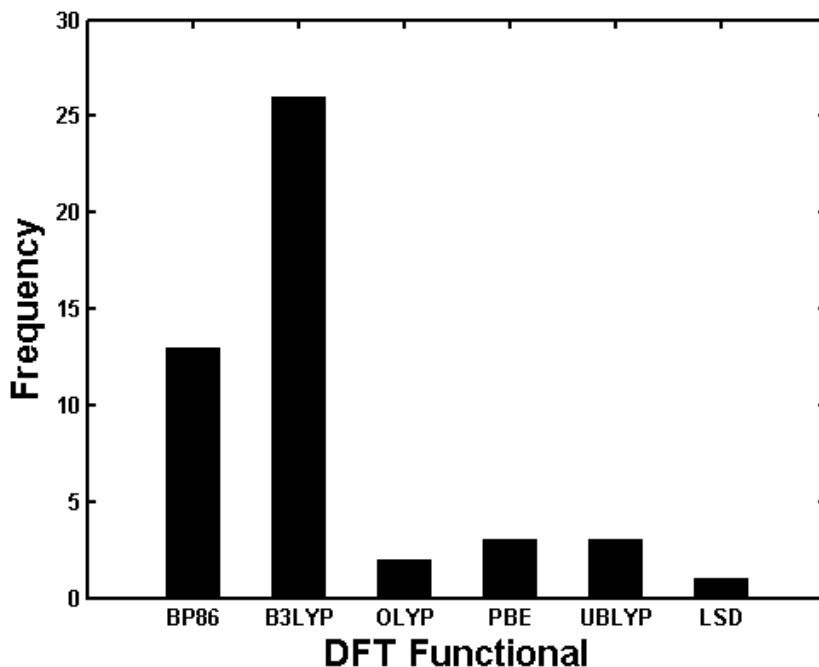


Figure 7.7-1, Results of web of science search “DFT calculations hemes” performed 20/06/11.

These functionals are the most widely used by a clear margin.

## 7.8 DFT calculations of nitrite binding modes

A very recent communication attempted to address the feasibility of a proposed nitrite anhydrase function of hemoglobin (Hb) [15]. The first part of this work aimed to assess the preferred binding mode of nitrite. To determine this model systems were computationally created with nitrite orientated as found in several different crystal structures, including the *N*-bound and *O*-bound modes (three different *O*-bound conformations were examined). The constraints of the model were based on previous computations by Basu *et al* [16]. These orientations were optimised at BP86/TZVP theory level. These models only took into account a cut-down version of the heme and the proximal and distal histidine residues. The study found the *N*-bound mode to be energetically more favourable, but that the *O*-bound mode was necessary for the formation of  $N_2O_3$ . It was decided to adopt the method employed in

this work to an examination of the nitrite binding mode in Mb, initially to determine the most energetically favourable nitrite confirmation and secondly to gain insight on the possible role of the different binding modes.

### 7.8.1 Constructing Model Geometries

Four models were selected for investigation and are depicted schematically in **Figure 7.8-1**.

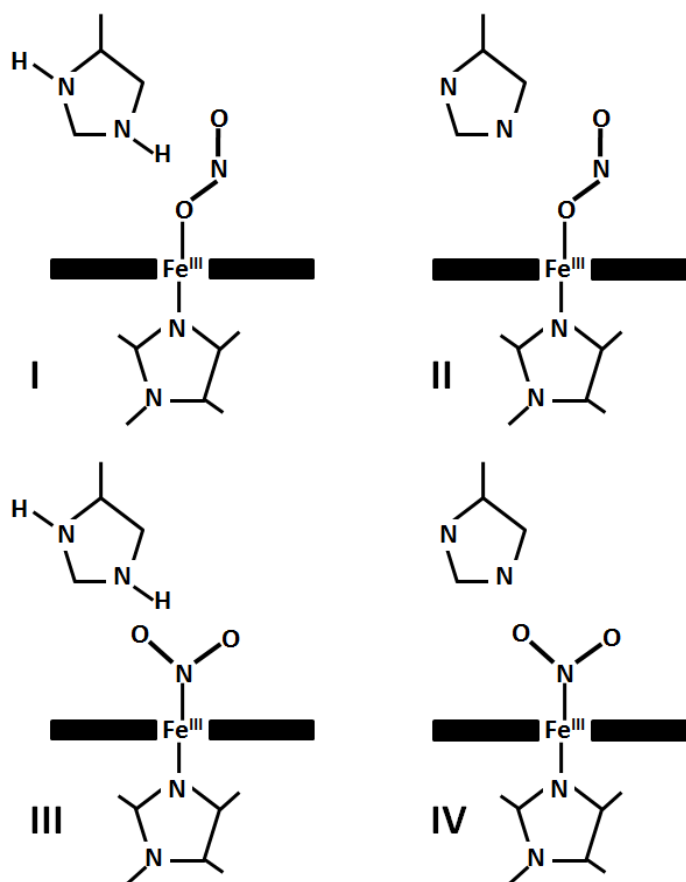


**Figure 7.8-1**, Myoglobin-nitrite model schemes to be examined.

The models contained a cut-down version of the heme motif and the nitrite anion as well as cut-down proximal and distal histidine residues. Both binding modes were investigated with the distal histidine in two states of protonation to yield four separate models with species having  $S = 1/2$ . Initial geometries in all cases were adapted from the high-resolution crystal structures of Richter-Addo [17] using the molecular visualization software PyMOL. Structures

were edited and viewed in the quantum chemistry visualization program ChemCraft. For the *O*-bound models the structure 2FRF of *O*-bound nitrite in a wild-type (w.t.) protein was used. *N*-bound nitrite was added to the same system but with insights into the nitrite conformation from the Mb mutant structure 3HEP (O-N-O bond angle  $120^\circ$ , however an initial Fe-N bond distance  $2.12 \text{ \AA}$  was chosen instead of the unusually large structure distance of  $2.57 \text{ \AA}$ ). Initial geometry optimizations were carried out using the unrestricted Kohn-Sham method [18] and optimized at the BP86/TZVP level. The geometries of the models were constrained to aid optimization as follows: To facilitate optimization components of the models were labeled as “fragments” so that they could be individually constrained. The assignment of the fragments is shown in **Figure 7.8-2**.

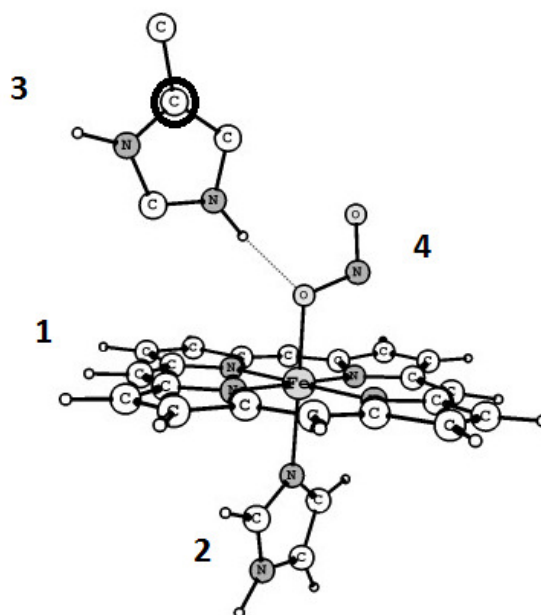


**Figure 7.8-2, Fragment construction for Mb-nitrite *O*-bound mode.**

The internal coordinates of the heme and distal histidine were constrained as well as the Cartesian coordinates of the heme iron and the distal histidine C2 atom (circled). The dihedral angles between fragments were also constrained to model the effect of the protein backbone. The hydrogen atoms were not constrained during the optimization process. Initial calculations were performed expecting slow convergence for geometry optimizations ( $0.5 \times 10^{-6} \text{ Eh}$ ), although the SCF was still optimized to a tight convergence. The final single point energies of these models may be found in **Table 7-1**.

Model	Kcal/mol
I	+25
II	+289
III	Ground State
IV	Ground State

**Table 7-1, Difference in final single-point energies of models using BP86/TZVP level of theory. Comparison made between models I and III and II and IV.**

It can be seen that the calculations in this case show the *N*-bound form to be the ground-state by a large degree in both cases (In the unprotonated models by a very large amount comparable to the energy of a triple covalent bond). In the Berto and Lehnert [15] calculation with Hb however, the difference between minimum and maximum energies was determined to be only 9.0 kcal/mol. As the modeled structures in this case examined three different *O*-bound conformations, it is likely that the nitrite anion was more constrained than in the models constructed for this work. Indeed for models III and IV it was found that the internal coordinates of the nitrite had to be constrained in order to maintain the *N*-bound nitrite confirmation. It is therefore probable that the unfavorable conformations forced on the calculation were largely responsible for the difference in relative energies of the investigated structures. Importantly the more qualitative insights provided by the necessity of adding particular constraints may have more significance with regards to understanding the binding mode. **Figure 7.8-3** shows the initial *N*-bound nitrite geometry and final stage of geometry optimization in the case where the internal coordinates of the nitrite were unconstrained.

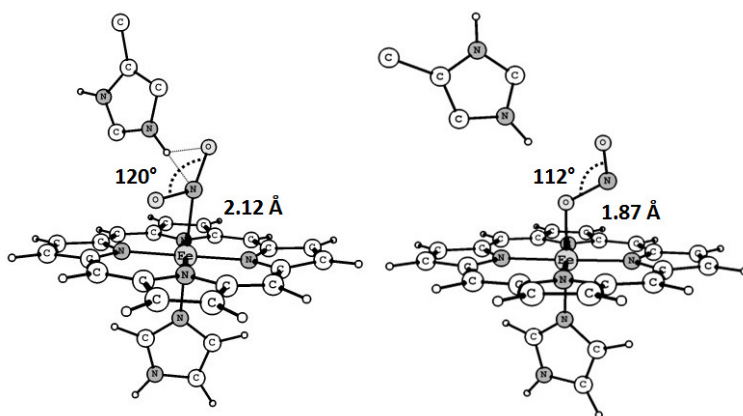


**Figure 7.8-3, Initial and final geometries for unconstrained *N*-bound nitrite. Fe-X bond-lengths shown (where X indicates atom of nitrite coordinated to Fe).**

Clearly the final geometry shows *O*-bound nitrite. It is also interesting that in 2FRF for the *O*-bound case, the O-N-O dihedral angle is  $113^\circ$  and the Fe-O bond length  $1.94 \text{ \AA}$  (c.f.  $112^\circ$  and  $1.87 \text{ \AA}$ ). The distal histidine has moved considerably although still maintains an orientation consistent with stabilization of the binding mode via hydrogen-bonding. When the internal coordinates of the nitrite anion fragment were constrained in this situation and the Cartesian coordinates of the distal histidine constrained via the non-ring carbon atom (indicated in **Figure 7.8-4**) the geometry optimization provided another insight shown in **Figure 7.8-4** (left).

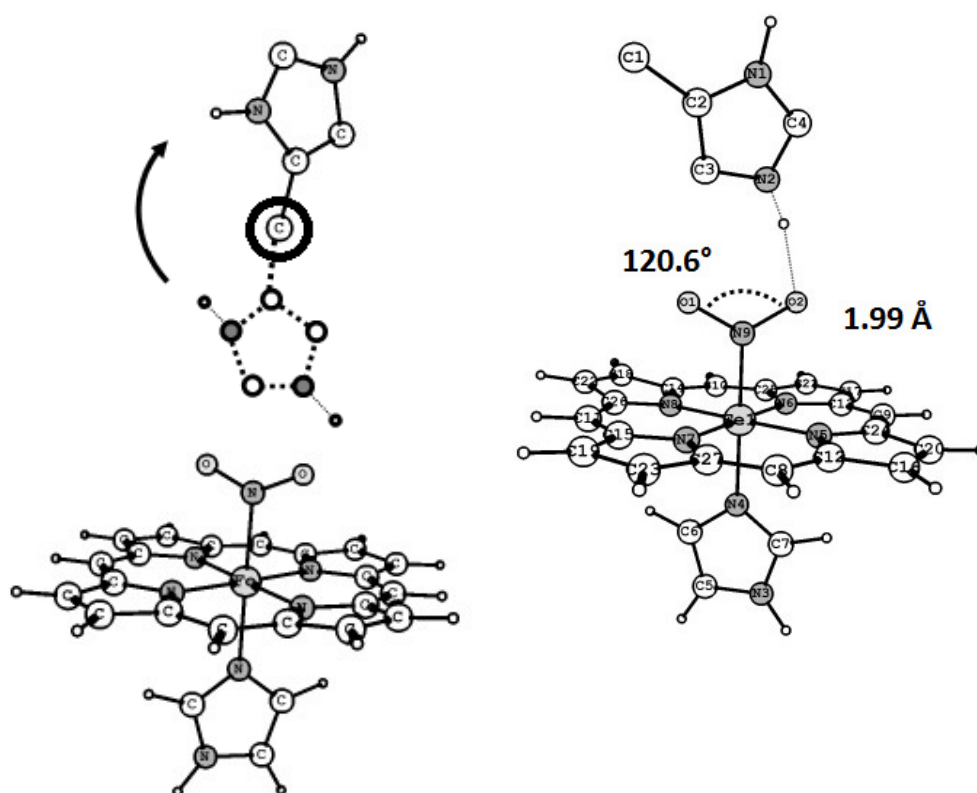


**Figure 7.8-4, Left:** Rotation of distal histidine away from nitrite, when constrained at non-ring carbon (highlighted). **Right:** final optimized *N*-bound nitrite structure.

In this situation the distal histidine rotated away from the nitrite fragment out of the binding-pocket. Although in both of these calculations the wave-functions did not ultimately converge, the qualitative trends seen in the geometry optimization confirm the importance of the distal histidine on the nitrite binding mode suggested by the mutation study [19]. Both observations discussed seem to suggest that a protonated distal histidine promotes the *O*-

bound form. With additional constraints however, it was possible to optimize the *N*-bound protonated model III (**Figure 7.8-4- right**) indicating that the model is possible but perhaps energetically unfavorable and therefore unlikely to be a ground-state. These considerations also highlight the importance that the constraints have on a calculation and that the biological relevance of such a constraint should be considered part of the experimental philosophy, as each subsequent addition of a constraint offsets the calculated ground-state energy. The spin densities determined from the calculated model geometries is shown in **Figure 7.8-5**

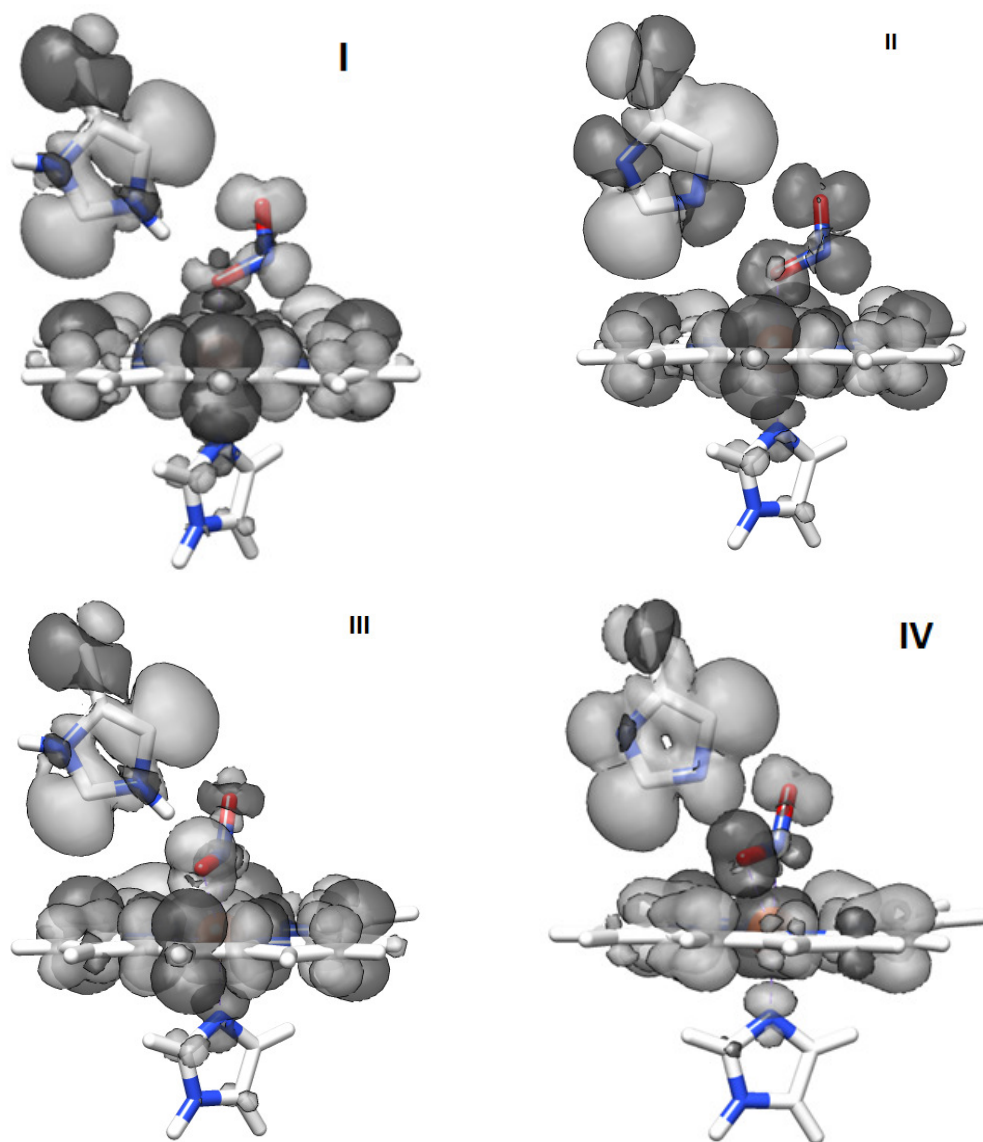


**Figure 7.8-5, Spin density plots of model geometries. *O*-bound (top), *N*-bound (bottom), Protonated distal His (left) and unprotonated distal His (right).**

The models are arranged as in **Figure 7.8-1**. The effect of protonation on the spin density of the distal histidine may be clearly seen. As may perhaps be expected the N-bound nitrite models display a higher degree of spin density symmetry for the nitrite oxygen atoms.

The model geometries were optimized with the B3LYP functional and an SV(P) basis set (due to constraints on the length of calculations imposed by the UEA cluster). The optimizations contained the same constraints as the BP86 calculations. The final single point energies of the models are presented in **Table 7-2**. Interestingly the calculation time for model III exceeded that allowed on the cluster (It is tempting to propose that this is indicative of an unfavorable state).

Model	Kcal/mol	Time (s)
I		110595
II	+44	156799
III	-	-
IV	0	288143

**Table 7-2, Final single-point energies of models using B3LYP/SV(P) level of theory.**

The time (s) required for the calculations is also tabulated (max time of cluster = 345600 s).

## 7.9 Relaxed surface-scans

A relaxed surface scan allows one geometrical variable to be altered whilst the others are relaxed. This may provide an insight into the potential energy surfaces involved with a reaction. For the models outlined in § 7.8.1 such scans were initially performed whilst incrementing the Fe-X bond length (where X is the coordinating nitrite atom). At each value of the bond length the final single point energy was calculated. Such calculations are however, computationally expensive which normally must be offset with a reduced basis set or less demanding functional. Relaxed surface scans using the BP86/TZVP optimized geometries described in § 7.8.1 were performed by increasing the iron to nitrite coordinating atom bond-length from 1.5 to 3.0 Å with a reduced basis set of SV(P). Minimal variation in calculated energies was seen for the scanned bond-lengths the minimum and maximum standard deviations (STD) of the data were: Model I STD 0.018 Eh, Model III STD 0.041 Eh.

## 7.10 Indication of High-Spin State of *N*-bound Form

In the DFT calculations presented the spin-state of the system was an initial parameter of the calculation. Negligible differences were found in the calculated final single point energies of the BP86/TZVP geometry optimized models when a HS spin-state was modeled. Previous DFT calculations attempted to determine the lowest ground state energies of a models composed of the heme and proximal histidine of Mb-nitrosyl complexes with different spin-states. These were performed again using the BP86 functional and an SV(P) basis set, the results of a relaxed surface scan of the Mb-nitrosyl bond length (18 to 30 nm) may be seen in **Figure 7.10-1**.

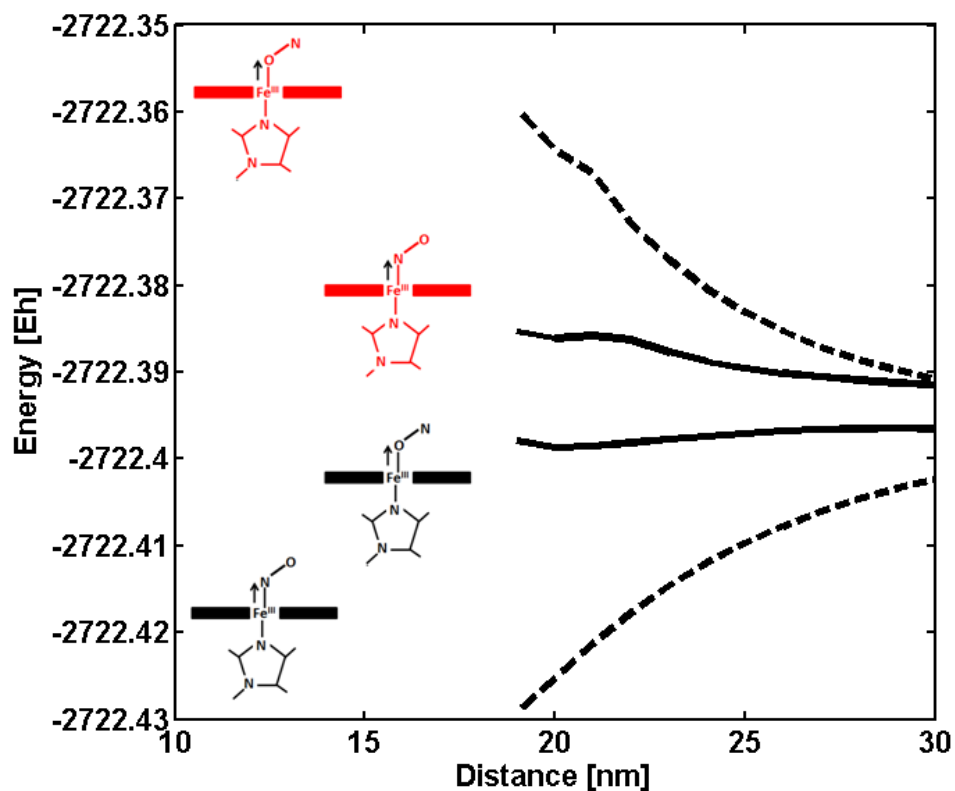
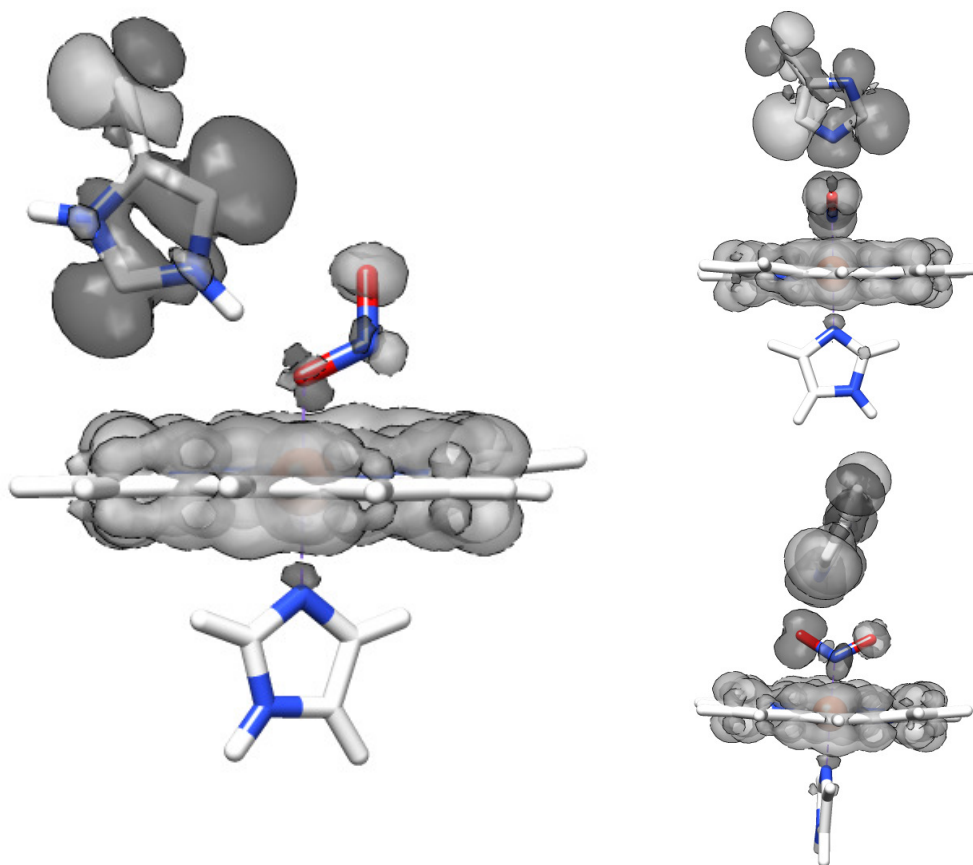


Figure 7.10-1, Relaxed Surface scan of HS (light structures) and LS (black structures) nitrosyl-Mb models using BP86 functional and SV(P) basis set.

The change in energies of the models during the scans was minimal as has been seen for the previous calculations described in this chapter. A review describing the computation of spin-

state energetic of transition metals using DFT emphasizes the variation in the success of such calculations [20] using existing DFT functionals.

According to Walker [21] the main factor contributing to the spin-state of a heme iron with be the  $\sigma$ -donor strength of the axial ligands. In § 7.8.1 during a description of the spin density plots for the BP86 geometry optimized models, it was remarked that the *N*-bound nitrite had a more symmetrical electron distribution among the oxygen atoms of nitrite. It is possible that in the *N*-bound form the higher electro-negativity of the oxygen atoms produces an inductive effect [22] that ultimately reduces the spin-density at the N-atom leading to a HS state. In the *O*-bound form the opposite situation would arise and may be enhanced by hydrogen bonding to the distal histidine. **Figure 7.10-2** shows the spin density plots of the *N*-bound and *O*-bound forms of Mb-nitrite at a B3LYP/SV(P) level.



**Figure 7.10-2, Spin Density of *O*-bound (left) and *N*-bound (right) Mb-nitrite. Calculated at B3LYP/SV(P) level of theory.**

A different distribution of spin-density may be seen between the two binding modes. The calculated *s*-orbital density of the coordinating oxygen in the *O*-bound form is -0.104 and the nitrogen of the *N*-bound form -0.00423, with the majority of the spin density of the bond residing at the iron atom (hence the negative value).

### 7.11 Conclusion

It is perhaps not surprising that the computational investigation described in this chapter failed to produce definite answers to the question of nitrite binding mode in myoglobin. A previous computational investigation into the electronic structure of nitrosyl porphyrin complexes from Scheidt *et al* concluded that heme-nitrosyl complexes exhibit a high degree of variability with the respect to the computational method employed and that the most commonly used DFT functionals are not fully successful in describing the trans interaction between porphyrin axial ligands [23]. The authors speculate that the observed variability in results from computational method reflects an inherent electronic instability that the protein may exploit to tune its reactivity. Whether this speculation is true or not, the application of DFT to ferric-porphyrin systems would benefit from a more in-depth study.

---

---

## References

1. Jensen, F., *Introduction to Computational Chemistry*. 1999: John Wiley & Sons.
  2. Baerends, E.J., D.E. Ellis, and P. Ros, *Self-consistent molecular Hartree-Fock-Slater calculations - I. The computational procedure*. Chemical Physics, 1973. **2**(1): p. 41-51.
  3. Slater, J.C., *A Simplification of the Hartree-Fock Method*. Physical Review, 1951. **81**(3): p. 385-390.
  4. Lowdin, P.O., *Correlation Problem in Many-Electron Quantum Mechanics .1. Review of Different Approaches and Discussion of Some Current Ideas*. Advances in Chemical Physics, 1959. **2**: p. 207-322.
  5. Becke, A.D., *Density-Functional Thermochemistry .3. The Role of Exact Exchange*. Journal of Chemical Physics, 1993. **98**(7): p. 5648-5652.
  6. Schafer, A., H. Horn, and R. Ahlrichs, *Fully Optimized Contracted Gaussian-Basis Sets for Atoms Li TO Kr*. Journal of Chemical Physics, 1992. **97**(4): p. 2571-2577.
  7. Schafer, A., C. Huber, and R. Ahlrichs, *Fully Optimized Contracted Gaussian-Basis Sets of Triple Zeta Valence Quality for Atoms Li to Kr*. Journal of Chemical Physics, 1994. **100**(8): p. 5829-5835.
  8. Perdew, J.P., *Density-Functional Approximation for the Correlation-Energy of the Inhomogenous Electron-Gas*. Physical Review B, 1986. **33**(12): p. 8822-8824.
  9. Buehl, M. and H. Kabrede, *Geometries of transition-metal complexes from density-functional theory*. Journal of Chemical Theory and Computation, 2006. **2**(5): p. 1282-1290.
  10. Zhao, Y. and D.G. Truhlar, *Density functionals with broad applicability in chemistry*. Accounts of Chemical Research, 2008. **41**(2): p. 157-167.
  11. Lee, C.T., W.T. Yang, and R.G. Parr, *Development of the Colle-Salvetti Correlation-Energy Formula into a Functional of the Electron-Density*. Physical Review B, 1988. **37**(2): p. 785-789.
  12. Neese, F., *Quantum chemical calculations of spectroscopic properties of metalloproteins and model compounds: EPR and Mössbauer properties*. Current Opinion in Chemical Biology, 2003. **7**(1): p. 125-135.
  13. Neese, F., *A spectroscopy oriented configuration interaction procedure*. Journal of Chemical Physics, 2003. **119**(18): p. 9428-9443.
-

- 
14. Radoul, M., et al., *Revisiting the nitrosyl complex of myoglobin by high-field pulse EPR spectroscopy and quantum mechanical calculations*. Physical Chemistry Chemical Physics, 2011. **12**(26): p. 7276-7289.
  15. Berto, T.C. and N. Lehnert, *Density Functional Theory Modeling of the Proposed Nitrite Anhydrase Function of Hemoglobin in Hypoxia Sensing*. Inorganic Chemistry, 2011. **50**(16): p. 7361-7363.
  16. Basu, S., et al., *Catalytic generation of N<sub>2</sub>O<sub>3</sub> by the concerted nitrite reductase and anhydrase activity of hemoglobin*. Nature Chemical Biology, 2007. **3**(12): p. 785-794.
  17. Copeland, D.M., et al., *Crystal structures of the nitrite and nitric oxide complexes of horse heart myoglobin*. Journal of Inorganic Biochemistry, 2006. **100**(8): p. 1413-1425.
  18. Kohn, W. and L.J. Sham, *Self-Consistent Equations Including Exchange and Correlation Effects*. Physical Review, 1965. **140**(4A): p. 1133-&.
  19. Yi, J., et al., *The Distal Pocket Histidine Residue in Horse Heart Myoglobin Directs the O-Binding Mode of Nitrite to the Heme Iron*. Journal of the American Chemical Society, 2009. **131**(50): p. 18119-18128.
  20. Harvey, J., *DFT Computation of Relative Spin-State Energetics of Transition Metal Compounds* 2004, Springer Berlin. p. 81-102.
  21. Walker, F.A., *Proton NMR and EPR Spectroscopy of Paramagnetic Metalloporphyrins*, in *NMR and EPR*, K.M. Kadish, K.M. Smith, and R. Guilard, Editors. 2011, World Scientific.
  22. Smith, A.P., A.E. McKercher, and R.C. Mawhinney, *Inductive Effect: A Quantum Theory of Atoms in Molecules Perspective*. The Journal of Physical Chemistry A, 2011. **115**(45): p. 12544-12554.
  23. Scheidt, W.R., et al., *Electronic Structure and Dynamics of Nitrosyl Porphyrins*. Inorganic Chemistry, 2010. **49**(14): p. 6240-6252.
-

---

## 8 CHAPTER Conclusions and Outlook

---

### 8.1 Conclusions

#### 8.1.1 EPR Insights to Nitrite Binding in Myoglobin

In summary it has been shown in § 4.3.9 that where optical spectroscopy fails to do so, Continuous-Wave Electron Paramagnetic Resonance (CW-EPR) may unambiguously demonstrate nitrite binding to ferric myoglobin (Mb) resulting in a rhombic EPR spectrum indicative of LS Fe(III). The same technique also indicates an increase in the contribution to the high-spin (HS) component of the spectra with the addition of nitrite at pH 10.8 (§ 5.2) that was attributed to the binding of nitrite to the heme in a different manner than is responsible for the observation of the LS species. An hypothesis was proposed that the LS signal was due to *O*-bound nitrite whilst the HS signal indicated the contribution of the *N*-bound form [1]. In § 6.6.2 HYSCORE [2] was able to measure contributions to the spectra of HS Mb from hyperfine coupled protons but failed to reveal proton couplings for the increased HS component associated with nitrite. This ruled-out assignment of the HS signal to the coordination of water or hydroxide indicating it must be due to coordinated nitrite. The contribution of the HS and LS iron signals associated with Mb-nitrite and LS Mb-OH<sup>-</sup> was quantified via simulation with EasySpin [3] in samples with pH values of 6.5, 7.5, 8.5, 9.5 and 10.8 in § 5.2. Using the simulation of the HS iron signal of Mb at each pH value before and after the addition of nitrite to the sample allowed the pH values at which the HS signal increased (and could therefore be assigned to Mb-nitrite) to be determined. It was found that this occurred in the pH 9.5 and 10.8 samples. These pH values were discussed in relation to the pK<sub>a</sub> of the protonation of the distal histidine (H64) which is typically around 6 [4]. The observation of the *O*-bound nitrite form in mutants of Mb had previously been shown to be due to hydrogen bonding to this histidine residue [5]. This study found that if this residue

---

---

were replaced with an amino acid incapable of hydrogen bond formation the resulting structures would display *N*-bound nitrite conformation. This suggested that the HS Mb-nitrite signal was attributable to *N*-bound nitrite as the distal histidine would be unlikely to be protonated as thus be able to form hydrogen-bonds at these pH values. Electron Spin Echo Envelope Modulation (ESEEM) spectroscopy [6] combined with  $^{15}\text{N}$  isotope labeled nitrite substitution (§ 5.3.7) was able to resolve the contribution to the ESEEM frequency domain spectrum from the nitrogen of nitrite in the LS complex. Simulation of this contribution in § 5.3.8 led to the determination of the nuclear coupling parameters of this nucleus. The dipolar component of the hyperfine interaction was used to estimate the Fe- $\text{N}_{\text{Nitrite}}$  distance which compared well to that seen in the crystal structure of the *O*-bound case (2FRF) [1]. HYSCORE of the LS Mb-nitrite case in § 5.3.11 reinforced the assignment of the LS Mb-nitrite signal to the *O*-bound case from the appearance of the nitrogen couplings in the (+,+) weak coupling quadrant indicative of nitrogen not directly coordinated to the heme iron. § 6.3 described the application of multi-frequency CW-EPR to investigate the findings of a previous EPR study on nitrite binding to methemoglobin (Hb) that revealed signals consistent with two LS species, [7]. Only one LS species was seen in the Mb nitrite case at both S and Q-band (4 and 34 GHz respectively). It is likely that the two sets of *g*-values present in Hb correspond to slightly different nitrite ligation geometries in the two subunits of hemoglobin. As Mb and Hb are highly structurally related a similar situation of two slightly different nitrite ligation geometries in Mb would also be likely to result in two LS species indicating the HS signal to be due to a markedly different binding confirmation. In the Hb study the two LS species were asserted to be due to two *N*-bound forms of Mb-nitrite. However, this assertion was based on the Blumberg Peisach method of *g*-value analysis [8] the validity of which has been questioned [9]. The data presented in the Hb study showed a large HS signal, maximum at pH 10.8, that decreased as the pH was lowered to pH 5.0 which was not discussed. This clearly agrees with the findings presented in thesis and perhaps a similar nitrite binding in Hb may be inferred. Matched-HYSCORE [10] of the  $g_x$ -position associated with the LS Mb-nitrite spectrum described § 6.4.1 revealed that the correlations associated with the Double Quantum (DQ) transitions of the heme and histidine nitrogens became more defined as the pH was lowered from pH 9.5 to 8.5 and to 7.5. This was indicative of a more rigid nitrite binding to Mb with a

---

lowering of pH as would be expected if hydrogen bonding were to be involved as is expected in the *O*-bound case. In § 6.6 the Field-Swept Echo (FSE) spectra of Mb and Mb-nitrite at a number of pH values were presented. These spectra were measured with experimental parameters optimized to a HS species. Spectra originating from HS-Mb samples expected to have water coordinated to the heme were found to display low-field *g*-values (near  $g = 6$ ) markedly different from those that were expected to coordinate *N*-bound nitrite additionally validating the hypothesis. Finally the Electron Nuclear Double Resonance (ENDOR) [11] spectra of the LS-nitrite species in § 6.7.1 did not show an additional nitrogen coupling than those seen in ESEEM or HYSCORE experiments of the same samples, which may have been expected if the LS form was due to *N*-bound nitrite.

In conclusion it is asserted that the hypothesis that nitrite may bind to the heme iron in Mb in both the *O*-bound and *N*-bound forms resulting in a LS and HS signal respectively in the EPR spectrum has been proven.

### 8.1.2 General insights for EPR

During the description of further insights to Mb gained from EPR presented in Chapter 6 two findings highlighted situations in which specific EPR experiments provided a greater or slightly different insight than generally attributed to them.

The application of Double Nuclear Coherence Transfer (DONUT) HYSCORE [12] in § 6.4.2 revealed contributions to the spectra from the  $^{15}\text{N}$  of isotope labeled nitrite which was unresolved in three-pulse ESEEM and HYSCORE experiments. The failure of the experiments to resolve this contribution was attributed to a peak-suppression effect [13]. The DONUT-HYSCORE experiment therefore seems to be more resilient over the standard HYSCORE experiment in this case.

The FSE spectra of the HS systems described in § 6.6 and mentioned above exhibited a low-field *g*-value sensitivity to the heme coordination environment that enabled resolution of different molecules proposed to be coordinated to the heme iron in the HS state. This sensitivity was not seen in corresponding CW-EPR spectra. The increased sensitivity of the

---

pulsed method was theorized to be due to the different relaxation phenomena responsible for the observation of spectra in each case.

### 8.1.3 Density Functional Theory

As discussed in Chapter 7 the findings from Density Functional Theory were qualitative rather than quantitative. The model geometries outlined and in § 7.6.1 resulted in similar final single point energies when optimized using both BP86 [14] and B3LYP [15] functionals and TZVP basis set. If the calculated energies are accurate the *N*-bound mode would appear to be the ground-state but both binding modes of nitrite would appear to be energetically valid depending on the degree of histidine protonation. In their report of *O*-bound nitrite in human Hb [16] Yi and Richter-Addo cite a previous DFT study on an iron porphyrin model system that concluded the *N*-bound form was energetically more stable than the *O*-bound form by  $\sim 4.3$  kcal/mol [17], such systems of course did not include hydrogen bonding residues present in Mb. This thesis has already highlighted the role of hydrogen-bonding to the nitrite binding mode. It would therefore seem unlikely that accurate correlations would exist between the stability of nitrite binding in such model complexes with binding in Mb. The calculations described in this section also reinforced the importance of the distal histidine residue (His64) on the binding mode seen in the mutant protein structures [5].

## 8.2 Role of Mb as a Nitrite Reductase

In § 2.2.2 it was stated that the high intermediate and low-spin states of ferric and ferrous hemes were energetically close to each other. The observation of both the *O*-bound and *N*-bound forms of nitrite to the heme iron in ferric Mb as LS and HS Fe(III) species clearly supports this statement. This spin-state equilibrium may be considered a mechanism by which the substituent components of the protein (porphyrin, amino acid sequence, iron and ligands) interact to dictate the protein function. From the experiments and calculations described in this work it can be seen that the oxygenation of the protein environment (simulated with pH) determines the degree of hydrogen-bonding between the nitrite anion and distal histidine residue. A low-oxygen environment (low pH) promotes hydrogen bonding and the *O*-bound form of nitrite. Conversely a high-oxygen environment (high-pH) makes hydrogen-bonding

---

less likely and favors the *N*-bound form of nitrite. There is evidence that the dynamics of hydrogen-bonding may be related to enzymatic activity in at least one other heme protein [18] and hydrogen-bonding is responsible for differing oxygen binding energies in Mb and Hb from different species [19]. It is therefore proposed that a nitrite reductase activity of Mb may be facilitated by hydrogen bonding. In **Figure 5.1.1.2** the varying spectral contributions of LS Mb, LS Mb-nitrite and the HS signal determined by simulation of the CW-EPR spectra of Mb in the presence of nitrite with time measured at pH 10.8 was shown. It may be seen that over the 120 minutes course of the experiment the contribution from LS Mb-nitrite decreased whilst the LS-Mb contribution increased. During this time the contribution attributed to a HS-Mb species remained approximately constant. The spectra in this case were normalized to the intensity of the advantageously bound iron signal which is assumed to remain constant during the course of the experiment. It may therefore be theorized that the nitrite binds to Mb initially exhibiting both binding modes but that the *O*-bound mode giving rise to the LS-nitrite is reduced (with the aid of hydrogen-bonding) by Mb to nitric oxide which disassociates from the heme resulting in LS Mb-OH<sup>-</sup>. During this reduction the *N*-bound nitrite proposed to be responsible for the observation of the HS signal is not reduced i.e. there is no reductase activity for this form. This indicates that the when found in the *N*-bound form nitrite is being stored by the protein.

This supports the nitrite reductase activity highlighted by Hendgen-Cotta [20] which may be summarized as follows: under normoxic conditions Mb plays the role of a nitric oxide scavenger, protecting the heart from the negative effects of excessive nitric oxide. During hypoxia however, Mb becomes a producer of nitric oxide which is proposed to down-regulate the cardiac energy status and reduce myocardial oxygen consumption. The reductase activity of Mb also leads to the formation of nitric oxide during reperfusion after ischemia which regulates respiration and cellular viability. This complex mechanism cannot be corroborated by the work presented in this thesis, however a similar activity based solely on the presented work may be proposed:

Under normoxic conditions Mb acts as an oxygen storage protein. When oxygen levels in the endothelium begin to decrease oxygen is released by Mb. The protein is now susceptible to nitrite binding. Nitrite may bind in the two conformations highlighted; under mild hypoxia

---

nitrite will be stored by Mb in the *N*-bound form. As hypoxia increases the *O*-bound form will be favored that may be enzymatically reduced to nitric oxide by Mb. As hypoxia increases towards anoxia the findings of § 6.2 (Mb-nitrite at low pH) may be used to assert that Mb stores nitric oxide preventing it from acting as a vasodilatory agent and thus prevents ischemic reperfusion injury. The protein also limits its further nitrite reductase activity until normoxic conditions are met.

### 8.3 Outlook

It had been the intention of this researcher to present ENDOR data of the HS-nitrite case. At the time of writing this had not however, been achieved. The Henry Wellcome Unit for biological EPR was not initially set-up for ENDOR measurements (which are technically more demanding than ESEEM experiments) when this research was undertaken. During the course of the project this was attempted to be rectified. Initial ENDOR experiments presented in § 6.7 were carried out using a radio-frequency (RF) amplifier borrowed from the John Innes Centre (JIC) part of the Norwich Research Park. This amplifier had to be returned shortly after these initial experiments. In order to be able to achieve a more permanent ENDOR capability, further calibration was undertaken using a high-power RF amplifier. The principle of application of this amplifier was proven by the measurement of the ENDOR spectrum of HS aquomet Mb (not presented) which agreed well with the literature [21]. At this time the HS-nitrite sample was also examined but cryogenic constraints prevented the acquisition of a resolved spectrum. Subsequent attempts have been prevented due to the need for a repair of the ENDOR resonator. It is hoped that this will be achieved in the near future and for the experiment to be undertaken successfully.

There is clearly scope for the findings and hypotheses raised in this thesis to be investigated further. The mechanism of action of Mb would perhaps also benefit from examination by techniques more conventionally applied to the determination of reaction rates, for example protein film voltametry for redox reactions, or by a more advanced spectrophotometrical investigation [22].

---

---

## References

1. Copeland, D.M., et al., *Crystal structures of the nitrite and nitric oxide complexes of horse heart myoglobin*. Journal of Inorganic Biochemistry, 2006. **100**(8): p. 1413-1425.
  2. Hofer, P., et al., *Hyperfine Sublevel Correlation (HYSCORE) Spectroscopy - A 2D Electron-Spin-Resonance Investigation of the Squaric Acid Radical*. Chemical Physics Letters, 1986. **132**(3): p. 279-282.
  3. Stoll, S. and A. Schweiger, *EasySpin, a comprehensive software package for spectral simulation and analysis in EPR*. Journal of Magnetic Resonance, 2006. **178**(1): p. 42-55.
  4. Bashford, D., et al., *Electrostatic calculations of side-chain pKa values in myoglobin and comparison with NMR data for histidines*. Biochemistry, 1993. **32**(31): p. 8045-8056.
  5. Yi, J., et al., *The Distal Pocket Histidine Residue in Horse Heart Myoglobin Directs the O-Binding Mode of Nitrite to the Heme Iron*. Journal of the American Chemical Society, 2009. **131**(50): p. 18119-18128.
  6. Deligiannakis, Y., M. Louloudi, and N. Hadjiliadis, *Electron spin echo envelope modulation (ESEEM) spectroscopy as a tool to investigate the coordination environment of metal centers*. Coordination Chemistry Reviews, 2000. **204**: p. 1-112.
  7. Schwab, D.E., J.S. Stamler, and D.J. Singel, *EPR Spectroscopy of Nitrite Complexes of Methemoglobin*. Inorganic Chemistry, 2010. **49**(14): p. 6330-6337.
  8. Blumberg W, E. and J. Peisach, *Low-Spin Compounds of Heme Proteins*, in *Bioinorganic Chemistry*. 1971, AMERICAN CHEMICAL SOCIETY. p. 271-291.
  9. Teixeira, M., et al., *Pitfalls in assigning heme axial coordination by EPR: c-Type cytochromes with atypical Met-His ligation*. FEBS Letters, 1993. **317**(3): p. 233-236.
  10. Liesum, L. and A. Schweiger, *Multiple quantum coherence in HYSCORE spectra*. Journal of Chemical Physics, 2001. **114**(21).
  11. Mims, W.B., *Pulsed ENDOR Experiments*. Proceedings of the Royal Society of London. Series A, Mathematical and Physical Sciences (1934-1990), 1965. **283**(1395): p. 452-457.
  12. Goldfarb, D., et al., *Double Nuclear Coherence Transfer (DONUT)-HYSCORE: A New Tool for the Assignment of Nuclear Frequencies in Pulsed EPR Experiments*. J. Am. Chem. Soc., 1998. **120**(28): p. 7020-7029.
  13. Stoll, S., et al., *Peak suppression in ESEEM spectra of multinuclear spin systems*. Journal of Magnetic Resonance, 2005. **177**(1): p. 93-101.
-

- 
14. Perdew, J.P., *Density-Functional Approximation for the Correlation-Energy of the Inhomogeneous Electron-Gas*. Physical Review B, 1986. **33**(12): p. 8822-8824.
  15. Lee, C.T., W.T. Yang, and R.G. Parr, *Development of the Colle-Salvetti Correlation-Energy Formula into a Functional of the Electron-Density*. Physical Review B, 1988. **37**(2): p. 785-789.
  16. Yi, J., M.K. Safo, and G.B. Richter-Addo, *The Nitrite Anion Binds to Human Hemoglobin via the Uncommon O-Nitrito Mode*. Biochemistry, 2008. **47**(32): p. 8247-8249.
  17. Novozhilova, I.V., et al., *Experimental and density functional theoretical investigations of linkage isomerism in six-coordinate {FeNO}(6) iron porphyrins with axial nitrosyl and nitro ligands*. Journal of the American Chemical Society, 2006. **128**(6): p. 2093-2104.
  18. Radoul, M., et al., *Dynamic Hydrogen-Bonding Network in the Distal Pocket of the Nitrosyl Complex of Pseudomonas aeruginosa cd1 Nitrite Reductase*. Journal of the American Chemical Society, 2011. **133**(9): p. 3043-3055.
  19. Kitagawa, T., et al., *Evidence for hydrogen bonding of bound dioxygen to the distal histidine of oxycobalt myoglobin and haemoglobin*. Nature, 1982. **298**(5877): p. 869-871.
  20. Hendgen-Cotta, U.B., M. Kelm, and T. Rassaf, *A highlight of myoglobin diversity: The nitrite reductase activity during myocardial ischemia-reperfusion*. Nitric Oxide-Biology and Chemistry. **22**(2): p. 75-82.
  21. Fielding, A.J., et al., *Multifrequency Electron Paramagnetic Resonance Characterization of PpoA, a CYP450 Fusion Protein that Catalyzes Fatty Acid Dioxygenation*. Journal of the American Chemical Society, 2011. **133**(23): p. 9052-9062.
  22. Shiva, S., et al., *Deoxymyoglobin is a nitrite reductase that generates nitric oxide and regulates mitochondrial respiration*. Circulation Research, 2007. **100**(5): p. 654-661.
-

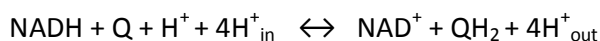
---

# 1 Appendix **S-band CW-EPR: Complex I**

---

## 1.1 Introduction

Complex I (NADH dehydrogenase) is the first enzyme in the electron-transfer chain (ETC) although initially discovered in mitochondria [1] it was subsequently found in several eubacteria. It catalyses the first stage in the mitochondrial ETC, the reduction of ubiquinone (Q) by Nicotinamide adenine dinucleotide (NADH) and couples this to the translocation of four protons across the inner-mitochondrial membrane [2, 3].



Thus Complex I is able to contribute to the proton-motive force that generates ATP production. It is by far the largest and also most complicated enzyme within the ETC. These factors have hindered the determination of its molecular structure despite the fact it was first purified from bovine heart mitochondria over 40 years ago [1]. The realization that complex I is involved in a number of degenerative processes and pathological conditions [4, 5] has led to increased efforts for the determination of its structure. The low resolution structure of Complex I was recently solved [6].

## 1.2 Structure

Complex I is a multi-subunit enzyme found in many different organisms. Within all of these organisms a common set of 14 subunits has been discovered and it has been shown that these subunits are sufficient for energy transduction [7, 8]. **Figure 1.2-1** shows the Structure of the Hydrophilic Domain of Complex I from *Thermus thermophilus* 2FUG [9]. Iron Sulphur clusters in the diagram are labeled as per the Ohnishi convention [10]. The orientation of the protein with respect to the mitochondrial membrane is also shown.

---

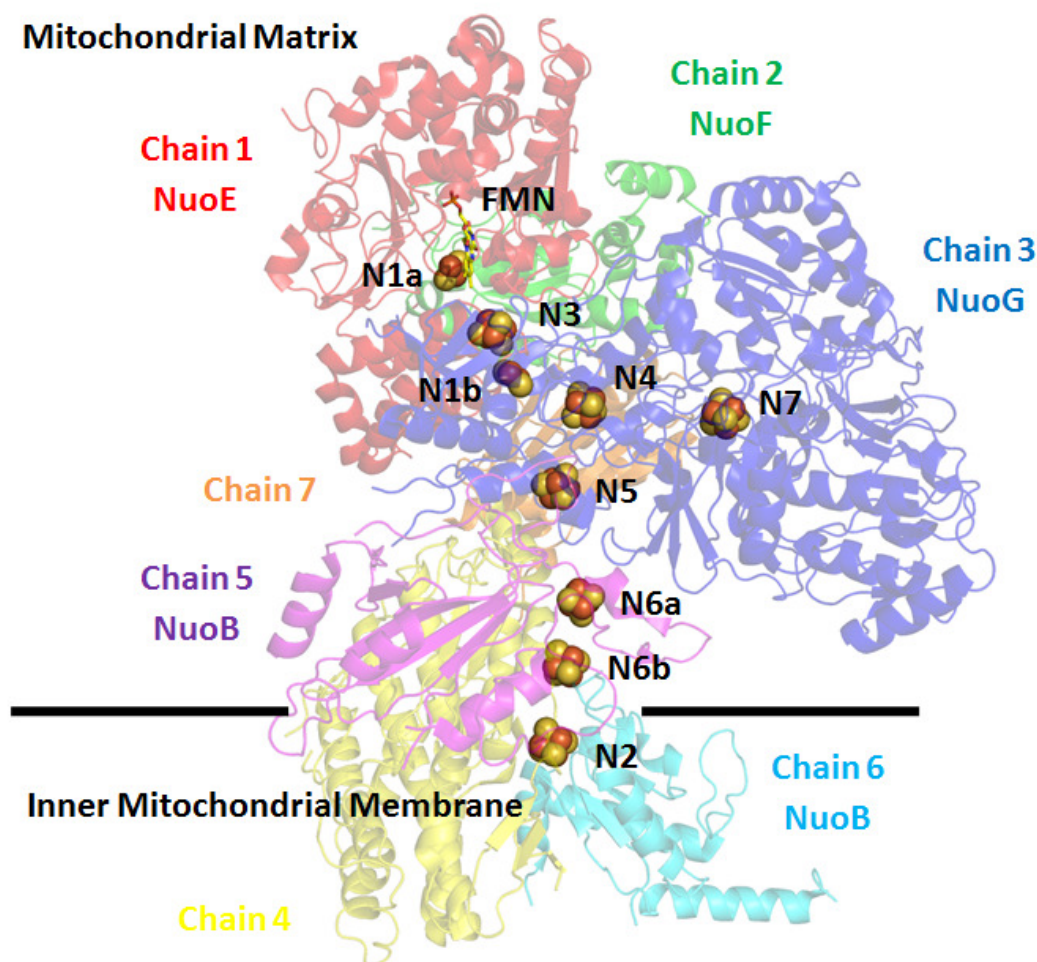


Figure 1.2-1, Structure of the hydrophilic domain of Complex I from *Thermus thermophilus* 2FUG [9] Ohnishi nomenclature used for iron-sulphur cluster labels. NuoF etc. indicate *E. coli* subunit labeling.

The redox centres found within this core are flavine mononucleotide (FMN) and up to nine iron-sulphur clusters [11]. For most organisms seven of these subunits have been found to be predominantly hydrophilic and encoded in the nucleus, and the other seven to be predominantly hydrophobic and encoded within the mitochondria. This has led to speculation that the hydrophilic and hydrophobic portions of the enzyme evolved separately and later joined to produce complex I. Electron microscopy initially performed on *Neurospora crassa* [12], revealed the now familiar L-shaped structure of complex I. This structure can be thought of as composed of two units, one bound within the membrane and the other protruding into the matrix for mitochondria and into the cytoplasm for bacteria. In addition to this central

---

core mitochondrial complex I contains up to 32 additional subunits producing a total molecular mass in excess of 1000 kDa [13]. The function of these is largely unknown, and many show sequence similarities to other proteins. This area is being investigated more fully by the study of complex I from various organisms. Investigation of the hydrophilic domain of complex I from *Thermus thermophilus* [9] has suggested a transfer of electrons from flavine to quinone via a chain of seven iron-sulphur clusters. One iron-sulphur cluster termed N7 is located too far from the other clusters to be able to transfer electrons effectively [14], and it is supposed that it may act as an anti-oxidizing cluster.

Cluster N2 is uniquely coordinated to two consecutive cysteines (Cys) and it is likely that this has some importance for the mechanism of coupling between electron transfer and proton translocation. The midpoint potential of this cluster is also pH-dependant, suggesting its reduction is coupled to proton binding [15]. It has been discovered that the redox components with the lowest redox potentials are located within the peripheral arm, whilst the cluster N2 with the highest value is located close to the interface between this arm and the membrane [16]. It has been proposed that complex I was assembled from pre-existing units during its evolution [17], and this may explain the presence of so many iron-sulphur clusters [9]. Different numbers of iron-sulphur clusters have been identified within complex I depending on the origin of the enzyme. In the reduced form these clusters possess the  $S = 1/2$  paramagnetic spin state, and so may be detected using EPR at low temperatures. Bovine Heart mitochondrial complex I contains six EPR detectable iron-sulphur clusters designated according to their increasing spin-relaxation rates as: N1a, N1b, N2, N3, N4, and N5 [11]. Examination of the yeast *Yarrowia Lipolytica* indicated five iron-sulphur clusters N1, N2, N3, N4 and N5 [18], and within *N. crassa* EPR spectroscopy has only been able to locate four clusters N1, N2, N3 and N4 so far [19]. Both bi-nuclear [ $\text{Fe}_2\text{S}_2$ ] and tetra-nuclear [ $\text{Fe}_4\text{S}_4$ ] clusters have been found. Bi-nuclear clusters can be detected at generally higher temperatures (> 30 K) than tetra-nuclear clusters (< 20 K) due to their slower spin-relaxation rates.

---

### 1.3 The Present Conflict within Complex I

The research group of Tomoko Ohnishi has been active in the field of Complex I research from multiple species since the 1970's. Much of the nomenclature commonly and consistently used to refer to the individual Fe-S clusters originated from this time from Ohnishi and from the initial EPR studies of mitochondria of Beinert and Orme-Johnson [20]. A recent paper [21] from the group of Judy Hirst, regarding Complex I from *E. coli* proposed that the EPR signals commonly attributed to N4 and N5 had been miss-assigned.

The paper puts forward two areas for contention:

- The EPR spectrum commonly attributed to Fe-S cluster N4 originates from the NuoL subunit not the NuoG subunit as consensus would have it.
- The N5 EPR spectrum is produced by a conserved cysteine ligated [4Fe-4S] cluster in NuoG not a 3Cys-His ligated cluster.

Hirst re-examined previous data regarding g-values of Fe-S clusters from Complex I from various species and used this data to state that N5 had been miss-assigned to N4, and that its previous initial assignment had not taken into account the N5 cluster (at this time it was not thought to be a constituent of the bacterial enzyme). However, Hirst also states within this paper that significant perturbation of the cluster environment within the NuoG subunit resulting in a severely modified N4 EPR signal could not be dismissed.

Hirst's group were also unable to detect cluster N5, they theorized that this may be due to two reasons:

- A lower reduction potential might exist in Complex I than the NuoG subunit. This may cause N5 not to be reduced and therefore be EPR silent.
- N5 may have been subject to additional inter-cluster interactions increasing its' relaxation rate and leading to the signal becoming too broad to be resolved.

It should be noted however that the EPR parameters used by Hirst's group (temp > 5 K and MW power 0.1mW) do not lend themselves to the detection of the fast-relaxing N5 cluster.

---

The group used the comparison of EPR detected for several different ligation mutations as their basis for stating N5 is due to a 4 Cys ligated [4Fe-4S] cluster.

In *P. denitrificans* a mutation of the His ligand of 4Fe[G]H to Cys yielded a protein containing a bi-nuclear and a tetra-nuclear cluster. The tetra-nuclear cluster displayed g-values indicative of the N5 cluster [22]. The same mutation in the groups *E. Coli* NuoG-MBP (Maltose-Binding Protein) showed no change in the EPR spectra compared with the wild-type strain. However mutation of the 4Fe[G]C led to spectra retaining the features of N7 but lacking those of N5. In *Y. lipolytica* the His ligand of 4Fe[G]H was mutated to Ala [23] and neither the N4 or N5 spectra were affected.

Recently Ohnishi has published a paper [24] to refute the claims made by Hirst. This paper explains some of the historical background to the assignment of EPR spectra to specific Fe-S clusters. Hirst's initial assertion that the EPR spectrum commonly attributed to Fe-S cluster N4 originates from the NuoI subunit not the NuoG subunit was dismissed by Ohnishi on the grounds that the knockout mutations used to assign N4 to the NuoG subunit did not contain a NuoI subunit. The paper also justifies the ligation of cluster N5 by His 3Cys. It confirms the historical point that N5 was not originally thought to be an integral part of Complex I, as its total spin concentration was found to be only 0.25/complex I although all other Fe-S clusters were found to be stoichiometric. This sub-stoichiometry could be explained however if this cluster had a mixed  $S = 1/2$  and  $S = 3/2$  ground states. A similar stoichiometry had been seen for the tetra-nuclear Fe-S cluster in *Azotobacter vinelandii* [25] and Mössbauer analysis was used to determine the ground states. An  $S = 3/2$  ground state will correspond to a g-value  $\sim 5$ , EPR detection of which requires much higher enzyme concentration than detection of an  $S = 1/2$  ground state. A sub-stoichiometric N5 cluster was also reported for complex I from the yeast *Y. lipolytica* [18]. In an attempt to detect N5 by EPR spectroscopy in *E. coli*, which has not previously been achieved Ohnishi's group constructed an extended series of mutant strains of the candidate ligand His 101 from the NuoG subunit. In the mutated sub-complexes no NuoI or NuoB sub-units were present, this removed Fe-S clusters N6a, N6b and N2 from the sub-complex. EPR experiments over a range of temperatures and MW powers indicated strong cross-relaxation phenomena between the spins of clusters N4 and N5. Comparison of the EPR spectra of N4 and N5 within these mutants at these range of EPR parameters

---

---

suggested to Ohnishi's group that the assignment of His 3Cys ligation to N5 was correct. Both papers referred to Waletko et al.[23], who also performed mutagenesis on the conserved His 3Cys residue and examined the effect on the EPR spectra of the N5 cluster. In this paper it was reported that the spectra of all clusters within the sub-complex underwent no alterations. Hirst used this as a basis for her assertion of miss-assignment, whereas Ohnishi found the papers findings hard to rationalize. Ohnishi states strongly that the EPR spectrum of cluster N4 is particularly sensitive to its micro-environment. A fact that she states was overlooked by Hirst. Some situations Ohnishi has given where the N4 spectrum varied due to its environment are as follows:

- Sub-Mitochondrial Particles (SMP) prepared from pigeon-heart mitochondria, displayed a large shift in the mid-point redox potential for cluster N4, whereas they remained constant for other Fe-S clusters[26].
- In an *N. crassa* Complex I system containing only Fe-S clusters N1, N3 and N4, the spectra of N1 and N3 remained the same but the EPR spectra of N4 was significantly broadened[27].

This variation in N4 spectra could lead to the miss-assignment of the N4 cluster by Hirst.

#### **1.4 Experimental Procedure**

In an attempt to gain more insight into the assignment of EPR spectra to Fe-S clusters within Complex I Torsten Reda from Judy Hirst's research group in Cambridge analyzed Complex I from bovine heart mitochondria at a potential of  $\sim -1$  V. The EPR spectra of this could then be compared with those from higher potentials and from the 24 kDa subunit and flavo-protein subunit. By performing X-band CW-EPR at various temperatures he stated that spectrum N1a from the 24 kDa (analogous to NuoE) subunit was not observable by EPR at any potential. N1b from the 75 kDa subunit (analogous to NuoG) exhibited a lower potential than clusters N3, N4 and N5. In the lowest potential sample, the spectra of cluster N5 was observed at unusually high temperatures. It was stated that this indicated a significant change to the cluster, or that another cluster had very similar g-values. The relaxation rate of N1b was seen to increase

---

probably due to the reduction of a near-by cluster, and a new feature with a g-value of 2.17 was seen. This new feature was attributed to an interaction between two reduced clusters.

S-band spectroscopy was performed on the Complex I samples at pH 7 [28] poised at reduction potentials of -400 mV, -300 mV and -1000 mV. The EPR spectra from 1300 G to 1600 G at S-band (MW frequency of  $\sim 4$  GHz) were measured at 20 K, 12 K, 8 K and 5K. They were then compared with simulations produced using the EasySpin [29] simulation module for Matlab. The g-values and line widths for the simulation in each reduction potential were taken from data supplied by Reda. The g-values and line-widths used in the simulation of each Fe-S cluster are shown in **Table 1-1**.

Cluster	Reduction						
	Potential (V)	$g_z$	$g_y$	$g_x$	$L_z$	$L_y$	$L_x$
<b>N1b</b>	-	2.03	1.949	1.936	0.6	0.4	0.5
<b>N2</b>	-	2.061	1.931		0.5	0.8	
	-0.3V			1.874	1.5		1.2
<b>N3</b>	-1V	2.048	1.932	1.869	1.1	0.5	1.8
	-0.3	2.115	1.936	1.890	1.5		1
<b>N4</b>	-1	2.116	1.945	1.887	1.5		
	-0.3	2.070	1.934	1.905		0.5	
<b>N5</b>	-1	2.076	1.937	1.904	0.6	0.4	0.8
<b>N<math>\alpha</math></b>	-1	2.168	1.925	1.918	1.8	1	0.5

**Table 1-1, Simulation parameters for individual Fe-S clusters of Complex I at pH 7, and their reduction state. (Values from T. Reda).**

A simulated spectrum using the  $g$ -value parameters presented in Table 1-1 is shown in **Figure 1.4-1**. It is clear that there is a large degree of spectral overlap at the  $g_y$ -position. The contribution from each cluster is however potentially resolvable from the  $g_z$ -value.

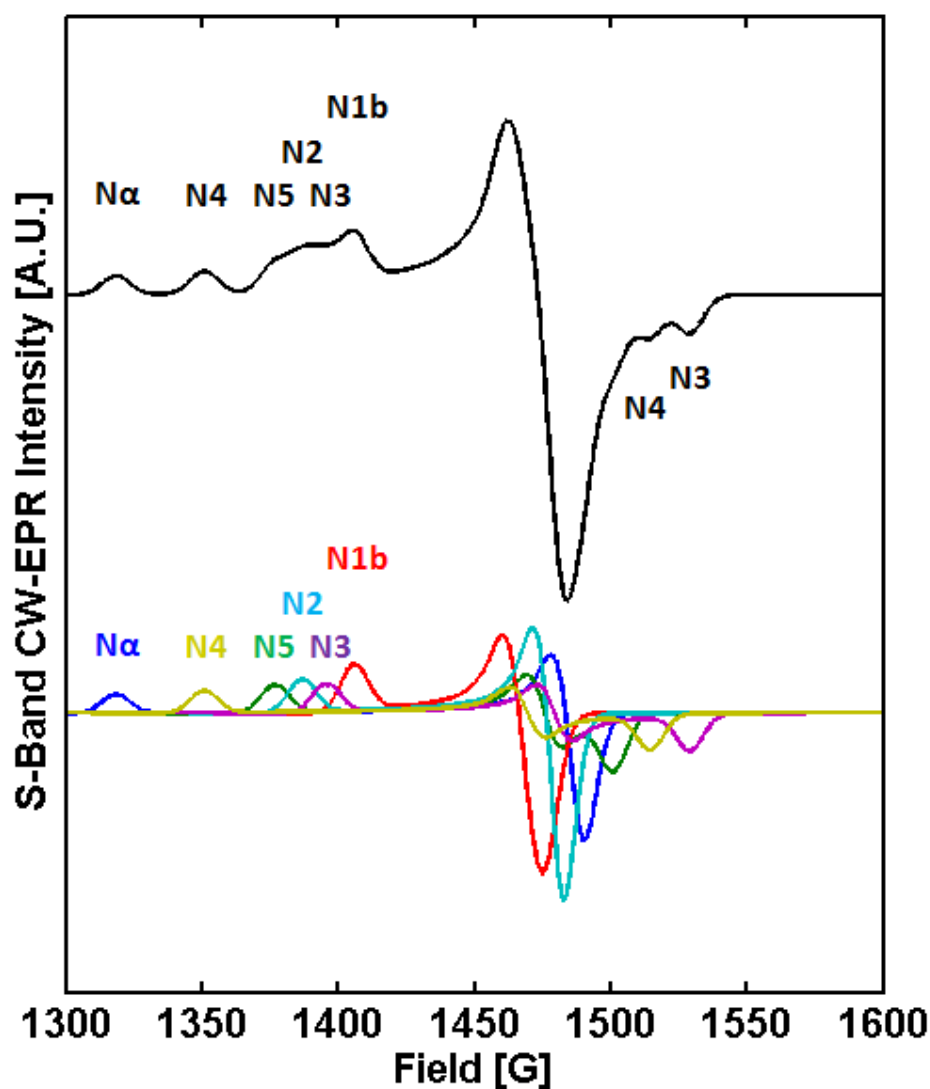


Figure 1.4-1, Simulation of complex I S-band CW-EPR using parameters presented in Table 1-1.

The magnetic field was calibrated using a DPPH standard. An 80 ms time constant, a 100 KHz modulation frequency, 10 G modulation amplitude and a MW power of 0.5 mW were used unless otherwise stated.

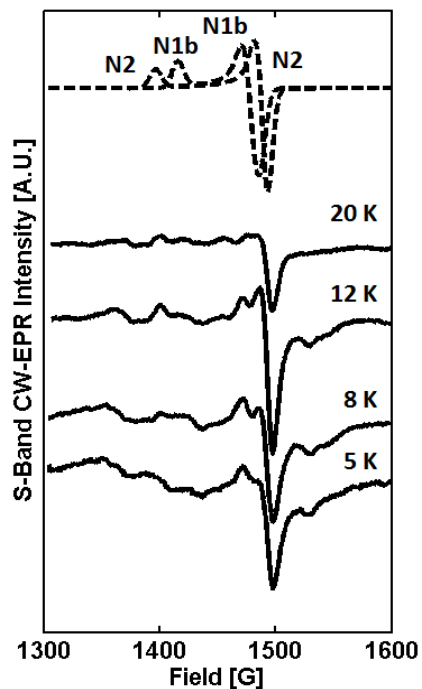


Figure 1.4-2, S-band EPR spectra of -400 mV Complex I at 4.02814 GHz. 20 K, 12 K, 8 K and 5 K measurements shown in comparison with simulations of clusters N1b and N2 (top). Experimental parameters: time constant 80 ms, modulation frequency 100 kHz, modulation amplitude 10 G. and a MW power of 0.5 mW.

**Figure 1.4-2** shows the Complex I sample poised at -400 mV. At this redox potential only the Fe-S clusters N1b and N2 should be reduced, for this reason the simulation plotted on this figure only represents these clusters. It can be seen that the general features of the simulation seem to fit the experimental data well, the best fitting being the spectrum obtained at 12 K.

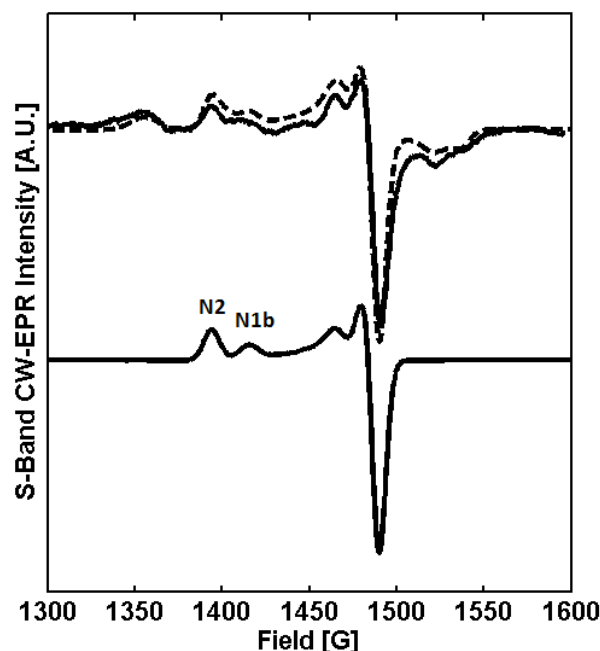


Figure 1.4-3, -400 mV poised Complex I spectrum at 12 K (top-solid), compared with simulation of clusters N1b and N2 (bottom solid). Stoichiometry of N1b altered to 0.3/complex and  $g_y$  changed from 1.949 to 1.955 to obtain a better fit. Dashed line indicates simulation of complete spectrum : [N1b N2 N3 N4].

**Figure 1.4-3** shows the 12 K spectrum of the -400 mV poised Complex I sample, plotted with simulations of the N1b and N2 Fe-S clusters. The contribution from both clusters can clearly be seen in the experimental spectrum. To obtain a better fit between the experiment and simulation the stoichiometry of the two simulated clusters as well as the  $g_y$ -tensor of N1b were altered. The justification for a variation of the given  $g$ -values is given above from the possible miss-calibration of the X-band field-axis, or by cluster N1b being especially sensitive to its' micro-environment [24]. It was changed from a value of 1.949 to 1.955. Variation in the stoichiometry of N1b relative to N2 revealed a "best-fit" when the content of N1b was lowered to 0.3/Complex. This variation from the stoichiometry (1:1) normally observed for this cluster [11, 24], could suggest a strong dependence on the local environment for the EPR spectra of Fe-S cluster N1b. However there is also some evidence [30] for a different stoichiometry of this Fe-S cluster.

The 12 K spectrum of the -300 mV potential Complex I sample is shown in **Figure 1.4-4**. The values used for the simulation were the same as those used for the simulation of the -400 mV sample presented in **Figure 1.4-2** save that the contribution of the Fe-S cluster designated as N2 was omitted.

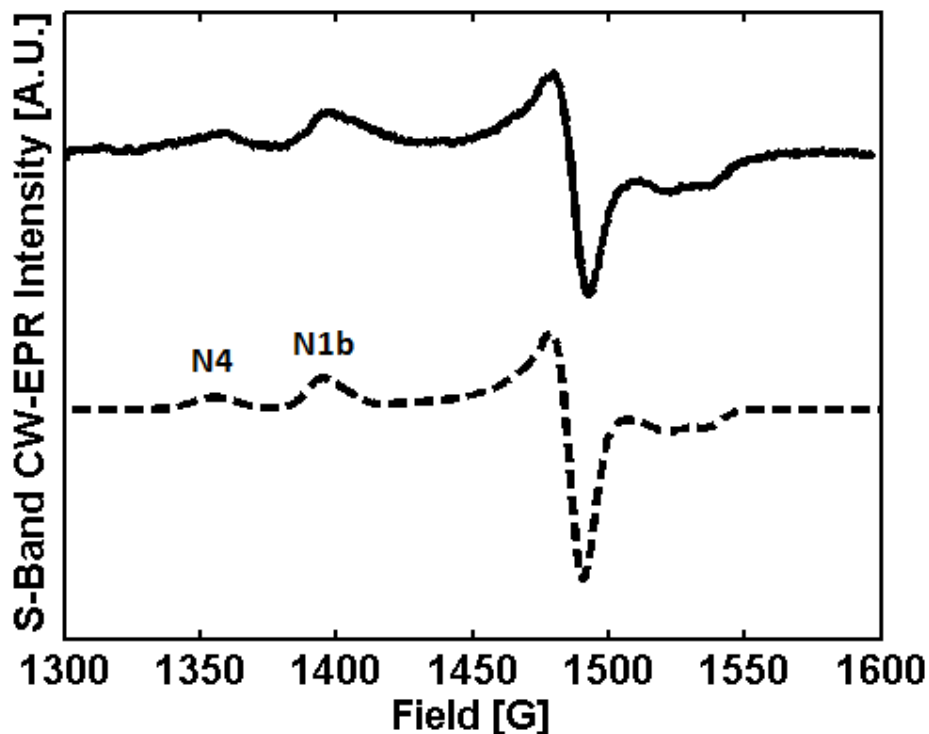


Figure 1.4-4, S-band EPR spectra of -300 mV potential complex I measured at 12 K (top) Simulation (bottom) includes FeS clusters N2, N3 and N4. i.e. no cluster N2.

It is clear from the preceding two spectra that the reduction potential of the N2 cluster is between -300 and -400 mV. This is not consistent with a recently published pulsed-EPR study using samples from the same group [31]. However, N2 is known to have a pH dependant reduction potential [32] and so it is possible this has influenced the reduction potential of the cluster in this case. The spectra of complex I at a reduction potential of -1 V measured at 20, 12, 8 and 5 K is shown in **Figure 1.4-5**, as expected these spectra exhibit the contribution of all the FeS clusters proposed in **Table 1-1**.

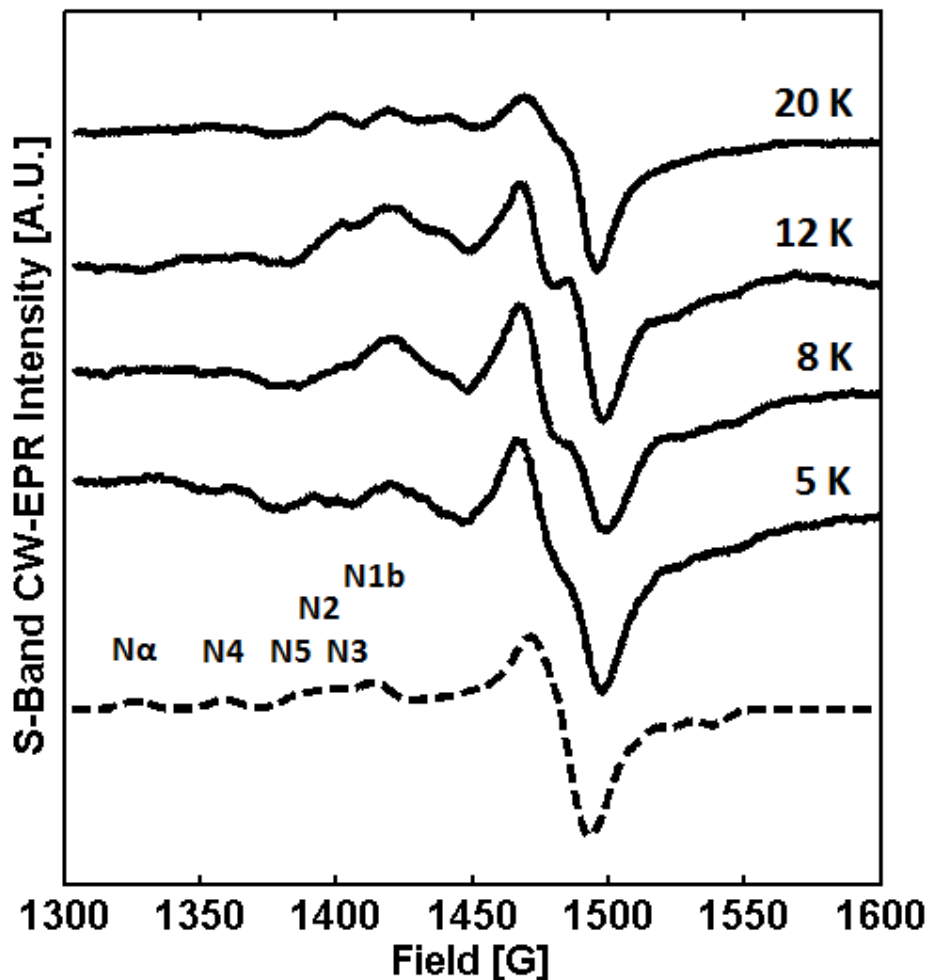


Figure 1.4-5, S-band EPR spectra of -1000 mV poised complex I sample. 20 K, 12 K, 8 K and 5 K measurements shown in comparison with simulations of clusters N1b, N2, N3, N4, N5 and  $N\alpha$ .

## 1.5 Conclusion

S-band CW-EPR was undertaken in an attempt to prove the Hirst *et al*s assertions outlined in § 1.3. The lower Zeeman splitting experienced at this frequency did not however, increase the spectral resolution from the X-band data. In order to do this Hirst undertook a W-band EPR investigation with the application of the Double Electron-Electron Resonance (DEER) technique [31]. This was not a failure of the technique however, which was proven to be able to successfully determine the contribution to the spectra from a number of spectrally overlapping paramagnetic centres.

---

## References

1. Hatefi, Y., A.G. Haavik, and D.E. Griffiths, *Studies on the Electron Transfer System. XL. Preparation and Properties of Mitochondrial DPNH-Coenzyme Q Reductase*. J. Biol. Chem., 1962. **237**(5): p. 1676-1680.
  2. Hirst, J., *Energy transduction by respiratory complex I—an evaluation of current knowledge*. Biochem. Soc. Trans., 2005. **33**(Pt 3): p. 525-529.
  3. Wikström, M., *Two protons are pumped from the mitochondrial matrix per electron transferred between NADH and ubiquinone*. FEBS Letters, 1984. **169**(2): p. 300-304.
  4. Cadenas, E. and K.J.A. Davies, *Mitochondrial free radical generation, oxidative stress, and aging*. Free Radical Biology and Medicine, 2000. **29**(3-4): p. 222-230.
  5. Wallace, D.C., *Mitochondrial Diseases in Man and Mouse*. Science, 1999. **283**(5407): p. 1482-1488.
  6. Efremov, R.G., R. Baradaran, and L.A. Sazanov, *The architecture of respiratory complex I*. Nature, 2010. **465**(7297): p. 441-445.
  7. Hirst, J., et al., *The nuclear encoded subunits of complex I from bovine heart mitochondria*. Biochimica et Biophysica Acta (BBA) - Bioenergetics, 2003. **1604**(3): p. 135-150.
  8. Weidner, U., et al., *The Gene Locus of the Proton-translocating NADH : Ubiquinone Oxidoreductase in Escherichia coli: Organization of the 14 Genes and Relationship Between the Derived Proteins and Subunits of Mitochondrial Complex I*. Journal of Molecular Biology, 1993. **233**(1): p. 109-122.
  9. Sazanov, L.A. and P. Hinchliffe, *Structure of the Hydrophilic Domain of Respiratory Complex I from Thermus thermophilus*. Science, 2006. **311**(5766): p. 1430-1436.
  10. Ohnishi, T., C.I. Ragan, and Y. Hatefi, *EPR studies of iron-sulfur clusters in isolated subunits and subfractions of NADH-ubiquinone oxidoreductase*. J. Biol. Chem., 1985. **260**(5): p. 2782-2788.
  11. Ohnishi, T., et al., *Structure-function studies of iron-sulfur clusters and semiquinones in the NADH-Q oxidoreductase segment of the respiratory chain*. Biochimica et Biophysica Acta (BBA) - Bioenergetics, 1998. **1365**(1-2): p. 301-308.
  12. Hofhaus, G., H. Weiss, and K. Leonard, *Electron microscopic analysis of the peripheral and membrane parts of mitochondrial NADH dehydrogenase (Complex I)*. Journal of Molecular Biology, 1991. **221**(3): p. 1027-1043.
-

13. Guénebaut, V., et al., *Three-dimensional structure of NADH-dehydrogenase from Neurospora crassa by electron microscopy and conical tilt reconstruction*. Journal of Molecular Biology, 1997. **265**(4): p. 409-418.
  14. Page, C.C., et al., *Natural engineering principles of electron tunnelling in biological oxidation-reduction*. Nature, 1999. **402**(6757): p. 47-52.
  15. Ohnishi, T., *Iron-sulfur clusters/semiquinones in Complex I*. Biochimica et Biophysica Acta (BBA) - Bioenergetics, 1998. **1364**(2): p. 186-206.
  16. Weiss, H., et al., *The respiratory-chain NADH dehydrogenase (complex I) of mitochondria*. European Journal of Biochemistry, 1991. **197**(3): p. 563-576.
  17. Finel, M., *Organization and evolution of structural elements within complex I*. Biochimica et Biophysica Acta (BBA) - Bioenergetics, 1998. **1364**(2): p. 112-121.
  18. Djafarzadeh, R., et al., *Biophysical and structural characterization of proton-translocating NADH-dehydrogenase (complex I) from the strictly aerobic yeast Yarrowia lipolytica*. Biochimica et Biophysica Acta (BBA) - Bioenergetics, 2000. **1459**(1): p. 230-238.
  19. Guénebaut, V., et al., *Consistent structure between bacterial and mitochondrial NADH:ubiquinone oxidoreductase (complex I)*. Journal of Molecular Biology, 1998. **276**(1): p. 105-112.
  20. Orme-Johnson, N.R., et al., *EPR detectable electron acceptors in submitochondrial particles from beef heart with special reference to the iron-sulfur components of DPNH-ubiquinone reductase*. Biochemical and Biophysical Research Communications, 1971. **44**(2): p. 446-452.
  21. Yakovlev, G., T. Reda, and J. Hirst, *Reevaluating the relationship between EPR spectra and enzyme structure for the iron sulfur clusters in NADH:quinone oxidoreductase*. Proceedings of the National Academy of Sciences, 2007. **104**(31): p. 12720-12725.
  22. Yano, T., et al., *Characterization of Cluster N5 as a Fast-relaxing [4Fe-4S] Cluster in the Nqo3 Subunit of the Proton-translocating NADH-ubiquinone Oxidoreductase from Paracoccus denitrificans*. J. Biol. Chem., 2003. **278**(18): p. 15514-15522.
  23. Waletko, A., et al., *Histidine 129 in the 75-kDa Subunit of Mitochondrial Complex I from Yarrowia lipolytica Is Not a Ligand for [Fe4S4] Cluster N5 but Is Required for Catalytic Activity*. J. Biol. Chem., 2005. **280**(7): p. 5622-5625.
  24. Ohnishi, T. and E. Nakamaru-Ogiso, *Were there any "misassignments" among iron-sulfur clusters N4, N5 and N6b in NADH-quinone oxidoreductase (complex I)?* Biochimica et Biophysica Acta (BBA) - Bioenergetics. **In Press, Uncorrected Proof**.
-

- 
25. Moura, J.J., et al., *Interconversions of [3Fe-3S] and [4Fe-4S] clusters. Mossbauer and electron paramagnetic resonance studies of Desulfovibrio gigas ferredoxin II.* J. Biol. Chem., 1982. **257**(11): p. 6259-6267.
  26. Ohnishi, T., *Thermodynamic and EPR characterization of iron-sulfur centers in the NADH-ubiquinone segment of the mitochondrial respiratory chain in pigeon heart.* Biochimica et Biophysica Acta (BBA) - Bioenergetics, 1975. **387**(3): p. 475-490.
  27. Wang, D.-C., et al., *The iron-sulfur clusters in the two related forms of mitochondrial NADH: ubiquinone oxidoreductase made by Neurospora crassa.* European Journal of Biochemistry, 1991. **197**(1): p. 257-264.
  28. Reda, T., C.r.D. Barker, and J. Hirst, *Reduction of the Iron-Sulfur Clusters in Mitochondrial NADH:Ubiquinone Oxidoreductase (Complex I) by Eull-DTPA, a Very Low Potential Reductant†.* Biochemistry, 2008. **47**(34): p. 8885-8893.
  29. Stoll, S. and A. Schweiger, *EasySpin, a comprehensive software package for spectral simulation and analysis in EPR.* Journal of Magnetic Resonance, 2006. **178**(1): p. 42-55.
  30. van Belzen, R., A. Mariette, and S.P.J. Albracht, *On the stoichiometry of the iron-sulphur clusters in mitochondrial NADH: ubiquinone oxidoreductase.* European Journal of Biochemistry, 1992. **209**(3): p. 1019-1022.
  31. Roessler, M.M., et al., *Direct assignment of EPR spectra to structurally defined iron-sulfur clusters in complex I by double electron-electron resonance.* Proceedings of the National Academy of Sciences of the United States of America, 2010. **107**(5): p. 1930-1935.
  32. Ingledew, W.J. and T. Ohnishi, *An analysis of some thermodynamic properties of iron-sulphur centres in site I of mitochondria.* Biochem. J., 1980. **186**(1): p. 111-117.
-

---

---

## 2 Appendix PELDOR: Ferric Binding Protein

---

### 2.1 Introduction

Distance determination in proteins and biomolecules using pulsed EPR (electron paramagnetic resonance) techniques is becoming an increasingly popular and accessible technique [1]. PELDOR (pulsed electron-electron double resonance), is a technique designed for distance determination over a nanoscopic scale. Here, ferric binding protein (Fbp) is used to demonstrate the practicability of this technique to Cu (II) metalloproteins. PELDOR is usually applied to bi-radicals or endogenous radicals, and distance determination using pulsed EPR of metal containing centres in biomolecules has been restricted to relaxation experiments, with few exceptions [2, 3]. PELDOR distance measurements between a Cu (II) ion and a nitroxide have previously only been reported for model compounds [4, 5].

Fbp as the name suggests usually, contains a Fe (III) ion centre. For the purposes of this investigation the Fe (III) ion was removed and replaced by a Cu (II) ion, after a nitroxide spin-label was added to the Fbp using site directed spin-labelling (SDSL). PELDOR was then applied to measure the distance between the two centres.

Simulation methods were then employed to fully investigate these data and allow a quantitative interpretation of the copper nitroxide PELDOR data. The observed PELDOR time traces were analysed using DEER analysis [6]

---

## 2.2 Ferric Binding Protein

Iron is an essential nutrient for nearly all living cells [7] however in spite of its abundance on earth, it is biologically unavailable in most environments. In aerobic inorganic environments of biological pH, iron is essentially in the Fe III form that usually forms insoluble oxy-hydroxide polymers. Different organisms have developed a variety of specialized mechanisms for the acquisition, transportation and storage of iron [8, 9]. Many pathogenic bacteria that cause disease within human hosts rely on iron-transport proteins as their primary iron source. Transferrin is the iron-transport protein for mammals, and as such is the predominant iron source for pathogenic bacteria infecting humans such as *Neisseria gonorrhoeae* [10].

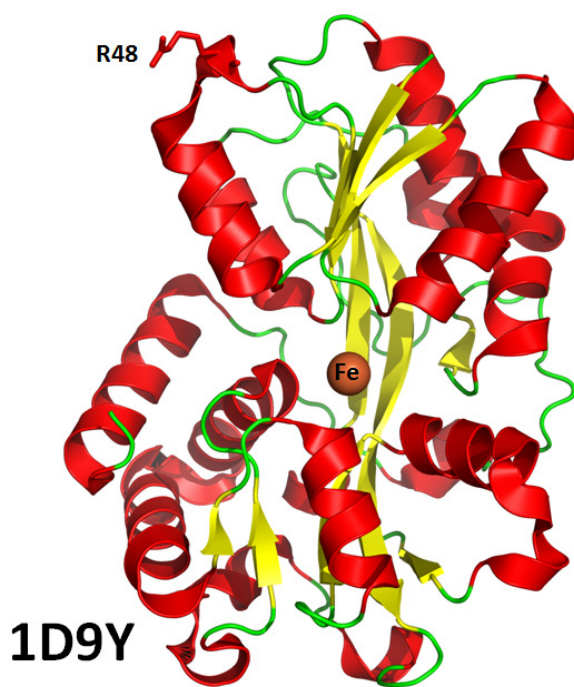


**Figure 2.2-1, Structure of ferric binding protein (FbpA) from *N. gonorrhoeae* 1D9Y (unpublished) Indicating location of iron and residue R48.**

These bacteria have developed efficient iron sequestering proteins in order to steal iron from their hosts. Termed ferric binding proteins (FBPs) **Figure 2.2-1** they have a considerable structural similarity to one lobe of transferrin, but without sequence homology (from studies of *Hemophilus influenzae* hFBP) [11]. The Fe(III) binding site in hFBP is similar to the two Fe(III) binding sites in transferrin, each containing two *cis*-Tyr and one His ligand, but with Fbp

containing a Glu residue instead of the Asp found in transferrin. One key feature to note is that the synergistic anion facilitating Fe(III) binding in each protein is different. In hFBP bonding is mediated via a mono-dentate tetrahedral phosphate anion in conjunction with a water molecule. Transferrins however, utilize bidentate bi-carbonate.

## 2.3 PELDOR

Magnetic resonance techniques may attempt to measure distances between selected sites, based on the proportionality of the dipole-dipole coupling  $\omega_{dd}$  between two spins to the inverse cube of the distance between them ( $r$ ).

$$\omega_{dd}(\theta, r) = \frac{2\pi g_1 g_2}{g_e^2} (3 \cos^2 \theta - 1) \frac{52.04}{r^3} [\text{MHz} / \text{nm}^3]$$

$g_e$  is the g-value of a free electron,  $g_1$  and  $g_2$  are the g-values of the two paramagnetic spins,  $\theta$  represents the angle between a vector connecting the two spins and the static field  $\mathbf{B}_0$ .

EPR techniques, which rely on a measurement of the coupling between unpaired electron spins are currently able to determine this distance between the range of 0.5 to 8 nm [12].

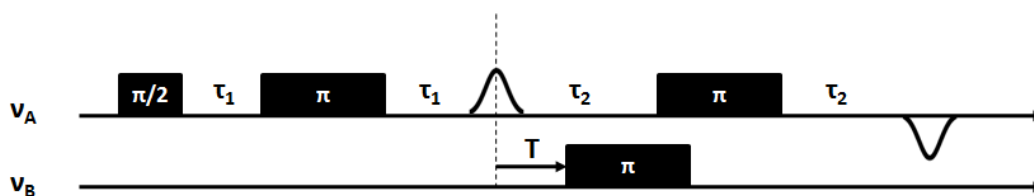


Figure 2.3-1, PELDOR pulse sequence.  $\nu_b$  and  $\nu_a$  indicate pump and observe frequencies.

One such method capable of this determination is PELDOR [13] sometimes also termed DEER (Double Electron-Electron Resonance) [14, 15]. A typical pulse sequence for this is the 4-Pulse PELDOR shown in **Figure 2.3-1**.

In this scheme a two pulse Hahn echo sequence with fixed pulse separation  $\tau_1$  at the observation frequency  $\nu_a$ , creates an echo from the resonant spins (A spins). An inversion pulse at the pumping frequency  $\nu_b$  ( $\nu_a \neq \nu_b$ ) and time  $t$ , flips spins resonant with this second frequency (B spins). This stimulated spin-flip is detected by the A spins via the dipolar

coupling, as a change in the Larmor frequency by  $\pm$  the dipolar coupling ( $\omega_{\text{dip}}$ ), the A spins then precess at this altered frequency in the transverse plane, which leads to an imperfect refocusing of the A spins at the echo time  $2\tau_1$ . Varying time the position  $t$  of the inversion pulse alters the de-phasing angle and induces a periodic modulation of the echo intensity. Another  $\pi$ -pulse at the observer frequency  $\nu_A$  refocuses the inverted echo to compensate for the system dead-time (the time after the creation of a pulse where the signal is not observable or is distorted by resonator ringing). It is the oscillation of the intensity of the refocused echo that contains information regarding the dipolar interaction. However this refocused echo decays with the phase-memory time  $T_M$  after the first observe pulse, and as the oscillation in echo intensity of a PELDOR experiment occurs over a larger timescale as the distance between the two species increases, this leads to a requirement for longer  $T_M$  times. These considerations greatly affect the choice of parameters needed for a successful experiment.

## 2.4 Experimental Procedure

Wild-type and R48C (from site-directed mutagenesis) mutant forms of FbpA from *N. gonorrhoeae* were produced by Dr. Dominic Campopiano currently (University of Edinburgh), and given to Dr. Gaye White at the University of East Anglia, who kindly made them available to this researcher. The relaxation properties of Fe(III) and anisotropy of its g-tensor in Fbp make distance determination to a nitroxide spin label via the dipole-dipole interaction experimentally challenging. For this reason PELDOR measurements involving nitroxide spin-labels and/or metal centres have frequently been conducted on either model compounds [4, 5] for Cu(II) to spin-label distances, or Cu(II) replaced native Fe(III)-containing proteins for metal-centre to metal-centre distance determination [2]. So far the measurement of distances between Cu(II) centres and spin labels in bio-macromolecules has not been achieved. The holo-forms of the R48C mutant had the Fe(III) removed to produce the apo-form, by following the process advised by T.A Mietzner [16, 17] of the department of Molecular Genetics and Biochemistry, University of Pittsburgh School of Medicine. The apo-forms then had a methanethiosulfonate (MTSL) spin-label attached to the mutated cysteine, the excess spin-

label was removed by passing the sample down two PD10 columns, and Cu(II) added to the apo-Fbp to a just below stoichiometric amount.

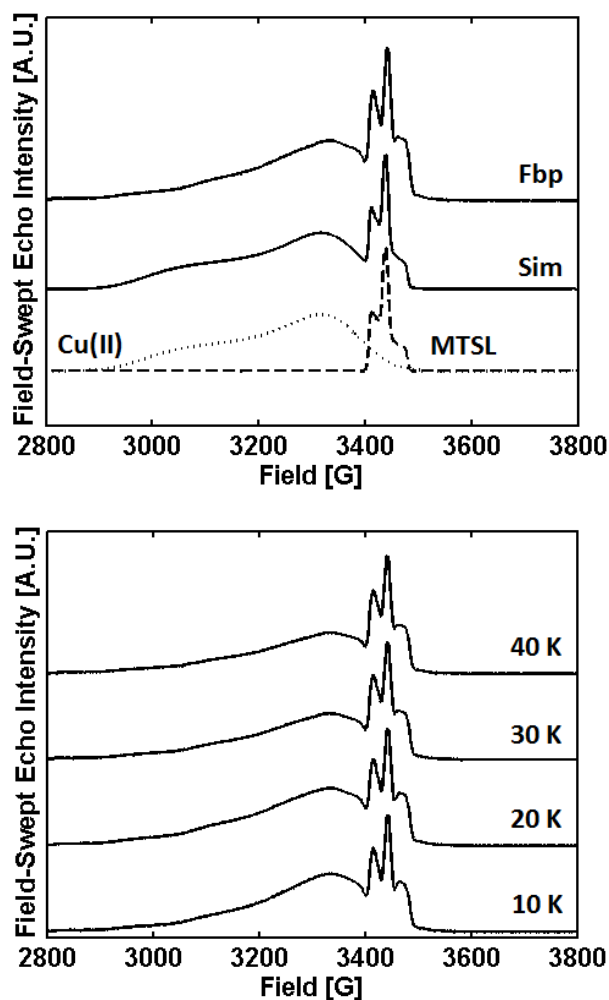
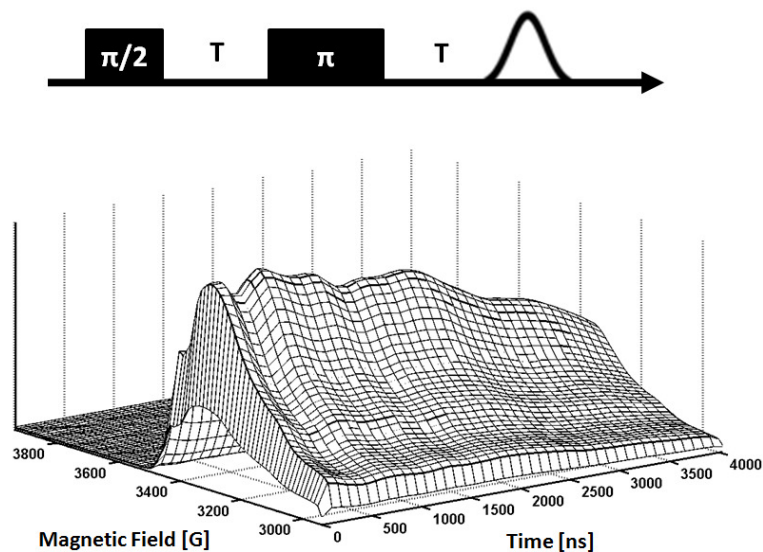


Figure 2.4-1, TOP: Simulation of MTSL spin-labeled Cu(II) Fbp R48C using EasySpin. Cu(II)  $g$ -values 2.032, 2.312,  $A = 30$  G. MTSL  $g$ -values 2.01, 2.0059, 2.002,  $A_{\parallel} = 6$  G,  $A_{\perp} = 36$  G. Simulated spectrum compared with FSE of Cu(II) MTSL spin-labeled Fbp R48C at 30K. BOTTOM: Field Swept Echo Spectrum (FSE) of Cu(II)Fbp at varying temperatures from 10K to 40K. The change in relative intensity of the two paramagnetic centres (Cu(II) and MTSL) can be clearly seen.

The oscillations in echo intensity in a PELDOR experiment have a longer periodicity as the distance between paramagnetic species becomes larger. The Pump pulse must then be varied over a longer time period in order to characterise the oscillations. This however requires longer values for  $t_2$  the spin-spin relaxation time. This need determines the temperature

chosen to perform the PELDOR experiment. It was quickly found that glycerol needed to be added to the sample in order to decrease unwanted spin-spin interactions (between the paramagnetic centres and their environments) and increase the phase-memory time  $T_M$  (In this case by a factor of 3). In this particular sample the difference in relaxation properties between the nitroxide spin-label and Cu (II) centre demands a long shot repetition time (SRT), the time between each pulse sequence, which leads to a long experiment time and ultimately overnight data acquisition **Figure 2.4-1** shows the echo-detected spectrum obtained at temperatures from 40K to 10K (bottom panel). A temperature of 10 K was chosen to maximize the spectral contribution from the Cu(II) centre (see simulation top panel). In these spectra the contributions from both paramagnetic species can clearly be seen. The low-field broad feature running from  $\sim 3000$ - $3400$  G is from the Cu(II) ion, whereas the rhombic signal  $3400$ - $3500$ G is generated by the nitroxide spin-label. This was achieved by performing a two-dimensional two-pulse experiment **Figure 2.4-2**. This sequence is similar to a field-swept echo spectrum, but the time between the  $\pi/2$  and  $\pi$ -pulse is incremented and the intensity of the top of the maximum echo is recorded, as the field is swept.



**Figure 2.4-2, Two-dimensional two-pulse  $t_2$  relaxation plot of Cu(II) Fbp at 10K. The pulse sequence is also shown (above), the field is also swept during this experiment.**

The relaxation plot clearly shows significant signal times of  $\sim 2000$  ns ( $2 \mu\text{s}$ ) indicating a  $T_M$  of this order of magnitude. The  $T_M$  needed to measure a distance of 2 nm by the PELDOR method

is 1  $\mu\text{s}$ , for 5-8nm it is 6  $\mu\text{s}$ . The equation describing the dipolar-coupling presented in § 3.3 may be rearranged and simplified to determine the distance between two paramagnetic

$$r = \sqrt[3]{\frac{52.04}{\nu_{\text{perp}} \text{ MHz}}} \text{ nm} \quad \text{centres } r \text{ from the perpendicular dipolar-coupling component } \nu_{\text{perp}}:$$

The crystal structure of Fbp from *N. gonorrhoeae* (1D9Y PDB unpublished) indicates the distance from the Fe(III) centre to the  $C_{\alpha}$  of native R48 is approximately 2.8 nm **Figure 2.4-3**.

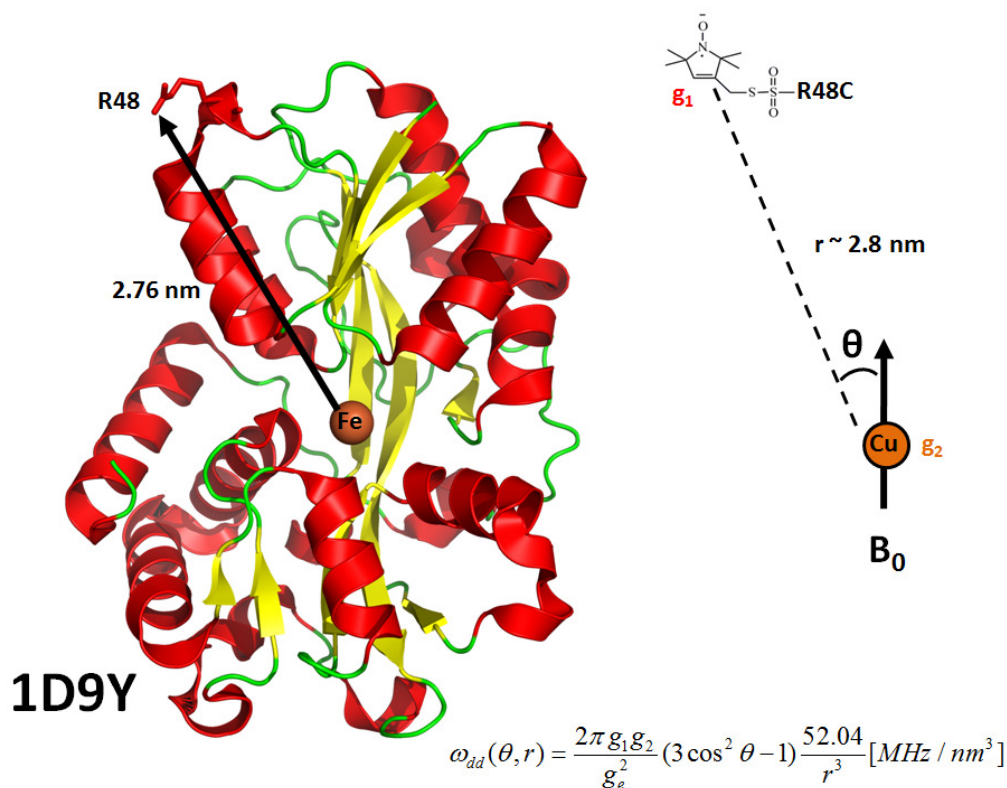


**Figure 2.4-3, Crystal structure 1D9Y and Cu(II) MTSL distance scheme. Dipolar-coupling ( $\omega_{dd}$ ) Equation described in § 3.3.**

Once it was confirmed that the  $T_M$  was sufficient to attempt the PELDOR experiment, the positions of the pump ( $\nu_A$ ), and observe ( $\nu_B$ ) pulses had to be chosen. For the initial experiment the field positions corresponding to the maximum spectral intensity from both

the Cu(II) centre and the nitroxide spin-label were selected **Figure 2.4-4** resulting in a difference in frequencies between the pump and observe pulses ( $\Delta\nu$ ) of 132 MHz. (The constraint on this separation being the operational bandwidth of the resonator).

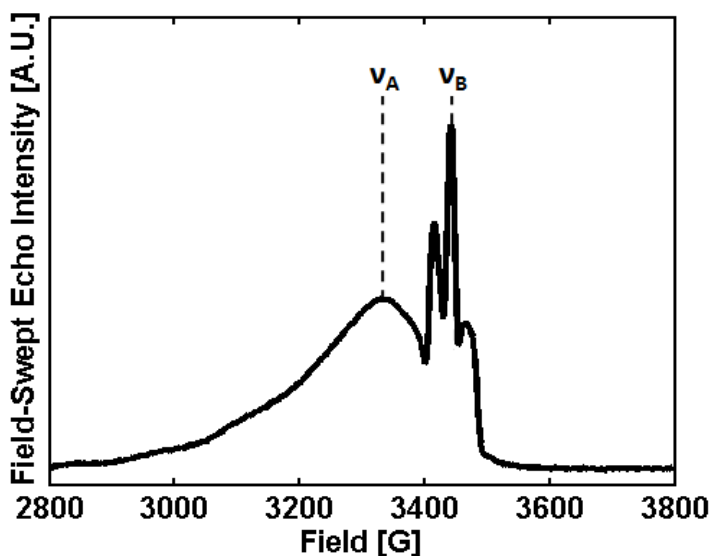


Figure 2.4-4, Pump ( $\nu_B$ ) and observe ( $\nu_A$ ) positions for initial PELDOR experiment Fbp 10K.

The PELDOR pulses and timings were then optimized. A nutation pulse sequence was used to optimize the inversion  $\pi$ -pulse. In this experiment the ELDOR or pump frequency is set to the observation frequency. A pump pulse of increasing length was then applied before a Hahn echo sequence is used to detect at the observe frequency. The echo intensity is measured as a function of the pump pulse length. The maximum inversion is therefore the first minimum of the spectrum and so the  $\pi$ -pulse. The PELDOR experiment was continued overnight.

## 2.5 Results

**Figure 2.5-1** shows the PELDOR spectra obtained for the experiment described above as well as that for an experiment performed with a  $\Delta\nu$  of 500 MHz. Both spectra display two characteristics indicative of a successful experiment. These are that initially the trace increases in intensity and then begins to exhibit an exponential decrease, and secondly that there is an oscillation observable in the intensity of the spectrum during the time of the experiment. In order to obtain a value for the distance measured via the dipolar interaction

between the free-electrons of the Cu(II) centre and nitroxide spin-label the correct data analysis procedure must be followed as described below.

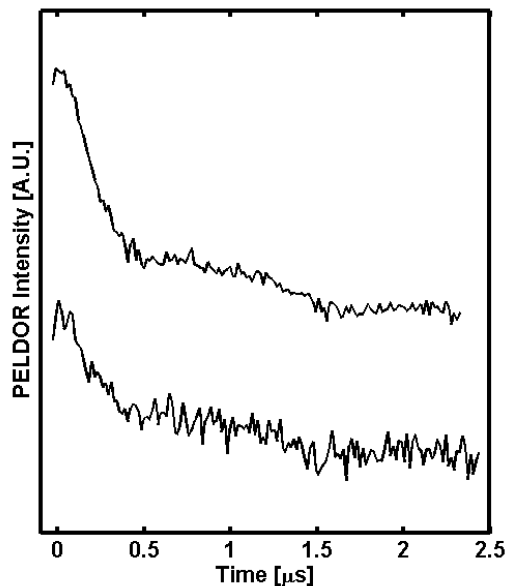


Figure 2.5-1, PELDOR traces of FbpA. Top:  $\Delta\nu = 132$  MHz, SRT 10,000. Bottom:  $\Delta\nu = 500$  MHz, SRT 20,000.  $\pi$ -pulse 32 ns,  $\pi/2$  pulse 16 ns, pump pulse 32 ns.

## 2.6 Data Analysis

Generally, Tikhonov regularization is used to gain information on the distance distributions within the sample directly from the time trace [1]. This is a highly efficient numerical algorithm constructed to produce consistent results within “ill-defined” problems. These are situations in which small variations in the experimental data may lead to significantly different solutions of the desired function. In order to carry out this regularization on the data described above the software package DeerAnalysis 2011 [6] was used **Figure 2.6-1**. This program is able to extract distance distributions from dead time free PELDOR [15] data. Initially pre-processing tools are implemented to correct for experimental imperfections (phase errors etc.) and to separate the desired intramolecular distances from the intermolecular background contribution. The program is also able to produce distance distributions via several independent approaches; this may be used to verify the reliability of the solution.

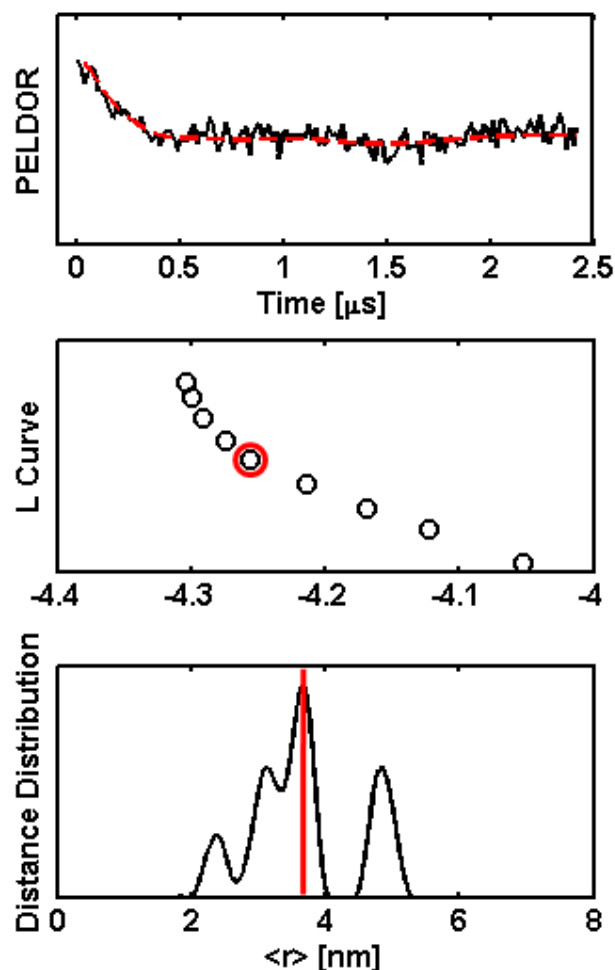


Figure 2.6-1, Data Analysis summary from DeerAnalysis 2011 of PELDOR trace at 10 K (top) L-curve for Tikhonov regularization with k-factor 100 (middle) and resulting distance distribution (bottom).

## 2.7 Discussion

A major consideration is that Tikhonov regularization is not valid if the system exhibits strong orientation dependence. After data manipulation a value of 3.65 nm was determined for the mean distance between the Cu(II) centre and the MTSL nitroxide spin-label. It can be seen from **Figure 2.6-1** that more than one distance is indicated in the distribution from DeerAnalysis, this is probably due to motion of the nitroxide spin label, but may also be an artifact of data manipulation. It was previously stated that the crystal structure of FbpA from *N. gonorrhoeae* yielded a distance of 2.8 nm between the Fe(III) centre and native arginine

residue. Taking into account the spin-label length of 0.7 nm, this leads to a theoretical Cu(II) to spin-label distance of up to 3.5 nm. As an initial determination this value seems reasonable, there are however, a number of considerations and refinements to be taken into consideration.

Previous investigations on nitroxide-labeled Cu(II) centre model compounds have shown that orientation selectivity [14] has a significant effect on the recorded PELDOR data [4]. This occurs when a large excitation bandwidth reduces the spectral selectivity of the pump and observe pulses and thereby reduces the possibility to determine the orientation of the paramagnetic centres with respect to each other. In some investigations[18] this effect has been shown not to be relevant but none the less had to be considered and proven not to be so. As such it is necessary for the Cu(II)Fbp-MTSL system to be modeled with a view to determining the spin-vectors of each centre with respect to each other, it might then also be possible to determine the orientation of both centres with respect to the laboratory frame. One possible way to produce this model would be via Density Functional Theory (DFT) [19, 20]. An initial understanding of the degree of orientational selectivity of this system may be obtained by positioning the pump and observe pulses for the PELDOR experiment at different positions. The less sensitive to orientation selection the system the more consistent will be the determined distance after data analysis. This has provisionally been undertaken as can be seen in **Figure 2.5-1** with the lower trace recorded with a difference between the pump and observe pulses ( $\Delta\nu$ ) equal to 500 MHz. As previously stated the constraint on this difference is governed by the bandwidth of the resonator, at present the maximum published value is 603 MHz [4]. Manipulation, again using DeerAnalysis 2011 indicated a similar distance to that already reported.

## 2.8 Outlook

Ultimately the aim of the project to determine distances between a Cu(II) centre and MTSL spin label in a biological macromolecule was successful. However, the project could be continued to further investigate the effects of orientation selectivity.

---

At the 42<sup>nd</sup> Annual International ESR Royal Society of Chemistry meeting held in Norwich, a data analysis program was presented that was created to deal with highly anisotropic spin systems. This software has recently been obtained from its author (Jeffrey Harmer, Centre for Advanced Electron Spin Resonance, University of Oxford) and it is hoped, will be applied to the system described above.

---

---

## References

1. Schiemann, O. and T.F. Prisner, *Long-range distance determinations in biomacromolecules by EPR spectroscopy*. Quarterly Reviews of Biophysics, 2007. **40**(01): p. 1-53.
  2. Kay, C.W.M., et al., *Pulsed ELDOR Determination of the Intramolecular Distance between the Metal Binding Sites in Dicumpric Human Serum Transferrin and Lactoferrin*. Journal of the American Chemical Society, 2007. **129**(16): p. 4868-4869.
  3. van Amsterdam, I.M.C., et al., *Measurement of a Cu-Cu Distance of 26 Å by a Pulsed EPR Method*. Angewandte Chemie International Edition, 2003. **42**(1): p. 62-64.
  4. Bode, B.E., et al., *PELDOR Measurements on a Nitroxide-Labeled Cu(II) Porphyrin: Orientation Selection, Spin-Density Distribution, and Conformational Flexibility*. J. Phys. Chem. A, 2008. **112**(23): p. 5064-5073.
  5. Narr, E., A. Godt, and G. Jeschke, *Selective measurements of a nitroxide-nitroxide separation of 5 nm and a nitroxide-copper separation of 2.5 nm in a terpyridine-based copper(II) complex by pulse EPR spectroscopy*. Angewandte Chemie-International Edition, 2002. **41**(20): p. 3907-3910.
  6. Jeschke, G., et al., *Deer Analysis 2006 a comprehensive software package for analyzing pulsed ELDOR data*. 2007.
  7. Lash, A. and A. Saleem, *Iron metabolism and its regulation. A review*. Ann Clin Lab Sci, 1995. **25**(1): p. 20-30.
  8. Braun, V. and H. Killmann, *Bacterial solutions to the iron-supply problem*. Trends in Biochemical Sciences, 1999. **24**(3): p. 104-109.
  9. Wandersman, C. and P. Delepelaire, *Bacterial iron sources: From siderophores to hemophores*. Annual Review of Microbiology, 2004. **58**: p. 611-647.
  10. Genco, C.A. and P.J. Desai, *Iron acquisition in the pathogenic Neisseria*. Trends in Microbiology, 1996. **4**(5): p. 179-184.
  11. Bruns, C.M., et al., *Structure of Haemophilus influenzae Fe<sup>3+</sup>-binding protein reveals convergent evolution within a superfamily*. Nat Struct Mol Biol, 1997. **4**(11): p. 919-924.
  12. Jeschke, G., *Distance Measurements in the Nanometer Range by Pulse EPR*. ChemPhysChem, 2002. **3**(11): p. 927-932.
  13. Milov, A.D., K.M. Salikohov, and M.D. Shirov, *Application of ENDOR in Electron-Spin Echo for Paramagnetic Center Space Distribution in Solids*. Fizika Tverdogo Tela, 1981. **23**(4): p. 975-982.
-

14. Larsen, R.G. and D.J. Singel, *Double electron--electron resonance spin--echo modulation: Spectroscopic measurement of electron spin pair separations in orientationally disordered solids*. The Journal of Chemical Physics, 1993. **98**(7): p. 5134-5146.
  15. Pannier, M., et al., *Dead-Time Free Measurement of Dipole-Dipole Interactions between Electron Spins*. Journal of Magnetic Resonance, 2000. **142**(2): p. 331-340.
  16. Bruns, C.M., et al., *Crystallographic and Biochemical Analyses of the Metal-Free Haemophilus influenzae Fe<sup>3+</sup>-Binding Protein*. Biochemistry, 2001. **40**(51): p. 15631-15637.
  17. Nowalk, A.J., et al., *Metal-Dependent Conformers of the Periplasmic Ferric Ion Binding Protein*. Biochemistry, 1997. **36**(42): p. 13054-13059.
  18. Yang, Z., J. Becker, and S. Saxena, *On Cu(II)-Cu(II) distance measurements using pulsed electron double resonance*. Journal of Magnetic Resonance, 2007. **188**(2): p. 337-343.
  19. Parr, R.G., *Density Functional Theory*. Annual Review of Physical Chemistry, 1983. **34**(1): p. 631-656.
  20. Geerlings, P., F. De Proft, and W. Langenaeker, *Conceptual Density Functional Theory*. Chemical Reviews, 2003. **103**(5): p. 1793-1874.
  1. Schiemann, O. and T.F. Prisner, *Long-range distance determinations in biomacromolecules by EPR spectroscopy*. Quarterly Reviews of Biophysics, 2007. **40**(01): p. 1-53.
  2. Kay, C.W.M., et al., *Pulsed ELDOR Determination of the Intramolecular Distance between the Metal Binding Sites in Dicumpric Human Serum Transferrin and Lactoferrin*. Journal of the American Chemical Society, 2007. **129**(16): p. 4868-4869.
  3. Bode, B.E., et al., *PELDOR Measurements on a Nitroxide-Labeled Cu(II) Porphyrin: Orientation Selection, Spin-Density Distribution, and Conformational Flexibility*. J. Phys. Chem. A, 2008. **112**(23): p. 5064-5073.
  4. Narr, E., A. Godt, and G. Jeschke, *Selective measurements of a nitroxide-nitroxide separation of 5 nm and a nitroxide-copper separation of 2.5 nm in a terpyridine-based copper(II) complex by pulse EPR spectroscopy*. Angewandte Chemie-International Edition, 2002. **41**(20): p. 3907-3910.
  5. Jeschke, G., et al., *Deer Analysis 2006 a comprehensive software package for analyzing pulsed ELDOR data*. 2007.
  6. Lash, A. and A. Saleem, *Iron metabolism and its regulation. A review*. Ann Clin Lab Sci, 1995. **25**(1): p. 20-30.
-

7. Braun, V. and H. Killmann, *Bacterial solutions to the iron-supply problem*. Trends in Biochemical Sciences, 1999. **24**(3): p. 104-109.
  8. Wandersman, C. and P. Delepelaire, *Bacterial iron sources: From siderophores to hemophores*. Annual Review of Microbiology, 2004. **58**: p. 611-647.
  9. Genco, C.A. and P.J. Desai, *Iron acquisition in the pathogenic Neisseria*. Trends in Microbiology, 1996. **4**(5): p. 179-184.
  10. Bruns, C.M., et al., *Structure of Haemophilus influenzae Fe<sup>3+</sup>-binding protein reveals convergent evolution within a superfamily*. Nat Struct Mol Biol, 1997. **4**(11): p. 919-924.
  11. Jeschke, G., *Distance Measurements in the Nanometer Range by Pulse EPR*. ChemPhysChem, 2002. **3**(11): p. 927-932.
  12. Milov, A.D., K.M. Salikohov, and M.D. Shirov, *Application of ENDOR in Electron-Spin Echo for Paramagnetic Center Space Distribution in Solids*. Fizika Tverdogo Tela, 1981. **23**(4): p. 975-982.
  13. Larsen, R.G. and D.J. Singel, *Double electron-electron resonance spin-echo modulation: Spectroscopic measurement of electron spin pair separations in orientationally disordered solids*. The Journal of Chemical Physics, 1993. **98**(7): p. 5134-5146.
  14. Pannier, M., et al., *Dead-Time Free Measurement of Dipole-Dipole Interactions between Electron Spins*. Journal of Magnetic Resonance, 2000. **142**(2): p. 331-340.
  15. Bruns, C.M., et al., *Crystallographic and Biochemical Analyses of the Metal-Free Haemophilus influenzae Fe<sup>3+</sup>-Binding Protein*. Biochemistry, 2001. **40**(51): p. 15631-15637.
  16. Nowalk, A.J., et al., *Metal-Dependent Conformers of the Periplasmic Ferric Ion Binding Protein*. Biochemistry, 1997. **36**(42): p. 13054-13059.
  17. Yang, Z., J. Becker, and S. Saxena, *On Cu(II)-Cu(II) distance measurements using pulsed electron double resonance*. Journal of Magnetic Resonance, 2007. **188**(2): p. 337-343.
  18. Parr, R.G., *Density Functional Theory*. Annual Review of Physical Chemistry, 1983. **34**(1): p. 631-656.
  19. Geerlings, P., F. De Proft, and W. Langenaeker, *Conceptual Density Functional Theory*. Chemical Reviews, 2003. **103**(5): p. 1793-1874.
-

---

---

### 3 Appendix **REFINE: Cytochrome $bc_1$**

---

The following section is a summary of the findings of the following paper:

**Resolving the EPR spectra in the Cytochrome  $bc_1$  Complex from *Saccharomyces cerevisiae* [1]**

#### 3.1 Introduction

Quinones are found extensively in living organisms, where they reside either in the lipid phase of the biological membrane: the so called quinone pool, or bound to specific sites within membrane-bound protein complexes. It is the ability of these bound quinones to be reduced or oxidized in two successive one-electron steps that determines their biological function. They are therefore utilized as electron acceptors or donors in a larger number of biological electron transfer steps during photosynthetic or respiratory processes. A one-electron reduction step forms an intermediate known as a semiquinone which is paramagnetic and so may be studied by EPR spectroscopy. This investigation involves the redox-active ubiquinone-6 of the yeast cytochrome  $bc_1$  complex from *S. cerevisiae* at the so-called  $Q_i$  site. Although the location of the  $Q_i$  binding pocket is well known, the nature of its precise binding is not, with three different crystallographic studies suggesting three different binding geometries for  $Q_i$ . Recent studies of the bacterial system *R. sphaeroides* have indicated a direct coordination to histidine as suggested by the chicken heart crystal structure model. In this study of the yeast system, EPR spectroscopy and especially REFINE spectroscopy is employed to investigate the  $Q_i$  binding site.  $^{14}\text{N}$ - ESEEM spectroscopy in conjunction with an inversion recovery filter (REFINE) is used to determine whether  $^{14}\text{N}$  modulations arise from interactions to  $Q_i^{\bullet-}$  or to the Rieske iron-sulphur cluster. The results are interpreted with regard to the location and possible function of  $Q_i$  in the enzyme.

---

### 3.2 Background

The cytochrome *bc*<sub>1</sub> complex is an energy-transducing membrane protein complex that is involved in respiration and photosynthesis [2, 3]. The enzyme transfers electrons from ubiquinone to cytochrome *c*, and couples this to the translocation of protons across the membrane. This mechanism is known as the Q-cycle [4], a necessary feature of which is the localization of two catalytic sites for ubiquinone redox reactions on opposite sides of the membrane. In the first half of the Q-cycle one molecule of ubiquinol is oxidized at the Q<sub>o</sub> site in a bifurcated manner. One of the electrons is transferred to the acceptor cytochrome *c* via two catalytic subunits, the Rieske protein and cytochrome *c*<sub>1</sub>. The second electron is transferred via a third catalytic subunit namely cytochrome *b* to the Q<sub>i</sub> site (**Figure 3.2-1**), at which one molecule of bound ubiquinone is reduced to ubiquinol.

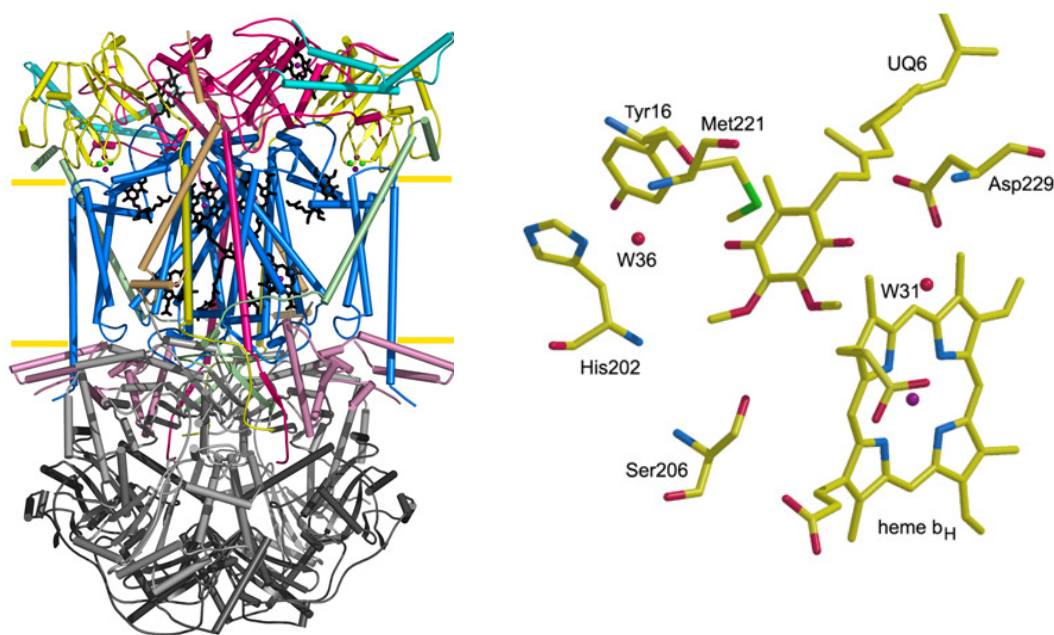


**Figure 3.2-1, Structure of yeast cyt *bc*<sub>1</sub> complex 1KB9 with redox-active cyt *b*, cyt<sub>c1</sub> and Rieske protein in blue, pink, & yellow, respectively. (left) Cofactor & ligands; UQ<sub>6</sub> at the Q<sub>i</sub> site (right).**

During the second half of this cycle a second ubiquinol molecule is oxidized at the Q<sub>o</sub> site, causing the reduction of another molecule of cytochrome *c*, the full reduction of the bound ubiquinol and its release as ubiquinol. During this process protons are taken up from the electronegative side of the membrane for ubiquinone reduction and released towards the

electropositive side after ubiquinol oxidization. It is the binding sites of these complexes that control the chemical properties of the respective quinone in a host of different respiratory and photosynthetic molecules. This enables the complex to function more effectively in electron and proton transfer kinetics. The  $Q_i$  site of the cytochrome  $bc_1$  complex has to stabilize the binding of ubiquinone and semiquinone, and also has to permit proton transfer most probable mediated via hydrogen bonds.

- The structure of the yeast cytochrome  $bc_1$  complex indicates a water molecule for the primary proton donor on one side of the substrate coenzyme  $Q_6$  ( $UQ_6$ ), and that the second proton is either donated by another water molecule or Asp 229 [5-7].
- The bovine complex from one group [8] shows direct ligation of the quinone head group with residues of the cytochrome  $b$ , with two residues in position for direct hydrogen bonding with one of the quinone carbonyl oxygen atoms. This suggests a direct proton transfer.
- Another bovine structure [9] suggests mediation by water molecules for both the aspartate and histidine hydrogen bonds.

There is then, some debate whether water molecules may be primary proton donors during ubiquinone reduction. The differences mentioned above may be due to differences between species and/or be due to differing redox states of the structures.

The redox state of each of these structures is unclear, and it is likely that each is only partly reduced, and that the substrate molecule is bound in its oxidized form.

EPR spectroscopy allows investigation of the environment of the substrate for a defined redox state, specifically for the semiquinone. Observations of a trapped semiquinone intermediate at the  $Q_o$  site, have only been reported recently [10], however, the radical state  $Q_i^{\bullet-}$  has been observable using X-band CW-EPR for some time [11]. This radical state in the purified bovine heart  $bc_1$  complex has also been investigated using CW-X-band ENDOR spectroscopy, a comparison of the spectra measured in  $H_2O/D_2O$  media yielded features associated with hydrogen bonded protons, as well as hyperfine couplings to protons of the quinone ring [12].

---

ESEEM as discussed in § 5.3.3, can provide valuable information about the ligation environment of the paramagnetic centre. This method has previously been used to investigate the stable electron acceptors of the bacterial reaction centres [13, 14], as well of both photo-systems of higher plants [15-17]. Many of these experiments produced assignments before the three-dimensional structures were resolved, and were later confirmed by them. ESEEM has also been used more recently to predict a direct interaction with a nitrogen atom for the terminal quinol oxidase from *E. coli* [18], which was then further characterized very recently [19]. As yet however, the crystal structure model has failed to reveal any bound quinones [20]. Similar experiments have also been performed on the bacterial  $bc_1$  complex from *Rps. sphaeroides* that propose direct binding to histidine [21, 22].

A major factor that must be kept in mind when studying electron transfer intermediates in mitochondrial or bacterial respiration chains with EPR spectroscopy is that often there may be more than one paramagnetic centre present. In many cases the contribution of these individual centres to the overall spectrum overlap, which causes problems when trying to interpret these spectra. As such, it is desirable to be able to distinguish the individual contributions of these centres. There are several ways by which this can theoretically be achieved. Biological and biochemical methods are the first, these methods are widely used but may not suppress unwanted contributions to the spectrum whilst at the same time maintain the desired redox state of the centre under investigation. Molecular biological alteration is also possible, but removal of an important amino-acid residue or prosthetic group may prevent the formation of the protein under consideration. Secondly spectroscopic techniques may be employed to resolve contributions from different paramagnetic species. A consideration of the different EPR parameters of the species dictates the method by which the centre may be resolved; if the species within the sample have different  $g$ -values, multi-frequency EPR may be able to separate them spectrally. High-field EPR is becoming an increasingly common means to increase the spectral resolution, particularly for organic radicals [23]. Differences in Rabi-oscillation (nutational) frequencies due to different spin quantum numbers  $S$  and  $m_s$ , may be exploited, as in the case of an organic radical and certain metal centres [24]. Spin-lattice relaxation times ( $T_1$ ) in conjunction with their temperature dependency may also be used to characterize and suppress the contributions of individual

---

---

species [25]. For reducing conditions where a stable semiquinone radical anion in the  $Q_i$  site of the cytochrome  $bc_1$  complex is observable the Rieske iron-sulphur centre is also EPR visible. This much broader EPR signal overlaps with the semiquinone. In order to use ESEEM spectroscopy to directly measure the interaction of the semiquinone radical with its protein environment, it is important that its spectrum may be resolved from that of the Rieske iron-sulphur centre.

A recent, and as yet infrequently attempted technique capable of achieving this is Relaxation Filtered Hyperfine (REFINE) spectroscopy [26]. This technique uses an inversion-recovery pulse in conjunction with a standard Hahn echo detection sequence (§ 5.3.1) to separate the spectral contributions of different paramagnetic species via their spin-lattice relaxation time. The time between the inversion-recovery pulse and the detection sequence is altered depending on the so-called filter time ( $T_F$ ), this makes it possible to suppress one of two overlapping EPR signals and thus record the individual spectrum of the second [26-28].

In this study, this technique is applied to resolve the individual EPR spectra from the semiquinone and the Rieske iron-sulphur cluster in the cytochrome  $bc_1$  complex. The ultimate aim being to determine experimental conditions where the individual species in such mixtures may be studied further by hyperfine spectroscopy (ENDOR, ESEEM) to directly address the issue of  $Q_i$  semiquinone coordination.

### 3.3 Experimental Procedure

The cytochrome  $bc_1$  complex from the yeast *Saccharomyces cerevisiae* was purified following the published protocol, by collaborators. This researcher's involvement with this project began only recently, but for a complete picture of the findings of this project and future intentions of this lab a discussion of the work undertaken by the other researchers involved must be included. The experimental work I undertook is shown in **Figure 3.3-2**. Samples were initially characterized by CW-EPR spectroscopy using a Bruker E-500 spectrometer. X-band pulsed EPR measurements performed by this researcher were undertaken using a Bruker E-680 spectrometer. **Figure 3.3-1** shows a series of spectra of

---

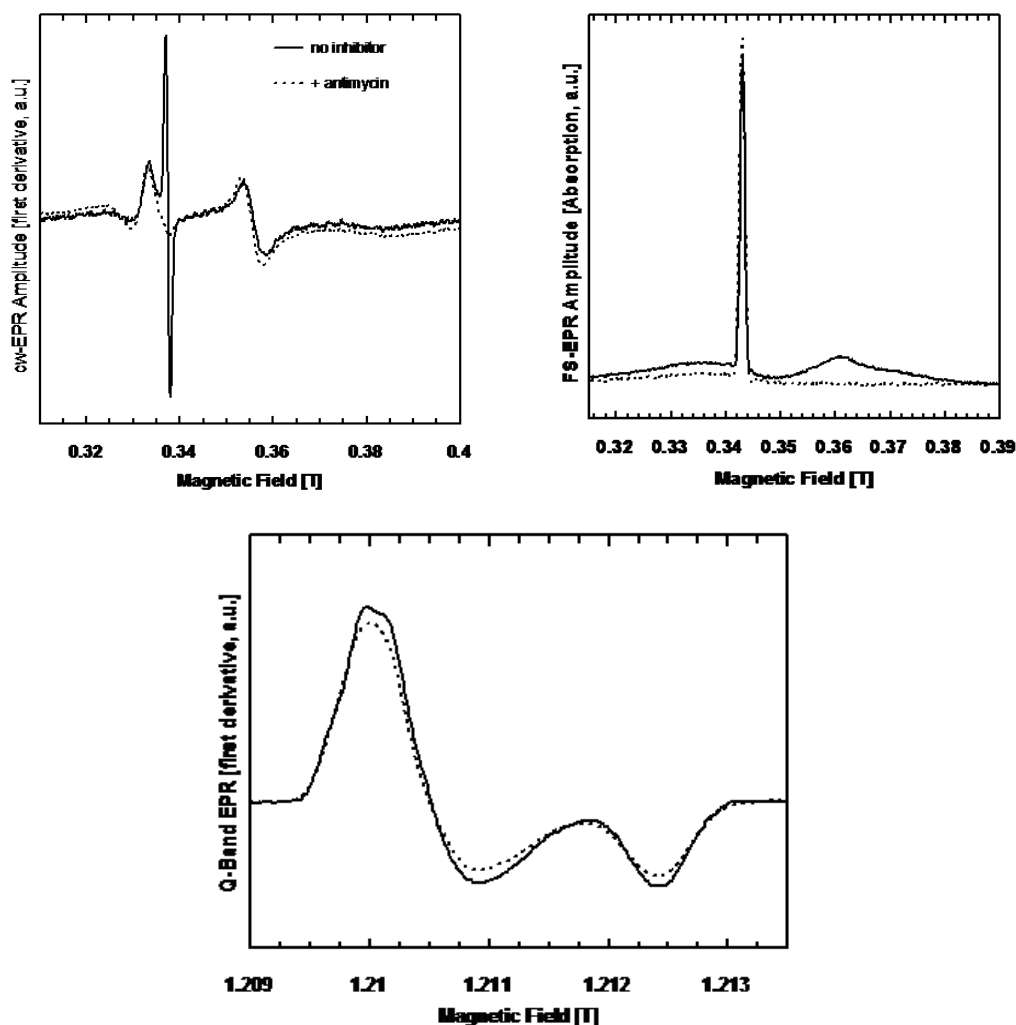


Figure 3.3-1, top-left: X-band cw-EPR spectra of the reduced  $bc_1$ -complex from yeast (solid line) and in the presence of antimycin A (dashed line). Experimental conditions: microwave power, 0.1mW; modulation frequency, 100 kHz; field modulation depth, 0.5 G; temperature, 20 K. Top-right: X-band field swept pulsed EPR spectra of the reduced  $bc_1$ -complex from yeast. Experimental conditions: Microwave frequency of 9.745446 GHz using a  $\pi/2$  pulse length of 8 ns and a  $\tau = 120$  ns and a shot repetition rate of 1ms; temperature, 20 K (solid trace) and 80K (broken trace). Bottom Q-band CW-EPR spectrum and simulation (broken trace) of the reduced  $bc_1$ -complex from yeast; Experimental conditions: microwave power, 2mW; modulation frequency, 10 kHz; modulation depth, 1 G; temperature, 80 K.

the reduced cytochrome  $bc_1$  complex from *S. cerevisiae* at 9 K recorded before this researchers involvement with the project, including the CW X-band EPR spectra of the reduced cytochrome  $bc_1$  complex from *S. cerevisiae* at 9 K (top-left). A broad signal from the reduced Rieske centre is clearly visible as well an intense narrow signal situated at  $g \sim 2.0042$  typical of a semiquinone [29]. The concentration of ubisemiquinone was determined to be

about 60% relative to that of the reduced Rieske EPR signal, which is to be expected. The dashed spectrum in this panel is from the  $bc_1$  complex reduced in the presence of the  $Q_i$  site inhibitor antimycin [30]. Again at 9 K a broad signal from the reduced Rieske centre is clearly visible but now no narrow signal is observed, clearly indicating that the narrow signal observed results from a semiquinone in the  $Q_i$  site. (top-right) shows the field swept pulsed X-band EPR spectra of the reduced  $bc_1$  complex from *S. cerevisiae*. Again a broad signal from the reduced Rieske centre and an intense narrow signal are observed at 9K. If this spectrum is recorded at higher temperatures e.g. 80K (dotted line) the narrow signal is present while the broad signal is not. At 80K the  $g$ -anisotropy of this radical signal was able to be resolved by performing EPR at higher microwave frequencies and magnetic fields (bottom). At Q-band (34 GHz), it has been shown that the  $g$ -tensor anisotropy of semiquinone radical anions can be partially resolved e.g., for the  $Q_H^{\bullet-}$  semiquinone radical anion in the *E. coli* terminal oxidase [31]. Simulation of this spectrum allows a direct determination of the  $g$ -tensor. These simulations were carried out using an anisotropic line width parameter characterized by a Gaussian line shape to account for hyperfine interactions from the methyl protons at position 5 and other smaller couplings (hydrogen bonded-,  $CH_2$ - and methoxy-protons).

If two species (e.g.  $Q_i^{\bullet-}$  and the Rieske FeS centre) have different  $T_1$  relaxation times, then different recovery times are observed with the application of a simple Hahn echo pulse sequence across a range of magnetic field values. In **Figure 3.3-2** (top-left) the observed relaxation times have been used to calculate the individual time traces for the two species as well as the sum of these two traces. By inspection it is clear that there is a point in time where the net magnetization crosses zero which is different for each of the individual time traces (indicated by the arrows). Alternatively a two-dimensional experiment can be performed (top-right) in this experiment the field swept EPR spectrum is measured as a function of this filter time ( $T_F$ ). Using an inversion recovery pulse sequence time traces can be recorded at different magnetic field positions [32] which observe the recovery of the  $M_z$  magnetization, that is inverted by a first  $\pi$ -pulse. These so-called filter times ( $T_F$ ) can be experimentally determined or calculated [33, 34] Specific traces can be extracted from this data (bottom-spectra) to demonstrate that it is possible to suppress the contribution from the narrow radicals species (bottom-left) and also, despite a significant degree of  $T_1$  anisotropy, suppress the contribution

from the broad Rieseke signal at the field position corresponding to the narrow  $Q_i$  radical signal (bottom-right).

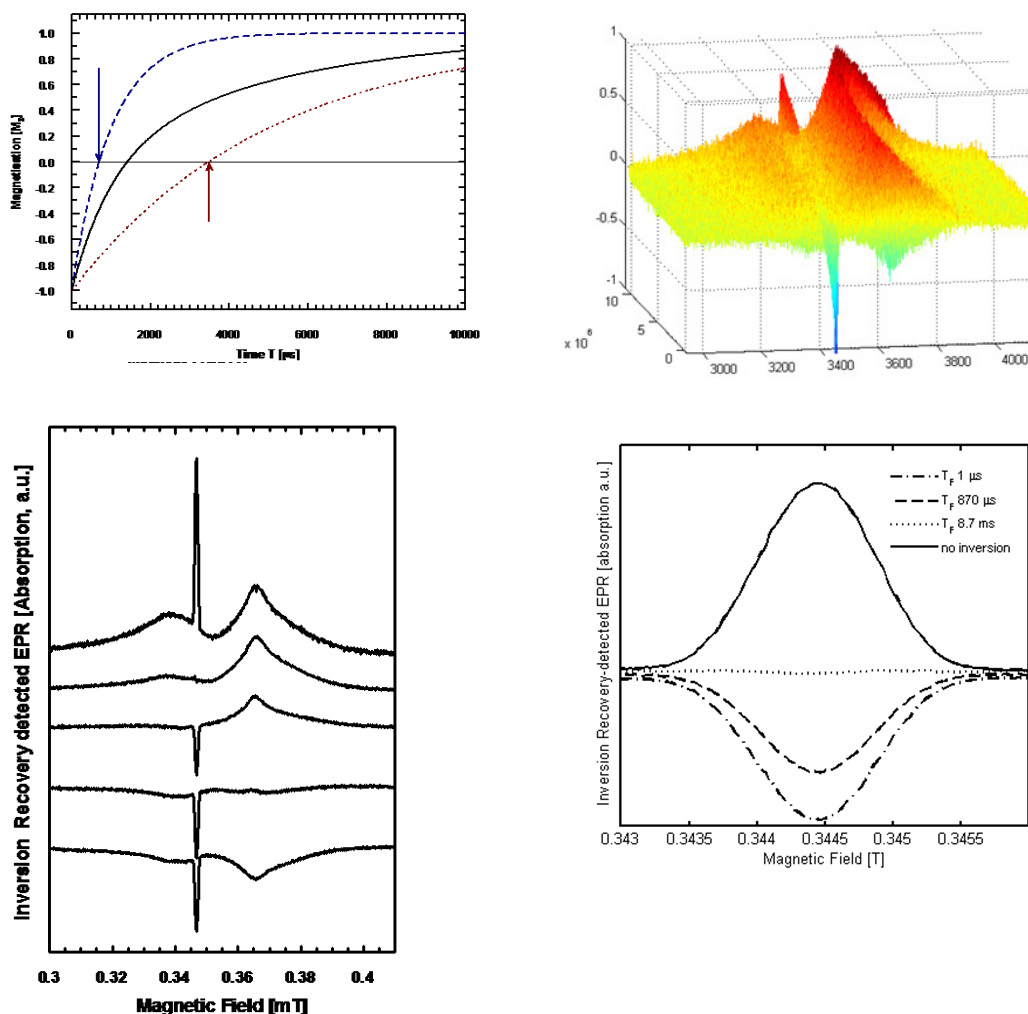


Figure 3.3-2, Top Left: Plot of the time traces observed using the relaxation times of the individual species (dashed and dotted traces) and their sum (solid trace). Two times, indicated by the arrows, are when the recovery of individual  $M_z$  magnetisations traverse zero. These times are used to filter the contributions of the individual species in the field-swept EPR spectra.

Top Right) 2D plot of field swept spectra versus the filter time  $T_F$ .

Bottom Left) How  $T_F$  effect the overall FSE spectrum using values of (top to bottom): no inversion, 8.7 ms, 870  $\mu\text{s}$ , 500  $\mu\text{s}$  and 1  $\mu\text{s}$ .

Bottom Right) Selected spectra from selected filter times ( $T_F$ ) to measure a narrow field range around the semiquinone species. Experimental conditions: microwave frequency, 9.67944 GHz using a  $\pi/2$  pulse length of 8 ns, an inversion Pulse of 16ns, and a  $\tau = 120$  ns and a shot repetition 300ms; temperature 10 K.

At a very short filter time (lowermost trace in bottom-left panel) the response from both the semiquinone and the Rieseke centre are inverted. Under these experimental conditions about

15% of the semiquinone signal was able to be inverted. At a slightly later time (in this case at 10K, 870 $\mu$ s), while the response from the semiquinone is still inverted, the response of the Rieske centre is zero (at the magnetic field position corresponding to the resonance position of the semiquinone). Here a pure spectrum from  $Q_i^{\bullet-}$  (yield  $\sim$  10%) can be obtained (middle trace). At a later time (8.7 ms, second uppermost trace) the response from the semiquinone is zero, and a spectrum from the Rieske centre can be observed. At much later times both signals can be observed (uppermost trace) again.

The ratio of relative amounts of species as well as their respective relaxation times determines how efficient this type of experiment can be. So far this technique has been applied to resolve overlapping organic radicals and spin labels as well as iron-sulphur centres (see discussion in [33, 34]). In the study presented here this technique is applied to refine the individual EPR spectra from a narrow organic radical and an iron-sulphur centre. The ultimate aim of this project and the soon to be published paper associated with it, is the application of ESEEM in conjunction with a REFINE filter to investigate the ligation of individual paramagnetic centres. The paper presents this work and conclusions drawn from it. However, This researcher has as yet had little to do with this aspect, and as such this data will not be presented, in so far as to say REFINE-ESEEM was proven to be applicable to this situation. Further REFINE-ESEEM experiments are intended to be performed in this laboratory and it is hoped that they will contribute more towards this researcher's dissertation. The conclusions of the paper will however be stated, as they form the basis of future experiments planned.

### 3.4 Conclusions

This was the first EPR/ESEEM report of an ubisemiquinone in the  $Q_i$  site of the yeast (*S. cerevisiae*) cytochrome  $bc_1$  complex. Clear evidence that it is specifically bound to the protein was provided by the sensitivity to the inhibitor antimycin and the observed g-tensor is typical of other bound semiquinone anion radicals suggestive of tight binding through hydrogen bonds to the protein.

While it is generally accepted that the ubisemiquinone anion radical is a stable intermediate in Q reduction at the  $Q_i$  site, details of its interaction with heme  $b_H$  and possible ligands are

---

still unresolved and H<sup>+</sup> pathways are debated. Three X-ray structures provide differing information, as they show different substrate binding patterns. The observed differences in the bovine, yeast and purple bacterium structures may be species-related and/or due to different redox states of the structures. The application of the REFINE technique described has shown that it is now possible to study the semiquinone species individually in the *bc*<sub>1</sub>-complex using hyperfine spectroscopy to resolve the important question of its binding to the protein. Further work to resolve the nature of quinone binding to this protein is envisaged.

---

---

## References

1. MacMillan, F., et al., *Resolving the EPR Spectra in the Cytochrome bc<sub>1</sub> Complex from Saccharomyces cerevisiae*. Applied Magnetic Resonance, 2010. **37**(1): p. 305-316.
  2. Hunte, C., et al., *A Structural Perspective on Mechanism and Function of the Cytochrome bc<sub>1</sub> Complex*. Results and Problems in Cell Differentiation, 2008: p. 253-278.
  3. Crofts, A.R., *The cytochrome bc<sub>1</sub> complex: Function in the context of structure*. Annual Review of Physiology, 2004. **66**: p. 689-733.
  4. Mitchell, P., *Possible molecular mechanisms of the protonmotive function of cytochrome systems*. Journal of Theoretical Biology, 1976. **62**(2): p. 327-367.
  5. Hunte, C., et al., *Structure at 2.3 angstrom resolution of the cytochrome bc<sub>1</sub> complex from the yeast Saccharomyces cerevisiae co-crystallized with an antibody Fv fragment*. Structure, 2000. **8**(6): p. 669-684.
  6. Hunte, C., *Insights from the structure of the yeast cytochrome bc<sub>1</sub> complex: crystallization of membrane proteins with antibody fragments*. FEBS Letters, 2001. **504**(3): p. 126-132.
  7. Lange, C., et al., *Specific roles of protein-phospholipid interactions in the yeast cytochrome bc<sub>1</sub> complex structure*. Embo Journal, 2001. **20**(23): p. 6591-6600.
  8. Huang, L.S., et al., *Binding of the respiratory chain inhibitor antimycin to the mitochondrial bc<sub>1</sub> complex: A new crystal structure reveals an altered intramolecular hydrogen-bonding pattern*. Journal of Molecular Biology, 2005. **351**(3): p. 573-597.
  9. Gao, X.G., et al., *Structural basis for the quinone reduction in the bc<sub>1</sub> complex: A comparative analysis of crystal structures of mitochondrial cytochrome bc<sub>1</sub> with bound substrate and inhibitors at the Qi site*. Biochemistry, 2003. **42**(30): p. 9067-9080.
  10. Zhang, H.B., et al., *Exposing the complex III Qo semiquinone radical*. Biochimica Et Biophysica Acta-Bioenergetics, 2007. **1767**(7): p. 883-887.
  11. Ohnishi, T. and B.L. Trumpower, *Differential-Effects of Antimycin on Ubisemiquinone Bound in Different Environments in Isolated Succinate Cytochrome-C Reductase Complex*. Journal of Biological Chemistry, 1980. **255**(8): p. 3278-3284.
-

12. Salerno, J.C., et al., *Electron Nuclear Double-Resonance (ENDOR) of the QC-Ubisemiquinone Radical in the Mitochondrial Electron-Transport Chain*. *Biochemistry*, 1990. **29**(30): p. 6987-6993.
  13. Lendzian, F., et al., *ENDOR and pulsed EPR studies of photosynthetic reaction centers: Protein-cofactor interactions*. *Berichte Der Bunsen-Gesellschaft-Physical Chemistry Chemical Physics*, 1996. **100**(12): p. 2036-2040.
  14. Spoyalov, A.P., et al., *Evidence that Ala M260 is hydrogen-bonded to the reduced primary acceptor quinone Q(A)(-center dot) in reaction centers of Rb-sphaeroides*. *Chemical Physics Letters*, 1996. **263**(5): p. 715-720.
  15. Deligiannakis, Y., A. Boussac, and A.W. Rutherford, *ESEEM study of the plastoquinone anion radical (Q(A)(center dot-)) in N-14- and N-15-labeled photosystem II treated with CN*. *Biochemistry*, 1995. **34**(49): p. 16030-16038.
  16. Hanley, J., et al., *ESEEM study of the phyllosemiquinone radical A(1)(center dot-) in N-14- and N-15-labeled photosystem I*. *Biochemistry*, 1997. **36**(39): p. 11543-11549.
  17. Jegerschold, C., et al., *Effects of copper and zinc ions on photosystem II studied by EPR spectroscopy*. *Biochemistry*, 1999. **38**(38): p. 12439-12445.
  18. Grimaldi, S., et al., *Q(H)(center dot-) ubisemiquinone radical in the bo(3)-type ubiquinol oxidase studied by pulsed electron paramagnetic resonance and hyperfine sublevel correlation spectroscopy*. *Biochemistry*, 2001. **40**(4): p. 1037-1043.
  19. Lin, M.T., et al., *Identification of the Nitrogen Donor Hydrogen Bonded with the Semiquinone at the Q(H) Site of the Cytochrome bo(3) from Escherichia coli*. *Journal of the American Chemical Society*, 2008. **130**(47): p. 15768-+.
  20. Abramson, J., et al., *The structure of the ubiquinol oxidase from Escherichia coli and its ubiquinone binding site*. *Nature Structural Biology*, 2000. **7**(10): p. 910-917.
  21. Dikanov, S.A., et al., *Hydrogen bonds between nitrogen donors and the semiquinone in the Q(i)-site of the bc(1) complex*. *Journal of Biological Chemistry*, 2007. **282**(35): p. 25831-25841.
  22. Kolling, D.R.J., et al., *Exploration of ligands to the Q(i) site semiquinone in the bc(1) complex using high-resolution EPR*. *Journal of Biological Chemistry*, 2003. **278**(41): p. 39747-39754.
  23. Moebius, K., *High-field EPR on low-symmetry proteins to reveal structure-dynamics-function relations*. *Biochimica Et Biophysica Acta-Bioenergetics*, 2006: p. 78-78.
  24. Stoll, S., et al., *Nutation-frequency correlated EPR spectroscopy: The PEANUT experiment*. *Journal of Magnetic Resonance*, 1998. **130**(1): p. 86-96.
-

- 
25. Lawrence, C.C., et al., *High-field EPR detection of a disulfide radical anion in the reduction of cytidine 5'-diphosphate by the E441Q R1 mutant of Escherichia coli ribonucleotide reductase*. Proceedings of the National Academy of Sciences of the United States of America, 1999. **96**(16): p. 8979-8984.
  26. Maly, T. and T.F. Prisner, *Relaxation filtered hyperfine spectroscopy (REFINE)*. Journal of Magnetic Resonance, 2004. **170**(1): p. 88-96.
  27. Maly, T., et al., *Relaxation Filtered Hyperfine (REFINE) Spectroscopy: A Novel Tool for Studying Overlapping Biological Electron Paramagnetic Resonance Signals Applied to Mitochondrial Complex I*. Biochemistry, 2004. **43**(13): p. 3969-3978.
  28. Maly, T., et al., *New pulsed EPR methods and their application to characterize mitochondrial complex I*. Biochimica et Biophysica Acta (BBA) - Bioenergetics, 2009. **1787**(6): p. 584-592.
  29. Burghaus, O., et al., *3-Mm High-Field Epr on Semiquinone Radical-Anions Q.- Related to Photosynthesis and on the Primary Donor P.+ and Acceptor Qa.- in Reaction Centers of Rhodobacter-Sphaeroides R-26*. Journal of Physical Chemistry, 1993. **97**(29): p. 7639-7647.
  30. Slater, E.C., *The mechanism of action of the respiratory inhibitor, antimycin*. Biochim Biophys Acta, 1973. **301**(2): p. 129-54.
  31. Grimaldi, S., et al., *Asymmetric binding of the high-affinity Q(H)(center dot-) ubisemiquinone in quinol oxidase (bo(3)) from Escherichia coli studied by multifrequency electron paramagnetic resonance spectroscopy*. Biochemistry, 2003. **42**(19): p. 5632-5639.
  32. Schweiger, A. and G. Jeschke, *Principles of pulse electron paramagnetic resonance*. 2001, Oxford, UK ; New York: Oxford University Press. xxvi, 578.
  33. Maly, T., et al., *Relaxation filtered hyperfine (REFINE) spectroscopy: a novel tool for studying overlapping biological electron paramagnetic resonance signals applied to mitochondrial complex I*. Biochemistry, 2004. **43**(13): p. 3969-78.
  34. Maly, T. and T.F. Prisner, *Relaxation filtered hyperfine spectroscopy (REFINE)*. J Magn Reson, 2004. **170**(1): p. 88-96.
-